NANOSCALE COORDINATION POLYMERS FOR BIOMEDICAL APPLICATIONS AND HYBRID MATERIALS FOR SOLAR FUEL CATALYSIS

Kathryn E. deKrafft

A dissertation submitted to the faculty of the University of North Carolina at Chapel Hill in partial fulfillment of the requirements for the degree of Doctor of Philosophy in the Department of Chemistry.

Chapel Hill
2012

Approved by:

Dr. Wenbin Lin

Dr. Michel Gagné

Dr. Joseph Templeton

Dr. Wei You

Dr. Mark Schoenfisch

ABSTRACT

KATHRYN E DEKRAFFT: Nanoscale Coordination Polymers for Biomedical Applications and Hybrid Materials for Solar Fuel Catalysis
(Under the direction of Wenbin Lin)

This dissertation describes the design, synthesis, and characterization of hybrid materials and their evaluation for use in several biomedical and solar fuel applications. Most of the materials are nanoparticles based on coordination polymers (CPs), a class of highly tunable hybrid materials composed of organic bridging ligands linked together by metal ions. Nanoscale CPs (NCPs) have been developed for biomedical imaging contrast enhancement and for drug delivery. They have been designed to carry high payloads of diagnostic or therapeutic agents, and to overcome the disadvantages of conventional small-molecule agents by improved pharmacokinetics and biodistribution.

NCPs containing elements with high X-ray attenuation have been developed for use as contrast agents for computed tomography (CT) imaging. NCPs based on an iodinated ligand or on Zr or Hf ions were synthesized, and their potential for CT contrast enhancement was demonstrated in phantom studies. The robust Hf-based NCPs were coated and functionalized to increase biocompatibility and performance, and were used for *in vivo* CT imaging. NCPs for drug delivery have been designed based on methotrexate, a molecular anticancer drug that is a first-line treatment for leukemia. The NCP approach to drug

formulations offers a potential way to target and deliver high payloads of methotrexate to cancer cells.

Photocatalytic and electrocatalytic materials have been developed toward the goal of storing harvested solar energy in chemical fuels by water splitting. A new CP-templated method has been developed for the synthesis of a metal oxide nanocomposite with interesting photophysical properties. Fe-containing NCPs were coated with amorphous titania, then calcined to produce crystalline Fe_2O_3/TiO_2 composite nanoparticles. This material enables photocatalytic hydrogen production from water using visible light, which cannot be achieved by either Fe_2O_3 or TiO_2 alone or a mixture of the two.

Molecular Ir and Ru complexes were directly and covalently grafted onto carbon electrodes, for electrocatalytic water oxidation. The catalysts had enhanced rates and stability when grafted and driven electrochemically compared to being chemically-driven in solution. This strategy provides a way to systematically evaluate catalysts under tunable conditions, potentially providing new insights into electrochemical water oxidation processes and water oxidation catalyst design.

ACKNOWLEGMENTS

I have many people to thank for supporting my work and contributing to my graduate education. I would like to thank my advisor, Dr. Wenbin Lin, for the opportunity to do research in his lab and to learn from him. He has generated many new and interesting ideas for me to pursue and has provided guidance in my work. I would also like to thank the other members of my dissertation committee, Dr. Michel Gagné, Dr. Joe Templeton, Dr. Mark Schoenfisch, and Dr. Wei You, for their time and consideration of my dissertation.

Many people have directly contributed toward the research presented in this dissertation. Dr. Zhigang Xie synthesized several organic molecules for my projects, and Dr. Liqing (Sam) Ma determined crystal structures for several materials. Members of Dr. Otto Zhou's group in the Department of Physics, in particular Guohua Cao and Laurel Burk, performed computed tomography studies. Rachel Huxford-Phillips worked closely with me on drug delivery and expanded the project to include targeting and cell studies. Cheng (Wave) Wang evaluated photocatalytic activity of several materials. Dr. Bruce Hinds and Xin Su of the University of Kentucky collaborated with me on electrochemical water oxidation studies. Undergraduate students Will Boyle, Sylvie Tran, and Yuli (David) Jiang helped with nanoparticle synthesis and characterization.

Several people have helped me obtain and interpret data from particular instruments. These people include Amar Kumbar, Carrie Donley, and Wallace Ambrose of the Chapel Hill Analytical and Nanofabrication Laboratory, Peter White of the X-ray Facility, and

Sohrab Habibi of the Mass Spectrometry Facility. Alessa Gambardella, Alexis Wells Carpenter, and Dr. Zuofeng Chen have been helpful in using other instrumentation.

I have learned a great deal and been given direction by people who have passed on their knowledge and lab techniques to me, including former Lin Lab members Dr. Kathryn Taylor-Pashow, Dr. Dave Mihalcik, and Dr. B.J. Rieter, and members of the School of Pharmacy Dr. Leaf Huang and Dr. Feng Liu. Members of the UNC Energy Frontier Research Center have shared useful information and made suggestions on projects concerning solar energy. In addition to the individuals already mentioned, I would also like to thank the following Lin Lab members for insightful conversations that aided in the progression of my work: Dr. Juan Vivero-Escoto, Joe Della Rocca, Joe Falkowski, Demin Liu, and Caleb Kent.

I would like to acknowledge financial support from the National Institutes of Health, the National Science Foundation, and the UNC Energy Frontier Research Center funded by the Department of Energy. I also thank the UNC Graduate School for a Dissertation Completion Fellowship.

TABLE OF CONTENTS

LIST OF TABLES

Table

LIST OF FIGURES

Figure

LIST OF ABBREVIATIONS AND SYMBOLS

º	degrees
@	denotes one component inside of another
μ	micro-
ν	frequency
λ	wavelength
θ	angle
Å	angstroms
aq.	aqueous
1	glassy carbon electrode grafted with [Cp*IrCl(4-NH_2-bpy)]Cl
2	glassy carbon electrode grafted with [Cp*IrCl(5-NH_2-bpy)]Cl
3	glassy carbon electrode grafted with [Cp*IrCl(*p*-NH_2-ppy)]
4	glassy carbon electrode grafted with [Ru(Mebimpy)(4-NH_2-bpy)OTf]OTf
5	glassy carbon electrode grafted with [Ru(tpy)(4-NH_2-bpy)Cl]Cl
A	amperes
A	[Cp*IrCl(4-NH_2-bpy)]Cl
atm	atmospheres
a.u.	arbitrary units
B	[Cp*IrCl(5-NH_2-bpy)]Cl
BDC	benzene dicarboxylic acid
BSA	bovine serum albumin
bpy	2,2'-bipyridine
c	centi-
C	Celsius *or* Coulombs

C	[Cp*IrCl(*p*-NH_2-ppy)]
$CDCl_3$	deuterated chloroform
CP	coordination polymer
Cp*	pentamethylcyclopentadienyl
CT	computed tomography
CTAB	cetyltrimethylammonium bromide
CV	cyclic voltammetry
d	distance
D	[Ru(Mebimpy)(4-NH_2-bpy)OTf]OTf
DEF	N,N'-diethylformamide
DLS	dynamic light scattering
DMF	N,N'-dimethylformamide
DMSO	dimethyl sulfoxide
E	reduction potential
E	[Ru(tpy)(4-NH_2-bpy)Cl]Cl
e^-	electron
ECG	electrocardiography
EDS	energy dispersive X-ray spectroscopy
EPR	enhanced permeability and retention
ESI	electrospray ionization
eV	electron volts
g	grams
GC	gas chromatography

h	Planck constant
h	hours
Hf-NMOF	$[Hf_6O_6(OH)_4(BDC)]$
HRTEM	high resolution transmission electron microscopy
HU	Hounsfield unit
Hz	hertz
I	current
I_4-BDC-H_2	2,3,5,6-tetraiodo-1,4-benzenedicarboxylic acid
I-CP-1	$[Cu(I_4\text{-BDC})(DMF)_2]$
I-CP-2	$[Cu(I_4\text{-BDC})(DEF)_2(H_2O)]$
I-CP-3	$[Cu(I_4\text{-BDC})(H_2O)_2]\cdot 2H_2O$
I-CP-4	$[Zn(I_4\text{-BDC})(DMF)_{2.5}]$
I-CP-5	$[Zn(I_4\text{-BDC})(EtOH)_2]\cdot 2EtOH$
ICP-MS	inductively coupled plasma mass spectrometry
IR	infrared
k	kilo-
K	Kelvin
K_{sp}	solubility product
L	liters
m	milli- *or* meters
M	mega- *or* molar
Mebimpy	2,6-bis(benzimidazol-2-yl)pyridine
MeOD	deuterated methanol

min	minutes
MOF	metal-organic framework
mol	moles
MS	mass spectrometry
MTX	methotrexate
m/Z	mass-to-charge ratio
n	nano-
N	nanoscale
NHE	normal hydrogen electrode
NMR	nuclear magnetic resonance spectroscopy
OTf	triflate
PBS	phosphate buffered saline
PEG	poly(ethylene glycol)
ppm	parts per million
ppy	2-phenylpyridine
psi	pounds per square inch
PVP	polyvinylpyrrolidone
PXRD	powder X-ray diffraction
RES	reticuloendothelial system
rpm	rotations per minute
sec	seconds
SEM	scanning electron microscopy
STEM	scanning transmission electron microscopy

TALH	titanium(IV) bis(ammonium lactato)dihydroxide
TEA	triethylamine
TEOS	tetraethyl orthosilicate
TEM	transmission electron microscopy
TGA	thermogravimetric analysis
TOF	turnover frequency
TON	turnover number
tpy	2,6-bis(2-pyridyl)pyridine
UV	ultraviolet
v	volume
V	volts
vis	visible
Vp	peak voltage
vs	versus
W	watts
W	water to surfactant molar ratio
wt	weight
WOC	water oxidation catalyst
XPS	X-ray photoelectron spectroscopy
Zr-NMOF	$[Zr_6O_6(OH)_4(BDC)]$

CHAPTER 1

Iodinated Nanoscale Coordination Polymers as Potential Contrast Agents for Computed Tomography

(Portions of this chapter were adapted with permission from deKrafft, K.E.; Xie, Z.; Cao, G.; Tran, S.; Ma, L.; Zhou, O.Z.; Lin. *Angew. Chem. Int. Ed.* **2009**, *48*, 9901. Copyright 2009 John Wiley and Sons.)

1.1. Introduction

1.1.1 Computed tomography

X-ray computed tomography (CT) is a type of biomedical imaging that is capable of providing three-dimensional images with excellent spatial resolution.[1, 2] Structures in the body can be rendered in three dimensions from a series of two-dimensional X-ray images taken from a single axis of rotation. CT is routinely used to image a wide range of structures throughout the entire body including organs, blood vessels, and bones. It is an important tool for diagnosing and monitoring diseases and abnormalities throughout the body, including tumors, calcifications, embolisms, aneurysms, and inflammation. CT is based on differences in X-ray attenuation, the ability of different materials to block X-rays to different degrees. Materials with high electron density appear bright while those with low electron density appear dark. A contrast agent with high X-ray attenuation is often used in CT imaging to provide better contrast between the tissue of interest and its surroundings.[3-6] Materials with high electron density block X-rays more effectively, therefore elements with high atomic numbers, like iodine, gold, bismuth, and gadolinium, have been considered for use as contrast agents. However, the only CT contrast agents currently approved for clinical use are

iodinated aromatic molecules (Fig. 1.1), and barium sulfate for gastrointestinal tract imaging. CT imaging with small-molecule contrast agents is limited by their nonspecific distribution, rapid renal clearance, and fast extravasation from blood and lymphatic vessels.[3-6] Due to these issues as well as the low sensitivity of this imaging modality, large doses (typically 30 g of I or 70 g total material) must be administered to achieve adequate contrast,[5] sometimes causing adverse reactions for the patients.

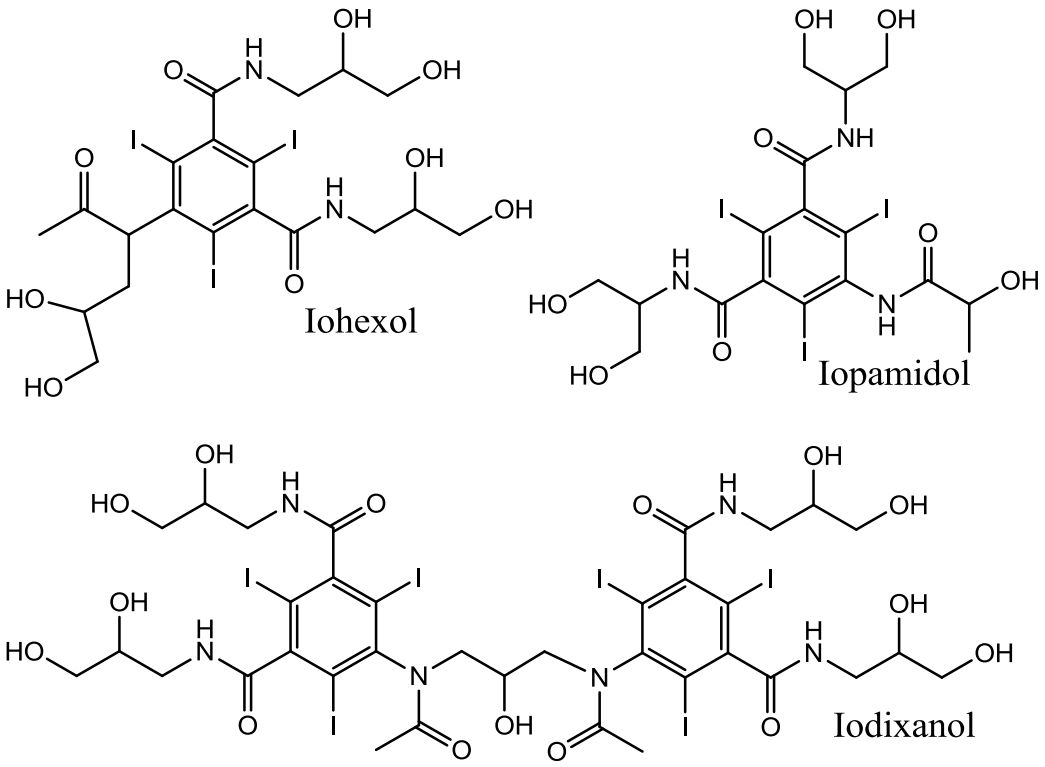

Figure 1.1. Examples of clinically used molecular CT contrast agents.

1.1.2. Nanoparticle contrast agents

Nanoparticles bridge the gap between molecular and bulk materials, and are defined as particles that are 1-1,000 nm in at least one dimension.[7] Scaling materials down to the nanometer-regime makes them suitable for biomedical applications. Organic nanomaterials like liposomes and polymer particles, as well as inorganic nanomaterials like iron oxide

nanoparticles, and quantum dots have been used for biological applications.[8-11] Many of the limitations of molecular contrast agents can be overcome by nanoparticulate contrast agents that can carry a high payload and be functionalized to increase blood circulation times and to endow target specificity.[12] Nanoparticles do not readily diffuse into extravascular space or undergo rapid renal clearance, thus allowing adequate time for accumulation at a disease site. These advantages could allow for a larger time window for imaging and enhanced image contrast at a lower dose. Several nanoparticle systems including Bi_2S_3,[13] gold,[14, 15] and iodinated organic nanoparticles,[16-18] have recently been evaluated as next-generation CT contrast agents. However, it is challenging to formulate nanoparticles with high loadings for elements having high atomic numbers that are also nontoxic and able to be cleared from the body in a timely fashion.

1.1.3. Nanoscale coordination polymers

Most nanoparticles contain either only organic or only inorganic components. Coordination polymers (CPs) have recently emerged as hybrid materials composed of organic bridging ligands that are coordinatively bonded to metal ions or metal ion clusters.[19-22] When CPs are crystalline and three-dimensional, they are often referred to as metal-organic frameworks (MOFs), depicted schematically in Fig. 1.2. CP composition is highly tunable due to an infinite number of possible metal and ligand combinations. There is also much structural diversity depending on coordination modes of the metals and steric or geometric constraints imposed by the ligands. The building blocks can assemble into one-dimensional chains, two-dimensional sheets, or three-dimensional networks with uniform pores and channels. The synthesis and development of a new class of nanomaterials has recently been demonstrated by scaling down CPs to the nanoregime.[23, 24] These nanoscale

CPs (NCPs) and nanoscale MOFs (NMOFs) have already shown great potential in biosensing,[25] magnetic resonance imaging,[26, 27] and drug delivery.[28] NCPs possess some potential advantages over existing nanoparticles because their composition, structure, and chemical properties are highly tunable and diverse. The labile metal-ligand bonds make NCPs intrinsically biodegradable, allowing clearance from the body after use. Given the clinical utility of iodinated aromatic molecules in CT imaging, it was surmised that iodinated NCPs could have potential applications as CT contrast agents owing to their ability to carry a very high payload of iodine. This has been demonstrated by synthesizing new iodinated coordination polymers and scaling them down to the nano-regime. The ability of iodinated NCPs to attenuate X-rays has been demonstrated in phantom studies.

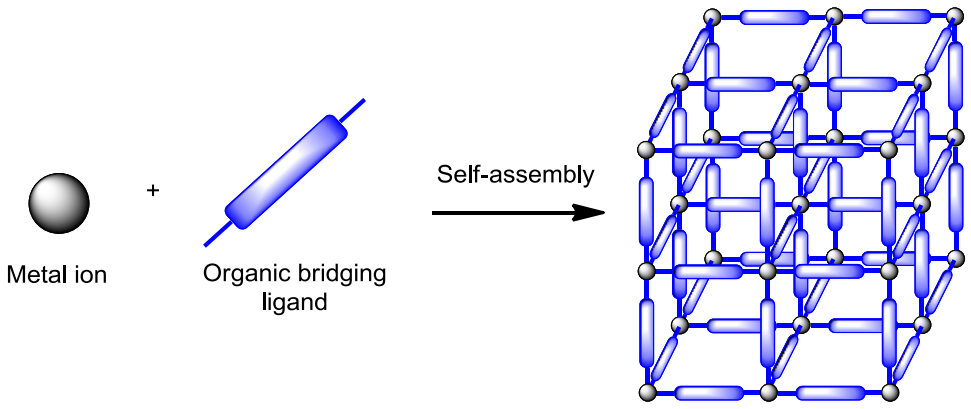

Figure 1.2. Schematic showing the self-assembly of metal-organic frameworks.

There are many methods of synthesizing NCPs and NMOFs, mostly by taking advantage of the reduced solubility of the particles compared to that of the individual components. Methods include simple mixing of precursor solutions,[29] precipitation by rapid addition of a poor solvent,[30] solvothermal synthesis,[31] reverse microemulsion,[26] and high-temperature surfactant-assisted synthesis.[32] Properties of the nanoparticles, like size and shape, can be tuned by varying many reaction parameters. Choice of solvent, metal and

ligand concentrations, metal to ligand ratio, temperature, and duration of the reaction can all affect the resulting particles. For the microemulsion and surfactant-assisted syntheses, other important parameters include choice of surfactant, pH of the aqueous phase, and *W* value (water to surfactant molar ratio). A reverse microemulsion, shown in Fig. 1.3, is a thermodynamically stable isotropic mixture of water droplets dispersed throughout a continuous immiscible organic phase, with the droplets stabilized by micelles, made of interfacial surfactant molecules. The *W* value and surfactant concentration determine the size and number of micelles. Reactants dissolved in the aqueous phase of two separate microemulsions can be combined so that they react in the microdroplets of water, which continuously exchange their contents through collision, coalescence, and division, resulting in a precipitate. In the high-temperature surfactant-assisted method, the microemulsion breaks down as the temperature is elevated, and the surfactant acts to stabilize particles against aggregation during synthesis. Nanoparticles can be isolated from their reaction mixtures by centrifugation and can be washed several times to remove impurities. Crystalline NCPs usually adopt well-defined, non-spherical morphologies because crystal lattice energy is the most influential factor in their growth. On the other hand, amorphous NCPs are usually spherical because this morphology minimizes interfacial free energy between the particles and solvent during their formation.[23] The crystallinity, size, and shape of particles are dependent on the rates of nucleation and growth, two kinetic phenomena that respond differently to reaction conditions.

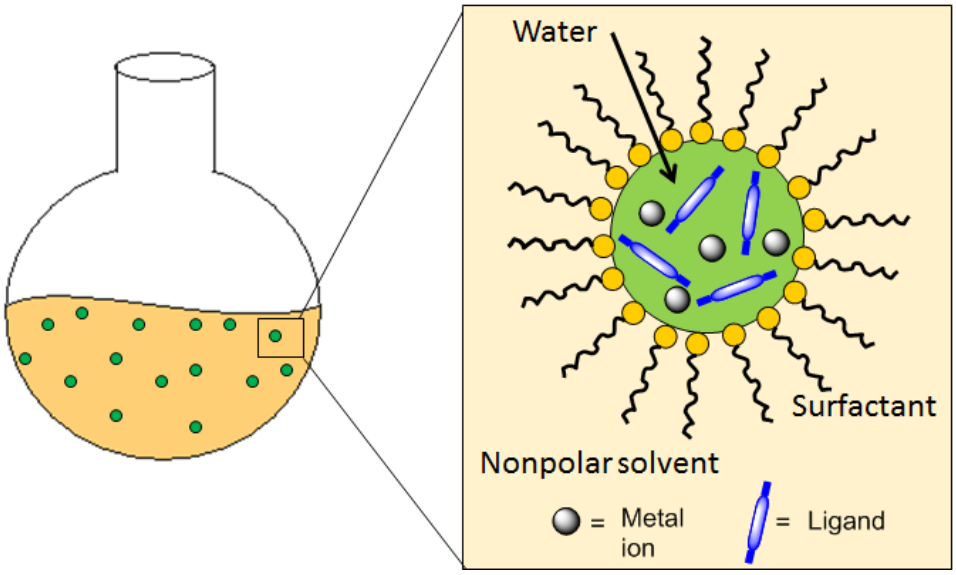

Figure 1.3. Schematic showing the synthesis of a NCP or a NMOF in a reverse microemulsion.

1.2. Results and Discussion

1.2.1. Synthesis and characterization of iodinated coordination polymers

As shown in Fig. 1.4, five new coordination polymers were synthesized using 2,3,5,6-tetraiodo-1,4-benzenedicarboxylate (I_4-BDC) bridging ligands and Cu^{2+} or Zn^{2+} metal connecting points. The reaction of I_4-BDC-H_2 and $Cu(NO_3)_2$ in N,N-dimethylformamide (DMF) at 80 ºC for 3 days led to blue rectangular plate-like crystals of [Cu(I_4-BDC)$(DMF)_2$] (**I-CP 1**) in 28% yield. Similar crystal growth in N,N'-diethylformamide (DEF) and in H_2O led to bluish-green rodlike crystals of [Cu(I_4-BDC)$(DEF)_2(H_2O)$] (**I-CP 2**) in 58% yield and green rod-like crystals of [Cu(I_4-BDC)$(H_2O)_2$]·$2H_2O$ (**I-CP 3**) in 69% yield, respectively. To demonstrate the generality of this synthetic approach, we have also synthesized iodinated coordination polymers with Zn^{2+} metal connecting points. Colorless rod-like crystals of [Zn(I_4-BDC)$(DMF)_{2.5}$] (**I-CP 4**) were obtained in 55% yield by the reaction of I_4-BDC-H_2 and $Zn(NO_3)_2$ in DMF at 60 ºC for 4 days. Colorless rod-like crystals of [Zn(I_4-

BDC)(EtOH)$_2$]·2EtOH (**I-CP 5**) were obtained in 28% yield by slow evaporation of a solution of I_4-BDC-H_2 and $Zn(NO_3)_2$ in ethanol. The synthesis of coordination polymers in H_2O and in ethanol (**I-CP 3** and **I-CP 5**) demonstrates the ability to obtain iodinated coordination polymers that contain nontoxic solvents, thus making them more relevant for potential biological and biomedical applications.

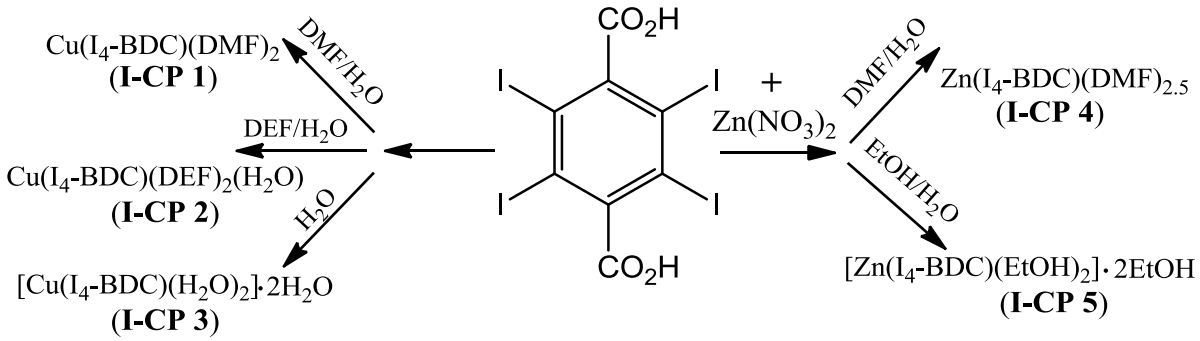

Figure 1.4. Scheme for the synthesis of iodinated coordination polymers (**I-CPs) 1**-**5**.

Single-crystal X-ray diffraction studies of **I-CPs 1**–**5** revealed one-dimensional polymeric structures for all five coordination polymers (Fig. 1.5). Table 1.1 contains unit cell parameters and other detailed crystallographic data. In **I-CP 1**, Cu^{2+} ions coordinate to two chelating carboxylate groups of the I_4-BDC ligand and two molecules of DMF in the axial positions to form a one-dimensional polymeric network (Fig. 1.6). In **I-CP 2**, both carboxylate groups of the I_4-BDC ligand are monodentate (Fig. 1.7). The Cu^{2+} ions adopt a square pyramidal geometry by coordinating to two monodentate carboxylate groups as well as one water and two DEF molecules. The structure of **I-CP 3** is ladder-like with one carboxylate group of the ligand acting in a monodentate fashion, while the other adopts the η^1, μ_2 bridging mode (Fig. 1.8). Each Cu^{2+} center thus coordinates to three carboxylate oxygen atoms and two water molecules in a square pyramidal geometry. The I_4-BDCs on

each side of the ladder polymer chain are offset by 2.25 Å along the *a* axis, while the distance between a pair of I_4-BDCs is 4.06 Å. In **I-CP 4**, one I_4-BDC ligand has both monodentate carboxylate groups whereas the other I_4-BDC ligand has one monodentate and one chelating carboxylate group (Fig. 1.9). The adjacent Zn^{2+} centers in the zigzag polymeric chain adopt a tetrahedral geometry by coordinating to two monodentate carboxylate groups and two DEF molecules, and a distorted octahedral geometry by coordinating to one monodentate and one chelating carboxylate groups and three DEF molecules, respectively. **I-CP 5** has a simpler zigzag polymeric chain structure with all the Zn^{2+} centers adopting tetrahedral geometry by coordinating to two monodentate carboxylate groups and two ethanol molecules (Fig. 1.10). Importantly, the steric bulk of the iodine atoms forces the carboxylate groups of the I_4-BDC ligand to be perpendicular to the tetraiodobenzene ring in all of these structures. We believe that the steric bulk of iodine atoms also discourages the carboxylate groups of the I_4-BDC ligands from adopting the bridging coordination mode (except in **I-CP 3**), which can lead to the formation of coordination polymers of higher dimensionality. The thermogravimetric analyses (TGA) of bulk crystals of **I-CPs 1**–**5** show solvent and organic weight loss that correspond closely to the formulas obtained from X-ray diffraction data (Table 1.2, Fig. 1.12-1.14). Heating the crystals to 600 ºC causes the solvents and organic ligands to burn away, leaving behind CuO for **I-CPs 1**-**3** and ZnO for **I-CPs 4**-**5**. For most, there is slightly less weight loss than the theoretical loss calculated from the formula due to evaporation of some of the solvent. For example, for **I-CP 4**, if it is assumed that DMF is gone by 230 °C (20.0% theoretical loss, 12.6% observed), theoretical weight loss due to I_4-BDC decomposition (by 600 °C) should be 88.9%, which matches the observed weight loss.

Table 1.1. Crystal data and structure refinement for **I-CPs 1-5**.

Compound	**I-CP 1**	**I-CP 2**	**I-CP 3**	**I-CP 4**	**I-CP 5**
Empirical Formula	$C_{14}H_{14}N_2O_6$-CuI_4	$C_{18}H_{22}N_2O_7$-CuI_4	$C_8H_8O_8CuI_4$	$C_{31}H_{35}N_5O_{13}$-Zn_2I_8	$C_{16}H_{22}O_8ZnI_4$
Formula Weight	877.41	949.52	803.28	1831.58	915.31
Temperature (K)	258	100	296	223	243
Wavelength (Å)	1.54178	1.54178	1.54178	1.54178	1.54178
Crystal System	Orthorhombic	Monoclinic	Monoclinic	Orthorhombic	Monoclinic
Space Group	$Cmc2_1$	$P2_1$	$P2_1/c$	$P2_12_12_1$	C2/c
Unit cell dimensions	a = 10.928(1)	a = 11.175(1)	a = 11.020(1)	a = 10.387(1)	a = 11.433(1)
	b = 21.668(2)	b = 10.114(1)	b = 9.690(1)	b = 11.758(1)	b = 14.879(1)
	c = 9.579(1)	c = 12.246(1)	c = 15.937(1)	c = 38.819(2)	c = 15.438(1)
	α = 90.00	α = 90.00	α = 90.00	α = 90.00	α = 90.00
	β = 90.00	β = 107.293	β = 105.164	β = 90.00	β = 95.718
	γ = 90.00	γ = 90.00	γ = 90.00	γ = 90.00	γ = 90.00
Volume ($Å^3$)	2268.1(3)	1321.5(1)	1642.5(2)	4740.9(3)	2613.16(9)
Z	4	2	4	4	4
Density (calcd. g/cm^3)	2.569	2.386	3.248	2.566	2.327
Absorption coeff. (mm^{-1})	44.39	38.196	61.23	42.676	38.723
F (000)	1604	882	1444	3376	1696
Crystal size (mm)	0.11x0.11x 0.06	0.19x0.17x 0.12	0.10x0.10x 0.10	0.15x0.12x 0.08	0.18x0.18x 0.05
Crystal color and shape	blue rectangular plate	bluish-green rod	green rod	colorless rod	colorless rod
θ data collection	4.08-65.32	3.78-68.10	4.16-66.27	2.28-66.34	4.89-69.34

Limiting indices	-12< h <11	-13< h <13	-13< h <12	-12< h <12	-12< h <13
	-21< k <25	-11< k <11	0< k <11	-13< k <12	-18< k <16
	-10< l <10	-14< l <14	0< l <18	-46< l <45	-18< l <18
Reflections collected	3939	6111	2802	36860	8117
Independent reflections	1676	3786	2802	8134	2401
Refinement Method	Full-matrix least-square on F^2				
Data/ restraints/ parameters	1676/127/1	3786/258/1	2802/192/47	8134/297/0	2401/135/0
Goodness-of-fit on F^2	0.999	0.910	1.011	1.048	1.042
	(0.998, restrained)	(0.910, restrained)	(1.005, restrained)	(1.048, restrained)	(1.042, restrained)
Final R indices $[I>2\sigma(I)]^{a,b}$	R1 = 0.0666	R1 = 0.0288	R1 = 0.0560	R1 = 0.0456	R1 = 0.0340
	wR2 =0.1665	wR2 =0.0627	wR2 =0.1304	wR2 =0.0958	wR2 =0.0838
R indices (all data)	R1 = 0.0932	R1 = 0.0306	R1 = 0.0771	R1 = 0.0536	R1 = 0.0386
	wR2 =0.1847	wR2 =0.0636	wR2 =0.1388	wR2 =0.0988	wR2 =0.0866
Flack	0.434(4)	0.020(7)	-	0.018(8)	-

[a] $R(F) = \Sigma||F_o| - |F_c||/\Sigma|F_o|$. [b] $R_W(F^2) = [\Sigma\{w(F_o^2 - F_c^2)^2\}/\Sigma\{w(F_o^2)^2\}]^{0.5}$; $w^{-1} = \sigma^2(F_o^2) + (aP)^2 + bP$, where $P=[F_o^2 + 2F_c^2]/3$ and *a* and *b* are constants adjusted by the program.

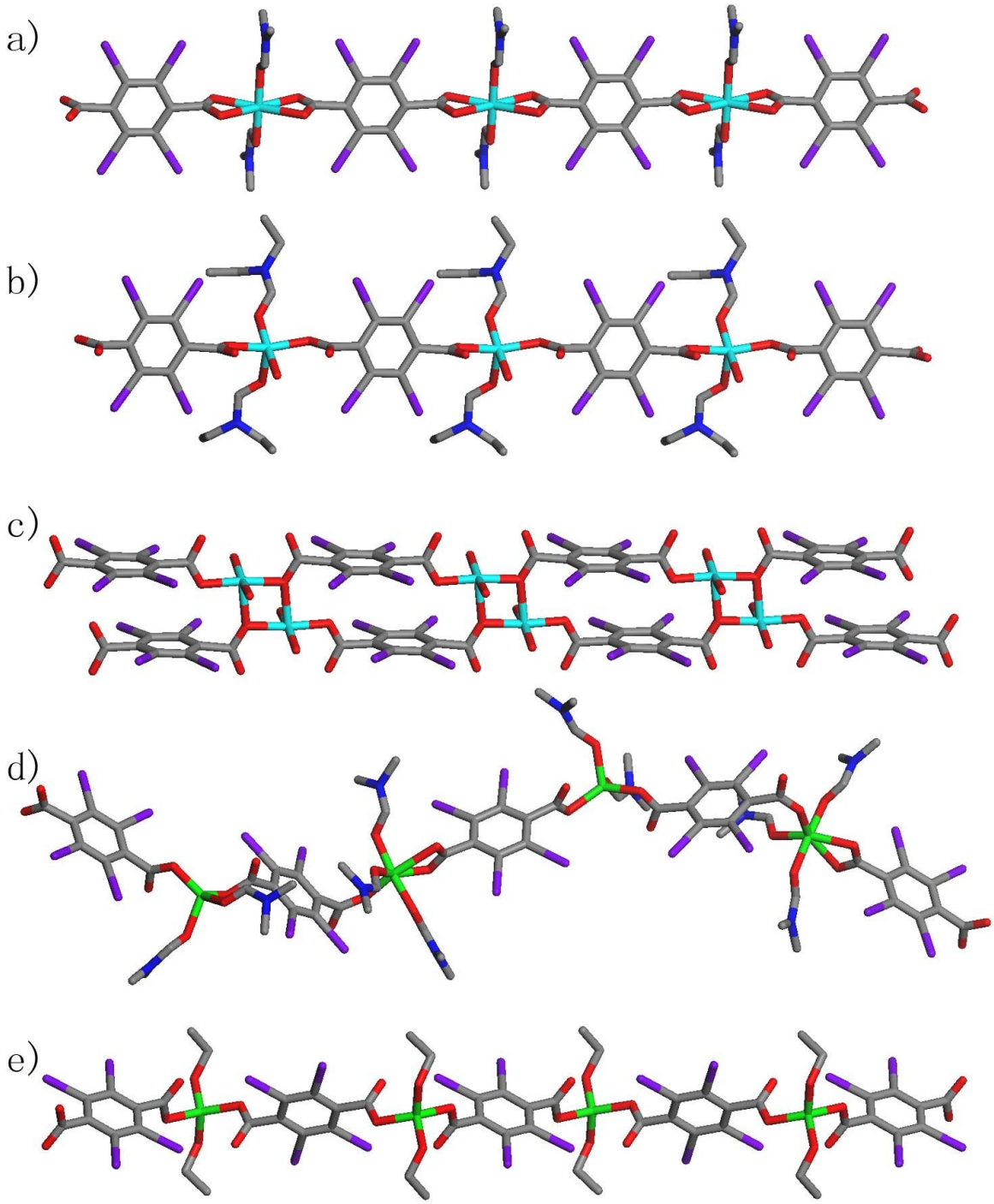

Figure 1.5. Stick models showing the one dimensional polymeric structure of (a) $Cu(I_4\text{-}BDC)(DMF)_2$ (**I-CP 1**), (b) $Cu(I_4\text{-}BDC)(DEF)_2(H_2O)$ (**I-CP 2**), (c) $[Cu(I_4\text{-}BDC)(H_2O)_2]\cdot 2H_2O]$ (**I-CP 3**), (d) $Zn(I_4\text{-}BDC)(DMF)_{2.5}$ (**I-CP 4**), and (e) $[Zn(I_4\text{-}BDC)(EtOH)_2]\cdot 2EtOH]$ (**I-CP 5**). Grey, blue, red, purple, aqua and green colors represent C, N, O, I, Cu, and Zn atoms, respectively.

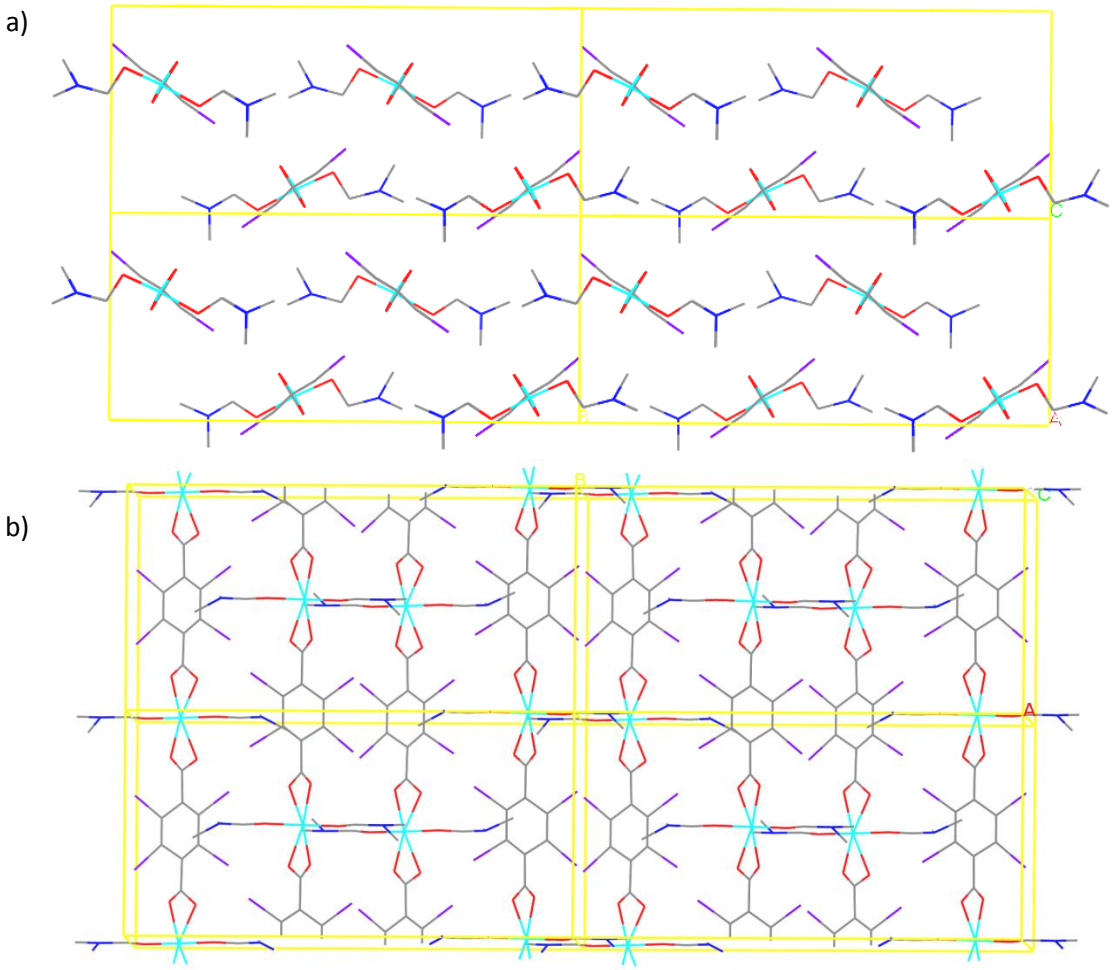

Figure 1.6. Packing diagrams of **I-CP 1** as viewed along (a) the *a* axis, and (b) the *c* axis. Grey, red, blue, purple, and aqua colors represent C, O, N, I, and Cu atoms, respectively.

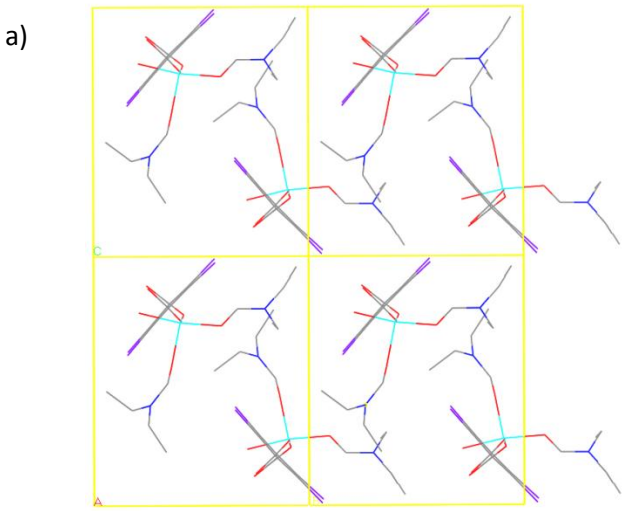

b)

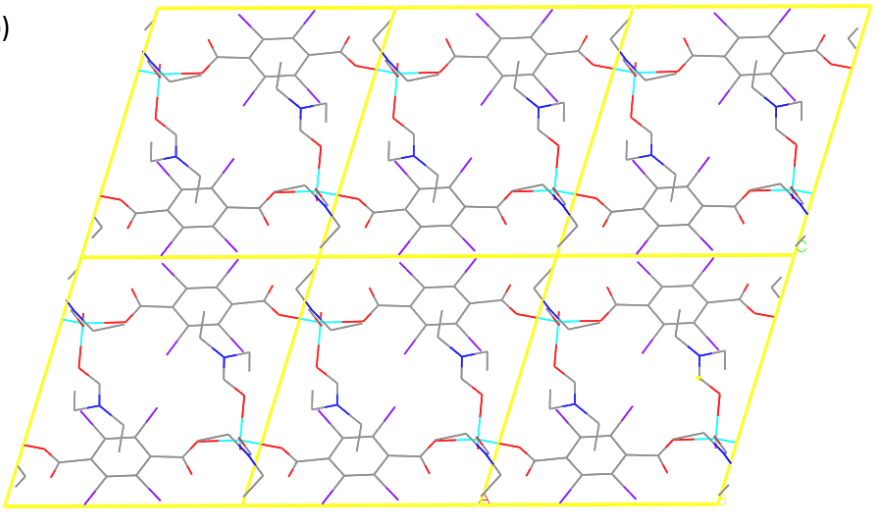

Figure 1.7. Packing diagram of **I-CP 2** as viewed along (a) the *a* axis, and (b) the *b* axis. Grey, red, blue, purple, and aqua colors represent C, O, N, I, and Cu atoms, respectively.

a)

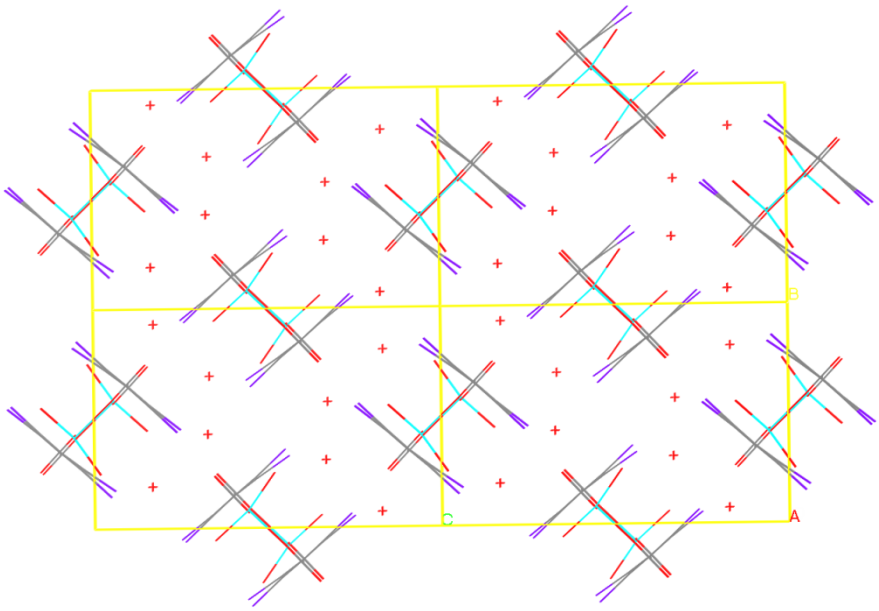

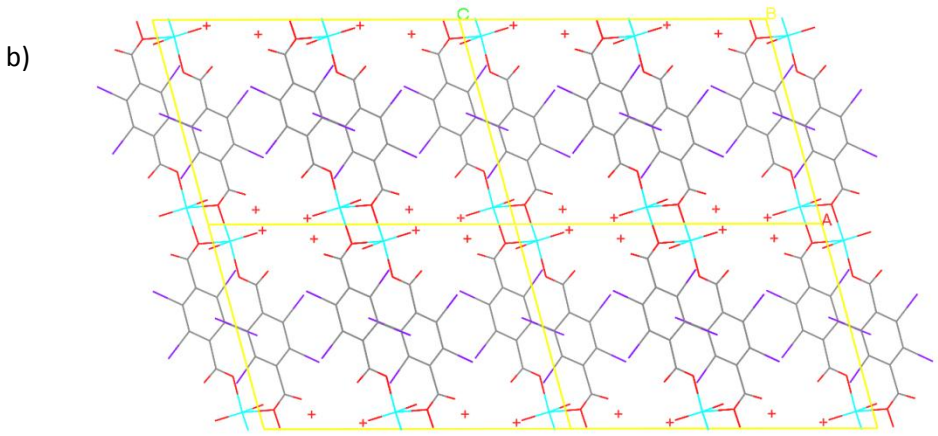

Figure 1.8. Packing diagram of **I-CP 3** as viewed along (a) the *a* axis, and (b) the *b* axis. Grey, red, purple, and aqua colors represent C, O, I, and Cu atoms, respectively.

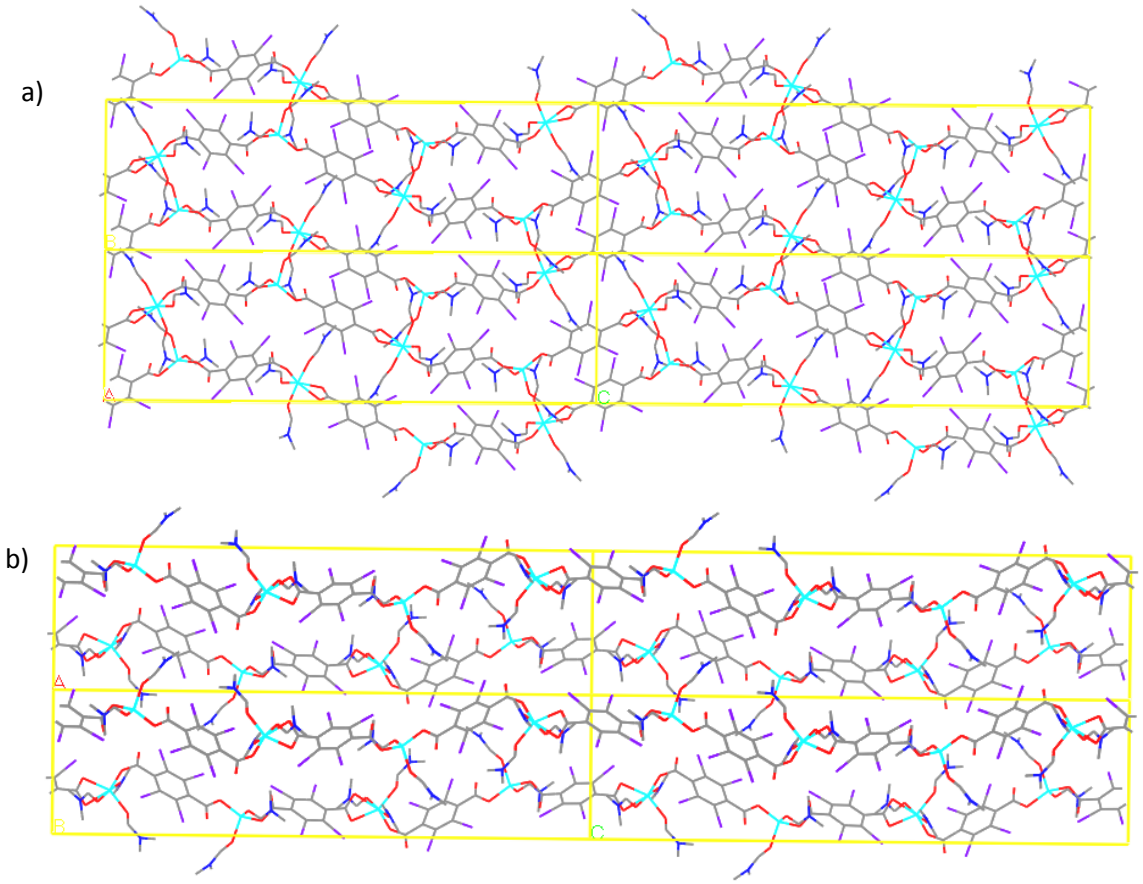

Figure 1.9. Packing diagram of **I-CP 4** as viewed along (a) the *a* axis, and (b) the *b* axis. Grey, red, blue, purple, and aqua colors represent C, O, N, I, and Zn atoms, respectively.

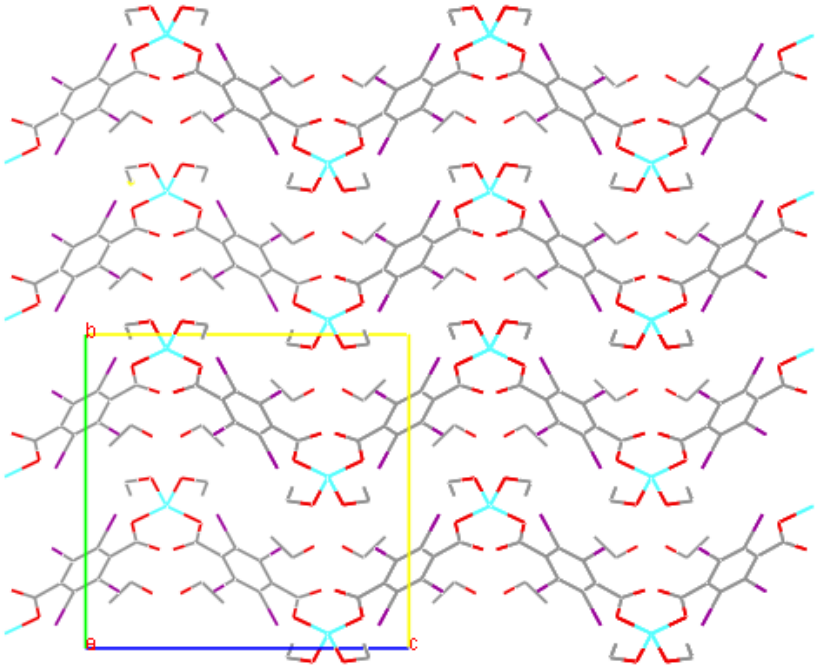

Figure 1.10. Packing of the zig-zag 1-D polymeric chains in **I-CP 5** as viewed along the *a* axis. Grey, red, purple, and aqua colors represent C, O, I, and Zn atoms, respectively.

Table 1.2. TGA weight loss from **I-CP 1**-**5**.

Compound	**I-CP 1**	**I-CP 2**	**I-CP 3**	**I-CP 4**	**I-CP 5**
Observed wt% loss, 25-600 ºC	89.7	89.8	90.8	90.3	90.7
Theoretical wt% loss, 25-600 ºC	90.9	91.6	89.6	91.1	91.1

1.2.2. Synthesis and characterization of iodinated nanoscale coordination polymers

We were able to synthesize nanoscale coordination polymers of both a Cu^{2+} and a Zn^{2+}-containing phase, with coordinating H_2O and ethanol molecules, respectively. Plate-like nanoparticles of **I-CP 3** (**I-NCP 3a**) were synthesized in 75% yield by stirring a microemulsion of 0.3 M Triton X-100 and 1.5 M 1-hexanol in cyclohexane with a water to surfactant ratio of 15 (*W* value), which contained equal molar amounts of $Na_2(I_4\text{-BDC})$ and $Cu(NO_3)_2$ at room temperature for 2 h. The **I-NCP 3a** particles were isolated by

centrifugation and washed with ethanol. Scanning electron microscopy (SEM) images showed that plate-like particles of **I-NCP 3a** have a diameter of 300 nm and are 50 nm thick (Fig. 1.11a). Powder X-ray diffraction (PXRD) studies indicate that the **I-NCP 3a** particles are crystalline and have the same structure as the bulk phase of **I-CP 3** (Fig. 1.11c). Interestingly, nanoparticles of **I-CP 3** with a rod-like morphology (**I-NCP 3b**) were obtained in 60% yield when the same reaction was carried out in a microemulsion of 0.1 M cetyltrimethylammonium bromide (CTAB) and 0.5 M 1-hexanol in isooctane (W=15). SEM images show that **I-NCP 3b** particles are about 1.5 μm in length and 200 nm in width (Fig. 1.11b), and PXRD studies indicate that the particles are crystalline and also have the same structure as the bulk phase of **I-CP 3**. Slight peak shifts in the PXRD patterns can be attributed to differences in the temperatures at which data were acquired and the degree of solvent loss from the sample, both of which can slightly change the size of the unit cell. Many of the diffraction peaks are missing in the PXRD patterns of the NCPs because of the preferential growth along certain crystallographic faces. The composition of **I-NCPs 3a** and **3b** was also confirmed by TGA (Fig. 1.12) and energy dispersive X-ray spectroscopy (EDS) results (Fig. 1.16a-b). The ready loss of solvents from NCPs complicates the TGA data analysis for **I-NCPs 3a** and **3b**. If it is assumed that all H_2O solvent molecules are gone by 190 °C, theoretical weight loss due to I_4-BDC decomposition (by 600 °C) should be 89.1%. The observed weight loss from 190 to 600 °C is 89.5% (+0.45% difference) for bulk crystals of **I-CP 3**, 79.3% (-11.4% difference) for **I-NCP 3a**, and 85.6% (-4.4% difference) for **I-NCP 3b**. The slightly reduced organic weight loss for **I-NCPs 3a** and **3b** in the 190-600 °C temperature range could be attributed to the presence of small amounts of amorphous copper oxide/hydroxide due to the high pH conditions for their synthesis.

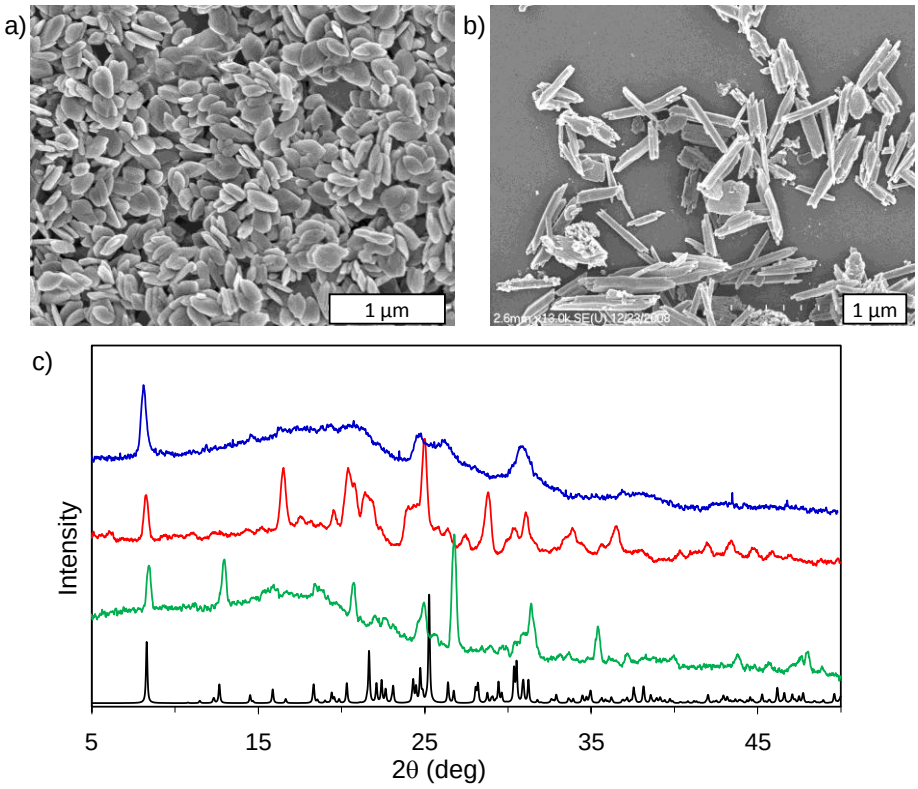

Figure 1.11. (a) SEM images of **I-NCP 3a** and (b) **I-NCP 3b**. (c) Simulated PXRD pattern of **I-CP 3** (black), and experimental PXRD patterns of bulk crystals of **I-CP 3** (green), **I-NCP 3a** (red), and **I-NCP 3b** (blue).

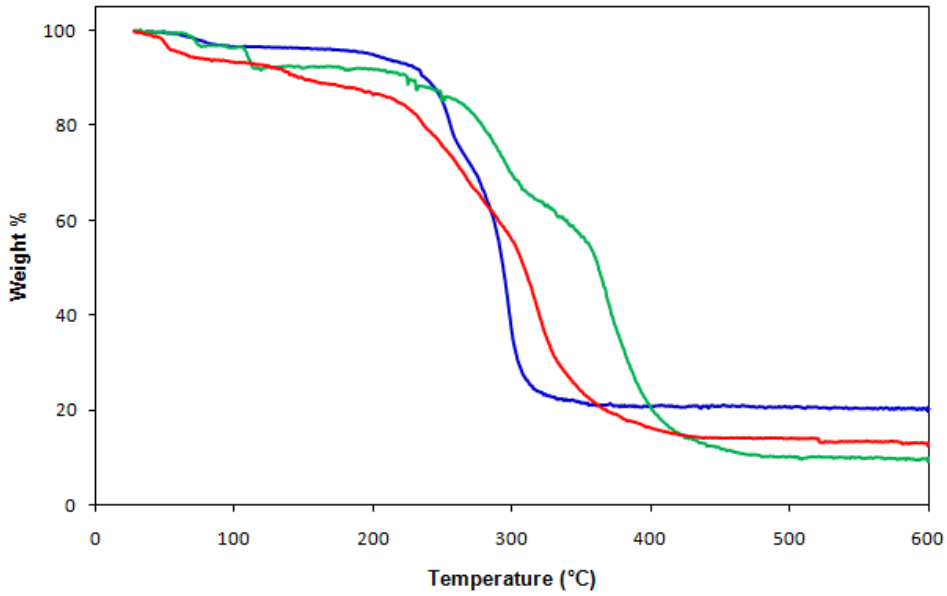

Figure 1.12. TGA of bulk crystals of **I-CP 3** (green), **I-NCP 3a** (blue), and **I-NCP 3b** (red).

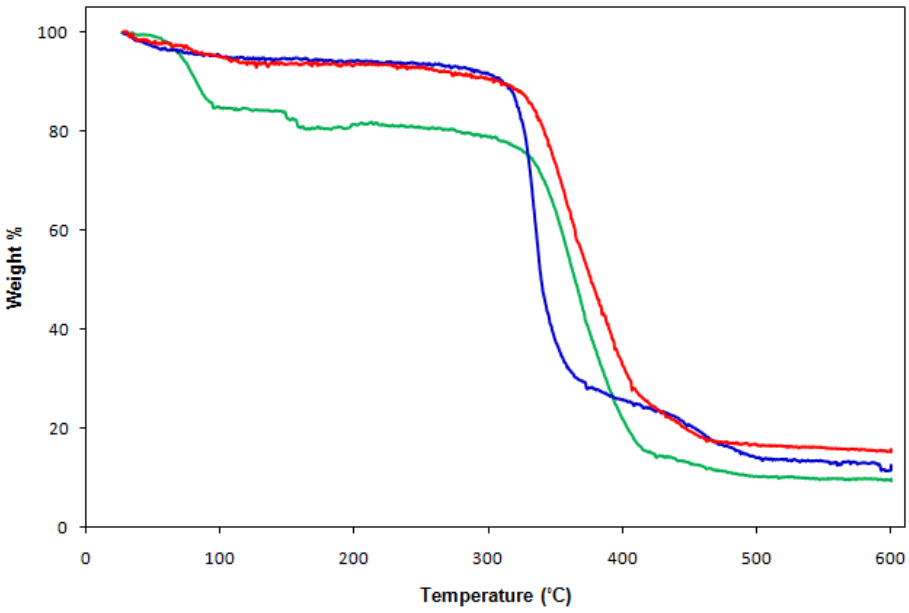

Figure 1.13. TGA of bulk crystals of **I-CP 5** (green), **I-NCP 5a** (red), and **I-NCP 5b** (blue).

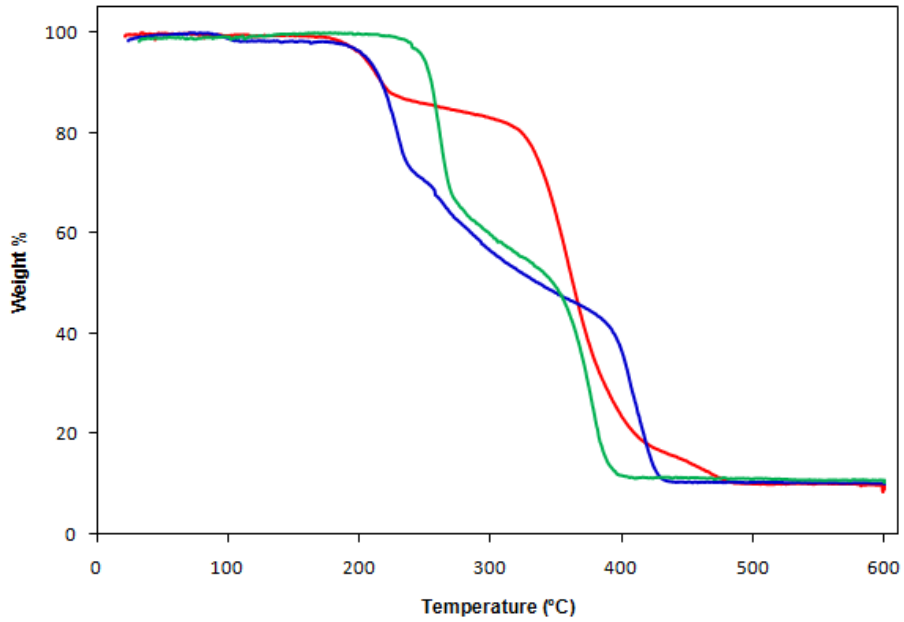

Figure 1.14. TGA of bulk crystals of **I-CP 1** (green), **I-CP 2** (blue), and **I-CP 4** (red).

We synthesized microparticles of **I-CP 5** using a rapid precipitation procedure.[28] A dilute aqueous solution of $Na_2(I_4\text{-BDC})$ and $Zn(NO_3)_2$ in an equal molar ratio was added to ethanol with rapid stirring. SEM and PXRD studies showed that the resulting particles (**I-NCP 5a**) were crystalline rods less than a μm in width and 10–30 μm in length (Fig. 1.15a, c). Smaller particles **I-NCP 5b** could be obtained by addition of a more concentrated aqueous precursor solution (pH 6.6) to ethanol. The resulting white cloudy dispersion was stirred at room temperature for 1 hour. The **I-NCP 5b** nanoparticles were isolated in 82% yield by centrifugation and washed with ethanol. SEM images show that the **I-NCP 5b** particles have a truncated cube morphology with a diameter of 200–600 nm (Fig. 1.15b). PXRD studies show that they match the bulk phase of **I-CP 5** (Fig. 1.15c), but the very broad peak indicates a large degree of disorder in the structure of these partially crystalline particles. The composition of **I-NCP 5a** and **I-NCP 5b** was also confirmed by TGA (Fig. 1.13) and EDS results (Fig. 1.16c,d). As with **I-NCP 3a** and **3b**, the ready loss of solvents from NCPs complicates the TGA data analysis for **I-NCP 5a** and **5b**. If it is assumed that all ethanol molecules are lost by 190 °C, theoretical weight loss due to I_4-BDC decomposition (by 600 °C) should be 88.9%. The observed weight loss from 190 to 600 °C is 88.6% (-0.34% difference) for **I-CP 5**, 83.7% (-5.8% difference) for **I-NCP 5a**, and 87.5% (-1.6% difference) for **I-NCP 5b**. The slightly reduced organic weight loss for **I-NCPs 5a** and **5b** in the 190-600 °C temperature range could be attributed to the presence of small amounts of amorphous zinc oxide/hydroxide.

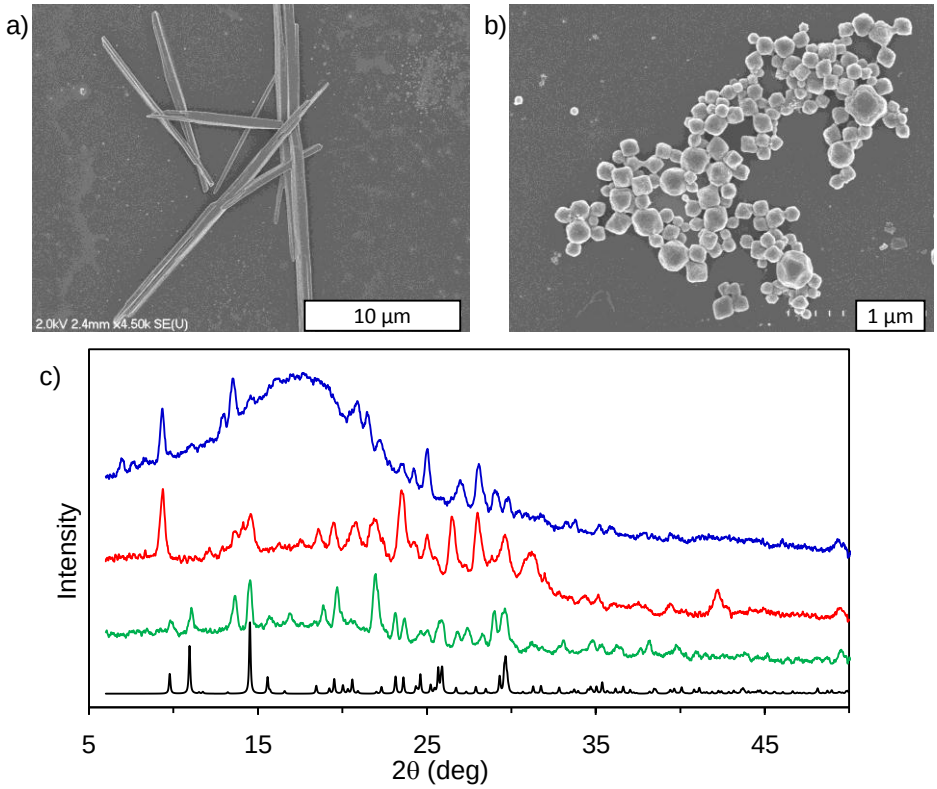

Figure 1.15. (a) SEM images of **I-NCP 5a** and (b) **I-NCP 5b**. (c) Simulated PXRD pattern of **I-CP 5** (black), and experimental PXRD patterns of bulk crystals of **I-CP 5** (green), **I-NCP 5a** (red), and **I-NCP 5b** (blue).

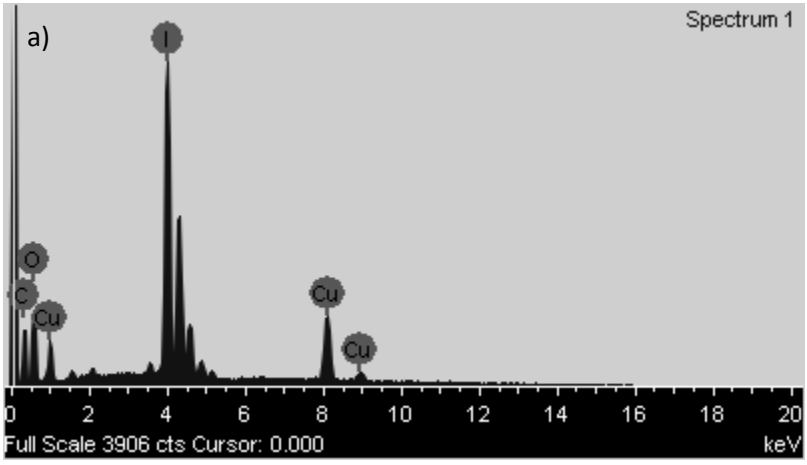

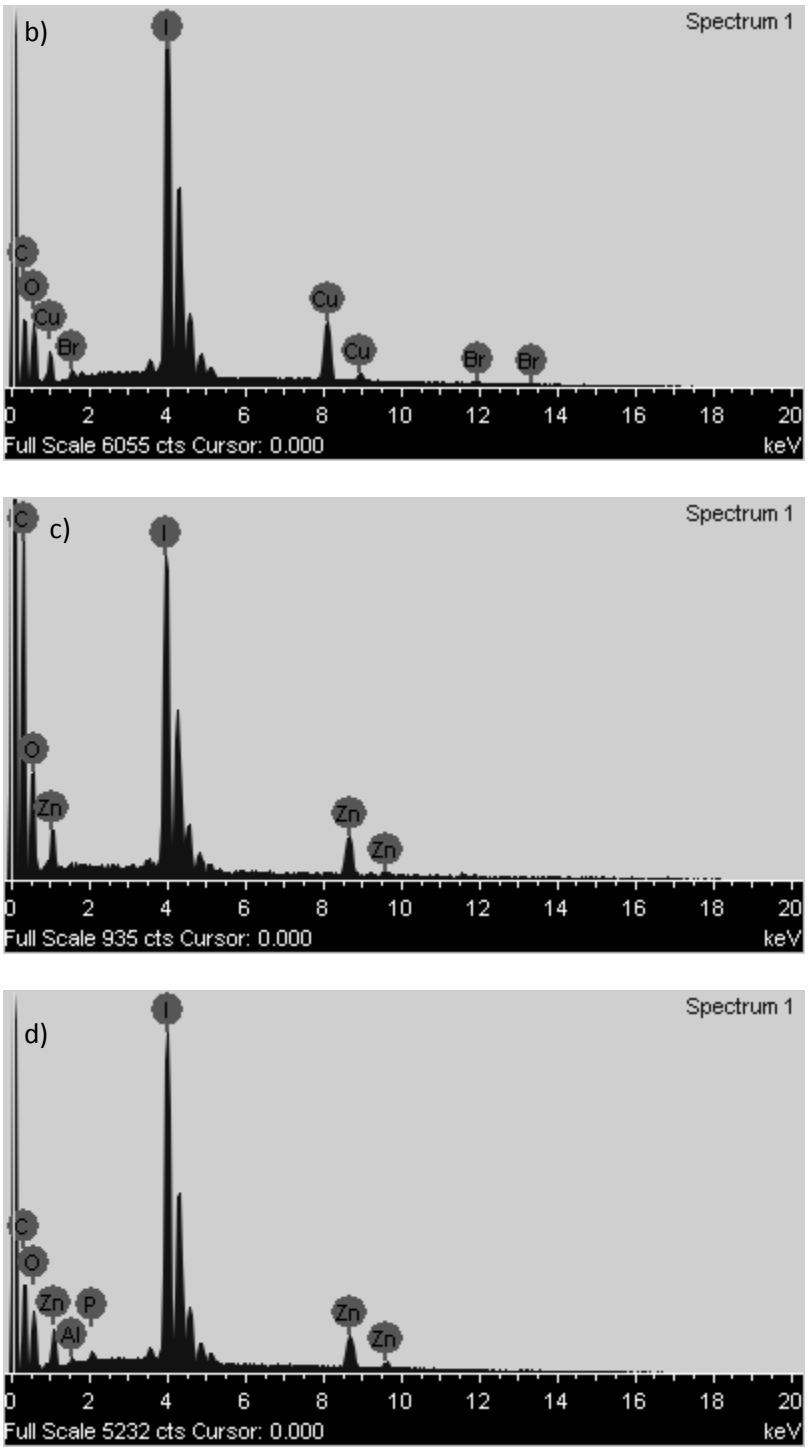

Figure 1.16. EDS spectra of (a) **I-NCP 3a**, (b) **I-NCP 3b**, (c) **I-NCP 5a**, and (d) **I-NCP 5b**.

1.2.3. Phantom computed tomography studies

Phantom studies were conducted on **I-NCP 3a** and **I-NCP 5b** to evaluate their potential for use as CT contrast agents. Scans were done on ethanol dispersions with corresponding iodine concentrations of 0.075–0.3 M (Fig. 1.17a, b). For comparison, samples of aqueous solutions of Iodixanol, a clinically used iodinated contrast agent, were also scanned at the same iodine concentrations (Fig. 1.17c). Both **I-NCP 3a** and **I-NCP 5b** contain 63 wt% iodine, while Iodixanol contains only 49 wt% iodine. The amount of iodine that can be incorporated in small-molecule agents is limited by the need for side chains that increase hydrophilicity and decrease osmolality, viscosity, and toxicity.[5] Higher iodine content can be achieved in the iodinated NCPs because it is not necessary for the I_4-BDC ligand to have these side chains. The theoretical iodine payload is 63.2 and 55.3 wt% for **I-NCP 3a** and **5b**, respectively, based on the formulas determined by X-ray diffraction data. The higher than predicted iodine payload for **I-NCP 5b** is due to ready loss of ethanol molecules from the nanoparticles as shown in the TGA. For comparison, a recently reported polymer-stabilized lipid nanoparticle contains only 19 wt% iodine in the core, and iodine loading is even lower when the polymer shell is taken into consideration.[16] The Hounsfield unit (HU)[33] value is an indicator of the ability of a material to attenuate X-rays with respect to water (0 HU). The intensity of transmitted energy is logarithmically dependent on attenuation. The measured value (HU) is an indicator of attenuation, which is linearly dependent on concentration. The slopes of the lines produced by plotting HU values against iodine concentrations for **I-NCP 3a**, **I-NCP 5b**, and Iodixanol are 4653±520, 4513±408, and 3840±560 HU/M, respectively (Fig. 1.17d). The nanoparticles thus show X-ray attenuation coefficients comparable to that of the molecular contrast agent. The slightly higher X-ray attenuation of the NCPs can be attributed to the contribution from Cu and Zn, calculated to

be approximately 5% based on the weight% of these metals in the materials and the attenuation of the metals compared to that of iodine.

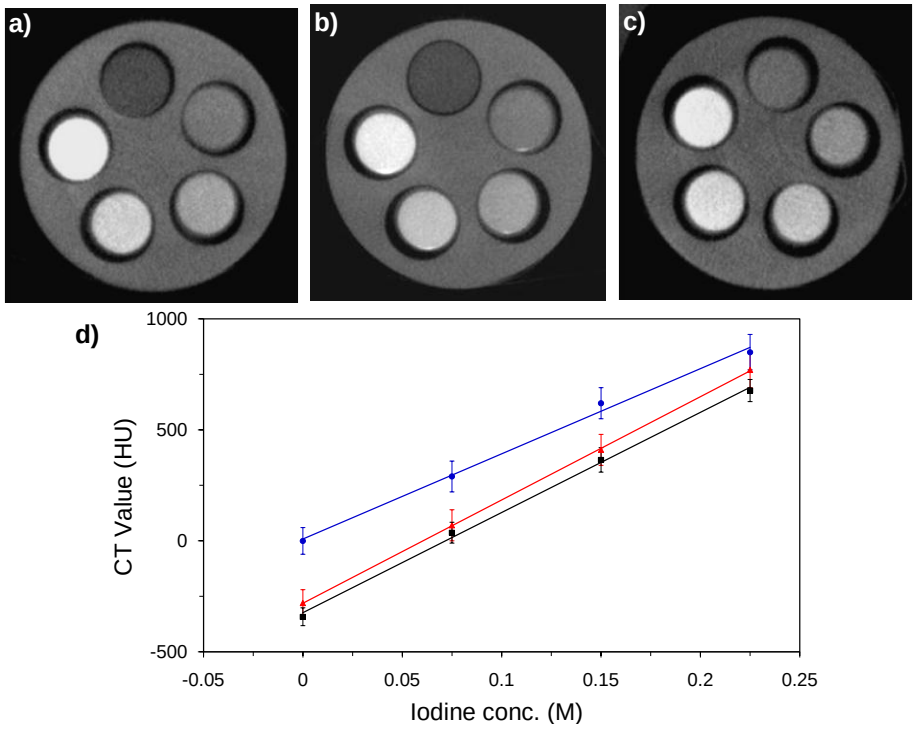

Figure 1.17. CT phantom images of (a) **I-NCP 3a** and (b) **I-NCP 5b** dispersed in ethanol, and (c) Iodixanol in aqueous solution. From the top, clockwise, the slots have [I]=0, 0.075, 0.150, 0.225, and 0.300 M. (d) X-ray attenuation as a function of [I] for **I-NCP 3a** at 40 kVp (red), **I-NCP 5b** at 50 kVp (black), and Iodixanol at 40 kVp (blue).

1.2.4. Degradation behavior and silica coating

The biodegradable nature of NCPs makes them attractive candidates for imaging applications, because it is important that a diagnostic agent be cleared from the body after use.[23, 27] This is an advantage over many purely inorganic nanoparticles that are used for biomedical applications and are not readily cleared from the body. However, it is important that the particles be stable enough to perform their function before degrading significantly. To determine the dissolution (degradation) behavior of the iodinated NCPs in a biologically relevant environment, 0.6 mg of **I-NCP 3a** was dialyzed against 250 mL of 8 mM phosphate

buffered saline (PBS; pH 7.4) at 37 ºC. Inductively coupled plasma mass spectrometry (ICP-MS) was used to measure I concentration in aliquots taken at various time points. The particles were completely dissolved after approximately 46 hours, with a half-life of about 1.5 hours (Fig. 1.18). This result demonstrates the biodegradable nature of the NCPs while they are still stable enough to allow for longer circulation time as compared to molecular iodinated contrast agents (<10 min).

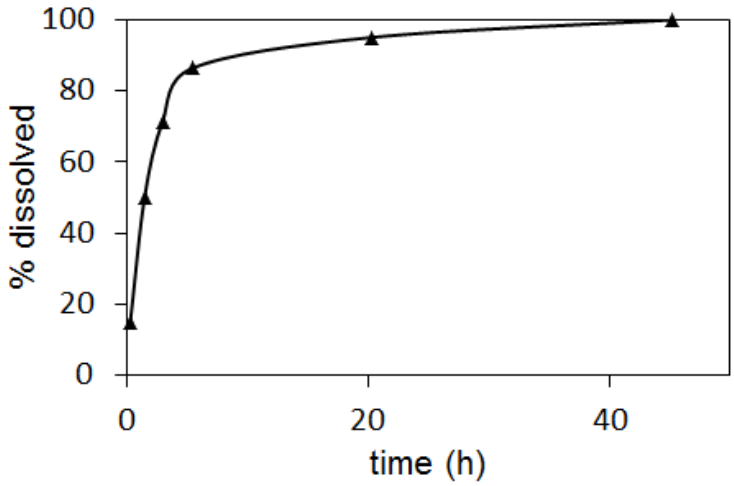

Figure 1.18. Release profile for **I-NCP 3a**, obtained by plotting the % I released against time.

In order for iodinated NCPs to be used *in vivo*, the particles would need to be modified for increased stability and biocompatibility. Silica coating makes NCPs more biocompatible and has been shown to slow their dissolution under physiological conditions, due to slow diffusion of the constituents through the pores of the shell.[25] Functionalization of nanoparticles with passivating moieties is often needed to prevent rapid uptake by cells of the mononuclear phagocyte system (MPS), which is responsible for removing debris and foreign materials from the bloodstream.[7] A silica coating can facilitate attachment of silyl-derived functional molecules such as passivating moieties. **I-NCP 3a** was coated with a layer of

poly(vinylpyrrolidone) (PVP) to reduce aggregation and make the particles more dispersible (Fig. 1.19) so that they could be coated with silica by a sol-gel method. Tetraethyl orthosilicate (TEOS) was added to a dispersion of **I-NCP 3a**@PVP in ethanol with ammonium hydroxide to catalyze the hydrolysis and condensation of TEOS to coat the particles with a layer of amorphous silica (**I-NCP 3a**@SiO_2). A silica coating can be seen on the resultant particles by SEM (Fig. 1.20a) and confirmed by Si peaks in the EDS spectrum (Fig. 1.20b). However, the particles are severely etched under the basic coating conditions and a large amount of the iodinated ligand is lost, as evidenced by a lowered I to Cu ratio according to EDS after coating. The Zn-based NCPs are even less stable than the Cu-based NCPs, as they dissolve in water alone. The one-dimensional nature of the polymer chains in the iodinated CPs is one reason for their instability. CPs of higher dimensionality are expected to be more robust and therefore more tolerant of reaction conditions used to modify and functionalize them for in vivo use.

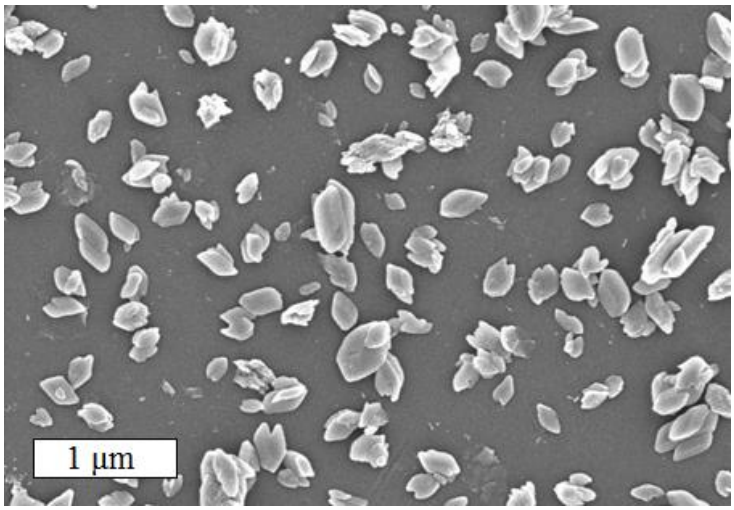

Figure 1.19. SEM image of **I-NCP 3a**@PVP.

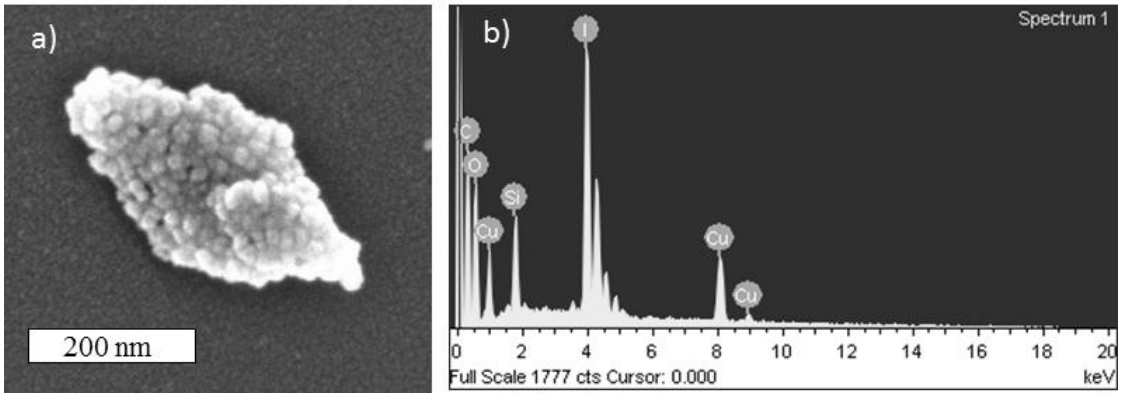

Figure 1.20. (a) SEM image and (b) EDS spectrum of **I-NCP 3a**@SiO_2.

1.3. Conclusion

Novel iodinated coordination polymers have been synthesized as well as their corresponding nanoparticle phases with controllable morphologies, and their potential for CT contrast enhancement has been demonstrated. These new nanomaterials are capable of carrying high payloads of iodine and offer a new strategy for designing efficient CT contrast agents that do not suffer from the inherent drawbacks of small-molecule agents. While these NCPs based on an iodinated ligand are not stable enough to tolerate further functionalization or exposure to biological conditions, the NCP approach can be taken in different directions to achieve practically useful CT contrast agents. NCPs with more robust framework structures or stronger metal-ligand bonds may provide a solution to this problem. Metal connecting points with high X-ray attenuation may also be considered as the active component of an NCP contrast agent. These possibilities are explored in Chapter 2.

1.4. Experimental Details

1.4.1 Materials and methods

Zinc nitrate, copper nitrate, 1-hexanol, TEOS, and all solvents were purchased from Fisher. TritonX-100, CTAB, and PVP were purchased from Aldrich. All starting materials were used without further purification. Thermogravimetric analysis (TGA) was performed using a Shimadzu TGA-50 equipped with a platinum pan, and all samples were air-dried and heated at a rate of 4 °C per minute under air. Scanning electron microscopy (SEM) was used to image the particles, using a Hitachi 4700 field emission scanning electron microscope. A Cressington 108 Auto Sputter Coater equipped with a Au/Pd (80/20) target and an MTM-10 thickness monitor was used to coat the samples with a conductive layer before taking SEM images. Each SEM sample was prepared by first suspending the nanomaterial in ethanol, then a drop of the suspension was placed on a glass slide and the solvent was allowed to evaporate. Energy dispersive X-ray spectroscopy (EDS) was used to determine elemental composition of the particles, using an Oxford 7200 IncaPentaFET-x3 energy dispersive X-ray spectrometer. The EDS data was processed with the Inca Microanalysis Suite. Each EDS sample was prepared by placing a drop of an ethanol suspension of the nanomaterial on a strip of carbon tape affixed to an aluminum sample holder, and the ethanol was allowed to evaporate. A Varian 820-MS Inductively Coupled Plasma-Mass Spectrometer (ICP-MS) was used to measure I concentration during the release profile. Powder X-ray diffraction (PXRD) analyses were carried out using a Bruker SMART Apex II diffractometer using Cu radiation. The PXRD patterns were processed with the Apex II package using the phase ID plugin.

Single crystal X-ray diffraction experiments were carried out on a Bruker SMART Apex II CCD-based X-ray diffractometer system equipped with a Cu –target X-ray tube (λ = 1.54178 Å) and operated at 1600 W. The frames were integrated with the Bruker SAINT© built in Apex II software package using a narrow-frame integration algorithm, which also

corrects for the Lorentz and polarization effects. Absorption corrections were applied using SADABS. All of the structures were solved by direct methods and refined to convergence by the least squares method on F^2 using the SHELXTL software suite. All non-hydrogen atoms are refined anisotropically, except some solvent molecules and some of the ligand atoms in compounds **I-CP 2** and **I-CP 4**.

Computed tomography (CT) phantom images and X-ray attenuation data were obtained using a micro-computed tomography scanner equipped with a carbon nanotube based field emission micro-focus X-ray source.[34, 35] All CT scans were done at either 40 or 50 kVp, 0.7 mA, 0.5 mm Al filtration, and 100 msec (for 40 kVp) or 50 msec (for 50 kVp) exposure per projection. A higher peak voltage was used for **I-NCP 5b** than for **I-NCP 3a** and Iodixanol (50 kVp vs 40 kVp) because the X-ray tube needed to be replaced between the dates that these experiments were conducted, and the two X-ray tubes required operation at different peak voltages. X-ray attenuation is slightly lower at the higher peak voltage, but the difference is not large enough to significantly affect the results. Four hundred projections were used over a circular orbit of 200° at a step angle of 0.5° and were reconstructed at 76 μm isotropic voxel spacing.

1.4.2. Synthesis of iodinated ligand and coordination polymers.

Synthesis of 2,3,5,6-tetraiodo-1,4-benzene dicarboxylic acid (I_4-BDC-H_2): Tetraiodobenzene dicarboxylic acid was synthesized and purified by using a procedure previously described.[36] In brief, 1,4-benzenedicarboxylic acid (20 g, 0.12 mol) was dissolved in sulfuric acid (90 mL, fuming, 30%) at 80 °C. Iodine (80 g, 0.315 mol) was added in six portions over 2 h. The reaction mixture was heated to 175 ℃ and stirred for another 3 h. After cooling, it was treated with NaOH (2 M) solution to a pH of 9. The precipitate was

filtered out, and the filtrate was acidified with concentrated HCl to a pH of 4. The crude product was collected by filtration, and then heated to reflux in methanol with several drops of concentrated sulfuric acid overnight. After removing the solvent, the crude product was dissolved in water (200 mL) and treated with NaOH (2 M) solution to a pH of 9. After filtration, the filtrate was acidified with concentrated HCl to a pH of 3. The precipitate obtained by filtration was recrystallized in acetic acid to give the white crystalline product. Yield: 7.4 g (9.2 %)

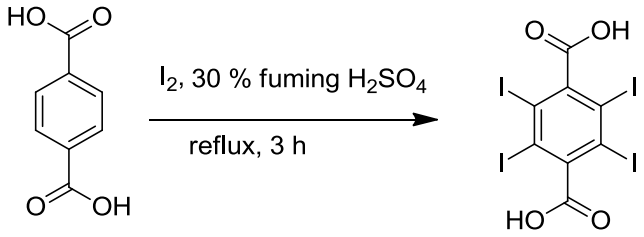

Figure 1.21. Scheme for the synthesis of I_4-BDC.

Synthesis of Cu(I_4-BDC)$(DMF)_2$ (I-CP 1): Tetraiodobenzene dicarboxylic acid (4.02 mg, 6.00 mmol) and $Cu(NO_3)_2 \cdot 3H_2O$ (1.45 mg, 6.00 mmol) were dissolved in a mixture of DMF (670 mL) and H_2O (34 mL) with HCl (1 equiv, 6.00 mmol). The vial containing the resulting clear solution was capped and placed in an 80 ºC oven. After 3 days, blue rectangular plate-shaped crystals were obtained. Yield: 1.46 mg (27.7%).

Synthesis of Cu(I_4-BDC)$(DEF)_2(H_2O)$ bulk crystals (I-CP 2): Tetraiodobenzene dicarboxylic acid (5.32 mg, 7.94 µmol) and $Cu(NO_3)_2 \cdot 3H_2O$ (1.92 mg, 7.94 µmol) were dissolved in a mixture of 260 µL DEF and 44 µL H_2O. The vial containing the resulting clear solution was capped and placed in an 80 °C oven. After 1 day, bluish-green rod-shaped crystals were obtained. Yield: 4.33 mg (57.3%)

Synthesis of [Cu(I_4-BDC)(H_2O)$_2$]·2H_2O bulk crystals (I-CP 3): Tetraiodobenzene dicarboxylic acid (3.00 mg, 4.48 μmol) and Cu(NO_3)$_2$·3H_2O (1.08 mg, 4.48 μmol) were dissolved in 1.23 mL of water. The vial containing the resulting clear solution was capped and placed in an 80 °C oven. After 1 day, green thin rod-shaped crystals were obtained. Yield: 2.54 mg (68.7%)

Synthesis of Zn(I_4-BDC)(DMF)$_{2.5}$ bulk crystals (I-CP 4): Tetraiodobenzene dicarboxylic acid (8.87 mg, 13.2 μmol) and Zn(NO_3)$_2$·6H_2O (3.93 mg, 13.2 μmol) were dissolved in a mixture of 1.4 mL DMF and 88 μL H_2O. The vial containing the resulting clear solution was capped and placed in a 60 °C oven. After 4 days, colorless rod-shaped crystals were obtained. Yield: 6.68 mg (55.3%)

Synthesis of [Zn(I_4-BDC)(EtOH)$_2$]·2EtOH bulk crystals (I-CP 5): Tetraiodobenzene dicarboxylic acid (2.75 mg, 4.11 μmol) was dissolved in 2.0 mL of ethanol in a vial. Zn(NO_3)$_2$·6H_2O (1.22 mg, 4.11 μmol) was added as 41 μL of a 0.1 M aqueous solution. The vial containing the resulting clear solution was capped with a septum pierced by a syringe needle to allow for slow evaporation of the solvent. After 12 h at room temperature, colorless thin rod-shaped crystals were obtained. Yield: 0.94 mg (28%)

Synthesis of I-NCP 3a: Two microemulsions with *W*=15 were prepared by the addition of 1.215 mL of an aqueous solution of I_4-BDC sodium salt (0.1 M, pH 9.6) and 1.215 mL of a 0.1 M Cu(NO_3)$_2$ aqueous solution to separate 15 mL aliquots of a 0.3 M Triton X-100 and 1.5 M 1-hexanol in cyclohexane. The separate microemulsions were stirred vigorously for 10 min at room temperature before the two microemulsions were combined, and the resultant 30 mL microemulsion with *W*=15 was stirred for an additional 2 h at room temperature. The nanoparticles were isolated by centrifugation at 13,000 rpm for 10 min.

After the removal of the supernatant, the particles were washed twice using 10 mL of ethanol each time. For each wash, the particles were re-dispersed by sonication and then recovered by centrifugation at 13,000 rpm for 10 min. Yield: 69.9 mg (75.0%).

Synthesis of I-NCP 3b: Two microemuslsions with *W*=15 were prepared by the addition of 135 µL of an aqueous solution of I_4-BDC sodium salt (0.2 M, pH=9.5) and 135 µL of a 0.2 M $Cu(NO_3)_2$ aqueous solution to separate 5 mL aliquots of a 0.1 M CTAB/0.5 M 1-hexanol/isooctane mixture. The separate microemulsions were stirred vigorously for 10 min at room temperature, after which the two microemulsions were combined, and the resultant 10 mL microemulsion with *W*=15 was stirred for an additional 2 h at room temperature. The product was isolated and washed as described above for **I-NCP 3a**. Yield: 12.5 mg (60.3%)

Synthesis of I-NCP 5a: A 300 µL aqueous precursor solution of 16.7 mM $Na_2(I_4$-BDC) and 16.7 mM $Zn(NO_3)_2$ was quickly pipetted into 1.4 mL of ethanol in a vial with rapid stirring. This resulted in the formation of a white cloudy dispersion after several minutes, which was stirred at room temperature for 1 h. The product was isolated and washed as described above for **I-NCP 3a**. Yield: 2.09 mg (50.5%)

Synthesis of I-NCP 5b: A 200 mL aqueous precursor solution of 0.05 M $Na_2(I_4$-BDC) and 0.05 M $Zn(NO_3)_2$ was prepared and its pH was adjusted to 6.6 with NaOH. This precursor solution was quickly transferred into 25 mL of ethanol in a 50 mL round bottom flask with rapid stirring. This resulted in the immediate formation of a white cloudy dispersion, which was stirred at room temperature for 1 h. The product was isolated and washed as described above for **I-NCP 3a**. Yield: 6.35 mg (81.5%)

Synthesis of I-NCP 3a@PVP: PVP (MW 40,000) (168.7 mg, 4.22 μmol) was added to an ethanol dispersion containing 80 mg of **I-NCP 3a**. The total volume was then raised to 40 mL with additional ethanol. The mixture was stirred for 18 h at room temperature. The product was isolated and washed as described above for **I-NCP 3a**. Yield: 62.9 mg (78.6% based on initial mass of **I-NCP 3a**)

Synthesis of I-NCP 3a@SiO_2: **I-NCP 3a**@PVP (9.0 mg) was dispersed in 15 mL of ethanol. This dispersion was added to a solution of 810 μL ammonium hydroxide (14.8 M, 12 mmol) in 14.18 mL of ethanol, then TEOS (12 μL, 54.1 μmol) was added. The final 30-mL reaction mixture contained 0.3 mg of particles/mL with 0.4 M NH_4OH and 1.8 mM TEOS. The reaction was stirred at room temperature for 21 h. The product was isolated and washed as described above for **I-NCP 3a**. Yield: 6.39 mg (71.0% based on initial mass of **I-NCP 3a**@PVP)

1.5. References

(1) Seeram, E., *Computed Tomography: Physical Principles, Clinical Application, and Quality Control, 3rd ed.;* Saunders/Elsevier: St. Louis, **2009**.

(2) Kalender, W. A. *Phys. Med. Biol.* **2006**, *51*, R29.

(3) Speck, U. Contrast Agents: X-ray Contrast Agents and Molecular Imaging -- A Contradiction? In *Handbook of Experimental Pharmacology*; Semmler, W., Schwaiger, M., Eds.; Springer-Verlag: Berlin, **2008**; Vol. 185; p 167.

(4) Rutten, A.; Prokop, M. *Anti-Cancer Agents Med. Chem.* **2007**, *7*, 307.

(5) Krause, W.; Schneider, P. W. Chemistry of X-ray Contrast Agents. In *Topics in Current Chemistry*; Krause, W., Ed.; Springer-Verlag: Berlin, **2002**; Vol. 222; p 107.

(6) Yu, S.; Watson, A. D. *Chem. Rev.* **1999**, *99*, 2353.

(7) Ferrari, M. *Nat Rev Cancer* **2005**, *5*, 161.

(8) Davis, M. E.; Chen, Z.; Shin, D. M. *Nat. Rev. Drug Discov.* **2008**, *7*, 771.

(9) De Jong, W. H.; Borm, P. J. A. *Int. J. Nanomed.* **2008**, *3*, 133.

(10) Peer, D.; Karp, J. M.; Hong, S.; Farokhzad, O. C.; Margalit, R.; Langer, R. *Nat. Nanotechnol.* **2007**, *2*, 751.

(11) Taylor-Pashow, K. M. L.; Della Rocca, J.; Huxford, R. C.; Lin, W. *Chem. Commun.* **2010**, *46*, 5832.

(12) Matsuura, N.; Rowlands, J. A. *Med. Phys.* **2008**, *35*, 4474.

(13) Rabin, O.; Perez, J. M.; Grimm, J.; Wojtkiewicz, G.; Weissleder, R. *Nat. Mater.* **2006**, *5*, 118.

(14) Kim, D.; Park, S.; Lee, J. H.; Jeong, Y. Y.; Jon, S. *J. Am. Chem. Soc.* **2007**, *129*, 7661.

(15) Kattumuri, V.; Katti, K.; Bhaskaran, S.; Boote, E. J.; Casteel, S. W.; Fent, G. M.; Robertson, D. J.; Chandrasekhar, M.; Kannan, R.; Katti, K. V. *Small* **2007**, *3*, 333.

(16) Pan, D.; Williams, T. A.; Senpan, A.; Allen, J. S.; Scott, M. J.; Gaffney, P. J.; Wickline, S. A.; Lanza, G. M. *J. Am. Chem. Soc.* **2009**, *131*, 15522.

(17) Hyafil, F.; Cornily, J.-C.; Feig, J. E.; Gordon, R.; Vucic, E.; Amirbekian, V.; Fisher, E. A.; Fuster, V.; Feldman, L. J.; Fayad, Z. A. *Nat. Med.* **2007**, *13*, 636.

(18) Galperin, A.; Margel, D.; Baniel, J.; Dank, G.; Biton, H.; Margel, S. *Biomaterials* **2007**, *28*, 4461.

(19) Yaghi, O. M.; O'Keeffe, M.; Ockwig, N. W.; Chae, H. K.; Eddaoudi, M.; Kim, J. *Nature* **2003**, *423*, 705.

(20) Evans, O. R.; Lin, W. *Acc. Chem. Res.* **2002**, *35*, 511.

(21) Wu, C.; Hu, A.; Zhang, L.; Lin, W. *J. Am. Chem. Soc.* **2005**, *127*, 8940.

(22) Férey, G.; Mellot-Draznieks, C.; Serre, C.; Millange, F. *Acc. Chem. Res.* **2005**, *38*, 217.

(23) Lin, W.; Rieter, W. J.; Taylor, K. M. L. *Angew. Chem. Int. Ed.* **2009**, *48*, 650.

(24) Spokoyny, A. M.; Kim, D.; Sumrein, A.; Mirkin, C. A. *Chem. Soc. Rev.* **2009**, *38*, 1218.

(25) Rieter, W. J.; Taylor, K. M. L.; Lin, W. *J. Am. Chem. Soc.* **2007**, *129*, 9852.

(26) Rieter, W. J.; Taylor, K. M. L.; An, H.; Lin, W.; Lin, W. J. *J. Am. Chem. Soc.* **2006**, *128*, 9024.

(27) Taylor, K. M. L.; Rieter, W. J.; Lin, W. *J. Am. Chem. Soc.* **2008**, *130*, 14358.

(28) Rieter, W. J.; Pott, K. M.; Taylor, K. M. L.; Lin, W. *J. Am. Chem. Soc.* **2008**, *130*, 11584.

(29) Sun, S.; Dong, S.; Wang, E. *J. Am. Chem. Soc* **2005**, *127*, 13102.

(30) Oh, M.; Mirkin, C. A. *Nature* **2005**, *438*, 651.

(31) Jung, S.; Oh, M. *Angew. Chem. Int. Ed.* **2008**, *47*, 2049.

(32) Taylor, K. M. L.; Jin, A.; Lin, W. *Angew. Chem. Int. Ed.* **2008**, *47*, 7722.

(33) Brooks, R. A. *J. Comput. Assist. Tomo.* **1977**, *1*, 487.

(34) Cao, G.; Lee, Y. Z.; Peng, R.; Liu, Z.; Rajaram, R.; Calderon-Colon, X.; An, L.; Wang, P.; Phan, T.; Sultana, S.; Lalush, D. S.; Lu, J. P.; Zhou, O. *Phys. Med. Biol.* **2009**, *54*, 2323.

(35) Cao, G.; Calderon-Colon, X.; Wang, P.; Burk, L.; Lee, Y. Z.; Rajaram, R.; Sultana, S.; Lalush, D.; Lu, J.; Zhou, O. *Proc. of SPIE* **2009**, *7258*, 72585Q1-7.

(36) Zhang, L. G.; Luo, S. N.; Liu, X. Y.; Xie, M. H.; Zou, P.; Liu, Y. L.; He, Y. J. *Huaxue Shiji* **2006**, *28*, 423.

CHAPTER 2

Hf-Based Metal-Organic Framework as a Contrast Agent for Computed Tomography

2.1. Introduction

2.1.1 Hf- and Zr-based nanoscale metal-organic frameworks

Background information on X-ray computed tomography (CT), nanoparticle contrast agents, and coordination polymers (CPs) is given in the Chapter 1 Introduction. Chapter 1 presented several iodinated nanoscale CPs (NCPs) as potential CT contrast agents. While these NCPs had several properties that gave them advantages over molecular contrast agents and other types of nanoparticles, they were not stable enough to be further functionalized or used *in vivo*. The steric bulk of the I atoms on the bridging benzene rings forced the CPs to adopt structures of one-dimensional chains. Structures with higher dimensionality may have greater stability, making them more feasible for *in vivo* use.

In this work, crystalline nanoscale metal-organic frameworks (NMOFs) with three-dimensional network structures are synthesized and characterized. Instead of incorporating the element with a high atomic number into the bridging ligand of the structure, as with the iodinated NCPs, in this case the heavy elements (hafnium and zirconium) are incorporated into NMOFs in the secondary building units. While clinically-used contrast agents are iodinated molecules, iodine is not the best choice for a contrast agent in terms of X-ray attenuation efficiency, but is used mainly due its low toxicity and low cost.[1] Elements with higher attenuation at relevant X-ray photon energies could provide adequate contrast at a

lower dose and decrease the amount of radiation to which a patient must be exposed. Hf- and Zr-based NMOFs were evaluated for X-ray attenuation and were further functionalized to make them suitable for in vivo CT imaging.

UiO-66 is a metal-organic framework (MOF) composed of the Zr-carboxylate cluster $Zr_6(\mu_3\text{-}O_4)(\mu_3\text{-}OH)_4(CO_2)_{12}$, which serves as a secondary building unit, bridged by benzenedicarboxylate linkers.[2] UiO-66 is more chemically, thermally, and mechanically stable compared to other MOFs, owing mainly to the strength of the Zr-carboxylate bond. The MOF structure stays intact under aqueous conditions, even when exposed to HCl (pH 1).[3] Since it was first reported in 2008, UiO-66 has been used for a wide variety of applications including catalysis, photochemical reactions, and molecule separations.[4] While Zr has an atomic number of 40, which may make it useful as a component of a CT contrast agent, Hf shows similar chemical behavior and has an even higher atomic number (72). Therefore, a Hf analog of the Zr UiO-66 MOF has been made, and has been evaluated as a CT contrast agent.

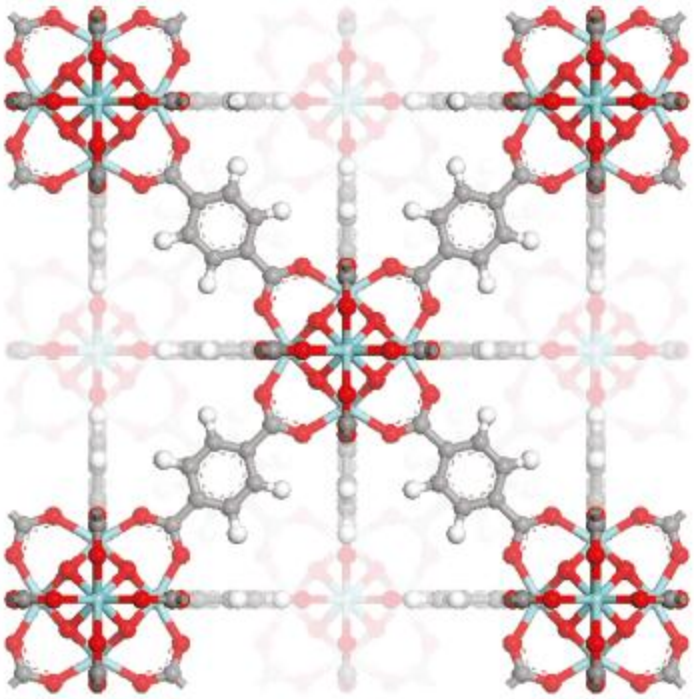

Figure 2.1. Framework structure of UiO-66 as determined from powder X-ray diffraction data. Blue, red, gray, and white colors represent Zr, O, C, and H atoms, respectively. Reprinted from reference 3 with permission (copyright 2008 American Chemical Society).

2.1.2. Physiological response to nanoparticles

Sufficient blood circulation time of nanoparticles is necessary for imaging applications, especially if the nanoparticles are targeted, as they need to circulate long enough to allow accumulation at a targeted site.[5, 6] When nanoparticles are used in vivo, they need to be modified with passivating moieties to prevent rapid clearance from the bloodstream.[7-10] Proteins in the bloodstream adsorb onto the surface of bare nanoparticles, causing them to be easily recognized by the immune system as foreign material. The mononuclear phagocyte system (MPS) is part of the immune system and includes phagocytic macrophages that are responsible for removing bacteria, debris, and foreign materials from the bloodstream. The MPS quickly clears recognized nanoparticles from the bloodstream, and they are taken up by organs that are rich in macrophages, like the liver and spleen.

Particle size is an important parameter to consider when nanomaterials are used *in vivo*. Large nanoparticles (>500 nm) tend to be taken up more readily by macrophages,[11] while nanoparticles larger than about 200 nm tend to accumulate in the spleen due to filtration from the bloodstream.[10] Even if smaller nanoparticles are used, aggregation must be prevented to limit the effective size of the nanoparticles under biological conditions. Nanoparticles tend to aggregate in media with high ionic strength, such as blood plasma, due to charge shielding.[10] Large aggregates (>5 μm) can clog blood vessels, causing pulmonary embolism or myocardial infarcation.[11, 12] Poly(ethylene glycol) (PEG) is a hydrophilic polymer commonly used as an antibiofouling agent to coat nanoparticles and prolong their residence time in the bloodstream.[8, 9, 13, 14] PEG is a popular choice due to its low toxicity and its unsurpassed ability to prevent protein adsorption and aggregation, thereby masking nanoparticles from the immune system.

2.2. Results and Discussion

2.2.1. Synthesis and characterization of metal-organic frameworks

An NMOF with the formula $Zr_6O_6(OH)_4(BDC)$ (BDC = 1,4-benzenedicarboxylate) (**Zr-NMOF**) was synthesized by the solvothermal method reported in the literature.[2] Equal molar amounts of $ZrCl_4$ and benzene dicarboxylic acid (H_2BDC) were dissolved in N,N'-dimethylformamide (DMF) and heated at 120 ºC in a sealed vessel for 24 h. The resulting particles were observed by scanning electron microscopy (SEM) and transmission electron microscopy (TEM) to be ~50 nm cubes, many intergrown to form clusters up to ~200 nm in size (Fig. 2.2a,b). The reported crystal structure of UiO-66 was solved using powder X-ray diffraction (PXRD) data.[2] The PXRD pattern of Zr-NMOF matches the UiO-66 simulated

pattern based on structural data, confirming that **Zr-NMOF** is indeed $Zr_6O_6(OH)_4$(BDC) and has the UiO-66 structure (Fig. 2.3a). The extra peak at 12º is due to guest solvent molecules.

The Hf analog of **Zr-NMOF** was also synthesized by a solvothermal method, but using the same conditions as for **Zr-NMOF** resulted in poorly crystalline particles intergrown into clusters as large as 3 μm, with a large size distribution. In order to obtain more monodisperse smaller particle clusters with better crystallinity, small adjustments in the conditions were made and a modulator was used. **Hf-NMOF** ($Hf_6O_6(OH)_4$(BDC)) was synthesized by heating a solution of equal molar $HfCl_4$ and H_2BDC with 0.85 equivalents of acetic acid in DMF at 100 ºC in a sealed vessel for 48 h. Addition of ligands with only one coordination site has recently been introduced as a way to control NMOF growth.[15, 16] Acetic acid competes with BDC for coordination with the metal cations of **Hf-NMOF** and presumably also modulates growth by binding with soluble Hf^{4+} species in solution. The resulting particles were observed by SEM and TEM to be 50-200 nm clusters of intergrown ~30 nm cubes (Fig. 2.2c,d). The clusters of **Zr-NMOF** and **Hf-NMOF** appear larger by SEM than by TEM due to some aggregation upon solvent evaporation on the substrate used for SEM imaging. The PXRD pattern of **Hf-NMOF** is very similar to that of **Zr-NMOF**, indicating that Hf can replace Zr in the UiO-66 structure (Fig. 2.3a). Thermogravimetric analysis (TGA) of **Zr-NMOF** and **Hf-NMOF** shows 50.2% and 32.4% weight loss, respectively, due to dehydroxylation from 250-300 ºC and decomposition of BDC from 420-520 ºC to leave behind ZrO_2 and HfO_2 (Fig. 2.3b). The expected weight losses calculated from the formulas are 55.6% and 43.3% for **Zr-NMOF** and **Hf-NMOF**, respectively. The lower weight loss observed could be due to some Zr/Hf oxides formed during synthesis and trapped in the pores of the NMOF.

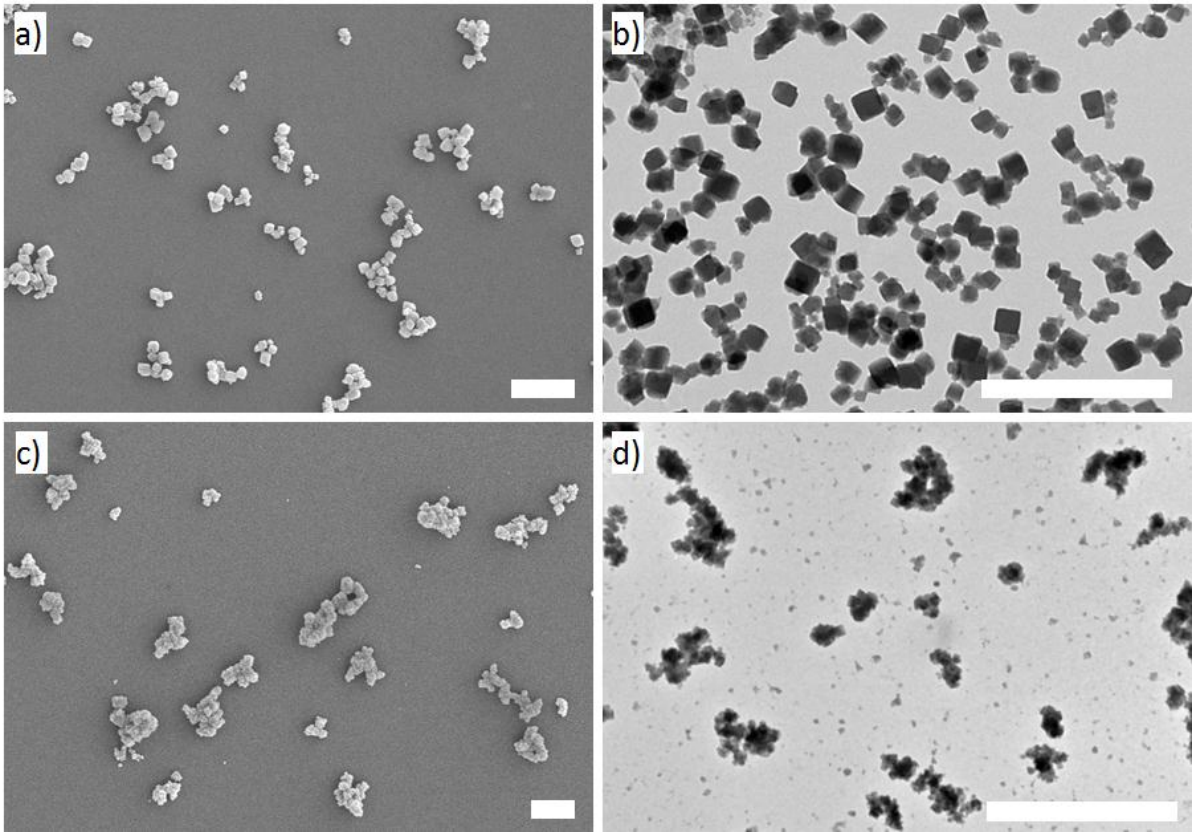

Figure 2.2. (a, c) SEM and (b, d) TEM images of (a, b) **Zr-NMOF** and (c, d) **Hf-NMOF**. The scale bars represent 500 nm.

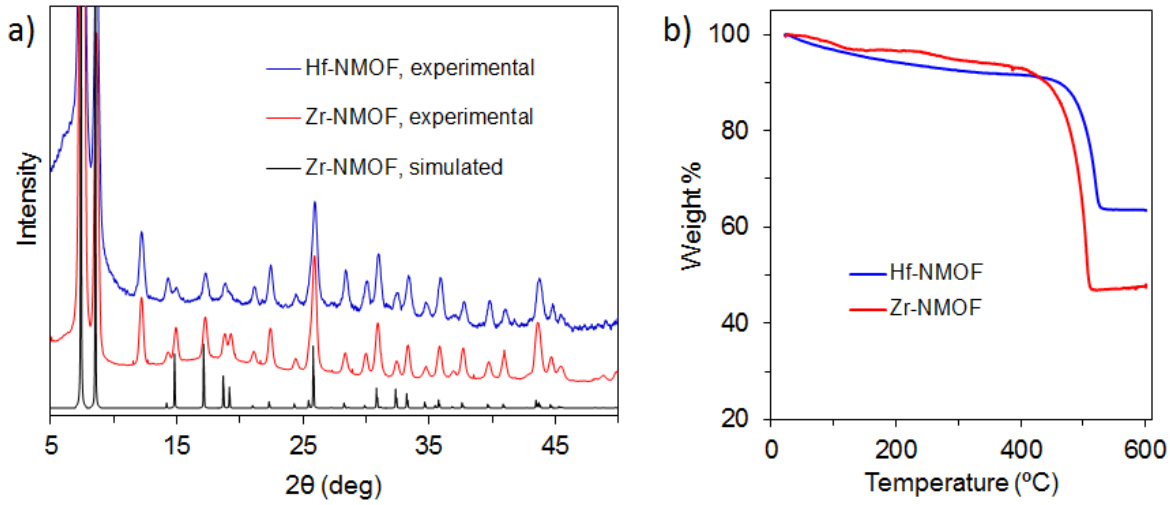

Figure 2.3. (a) Experimental PXRD patterns of **Zr-NMOF** and **Hf-NMOF**, along with the simulated pattern for **Zr-NMOF**. (b) TGA of **Zr-NMOF** and **Hf-NMOF**.

2.2.2. Phantom computed tomography studies

Phantom studies were conducted with **Hf-NMOF** and **Zr-NMOF** to evaluate their X-ray attenuation properties. Aqueous dispersions of each type of NMOF underwent CT scans with concentrations ranging from 0.05-0.20 M Hf or Zr. For comparison, samples of aqueous solutions of Iodixanol, a clinically used iodinated contrast agent, were also scanned containing the same concentrations of I. **Hf-NMOF** contains 57.3 wt% Hf and **Zr-NMOF** contains 37.0 wt% Zr, while Iodixanol contains 49 wt% I. The Hounsfield unit (HU)[17] value is an indicator of the ability of a material to attenuate X-rays with respect to water (0 HU). For images taken at 50 kVp (peak voltage), the slopes of the lines produced by plotting HU values against Hf/Zr/I concentrations for **Hf-NMOF**, **Zr-NMOF**, and Iodixanol are 10740±390, 5600±180, and 5390±230 HU/M, respectively (Fig. 2.5d).

The attenuation coefficient of a material is typically expressed in units of cm^{-1}. Fig. 2.5e shows attenuation coefficients of Hf, Zr, and I on a per mol basis vs the X-ray photon energy, derived from reported mass attenuation coefficient data.[18] The X-ray source produces photons with a wide energy distribution, with the kVp being the maximum, and the lowest energy photons are removed by filtration.[19] In this case, with a kVp of 50 keV, the photon energy distribution is centered around 22 keV. Attenuation coefficients increase sharply at the K shell electron binding energy (K edge) of a particular element. K edge energy is higher for heavier elements, and the K edge energies for Zr, I, and Hf, are 18.0, 33.2, and 65.4 keV, respectively. While Zr has higher attenuation than I in the 18.0-33.2 eV range, the higher attenuation of I below and above this range makes the overall attenuation of Zr and I very similar on a per mol basis. Hf has higher attenuation than both Zr and I by about a factor of two. The enhancement in attenuation compared to these lighter elements would be even more

pronounced at the higher kVp values (typically 120 kVp) used clinically for imaging human patients, due to the higher energy of the K edge. A Hf-based CT contrast agent could provide superior contrast at a lower dose compared to an I-based agent, and could decrease the amount of radiation to which the patient must be exposed.

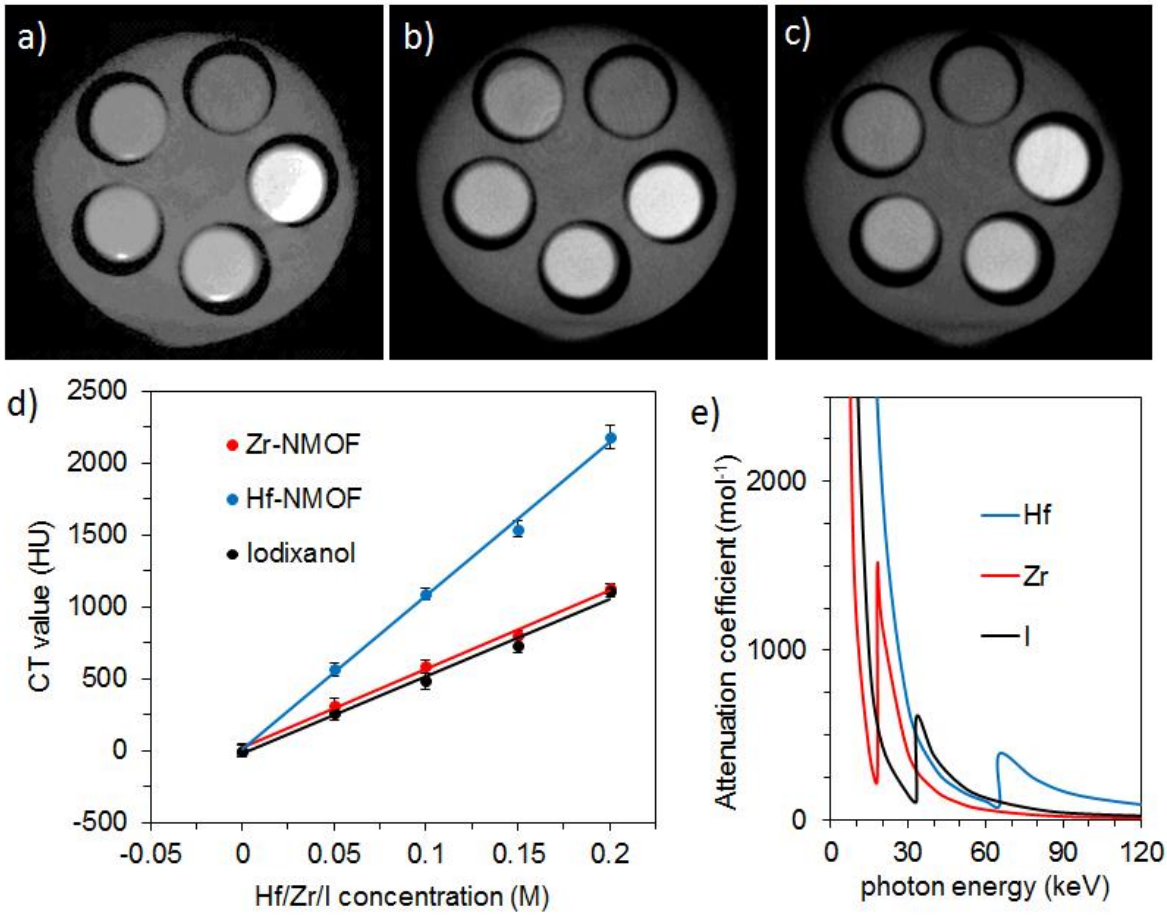

Figure 2.4. CT phantom images of (a) **Hf-NMOF,** (b) **Zr-NMOF**, and (c) Iodixanol dispersed in water. From the top, counterclockwise, the slots have [Hf/Zr/I] = 0, 0.05, 0.10, 0.15, and 0.20 M. (d) X-ray attenuation as a function of [Hf/Zr/I] for **Hf-NMOF**, **Zr-NMOF**, and **Iodixanol** at 50 kVp. (e) Attenuation coefficient on a per mol basis vs photon energy for Hf, Zr, and I.

2.2.3. Modification of Hf-NMOF

For *in vivo* use, **Hf-NMOF** must be modified to increase biocompatibility and to avoid quick uptake by the RES. PEG was modified to be terminated with a carboxylate group on one end, and it was grafted onto **Hf-NMOF** by stirring the particles at room temperature in an aqueous solution of $HO_2C\text{-}PEG_{2000}\text{-}OCH_3$. The resulting PEGylated **Hf-NMOF**@PEG particles appear similar to the bare particles by SEM (Fig. 2.5a). TGA shows an additional weight loss step from 220-350 ºC due to PEG loss (Fig. 2.6), which corresponds to particles that are 6.9 wt% PEG. The zeta potential increases from -24.6 mV for the bare particles to -2.0 mV, due to the presence of a neutral polymer coating. It was found that the PEG was lost from the particles after exposure to phosphate buffered saline (PBS) due to phosphate competing with coordinated PEG to form $Hf(PO_4)_x$. In fact, after prolonged sonication of **Hf-NMOF** in PBS, all of the organic ligand is replaced by phosphate, with retention of particle morphology (Fig. 2.5d). The transformation to $Hf(PO_4)_x$ was established by TGA, energy dispersive X-ray spectroscopy (EDS), and infrared (IR) spectroscopy.

In order to avoid the loss of PEG in the presence of phosphate, **Hf-NMOF** was coated with a silica shell, which can facilitate attachment of siloxy-derived molecules. Tetraethyl orthosilicate (TEOS) was added to a dispersion of **Hf-NMOF** in ethanol with ammonium hydroxide to catalyze the hydrolysis and condensation of TEOS to coat the particles with a layer of amorphous silica (**Hf-NMOF**@SiO_2). A siloxy-terminated version of PEG ($(OEt)_3Si\text{-}PEG_{2000}\text{-}OCH_3$) was then synthesized and grafted onto **Hf-NMOF**@SiO_2 by stirring the particles in a solution of $(OEt)_3Si\text{-}PEG_{2000}\text{-}OCH_3$ in ethanol under basic conditions (NH_4OH) to produce **Hf-NMOF**@SiO_2@PEG. Both **Hf-NMOF**@SiO_2 and **Hf-NMOF**@SiO_2@PEG look similar to the bare particles by TEM (Fig. 2.5b,c). The presence of silica is indicated by the appearance of a Si-O band in the IR spectrum of **Hf-**

NMOF@SiO_2 at 1051 cm^{-1} (Fig. 2.7). TGA shows an increase in weight remaining, corresponding to 13.2 wt% SiO_2, while **Hf-NMOF**@SiO_2@PEG has an additional weight loss step corresponding to 8.0 wt% PEG. The zeta potential becomes more negative, from -24.6 mV for the bare particles to -32.8 mV for the silica-coated particles, due to deprotonated surface silanol groups. As in the case of **Hf-NMOF**@PEG, PEG grafting raises the zeta potential closer to neutral, at -17.3 mV.

It is important that nanoparticles for *in vivo* use not aggregate under physiological conditions, in order to avoid rapid clearance, filtration by the spleen, or pulmonary embolism. **Hf-NMOF**@SiO_2@PEG showed no signs of aggregation by dynamic light scattering (DLS) done in 10 mM PBS. The average size of **Hf-NMOF**@SiO_2@PEG was measured by DLS to be 246 nm, somewhat larger than then 175 nm and 169 nm average sizes for **Hf-NMOF**@SiO_2 and **Hf-NMOF**, respectively.

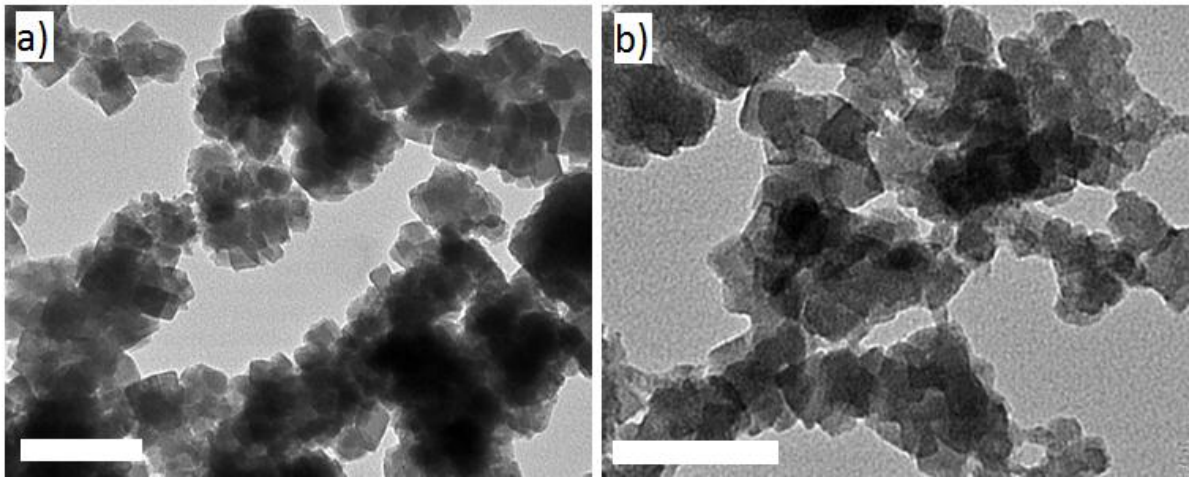

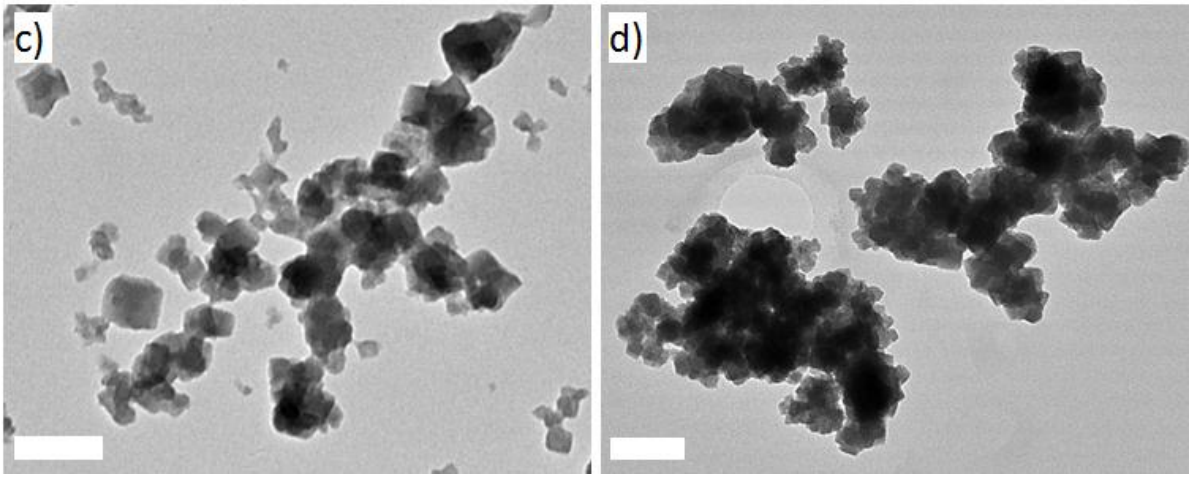

Figure 2.5. SEM images of (a) **Hf-NMOF**@PEG, (b) **Hf-NMOF**@SiO_2, (c) **Hf-NMOF**@SiO_2@PEG, and (d) **Hf-NMOF** after exposure to PBS. The scale bars represent 100 nm.

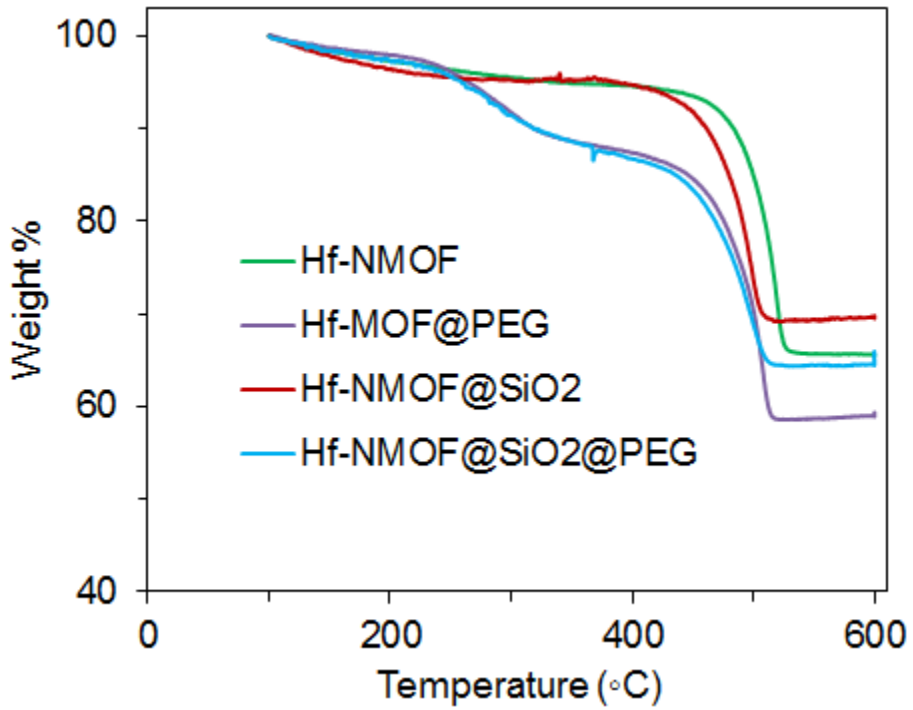

Figure 2.6. TGA of **Hf-NMOF**, **Hf-NMOF**@PEG, **Hf-NMOF**@SiO_2, and **Hf-NMOF**@SiO_2@PEG.

Table 2.1. **Hf-NMOF** and its modifications: weight %, zeta potential, and size.

Sample	Weight %[a]			Zeta potential (mV)[b]	Average size (nm)[c]
	Hf	SiO_2	PEG		
Hf-NMOF	57.3	-	-	-24.6	169
Hf-NMOF@PEG	51.6	-	6.9	-2.0	-
Hf-NMOF@SiO_2	50.4	13.2	-	-32.8	175
Hf-NMOF@SiO_2@PEG	46.4	12.2	8.0	-17.3	246

[a]Determined by TGA. [b]Measured in 1 mM aq. KCl. [c]Measured in 10 mM PBS.

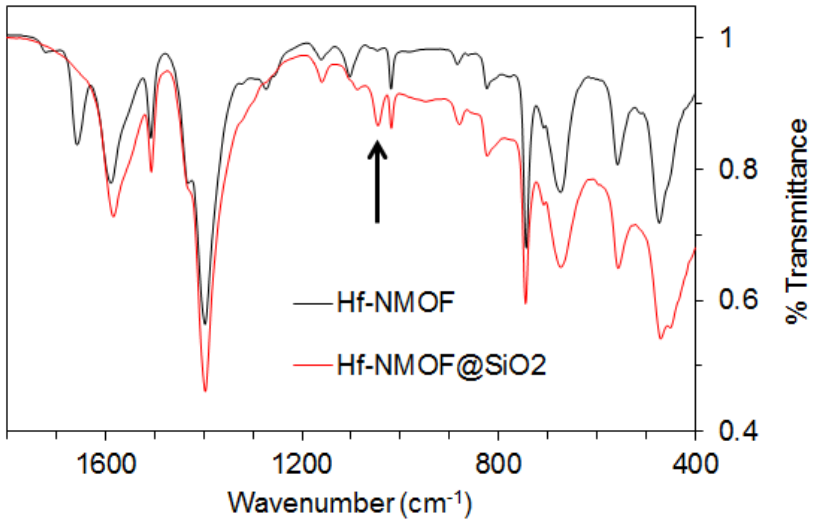

Figure 2.7. IR spectra of **Hf-NMOF** and **Hf-NMOF**@SiO_2. The arrow indicates the peak coming from SiO_2.

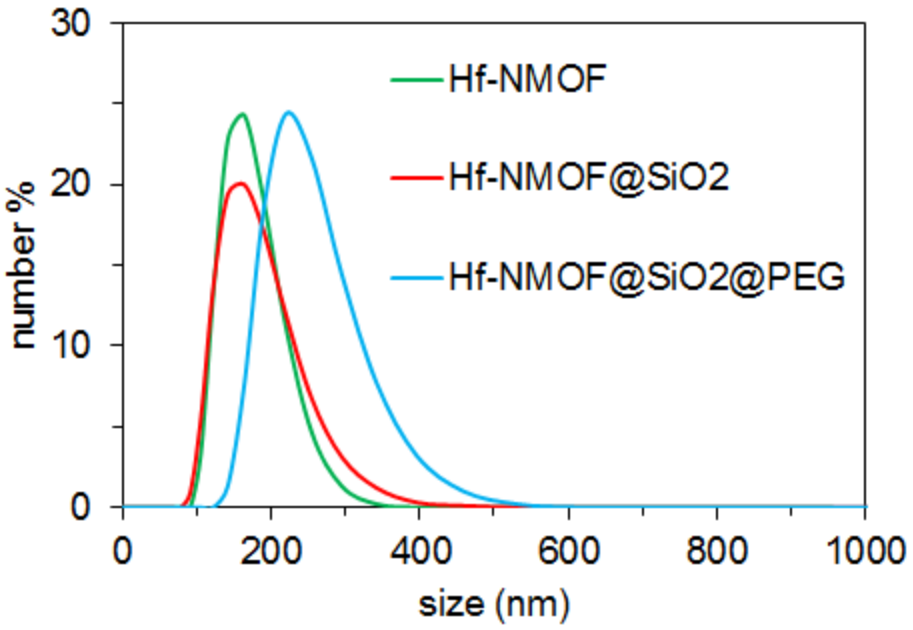

Figure 2.8. Size distribution by number obtained by DLS of **Hf-NMOF**, **Hf-NMOF**@SiO_2, and **Hf-NMOF**@SiO_2@PEG in 10 mM PBS.

2.2.4. In vivo computed tomography studies

In vivo CT imaging was performed on mice using a micro-CT with a carbon nanotube X-ray source, which could be synchronized and gated with physiological signals.[20, 21] Mouse respiration and electrocardiography (ECG) traces were monitored to allow respiratory-gated and cardiac-gated scans that minimize image blurriness caused by the animal's motion. A 20 g anesthetized mouse was administered 6.5 mg **Hf-NMOF**@SiO_2@PEG (46.4 wt% Hf, 3.0 mg Hf) dispersed in 10 mM PBS via tail vein injection. In general, a change in HU of 10-15 units is detectable, while ten times this is desirable for optimal contrast enhancement.[22] Without a contrast agent, most organs have HU values in the range of 40-60 HU. The 3.0 mg dose of Hf was expected to cause a change of about +95 HU in the blood pool, based on the attenuation data from the phantom studies. It was found, however, that the contrast agent was cleared from the bloodstream and accumulated in the spleen and liver within 15 min after

injection (Fig. 2.9a-d). The attenuation of the spleen and liver increased by 131 and 86 HU, respectively, while there was no attenuation enhancement in the heart (blood) (Fig. 2.9e-f). Based on the sizes of the organs and the changes in attenuation, about 6% of the particles went to the spleen, while about 50% went to the liver. It is likely that the particles were too large to evade filtration by the tissue in the spleen and uptake by the MPS.

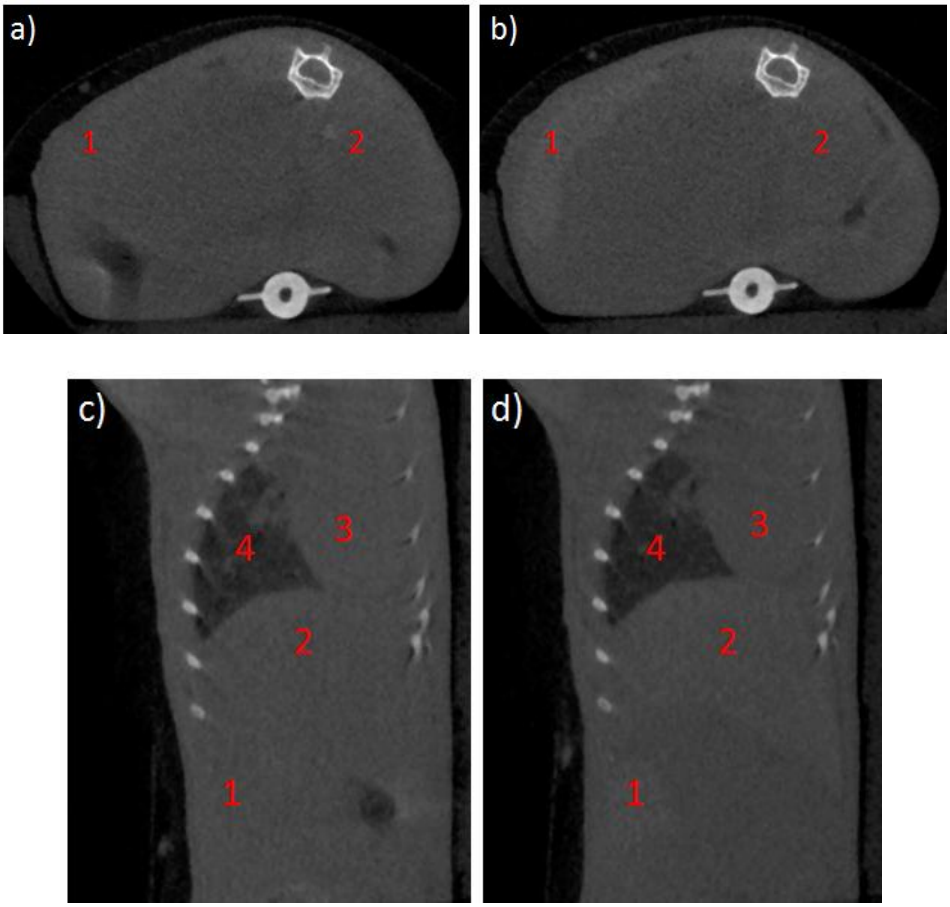

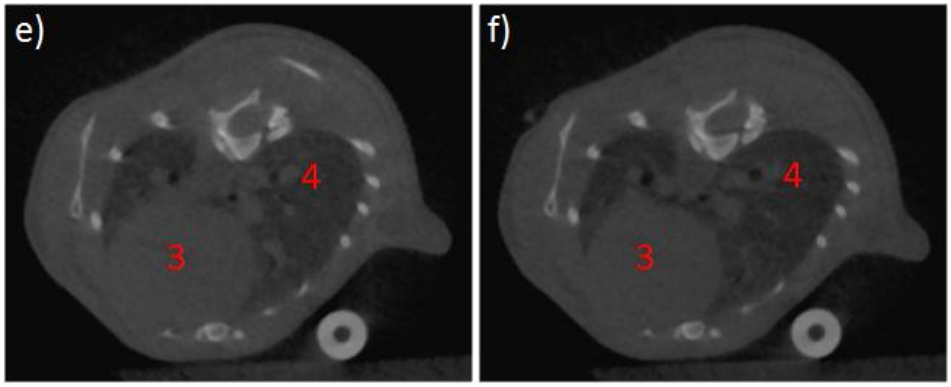

Figure 2.9. (a,b,e,f) Axial and (c,d) sagittal CT slices of a mouse (a,c,e) pre-contrast and (b,d,f) 15 min after injection of **Hf-NMOF**@SiO_2@PEG (3.0 mg Hf). The labels are: 1-spleen, 2-liver, 3-heart, 4-lungs.

2.2.5. Smaller Hf-NMOF particles

Smaller Hf-NMOF particles (**Hf-NMOF'**) were made in hopes that smaller particles would circulate longer and allow blood pool imaging, rather than accumulating quickly in the spleen and liver. **Hf-NMOF'** was synthesized by heating a solution of equal molar $HfCl_4$ and H_2BDC in DMF at 100 ºC in a sealed vessel for 48 h. This is the same method as used for **Hf-NMOF**, but the concentration of starting materials was lowered and the acid modulator was eliminated in order to decrease the size of the particles. The resulting spherical particles are about 50 nm in diameter by SEM (Fig. 2.10). TGA showed that **Hf-NMOF'** has the same Hf content as **Hf-NMOF** (57.3 wt%), but PXRD showed that the smaller particles are amorphous. **Hf-NMOF'** was coated with silica and then PEGylated, in a manner similar to **Hf-NMOF**, to result in **Hf-NMOF**@SiO_2@PEG' particles that contain 9.1 wt% SiO_2, 10.8 wt% PEG, and 46.5 wt% Hf, as determined by TGA. DLS in 10 mM PBS showed an average size of 102 nm, compared to 246 nm for the corresponding larger PEGylated particles (Fig. 2.11a). A test for non-specific protein adsorption was done to determine how **Hf-NMOF**@SiO_2@PEG' may behave in the bloodstream. Bovine serum albumin (BSA) was

added to **Hf-NMOF**@SiO_2@PEG**'** in a 5:1 ratio (by weight) and particle size was monitored by DLS over 95 min. Particles tend to aggregate when proteins adsorb to the surface, which would be apparent by an increasing Z-average (an intensity-weighted measurement of particle size) and a decreasing signal intensity due to sedimentation of large aggregates. The Z-average stayed within a small range (192-200 nm) over the course of the experiment, and the signal intensity (counts) remained fairly constant, indicating the stability of **Hf-NMOF**@SiO_2@PEG**'** against aggregation in the presence of BSA (Fig. 2.11b).

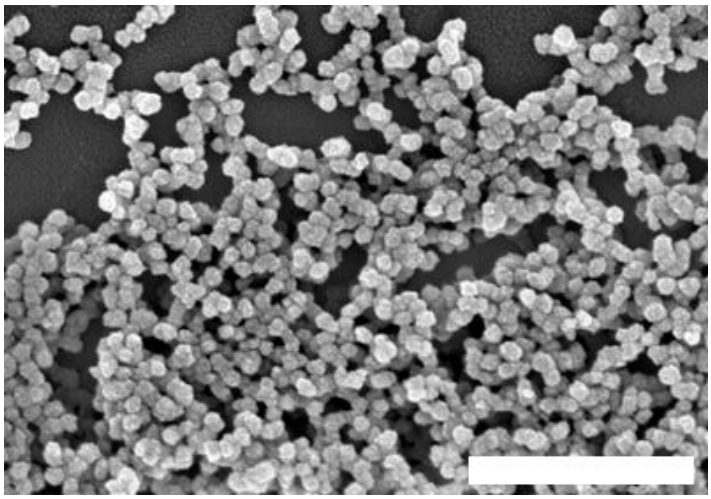

Figure 2.10. SEM image of **Hf-NMOF**@SiO_2@PEG**'**. The scale bar represents 500 nm.

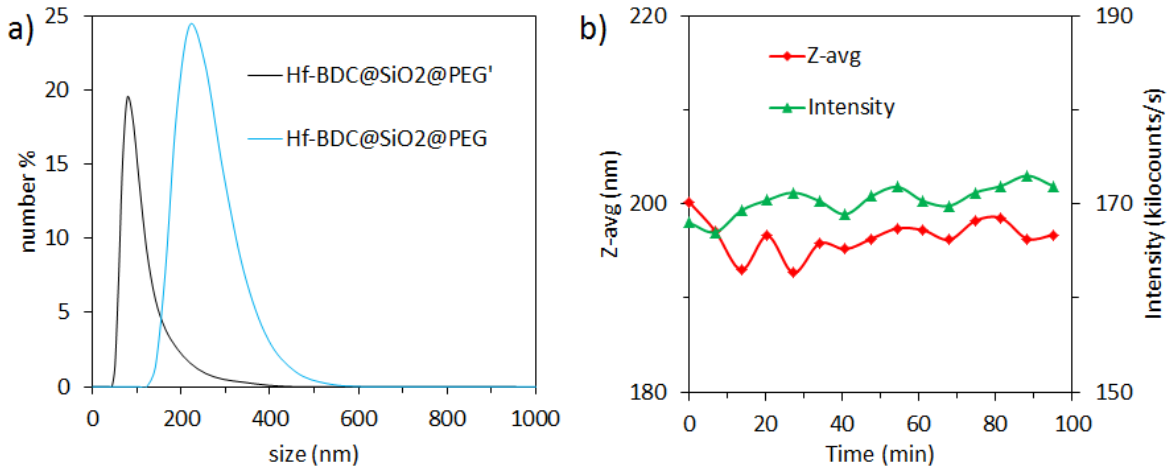

Figure 2.11. DLS in 10 mM PBS. (a) Size distribution by number of **Hf-NMOF**@SiO_2@PEG and **Hf-NMOF**@SiO_2@PEG**'**. (b) Stability test of **Hf-NMOF**@SiO_2@PEG**'** in the presence of BSA.

In vivo CT imaging was done using **Hf-NMOF**@SiO_2@PEG**'**. A 20 g anesthetized mouse was administered 6.5 mg **Hf-NMOF**@SiO_2@PEG**'** (46.5 wt% Hf, 3.0 mg Hf) dispersed in 10 mM PBS via tail vein injection. This is the same Hf dose used in the previous study with the larger particles. The mouse died immediately, and a CT scan revealed accumulation of particles in the lungs, with an increase in attenuation of 258 HU (Fig 2.12). Apparently, this dose was too high to avoid pulmonary embolism caused by particle aggregation, so a smaller dose of 4.3 mg particles (2.0 mg Hf) was used. In this case, the mouse survived, and a scan taken 15 min after injection revealed that the particles accumulated in the spleen and liver, with attenuation increases of 101 and 41 HU, respectively. There was no increase in attenuation in the bloodstream, as measured in the heart. A scan was also taken of a mouse that was administered 5.6 mg of **Hf-NMOF'** (57.3 wt% Hf, 3.2 mg Hf), 15 min after injection. Again, increases in attenuation are seen in the spleen (117 HU) and liver (63 HU) (Fig. 2.13), while no increase in seen in the bloodstream, as expected for bare nanoparticles. The clearance of the contrast agents from the blood is rapid, as similar results are seen for both types of particles just ~3-5 min after injection. The CT results obtained using Hf-NMOF@SiO_2@PEG**'** compared to larger **Hf-NMOF**@SiO_2@PEG and compared to non-PEGylated **Hf-NMOF'** are quite similar. It is possible that these smaller particles form aggregates in the bloodstream that are big enough to be filtered by spleen or taken up by the MPS, or that the PEGylation is ineffective at preventing protein adsorption.

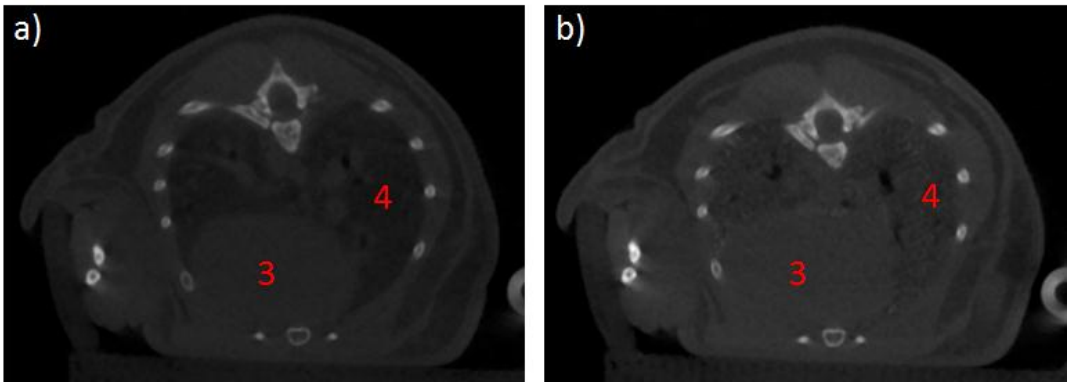

Figure 2.12. Axial CT slices of a mouse (a) pre-contrast and (b) 15 min after injection of **Hf-NMOF**@SiO_2@PEG**'** (3.0 mg Hf). The labels are: 3-heart, 4-lungs.

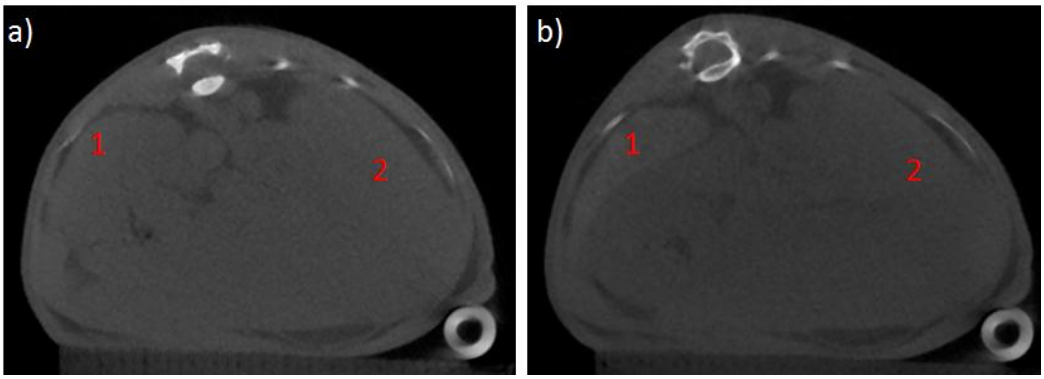

Figure 2.13. Axial CT slices of a mouse (a) pre-contrast and (b) 15 min after injection of **Hf-NMOF**@SiO_2@PEG**'** (2.0 mg Hf). The labels are: 1-spleen, 2-liver.

Table 2.2. Changes in X-ray attenuation *in vivo*

Contrast agent	mg Hf	Organ	Δ avg HU[a]
Hf-NMOF@SiO_2@PEG	3.0	Spleen	+131
Hf-NMOF@SiO_2@PEG	3.0	Liver	+86
Hf-NMOF@SiO_2@PEG**'**	3.0	Lungs	+258
Hf-NMOF@SiO_2@PEG**'**	2.0	Spleen	+101
Hf-NMOF@SiO_2@PEG**'**	2.0	Liver	+41
Hf-NMOF'	3.2	Spleen	+117
Hf-NMOF'	3.2	Liver	+63

[a]15 min after injection

2.3. Conclusion

Nanoscale metal-organic frameworks with Zr or Hf metal connecting points have been synthesized and evaluated for their potential as CT contrast agents. Hf-NMOFs were coated with silica and then functionalized with PEG to make the particles suitable for *in vivo* CT imaging. As-synthesized and PEGylated Hf-NMOFs of different sizes could be used as contrast agents for imaging the spleen or liver. While these particles were intended to be long-circulating and to increase attenuation in the blood pool, they were cleared quickly from the blood by spleen filtration and/or by the MPS. This could be due to particle aggregation or ineffective PEGylation. Despite the difficulties encountered with Hf-NMOFs, the NMOF platform provides a promising strategy for incorporating high loadings of heavy elements into nanoparticles that can be surface-functionalized for enhanced biocompatibility and *in vivo* performance.

2.4. Experimental Details

2.4.1 Materials and methods

All starting materials were purchased from Fisher or Aldrich and used without further purification. Proton nuclear magnetic resonance spectroscopy (^{1}H NMR) spectra were recorded on a Bruker NMR 400 at 400 MHz and referenced to the proton resonance resulting from incomplete deuteration of deuterated chloroform ($CDCl_3$, δ 7.26) or deuterated dimethyl sulfoxide (DMSO-d_6, δ 2.50). Thermogravimetric analysis (TGA) was performed using a Shimadzu TGA-50 equipped with a platinum pan, and all samples were air-dried and heated at a rate of 4 °C per minute under air. Scanning electron microscopy (SEM) was used to

image the particles, using a Hitachi 4700 field emission scanning electron microscope. A Cressington 108 Auto Sputter Coater equipped with a Au/Pd (80/20) target and an MTM-10 thickness monitor was used to coat the samples with a conductive layer before taking SEM images. Each SEM sample was prepared by first suspending the nanomaterial in ethanol, then a drop of the suspension was placed on a glass slide and the solvent was allowed to evaporate. Transmission electron microscopy (TEM) was obtained on a JEOL 100CX-II Transmission Electron Microscope using carbon-coated copper grids to hold samples. Nitrogen adsorption experiments were performed with a Quantachrome Autosorb-1C. Size and zeta potential information was obtained on a Malvern ZetaSizer dynamic light scattering instrument. Infrared spectroscopy (IR) was performed using a Bruker Alpha-T Fourier Transform Infrared Spectrometer in attenuated total reflectance (ATR) mode. Powder X-ray diffraction (PXRD) analyses were carried out using a Bruker SMART Apex II diffractometer using Cu radiation. The PXRD patterns were processed with the Apex II package using the phase ID plugin.

Computed tomography (CT) phantom and *in vivo* images and X-ray attenuation data were obtained using a micro-computed tomography scanner equipped with a carbon nanotube based field emission micro-focus X-ray source. All CT scans were done at 50 kVp, 0.7 mA, 0.5 mm Al filtration, and 50 msec exposure per projection. Four hundred projections were used over a circular orbit of 200° at a step angle of 0.5° and were reconstructed at 76 μm isotropic voxel spacing. In vivo imaging was carried out using protocol approved by University of North Carolina Institutional Animal Care and Use Committee. The animals were anesthetized with 1–2% isoflurane at a flow rate of 1.5–2 L min^{-1} from a vaporizer. The anesthetized animals were placed over the pressure sensor in the mouse sample holder and

secured with adhesive restraints. The animals were put in the prone position such that the respiration sensor was approximately in the position of the abdomen to achieve maximum sensor coupling. To obtain the cardiac signals, ECG electrodes were taped to the footpads. With the camera running at 1 frame per second, the scan time was typically 15–20 min depending on the mouse respiration and heart rates.

2.4.2. Synthesis of PEG and metal organic frameworks

Synthesis of carboxy-poly(ethylene glycol)2000 (HO_2C-PEG_{2000}-OCH_3): 1.00 g (0.50 mmol) of poly(ethylene glycol)-2000 monomethylether was dried under vacuum at 100 ºC for 5 h. After cooling the PEG to room temperature, it was dissolved in 25 mL dry tetrahydrofuran. 108 mg (4.50 mmol) of sodium hydride was added under N_2, and the dispersion was stirred vigorously for 1 h under N_2. 295 μL (2.00 mmol) of tert-butyl bromoacetate was then added, and the reaction was stirred at room temperature for 12 h. The reaction was filtered to remove NaBr, and the filtrate was concentrated by evaporation under vacuum. The $(CH_3)_3O_2C$-PEG_{2000}-OCH_3 product was precipitated by addition of diethyl ether, then filtered and dried under vacuum. The carboxy groups were deprotected by stirring the product in 60 mL of 70/30 (v/v) dichloromethane/trifluoroacetic acid at room temperature for 2 h. The resulting solution was concentrated by evaporation under vacuum, and HO_2C-PEG_{2000}-OCH_3 was precipitated by the addition of diethyl ether. ^1H NMR ($CDCl_3$, 400 MHz): 3.36 (s, 3H), 3.62 (s, 172H), 3.74 (t, 2H), 3.80 (t, 2H).

Synthesis of triethoxysilylpropyl carbamoyl-poly(ethylene glycol)2000 ($(OEt)_3Si$-PEG_{2000}-OCH_3): 1.00 g (0.50 mmol) of poly(ethylene glycol)-2000 monomethylether was dried under vacuum at 100 ºC for 5 h. After cooling the PEG to room temperature, it was dissolved in 4 mL anhydrous dimethyl sulfoxide (DMSO). 0.124 mL (0.50 mmol) of distilled

(3-isocyanatopropyl)triethoxysilane was then added, followed by 1 μL (0.742 mg, 5.7 μmol) of diisopropylethylamine (Hünig's base). The reaction was stirred at room temperature under N_2 for 12 h. The DMSO was removed under vacuum at 60 ºC. ^{1}H NMR (DMSO-d_6, 400 MHz): 0.51 (t, 2H), 1.14 (t, 9H), 1.43 (t, 2H), 2.92 (q, 2H), 3.35 (s, 3H), 3.50 (s, 174H), 3.73 (q, 6H), 4.03 (t, 2H), 7.22 (t, 1H).

Synthesis of Zr-NMOF: **Zr-NMOF** was synthesized using a reported procedure.[2] 1,4-benzene dicarboxylic acid (37.7 mg, 0.227 mmol) and $ZrCl_4$ (52.9 mg, 0.227 mmol) were dissolved in 26.4 mL DMF. This solution was sealed in a Teflon-lined autoclave and heated in an oven at 120 ºC for 24 h. After cooling to room temperature, the resulting solid was isolated be centrifugation at 10,000 rpm for 10 min. After removing the supernatant, the solid was washed three times, once using 20 mL of DMF, then twice using 10 mL of ethanol each time. For each wash, the particles were redispersed by sonication and then recovered by centrifugation at 10,000 rpm for 10 min. Yield: 48.8 mg (76.9%)

Synthesis of Hf-NMOF: **Hf-NMOF** was synthesized by a modification of the procedure for Zr-NMOF. 1,4-benzene dicarboxylic acid (45.1 mg, 0.272 mmol) and $ZrCl_4$ (63.3 mg, 0.272 mmol) were dissolved in 26.4 mL DMF, and acetic acid (13.2 μL, 0.231 mmol) was added. This solution was sealed in a Teflon-lined autoclave and heated in an oven at 100 ºC for 48 h. After cooling to room temperature, the resulting solid was isolated and washed as described for **Zr-NMOF**. Yield: 77.6 mg (78.2%)

Synthesis of Hf-NMOF@PEG: **Hf-NMOF** (60.0 mg) was dispersed in 10 mL H_2O, then added to a solution of HO_2C-PEG_{2000}-OCH_3 (12.0 mg, 5.87 μmol) in 10 mL H_2O. The reaction was stirred at room temperature for 18 h, then the resulting particles were isolated by

centrifugation and washed with H_2O and methanol, as described for **Zr-NMOF**. Yield: 52.1 mg (80.8%)

Synthesis of Hf-NMOF@SiO_2: **Hf-NMOF** (60.0 mg) was dispersed in 10 mL of ethanol. This dispersion was added to a solution of 2.03 mL ammonium hydroxide (14.8 M, 30.0 mmol) in 137.95 mL of ethanol, then TEOS (18.0 μL, 81.2 μmol) was added. The final 150-mL reaction mixture contained 0.4 mg of particles/mL with 0.2 M NH_4OH and 0.406 mM TEOS. The reaction was stirred at room temperature for 2 h, then the resulting particles were isolated by centrifugation and washed with ethanol, as described for **Zr-NMOF**. Yield: 52.8 mg (76.4%)

Synthesis of Hf-NMOF@SiO_2@PEG: **Hf-NMOF@SiO_2** (45.0 mg) was dispersed in a 10-mL solution of $(OEt)_3Si\text{-}PEG_{2000}\text{-}OCH_3$ (15.0 mg, 6.76 μmol) in ethanol. This dispersion was added to a solution of 0.305 mL ammonium hydroxide (14.8 M, 4.51 mmol) in 4.695 mL of ethanol. The final 15-mL reaction mixture contained 3 mg of particles/mL with 0.3 M NH_4OH and 0.45 mM PEG. The reaction was stirred at room temperature for 21 h, then the resulting particles were isolated by centrifugation and washed with H_2O and methanol, as described for **Zr-NMOF**. Yield: 40.5 mg (71.8%)

Synthesis of Hf-NMOF': 1,4-benzene dicarboxylic acid (21.9 mg, 0.132 mmol) and $ZrCl_4$ (30.7 mg, 0.132 mmol) were dissolved in 26.4 mL DMF. This solution was sealed in a Teflon-lined autoclave and heated in an oven at 100 ºC for 48 h. After cooling to room temperature, the resulting solid was isolated and washed as described for **Zr-NMOF**. Yield: 41.6 mg (86.4%)

Synthesis of Hf-NMOF@SiO_2': **Hf-NMOF'** (60.0 mg) was dispersed in 10 mL of ethanol. This dispersion was added to a solution of 1.52 mL ammonium hydroxide (14.8 M,

22.5 mmol) in 138.47 mL of ethanol, then TEOS (9.0 μL, 40.6 μmol) was added. The final 150-mL reaction mixture contained 0.4 mg of particles/mL with 0.15 M NH_4OH and 0.203 mM TEOS. The reaction was stirred at room temperature for 1 h, then the resulting particles were isolated by centrifugation and washed with ethanol, as described for **Zr-NMOF**. Yield: 56.4 mg (94.0%)

Synthesis of Hf-NMOF@SiO_2@PEG': The same procedure as for **Hf-NMOF**@SiO_2@PEG was used, except **Hf-NMOF**@SiO_2**'** was used instead of **Hf-NMOF**@SiO_2. Yield: 45.0 mg (100%)

2.5. References

(1) Yu, S.; Watson, A. D. *Chem. Rev.* **1999**, *99*, 2353.

(2) Cavka, J. H.; Jakobsen, S.; Olsbye, U.; Guillou, N.; Lamberti, C.; Bordiga, S.; Lillerud, K. P. *J. Am. Chem. Soc.* **2008**, *130*, 13850.

(3) Kandiah, M.; Nilsen, M. H.; Usseglio, S.; Jakobsen, S.; Olsbye, U.; Tilset, M.; Larabi, C.; Quadrelli, E. A.; Bonino, F.; Lillerud, K. P. *Chem. Mater.* **2010**, *22*, 6632.

(4) Kim, M.; Cohen, S. M. *Cryst. Eng. Comm.* **2012**, DOI: 10.1039/c2ce06491j.

(5) Rabin, O.; Perez, J. M.; Grimm, J.; Wojtkiewicz, G.; Weissleder, R. *Nat. Mater.* **2006**, *5*, 118.

(6) Kim, D.; Park, S.; Lee, J. H.; Jeong, Y. Y.; Jon, S. *J. Am. Chem. Soc.* **2007**, *129*, 7661.

(7) Ferrari, M. *Nat Rev Cancer* **2005**, *5*, 161.

(8) Karakoti, A. S.; Das, S.; Thevuthasan, S.; Seal, S. *Angew. Chem. Int. Ed.* **2011**, *50*, 2.

(9) *Poly(ethylene glycol): Chemistry and Biological Applications;* Harris, J.M., Zalipsky, S., Eds.; ACS Symposium Series 680; American Chemical Society: Washington, DC, 1997.

(10) Walkey, C. D.; Chan, W. C. W. *Chem. Soc. Rev.* **2012**, 41, 2780.

(11) Mansour, H. M.; Rhee, Y.-S.; Wu, X. *Int. J. Nanomed.* **2009**, *4*, 299.

(12) Faraji, A. H.; Wipf, P. *Bioorg. Med. Chem.* **2009**, *17*, 2950.

(13) Otsuka, H.; Nagasaki, Y.; Kataoka, K. *Adv. Drug. Deliv. Rev.* **2003**, *55*, 403.

(14) Prencipe, G.; Tabakman, S. M.; Welsher, K.; Liu, Z.; Goodwin, A. P.; Zhang, L.; Henry, J.; Dai, H. *J. Am. Chem. Soc.* **2009**, *131*, 4783.

(15) Umemura, A.; Diring, S.; Furukawa, S.; Uehara, H.; Tsuruoka, T. *J. Am. Chem. Soc* **2011**, *133*, 15506.

(16) Schaate, A.; Roy, P.; Godt, A.; Lippke, J.; Waltz, F. *Chem. Eur. J.* **2011**, *17*, 6643.

(17) Brooks, R. A. *J. Comput. Assist. Tomo.* **1977**, *1*, 487.

(18) National Institute of Standards and Technology. X-ray Mass Attenuation Coefficients. http://www.physics.nist.gov/PhysRefData/XrayMassCoef/tab3.html (accessed Feb 5, 2012).

(19) Sprawls, P. *Physical Principles of Medical Imaging*, 2nd ed.; Aspen Publishers: Gaithersburg, MD, 1993.

(20) Cao, G.; Calderon-Colon, X.; Wang, P.; Burk, L.; Lee, Y. Z.; Rajaram, R.; Sultana, S.; Lalush, D.; Lu, J.; Zhou, O. *Proc. of SPIE* **2009**, *7258*, 72585Q1-7.

(21) Cao, G.; Lee, Y. Z.; Peng, R.; Liu, Z.; Rajaram, R.; Calderon-Colon, X.; An, L.; Wang, P.; Phan, T.; Sultana, S.; Lalush, D. S.; Lu, J. P.; Zhou, O. *Phys. Med. Biol.* **2009**, *54*, 2323.

(22) Speck, U. Contrast Agents: X-ray Contrast Agents and Molecular Imaging -- A Contradiction? In Handbook of Experimental Pharmacology; Semmler, W., Schwaiger, M., Eds.; Springer-Verlag: Berlin, **2008**; Vol. 185, p 167.

CHAPTER 3

Nanoscale Coordination Polymers for Antifolate Drug Delivery

(Portions of this chapter were adapted with permission from Huxford, R.C.;† deKrafft, K.E.;† Boyle, W.S.; Liu, D.; Lin, W. *Chem. Sci.* **2012**, *3*, 198. †Contributed equally to this work.

3.1. Introduction

3.1.1. Nanoparticles for drug delivery

Chemotherapeutic drugs can kill tumors and halt the progression of cancer, but the drugs are typically small molecules with undesirable pharmacokinetic profiles and severe side effects. Nanoparticles can be used as drug delivery vehicles *in vivo* with several potential advantages over small molecule therapeutic agents.[1-3] Molecular drugs cannot be easily targeted to a specific site and typically must be given in large doses with the potential for systemic toxicity. Nanoparticles can provide a better way to administer therapeutic agents that minimizes the death of healthy cells while eradicating diseased cells. Nanoparticles can be designed to target only a specific area in the body, such as a tumor (Fig 3.1). One way this can be achieved is by passive accumulation of nanoparticles in a particular area due to the enhanced permeability and retention (EPR) effect. Blood vessels in tumors are leaky compared to those in healthy tissues, and lymphatic drainage is poor in the tumor tissue. Therefore, nanoparticles of an appropriate size are able to leak out of defective vasculature and accumulate in a tumor site.[4] Pores in the defective vessels within a tumor typically have a diameter of 40-80 nm, but can be as large as 1 μm, while pores in normal vasculature are typically no larger than 8 nm.[5] Nanoparticles can also be made to actively target a specific

tissue by conjugation of affinity molecules to the surface of the particles.[6] Binding of targeting moieties to certain receptors that are overexpressed by cancer cells further improves tumor uptake of nanotherapeutics.[7] For example, sigma receptors are overexpressed on a number of different human cancer cell lines, including lung, colorectal, breast, and others.[8] These sigma receptors can be targeted by small benzamides, such as anisamide.[9-11]

Nanoparticles can also be designed to evade the immune system and release therapeutic agents in a controlled manner. These desirable properties can often be achieved by encapsulating or coating nanoparticles with a suitable material that improves stability, biocompatibility, and ease of functionalization. The physiological response to nanoparticles is described in Chapter 2 (section 2.1.2), and many of the same issues must be considered with nanoparticle formulations of drugs as with nanoparticulate contrast agents. Therapeutic nanoparticles must have a long circulation time in the bloodstream to allow accumulation at a target, and they must not release a significant amount of their active agent until they have reached the target.

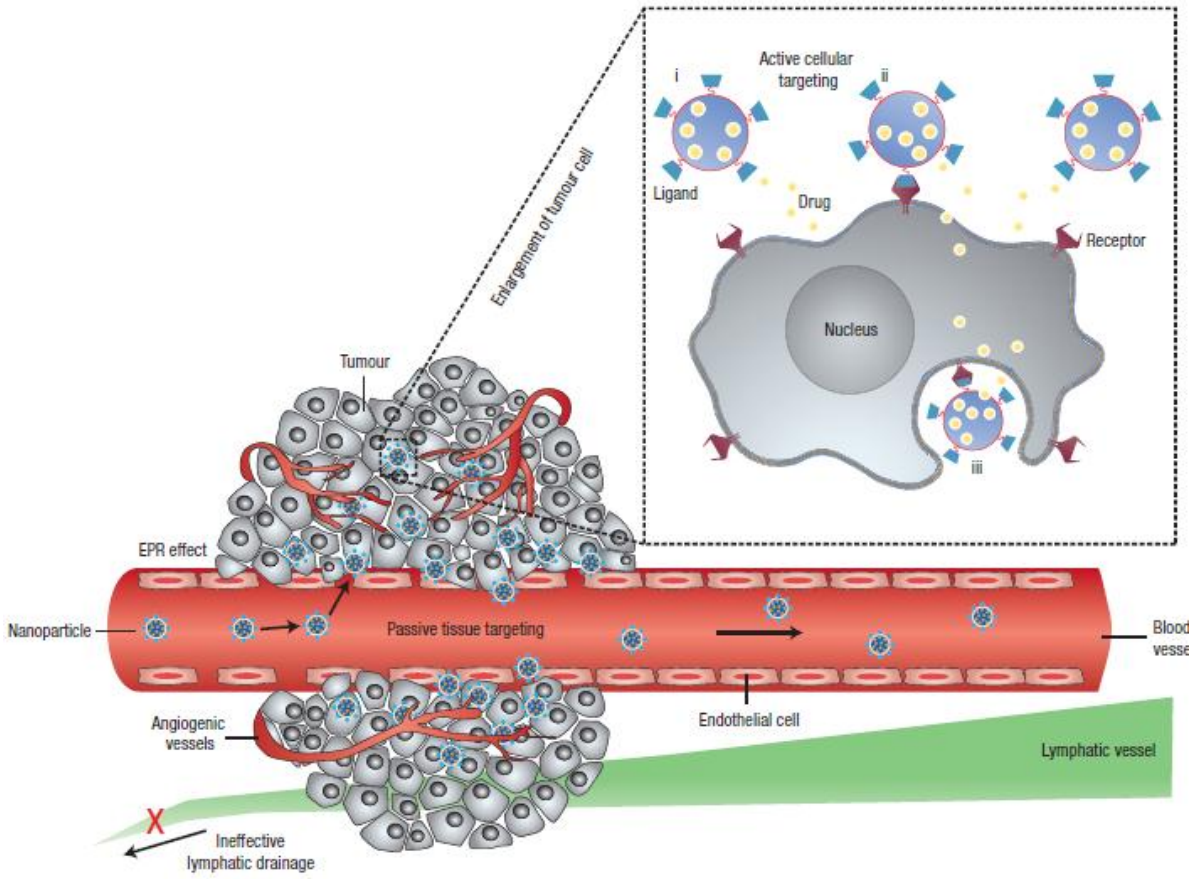

Figure 3.1. Schematic representation of drug delivery to a tumor by nanocarriers. Passive targeting is achieved by the EPR effect, while active targeting is achieved by functionalizing the nanocarrier surface with ligands that recognized specific cells. Reprinted from reference 3 with permission (copyright 2007 Nature Publishing Group).

3.1.2. Nanoscale coordination polymers for drug delivery

Several types of nanocarriers have been devised for delivery of chemotherapeutic agents to diseased tissue, resulting in improved pharmacokinetics and significant decreases in system toxicity.[1, 12] These carriers include liposomes, micelles, dendrimers, biomolecules, polymer particles, colloidal precipitates, and porous materials like mesoporous silica nanoparticles.[2, 13] For example, liposomes are lipid bilayer vesicles that are useful as drug carriers because they have low immunogenicity and can be taken up by cells.[14] Doxil is a

liposomal formulation of an anticancer drug that has significantly less toxicity in clinical tests compared to the small molecule drug.[15, 16]

Nanoscale coordination polymers (NCPs) are hybrid materials that can serve as drug carriers with several advantages over other types of nanoscale carriers. Background information on coordination polymers (CPs) and the usefulness of NCPs for biomedical applications is given in Chapter 1. There are several ways that drugs can be incorporated into NCPs. Cystalline NCPs with a framework structure can have high internal void volume, and the pores can be loaded with drugs. For example, the delivery of chemotherapeutics loaded into the pores of the MIL family of NCPs has been demonstrated.[17, 18] Alternatively, a drug can be directly incorporated as a component of the framework. Functionalities can also be included in the framework that allow post-synthetic covalent attachment of drug molecules. For example, cisplatin prodrugs have been successfully delivered by NCPs in which they were either directly incorporated or covalently attached after NCP synthesis.[19, 20] In this work, a different direct incorporation strategy was used to synthesize NCPs for delivery of an organic antifolate chemotherapeutic possessing functional groups that can bridge metal-connecting points in NCP formulations.[21, 22]

3.1.3. Methotrexate

Methotrexate (MTX) is a small molecule chemotherapeutic agent. As an antifolate drug, it works by inhibiting the enzyme dihydrofolate reductase, thereby preventing DNA synthesis.[23] While MTX is toxic to many cancer cells and is the first-line treatment for acute lymphoblastic leukemia (ALL), its efficacy is compromised by an array of drawbacks, including poor pharmacokinetics, low tolerated doses, and resistance.[24] Large doses of MTX are required as a result of its non-specific distribution and rapid renal clearance, which can

lead to systemic toxicity. Prolonged MTX treatment of cancer patients can result in numerous side effects such as mucositis, hematological toxicity, and secondary cancer. MTX delivery with nanoparticulate carriers can overcome many of the drawbacks of conventional chemotherapy, as nanoparticles can carry a large payload to a tumor and reduce systemic toxicity.[6] Although several nanoparticle systems have been examined for MTX delivery, relatively low drug loadings were achieved in these studies.[25-30] It was hypothesized that MTX could be incorporated into NCPs as a bridging ligand since it contains two carboxylate groups which can coordinate to metal connecting points (Fig. 3.2). Such a strategy could allow for very high loadings of MTX to be achieved in such NCP formulations. Several MTX-based NCPs were synthesized and characterized, and attempts were made to stabilize them.

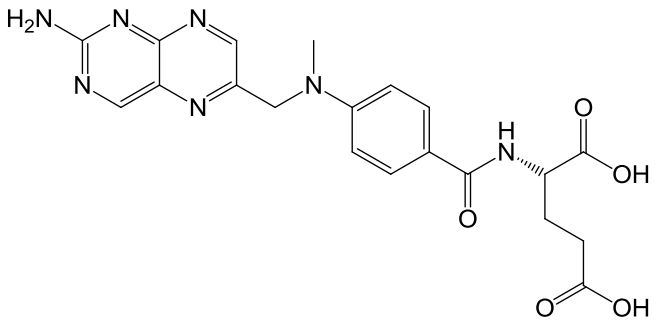

Figure 3.2. Structure of MTX.

3.2. Results and Discussion

3.2.1. Synthesis of Mn-, Cu-, and Zn-MTX NCPs

New NCPs were synthesized using MTX as the bridging ligand and either Mn^{2+}, Cu^{2+}, or Zn^{2+} ions as the metal-connecting points. The properties of the NCPs, especially stability, can be tuned by the choice of metal ion. While conventional heating can be used to

synthesize NCPs, microwave heating has recently been demonstrated to be a particularly useful method of synthesizing NCPs. Surfactant-assisted microwave synthesis has been used to make Mn-BDC (BDC = benzene dicarboxylate) NCPs,[31] while a simple solvothermal microwave synthesis method has been used to make Fe-BDC particles with the MIL-101 structure.[20] Microwave heating creates uniform seeding conditions that typically result in rapid formation of nanoparticles with controllable sizes and shapes.[32] Temperature and heating rate are important parameters that can be varied to control NCP particle nucleation and growth.

NCPs containing MTX and either Mn^{2+}, Cu^{2+}, or Zn^{2+} were synthesized by surfactant-assisted microwave heating. **Mn-MTX** and **Cu-MTX** were prepared in 78% and 18% yield, respectively, by first preparing two microemulsions of 0.1 M CTAB (CTAB = cetyltrimethylammonium bromide) and 0.5 M 1-hexanol in isooctane with a water-to-surfactant ratio (*W*) of 5. The aqueous phase that was added to the organic phase contained $[CH_3NH_3]_2$(MTX) in one microemulsion and $MnCl_2$ or $Cu(NO_3)_2$ in the other. After mixing the two microemulsions together, the final microemulsion was heated by microwave in a sealed vessel at 120 °C for 10 min, with stirring. The particles were isolated by centrifugation and washed with ethanol. Scanning electron microscopy (SEM) showed that **Mn-MTX** and **Cu-MTX** particles both had a twisted ribbon morphology, with ribbons about 1 μm long, 100 nm wide, and 50 nm thick (Fig. 3.3a-c). **Zn-MTX 1** particles with similar size and shape (Fig. 3.3d) were synthesized using $Zn(NO_3)_2$ as the metal precursor by the same procedure, except using a higher *W* value (15). These ribbon-like particles are not useful for drug delivery because they are too long in one dimension and their shape would likely make it difficult to encapsulate them or to functionalize them while maintaining high drug loading.

Smaller spherical Zn-MTX particles (**Zn-MTX 2**) could be made in 84% yield by using similar conditions as for **Zn-MTX 1**, but raising the pH of the $[CH_3NH_3]_2$(MTX) solution from 8.2 to 10.6 by addition of methylamine before adding it to the isooctane. Both SEM and transmission electron microscopy (TEM) showed that particles of **Zn-MTX 2** are spherical with a diameter between 40 and 100 nm (Fig. 3.4). Dynamic light scattering (DLS) in ethanol gives a number distribution with an average particle size of 161 nm, slightly larger than the size observed by microscopy due to slight aggregation in this medium (Fig. 3.5).

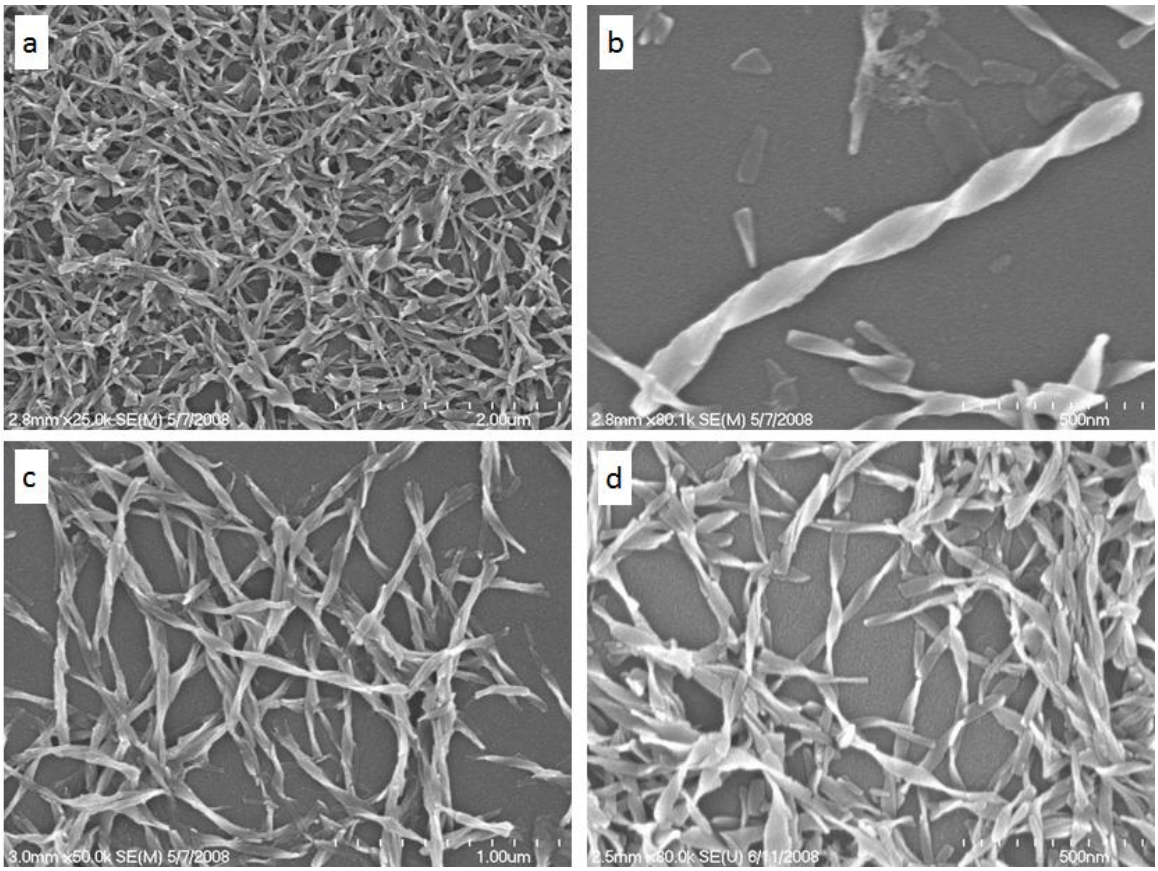

Figure 3.3. SEM images of (a-b) **Mn-MTX**, (c) **Cu-MTX**, and (d) **Zn-MTX 1**.

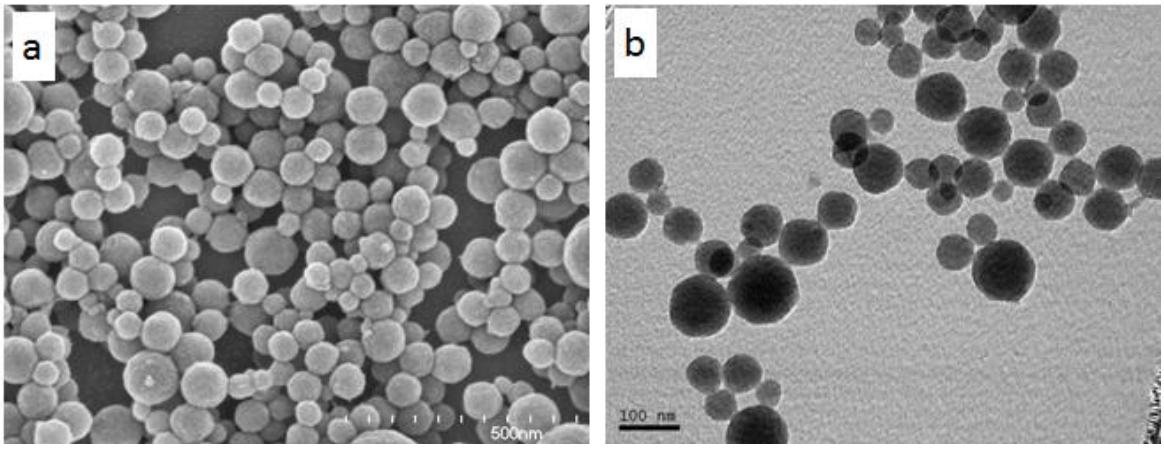

Figure 3.4. (a) SEM and (b) TEM images of **Zn-MTX 2**.

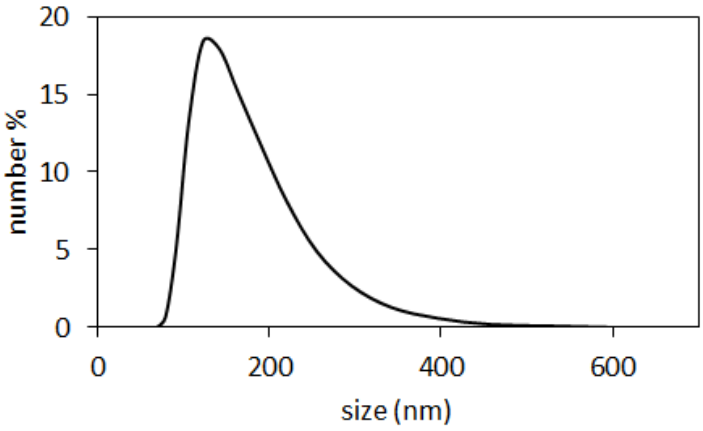

Figure 3.5. DLS of **Zn-MTX 2** in EtOH.

3.2.2. Characterization of Mn-, Cu-, and Zn-MTX NCPs

Mn-MTX, **Cu-MTX**, and **Zn-MTX 2** were shown by thermogravimetric analysis (TGA) to contain 87.0, 89.0, and 79.1 wt% MTX based on the organic weight loss that occurred between 200-500 °C (Fig. 3.6). If the metal-to-ligand ratio were 1:1, the MTX content would be 87-89 wt% of these NCPs. This corresponds well to the MTX content of **Mn-MTX** and **Cu-MTX**, while the lower MTX content of **Zn-MTX 2** is likely due to the formation of some Zn oxides or hydroxides at the higher pH used for its synthesis. The

powder X-ray diffraction (PXRD) patterns of **Mn-MTX** and **Cu-MTX** contain several weak peaks indicating that they have a low degree of crystallinity, and they share the same structure (Fig. 3.7). These peaks do not match pure MTX or any metal oxides that could be present in the particles as impurities. Attempts were made to grow single crystals of MTX-containing coordination polymers for structural determination by single crystal X-ray diffraction, however, all attempts were unsuccessful. The extremely broad peak and the lack of sharp peaks in the **Zn-MTX 2** PXRD pattern indicate a high degree of structural disorder. Raising the pH of the aqueous phase tends to increase the rate of particle formation, leading to less long-range order. The crystallinity, size, and shape of particles are dependent on the rates of nucleation and growth, two kinetic phenomena that respond differently to reaction conditions.[33] Crystalline NCPs usually adopt well-defined, non-spherical morphologies, as seen for **Mn-MTX** and **Cu-MTX**, because crystal lattice energy is the most influential factor in their growth. On the other hand, amorphous NCPs are usually spherical, as seen for **Zn-MTX 2**, because this morphology minimizes interfacial free energy between the particles and solvent during their formation.

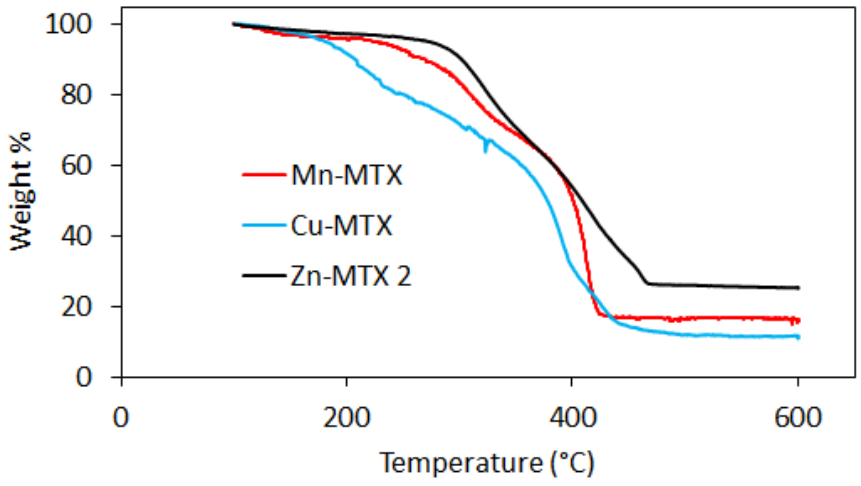

Figure 3.6. TGA of **Mn-MTX**, **Cu-MTX**, and **Zn-MTX 2**.

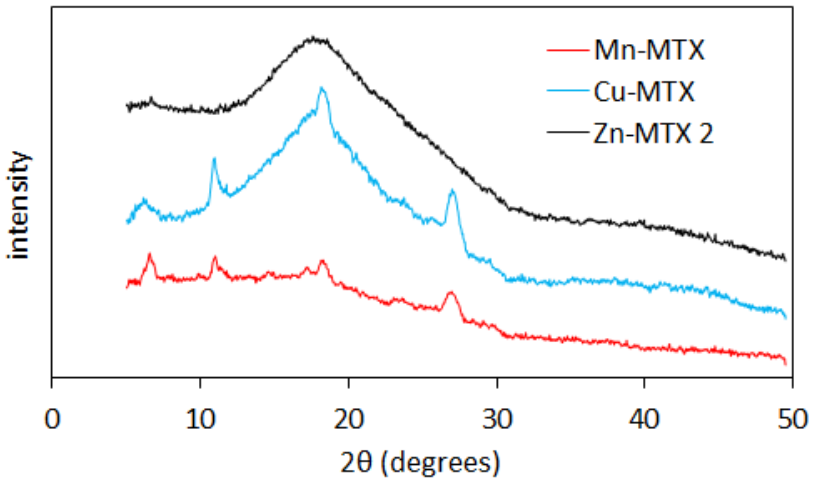

Figure 3.7. PXRD patterns of **Mn-MTX**, **Cu-MTX**, and **Zn-MTX 2**.

3.2.3. Release profile of Zn-MTX NCP

The stability of **Zn-MTX 2** under biological conditions was evaluated by dialyzing the particles against phosphate buffered saline (PBS) (pH = 7.4) at 37 °C (Fig. 3.8). The concentration of dissolved MTX was measured by the UV-vis absorbance at 305 nm. The absorption spectrum obtained from dissolved **Zn-MTX 2** matched that of MTX, indicating that MTX remains unchanged under the conditions used to synthesize the particles (Fig. 3.9). A solution of MTX alone took a significant amount of time to diffuse out of the dialysis bag. After 2.0 h, 50% of the MTX had diffused from the bag into the surrounding media. It took 6.6 h for 50% of the MTX from **Zn-MTX 2** to be released into solution, indicating that **Zn-MTX 2** has a half-life of about 4.6 h. However, DLS and SEM reveal that **Zn-MTX 2** particles quickly agglomerate into larger particles (>1 μm) in aqueous media (Fig. 3.10a), rendering them unsuitable for *in vivo* use. In order to improve stability and biocompatibility in biological media, several attempts were made to coat **Zn-MTX 2** with a silica shell,

however, the basic conditions used for coating caused severe erosion and fusion of the particles (Fig. 3.10b).

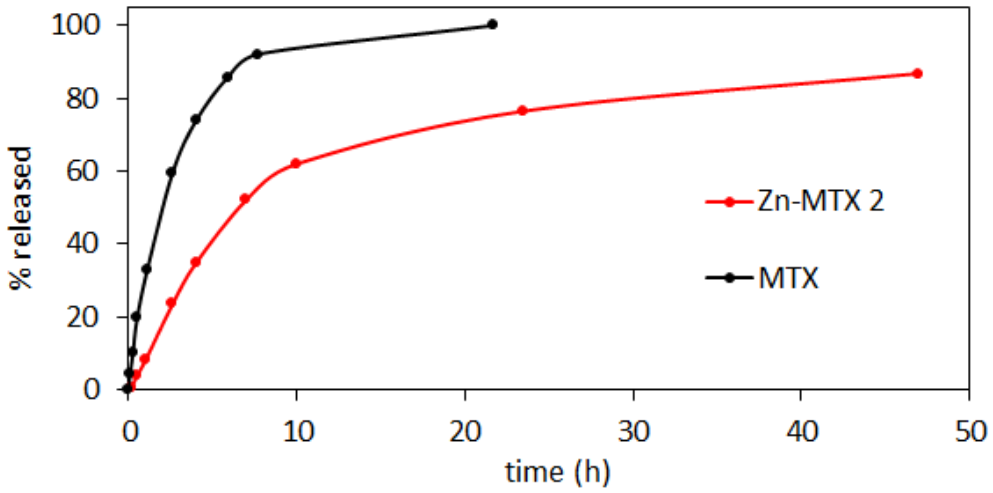

Figure 3.8. Release profiles for **Zn-MTX 2** and **MTX** alone dialyzed in PBS (pH = 7.4) at 37 °C.

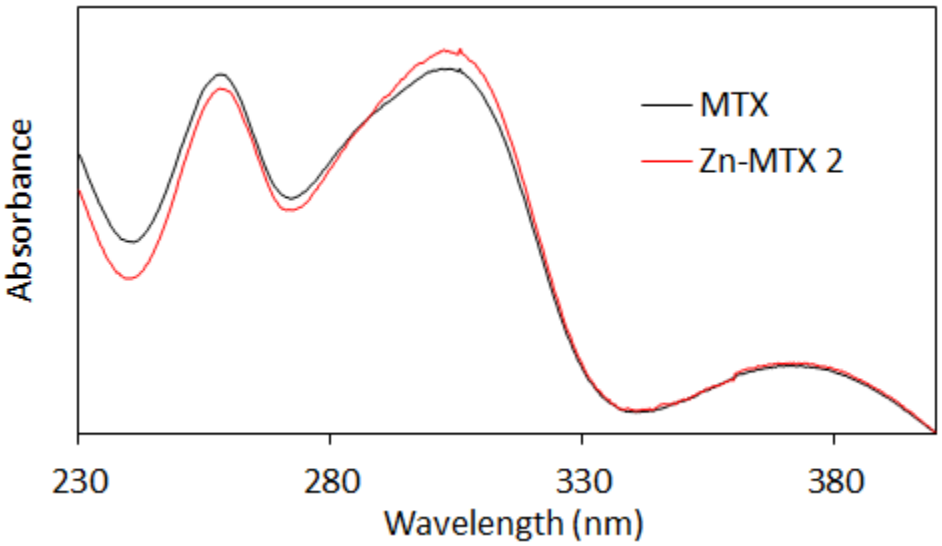

Figure 3.9. A UV-vis absorption spectrum of MTX compared to a spectrum of dissolved **Zn-MTX 2**.

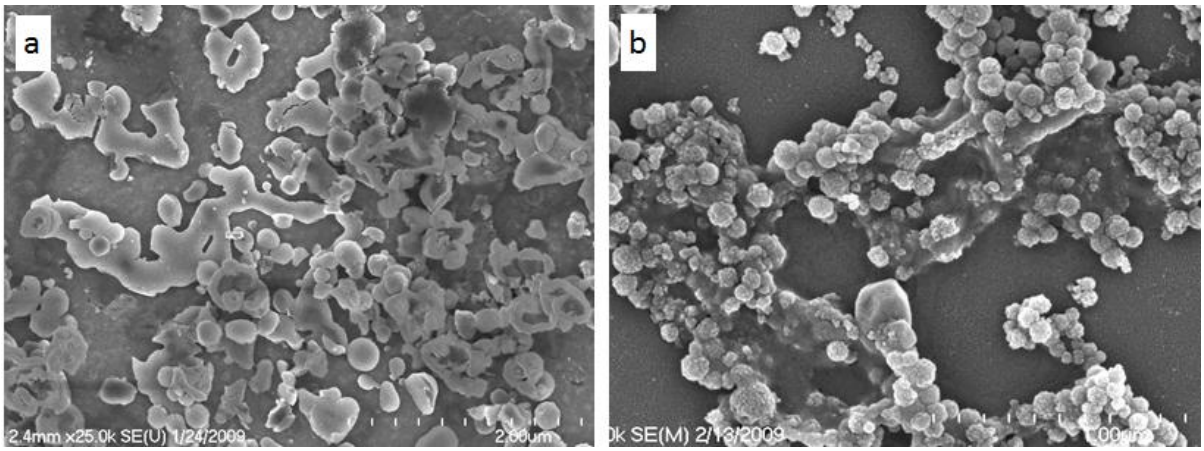

Figure 3.10. SEM images of **Zn-MTX 2** after exposure to (a) water and (b) silica-coating conditions.

3.2.4. Synthesis and characterization of Zr-MTX NCPs

It was hypothesized that more robust NCPs could be synthesized using Zr^{4+} in place of Zn^{2+} metal connecting points, due to the strength of the Zr-carboxylate bond.[34] **Zr-MTX** was synthesized in 54% yield by microwave heating of a solution of MTX and $ZrCl_4$ in N,N-dimethylformamide (DMF) at 60 °C for 5 min in a sealed vessel. The resulting spherical particles had a diameter of 70 to 180 nm by both SEM and TEM (Fig. 3.11), and DLS showed an average particle size of 136 nm in 1 mM aq. KCl (Fig. 3.12). **Zr-MTX** contains 78.7 wt% MTX, based on the organic weight loss seen by TGA (Fig. 3.13), and is amorphous by PXRD.

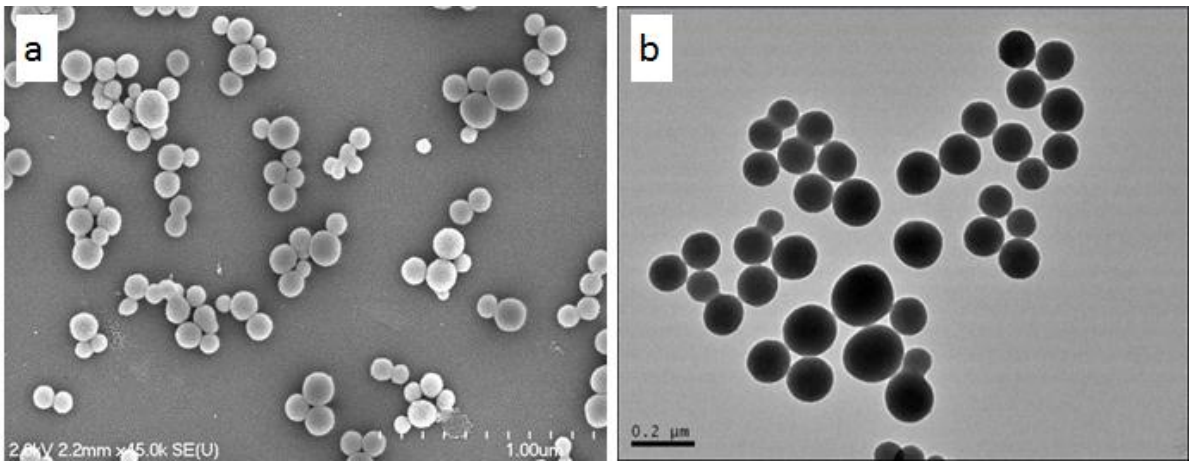

Figure 3.11. (a) SEM and (b) TEM images of **Zr-MTX**.

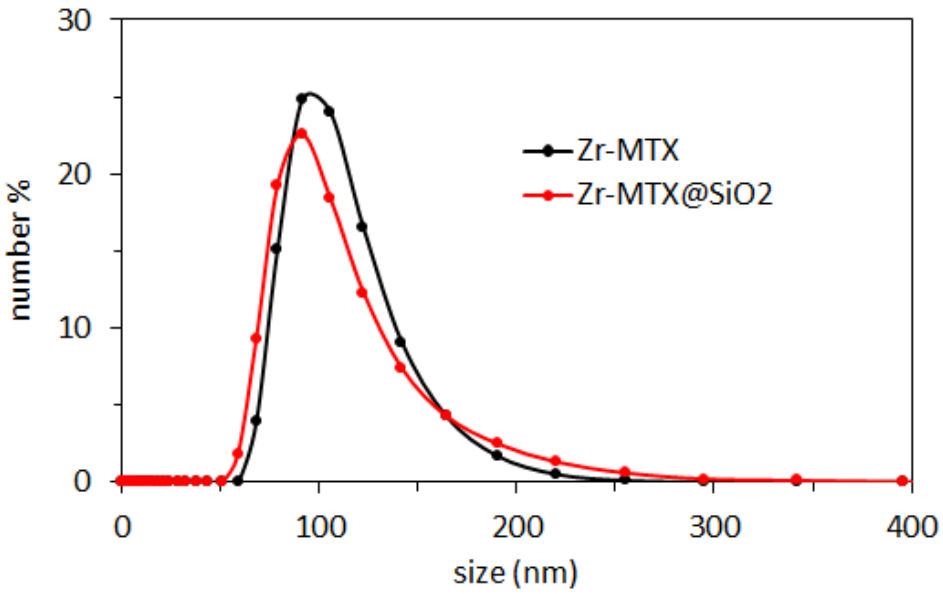

Figure 3.12. DLS of **Zr-MTX** and **Zr-MTX**@SiO_2 in 1 mM aq. KCl.

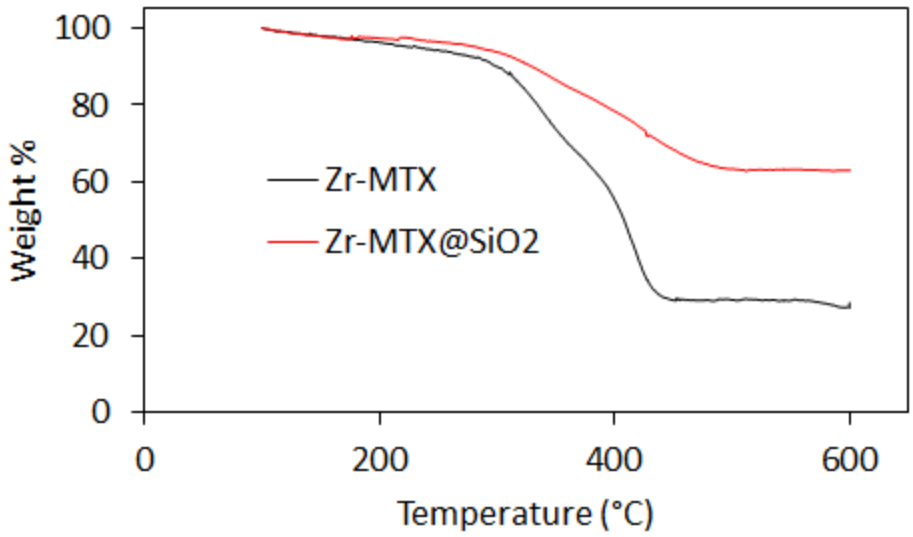

Figure 3.13. TGA of **Zr-MTX**.

3.2.5. Silica coating of Zr-MTX NCPs

Zr-MTX particles were coated with amorphous silica by base-catalyzed hydrolysis and condensation of tetraethylorthosilicate (TEOS) in ethanol to afford **Zr-MTX**@SiO_2. TEM showed that the particles remained discreet and retained their morphology during coating. There was no shell visible by TEM, but energy-dispersive X-ray spectroscopy (EDS) showed the presence of Si, with a Si/Zr atomic ratio of 4.1 (Fig. 3.14). DLS showed an increase in average particle size from 136 to 164 nm after coating, with no sign of **Zr-MTX**@SiO_2 particle aggregation in aqueous solution. The zeta potential, as measured by DLS in 1 mM aq. KCl, changed from -27.2 to -38.6 mV after coating, consistent with a layer of silica on the surface of the particles. TGA showed an increase in weight remaining at 600 °C, corresponding to a silica content of 50.6 wt% in the particles. The amount of silica deposited could be tuned by adjusting reaction parameters like the amount of TEOS, the base concentration, and the duration of the reaction. While particles with thinner silica coatings

(down to 3 wt%) could be synthesized, the heavily coated particles were chosen for stability testing.

3.2.6. Release profile of Zr-MTX NCP

Unlike **Zn-MTX 2**, **Zr-MTX** particles were stable in pure water. The stability of **Zr-MTX** under biological conditions was evaluated by dialyzing the particles against PBS (pH = 7.4) at 37 °C (Fig. 3.15). It took 2.8 h for 50% of the MTX from **Zr-MTX** to be released into solution, indicating that **Zr-MTX** has a half-life of about 0.8 h (after correcting for MTX diffusion time). The silica coating was expected to slow MTX release from the particles due to slow diffusion of MTX through the porous shell. **Zr-MTX**@SiO_2 particles were dialyzed under the same conditions, and it was found that silica coating extended the half-life of the particles to 2.1 h. Although **Zr-MTX** is more stable than **Zn-MTX 2** in water, the short half-life of **Zr-MTX** in PBS is due to fast formation of zirconium phosphate. The silica shell provides only a modest delay of this process due the extremely high driving force of **Zr-MTX** to form $Zr_3(PO_4)_4$ in the presence of phosphates. This hypothesis is reasonable as the solubility product (K_{sp}) of $Zr_3(PO_4)_4$ is 10^{-134}, which is dramatically smaller than that of $Zn_3(PO_4)_2$ (10^{-34}).

There may be other coating materials that would allow for slower controlled release of MTX from **Zr-MTX** or protect the particles from exposure to phosphate. The negative zeta potential of **Zr-MTX** particles, along with their stability in water, should allow for coating of these particles with a cationic lipid bilayer (liposome) to provide biocompatibility and stabilization in physiologically relevant media.[35-37]

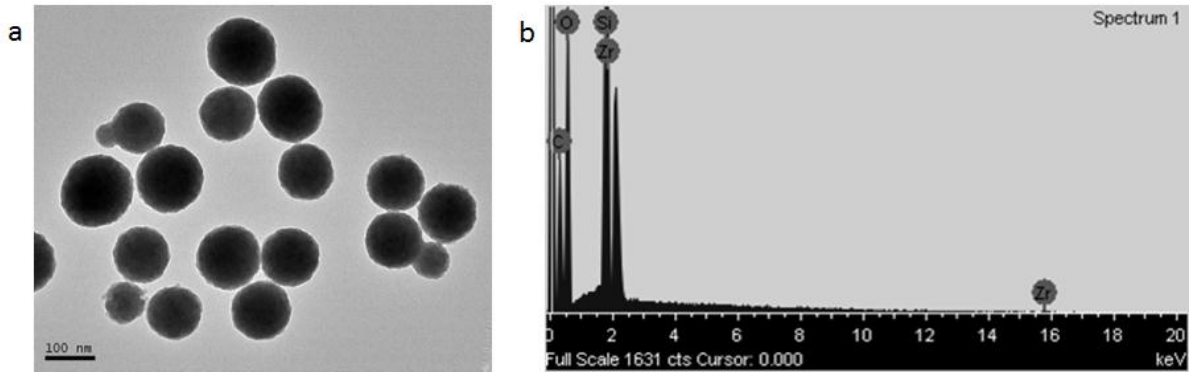

Figure 3.14. (a) TEM image and (b) EDS spectrum of **Zr-MTX**@SiO_2.

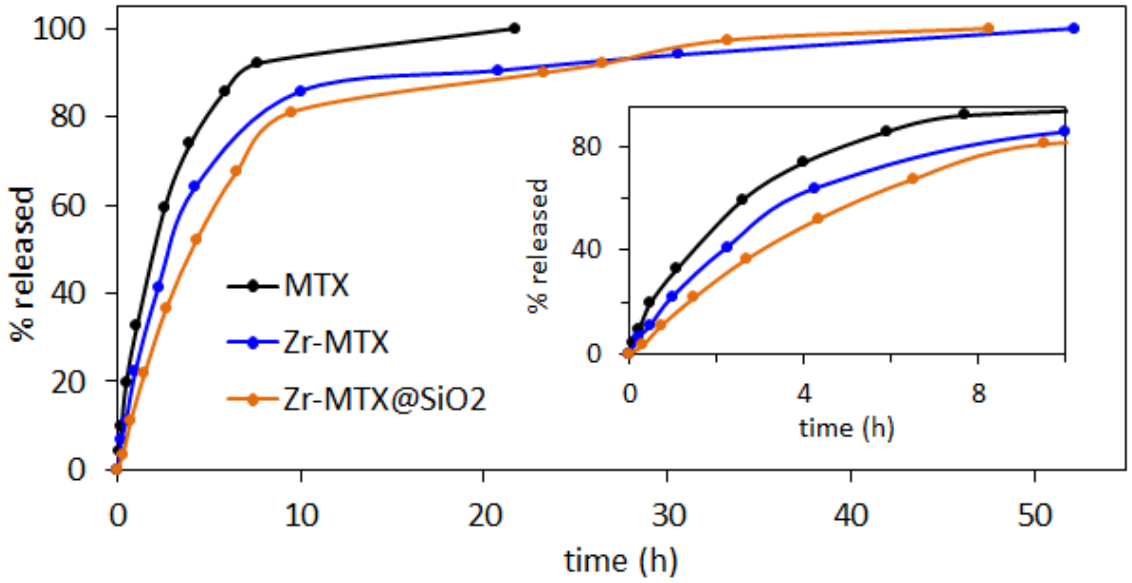

Figure 3.15. Release profiles for **Zr-MTX**, **Zr-MTX**@SiO_2, and **MTX** alone dialyzed in PBS (pH = 7.4) at 37 °C.

3.3. Conclusion

Several methotrexate-containing NCPs have been synthesized and evaluated for their potential as drug delivery vehicles. While MTX NCPs with Zn^{2+} and Zr^{4+} metal ion connecting points had sizes and shapes suitable for *in vivo* applications, the Zn-based NCP was too unstable for further functionalization, and the silica-coated Zr-based NCP was not

adequately stabilized due to the driving force for zirconium phosphate formation. Considering the challenges encountered with these NCPs, it seemed possible that a MTX NCP formulation containing a metal less labile than zinc, but with a phosphate K_{sp} much greater than that of $Zr_3(PO_4)_4$, would prove easier to stabilize. For example, trivalent lanthanide ions have much greater phosphate K_{sp} values (10^{23} for $Gd(PO_4)$) and would provide a good balance between particle stability and stabilization toward lanthanide phosphate formation. Silica-coating is an attractive method of stabilizing particles because a silica surface allows for attachment of silyl-derivatives of passivating molecules and targeting molecules. Other types of coatings, like lipid bilayers, may also be able to stabilize NCPs while allowing for further functionalization.

Gd-MTX particles were successfully synthesized, stabilized, and targeted to cancer cells *in vitro*; these results will be described in Rachel Huxford-Phillip's dissertation. Briefly, Gd-MTX nanoparticles containing 71.6 wt% MTX were synthesized and encapsulated in a lipid bilayer that allowed for controlled release of MTX, extending the half-life of the particles from 2 to 23 h under biological conditions. A molecule was conjugated to the lipid bilayer that targets receptors overexpressed on leukemia cancer cells, and the targeted particles were shown to have superior efficacy in *in vitro* cytotoxicity assays compared to the as-synthesized particles and the free drug. The NCP approach to formulation of MTX nanoparticles offers a potential way to target and deliver high payloads of MTX to cancer cells. This strategy is general and could be applied to design many other nanoparticle formulations of organic anticancer drugs.

3.4. Experimental Details

3.4.1 Materials and methods

All chemicals, unless otherwise noted, were purchased from Fisher or Sigma Aldrich and used without further purification. Methotrexate was purchased from TCI America. Microwave reactions were carried out in a CEM Discovery microwave or a CEM MARS 5 microwave. Scanning electron microscopy (SEM) was performed with a Hitachi 4700 Field Emission Scanning Electron Microscope, and transmission electron microscopy (TEM) was performed with a JEM 100CX-II Transmission Electron Microscope. A Cressington 108 Auto Sputter Coater equipped with a Au/Pd (80/20) target and MTM-10 thickness monitor was used to coat samples before SEM imaging. SEM micrographs were obtained on glass slides, and TEM micrographs were obtained on carbon-coated copper grids. Thermogravimetric analysis (TGA) was done on a Shimadzu TGA-50 equipped with a platinum pan, and samples were heated at a rate of 3°C/min under air. Powder x-ray diffraction (PXRD) data was gathered on a Bruker SMART APEX II diffractometer using Cu radiation, and powder patterns were analyzed with the APEX II package using the phase ID plugin. UV-vis absorption spectra were obtained using a Shimadzu UV-2401 PC UV-Vis recording spectrophotometer. Size and zeta potential information was obtained on a Malvern ZetaSizer dynamic light scattering instrument.

3.4.2. Synthesis of MTX-containing NCPs

Synthesis of Mn-MTX. Ribbon-shaped NCPs containing Mn^{2+} and MTX were synthesized by a high-temperature surfactant-assisted method. Two microemulsions with W=5 were prepared by the addition of 90 μL of an aqueous solution of MTX dimethylammonium salt (0.10 M) and 90 μL of an aqueous solution of $MnCl_2 \cdot 4H_2O$ (0.10 M) to separate 10 mL aliquots of a 0.1 M CTAB/0.5 M 1-hexanol/isooctane mixture. The

separate microemulsions were stirred vigorously for 10 min at room temperature, then the two microemulsions were combined, and the resultant 20 mL microemulsion with *W*=5 was transferred to a sealed microwave vessel. The reaction was rapidly heated to 120 °C, and held at this temperature for 10 min with stirring. After cooling, the nanoparticles were isolated by centrifugation at 13,000 rpm for 10 min. After the removal of the supernatant, the particles were washed twice, using 10 mL of ethanol each time. For each wash, the particles were re-dispersed by sonication and then recovered by centrifugation at 13,000 rpm for 10 min. Yield: 3.57 mg (78.2 %).

Synthesis of Cu-MTX. Ribbon-shaped NCPs containing Cu^{2+} and MTX were synthesized by the same method as **Mn-MTX**, but using $Cu(NO_3)_2 \cdot 2.5H_2O$ instead of $MnCl_2 \cdot 4H_2O$. Yield: 0.84 mg (18.1 %).

Synthesis of Zn-MTX 1. Ribbon-shaped NCPs containing Zn^{2+} and MTX were synthesized by a high-temperature surfactant-assisted method. Two microemulsions with *W*=15 were prepared by the addition of 270 μL of an aqueous solution of MTX dimethylammonium salt (0.05 M) and 270 μL of an aqueous solution of $Zn(NO_3)_2 \cdot 6H_2O$ (0.05 M) to separate 10 mL aliquots of a 0.1 M CTAB/0.5 M 1-hexanol/isooctane mixture. The separate microemulsions were stirred vigorously for 10 min at room temperature, then the two microemulsions were combined, and the resultant 20 mL microemulsion with *W*=15 was transferred to a sealed microwave vessel. The reaction was heated, cooled, and the nanoparticles were isolated as described for **Mn-MTX**. Yield: 2.88 mg (41.2 %).

Synthesis of Zn-MTX 2. Spherical NCPs containing Zn^{2+} and MTX were synthesized by the same method as **Zn-MTX 1**, but using higher concentrations of aqueous solutions of MTX dimethylammonium salt (0.10 M) and M $Zn(NO_3)_2 \cdot 6H_2O$ (0.11 M). The

pH of the MTX solution was raised from 8.2 to 10.6 by addition of CH_3NH_2 before adding it to the isooctane. Yield: 11.9 mg (85.1 %).

Synthesis of Zr-MTX. $ZrCl_4$ (6.99 mg, 0.03 mmol) was dissolved in 6 mL N,N-dimethylformamide (DMF), followed by 13.67 mg (0.03 mmol) methotrexate. The clear yellow solution was placed in a sealed microwave vessel and heated at 60 °C for 5 minutes (300 W, 200 psi) without stirring. The product was isolated from the resulting yellow dispersion by centrifugation at 13,000 rpm for 15 min, washed by sonication and centrifugation, with H_2O then EtOH, and dispersed in EtOH. Yield: 8.88 mg (54.4%).

Synthesis of Zr-MTX@SiO_2. Silica-coated Zr-MTX particles were made by treating Zr-MTX with tetraethylorthosilicate (TEOS) under sol-gel conditions. 6.0 mg of **Zr-MTX** particles suspended in 2 mL of ethanol were placed in a round-bottom flask. 405 μL of ammonium hydroxide was diluted with 12.6 mL ethanol and added to the particle suspension, resulting in 15 mL of 0.4 M NH_4OH in ethanol with 0.4 mg particles/mL. 24 μL TEOS (3.76:1 TEOS:particles w/w) was then added and the reaction was stirred at room temperature in darkness for 20 h. The nanoparticles were isolated by centrifugation at 13,000 rpm for 10 min. After the removal of the supernatant, the particles were washed twice, using 10 mL of ethanol each time. For each wash, the particles were re-dispersed by sonication and then recovered by centrifugation at 13,000 rpm for 10 min.

3.4.3. Release profile procedure

Release profiles were obtained by dialyzing small amounts of samples (1-3 mg) against large volumes (~300 mL) of 8 mM PBS (pH = 7.4) at 37 °C with stirring. The sample was dispersed in ~1 mL of media, then placed inside of dialysis tubing with a molecular weight cut off of 3500. The tubing was sealed and submerged in the media. Aliquots from the

solution outside of the dialysis bag were taken periodically and UV-vis was used to determine the concentration of MTX by measuring absorbance at 305 nm. A calibration curve was made for 0.5-50 μm MTX in the same media used for dialysis.

3.5. References

(1) Heath, J. R.; Davis, M. E.; Hood, L. *Sci. Am.* **2009**, *300*, 44.

(2) Al-Jamal, W. T.; Kostarelos, K. *Nanomed.* **2007**, *2*, 85.

(3) Peer, D.; Karp, J. M.; Hong, S.; Farokhzad, O. C.; Margalit, R.; Langer, R. *Nat. Nanotechnol.* **2007**, *2*, 751.

(4) Maeda, H. *Advan. Enzyme Regul.* **2001**, *41*, 189.

(5) Fox, M. E.; Szoka, F. C.; Fréchet, J. M. J. *Acc. Chem. Res.* **2009**, *42*, 1141.

(6) Davis, M. E.; Chen, Z.; Shin, D. M. *Nat. Rev. Drug Discovery* **2008**, *7*, 771.

(7) Brannon-Peppas, L.; Blanchette, J. O. *Adv. Drug. Deliv. Rev.* **2004**, *56*, 1649.

(8) Vilner, B. J.; John, C. S.; Bowen, W. D. *Cancer Res.* **1995**, *55*, 408.

(9) Aydar, E.; Palmer, C. P.; Djamgoz, M. B. A. *Cancer Res.* **2004**, *64*, 5029.

(10) Banerjee, R.; Tyagi, P.; Li, S.; Huang, L. *Int. J. Cancer* **2004**, *112*, 693.

(11) John, C. S.; Vilner, B. J.; Geyer, B. C.; Moody, T.; Bowen, W. D. *Cancer Res.* **1999**, *59*, 4578.

(12) Stathopoulos, G. P. *Anti-Cancer Drugs* **2010**, *21*, 732.

(13) Vallet-Regi, M.; Rámila, A.; del Real, R. P.; Pérez-Pariente, J. *Chem. Mater.* **2001**, *13*, 308.

(14) Torchilin, V. P. *Nature* **2005**, *4*, 145.

(15) Cattel, L.; Ceruti, M.; Dosio, F. *Tumori* **2003**, *89*, 237.

(16) Northfelt, D. W.; Dezube, B. J.; Thommes, J. A.; Levine, R.; Von Roenn, J. H.; Dosik, G. M.; Rios, A.; Krown, S. E.; DuMond, C.; Mamelok, R. D. *J. Clin. Oncol.* **1997**, *15*, 653.

(17) Horcajada, P., Chalati, T.; Serre, C.; Gillet, B.; Sebrie, C.; Baati, T.; Eubank, J. F.; Heurtaux, D.; Clayette, P.; Kreuz, C.; Chang, J. S.; Hwang, Y. K.; Marsaud, V.; Bories, P. N.; Cynober, L.; Gil, S.; Férey, G.; Couvreur, P.; Gref, R. *Nat. Mater.* **2010**, *9*, 172.

(18) McKinlay, A. C.; Morris, R. E.; Horcajada, P.; Férey, G.; Gref, R.; Couvreur, P.; Serre, C. *Angew. Chem. Int. Ed.* **2010**, *49*, 6260.

(19) Rieter, W. J.; Pott, K. M.; Taylor, K. M.; Lin, W. *J. Am. Chem. Soc.* **2008**, *130*, 11584.

(20) Taylor-Pashow, K. M. L.; Della Rocca, J.; Xie, Z.; Tran, S.; Lin, W. *J. Am. Chem. Soc.* **2009**, *131*, 14261.

(21) Imaz, I.; Rubio-Martinez, M.; Garcia-Fernandez, L.; Garcia, F.; Ruiz-Molina, D.; Hernando, J.; Puntes, V.; Maspoch, D. *Chem. Commun.* **2010**, *46*, 4737.

(22) Miller, S. R.; Heurtaux, D.; Baati, T.; Horcajada, P.; Greneche., J. M.; Serre, C. *Chem. Commun.* **2010**, *46*, 4526.

(23) Mastropaolo, D.; Camerman, A.; Carmerman, N. *J. Med. Chem.* **2001**, *44*, 267.

(24) Krajinovic, M.; Moghrabi, A. *Pharmacogenomics* **2004**, *5*, 819.

(25) Chen, Y.-H.; Tsai, C.-Y.; Huang, P.-Y.; Chang, M.-Y.; Cheng, P.-C.; Chou, C.-H.; Chen, D.-H.; Wang, C.-R.; Shiau, A.-L.; Wu, C.-L. *Mol. Pharmaceutics* **2007**, *4*, 713.

(26) Dhanikula, R. S.; Argaw, A.; Bouchard, J.-F.; Hildgen, P. *Mol. Pharm.* **2008**, *5*, 105.

(27) Kohler, N.; Sun, C.; Fichtenholtz, A.; Gunn, J.; Fang, C.; Zhang, M. *Small* **2006**, *2*, 785.

(28) Kohler, N.; Sun, C.; Wang, J.; Zhang, M. *Langmuir* **2005**, *21*, 8858.

(29) Wosikowski, K.; Biedermann, E.; Rattel, B.; Breiter, N.; Jank, P.; Loser, R.; Jansen, G.; Peters, G. J. *Clin. Cancer Res.* **2003**, *9*, 1917.

(30) Yang, X.; Zhang, Q.; Wang, Y.; Chen, H.; Zhang, H.; Gao, F.; Liu, L. *Colloid. Surface. B* **2008**, *61*, 125.

(31) Taylor, K. M. L.; Rieter, W. J.; Lin, W. *J. Am. Chem. Soc.* **2008**, *130*, 14358.

(32) Ni, Z.; Masel, R. I. *J. Am. Chem. Soc.* **2006**, *128*, 12394.

(33) Lin, W.; Rieter, W. J.; Taylor, K. M. L. *Angew. Chem. Int. Ed.* **2009**, *48*, 650.

(34) Cavka, J. H.; Jakobsen, S.; Olsbye, U.; Guillou, N.; Lamberti, C.; Bordiga, S.; Lillerud, K. P. *J. Am. Chem. Soc.* **2008**, *130*, 13850.

(35) Ashley, C. E.; Carnes, E. C.; Phillips, G. K.; Padilla, D.; Durfee, P. N.; Brown, P. A.; Hanna, T. N.; Liu, J.; Phillips, B.; Carter, M. B.; Carroll, N. J.; Jiang, X.; Dunphy, D. R.; Willman, C. L.; Petsev, D. N.; Evans, D. G.; Parikh, A. N.; Chackerian, B.; Wharton, W.; Peabody , D. S.; Brinker, C. J. *Nat. Mater.* **2011**, *10*, 389.

(36) Li, J.; Chen, Y.-C.; Tseng, Y.-C.; Mozumdar, S.; Huang, L. *J. Controlled Release* **2010**, *142*, 416.

(37) Liu, J.; Stace-Naughton, A.; Jiang, X.; Brinker, C. J. *J. Am. Chem. Soc* **2009**, *131*, 1354.

CHAPTER 4

Metal-Organic Framework Templated Synthesis of Fe_2O_3/TiO_2 Nanocomposite for Hydrogen Production

(Portions of this chapter were adapted with permission from deKrafft, K.E.; Wang, C.; Lin. *Adv. Mater.* **2012**, DOI: 10.1002/adma.201200330. Copyright 2012 John Wiley and Sons.)

4.1. Introduction

4.1.1. Metal oxides

Metal oxide nanomaterials are of great practical importance due to their stability, low cost, low toxicity, and useful photophysical properties.[1-4] With the ability to excite electrons to the conduction band or to generate holes in the valence band, metal oxide nanomaterials can be used to perform photocatalytic reactions, such as degradation of organic pollutants[5] or production of solar fuels like hydrogen.[6-8] Large-band gap metal oxides such as TiO_2 have suitable band positions for photocatalytic solar fuel production, but absorb only UV photons, which represent only about 5% of the energy in the solar spectrum. On the other hand, metal oxides with suitable band gaps for efficient absorption in the solar spectrum (e.g., Fe_2O_3) tend to have short carrier diffusion lengths (on the order of nanometers). This prevents reactions from taking place before charge recombination occurs, and makes these metal oxides ineffective in driving photocatalytic reactions. Catalytic metal oxide nanoparticles are often preferred over bulk materials due to the shorter distance that charger carriers must travel to reach the surface, thereby improving the quantum efficiency.[3, 4] Additionally, nanoparticles have high surface areas and therefore more reaction sites per unit than bulk

materials. Identifying scalable and economic approaches to synthesize metal oxide nanomaterials that not only absorb visible light (>400 nm) but also have suitable band positions to drive reactions is a major scientific and technological challenge. Mixed metal oxide nanocomposites offer a potential solution as a result of the synergy that is possible among the components.

4.1.2. Nanocomposite materials

There have been many reports of nanocomposite materials that perform better as photocatalysts under visible light compared to their individual components. The enhancement in activity is often due to one component acting as a trap for photogenerated carriers, allowing for better charge separation.[9, 10] This is the case for water oxidation using Fe_2O_3 coated with CoO_x, which extends the lifetime of photogenerated holes.[11] Alternatively, one component can act as a visible-light sensitizer for a large-band gap catalyst, as in a CdS/TiO_2 composite in which CdS absorbs visible light and transfers electrons to TiO_2.[12] This mechanism is, in some cases, dependent on doping at the interfaces to adjust the band potentials to be suitable for charge transfer.[13] For example, Fe_2O_3 can sensitize a $SrTiO_3$ shell due to Ti doping in Fe_2O_3 raising its conduction band higher than that of $SrTiO_3$.[14]

Here we report a simple, inexpensive, tunable, and scalable metal-organic framework (MOF)-templated strategy for the synthesis of a mixed metal oxide nanocomposite with useful photophysical properties. Although MOFs have been explored for a wide range of applications such as nonlinear optics,[15, 16] gas storage,[17-19] catalysis,[20, 21] chemical sensing,[22-25] and drug delivery,[26-28] there have been a few reports on using MOFs as templates in the synthesis of silica nanoshells,[29] nanoporous carbon,[30] and metallic nanoparticles.[31] In this work, we attempt to use nanoscale MOFs to prepare titania-based nanocomposites for

potential solar energy applications. Fe-containing nanoscale MOFs are coated with amorphous titania, then calcined to produce crystalline Fe_2O_3@TiO_2 composite nanoparticles, which enable visible light-driven hydrogen production from water (Fig. 4.1).

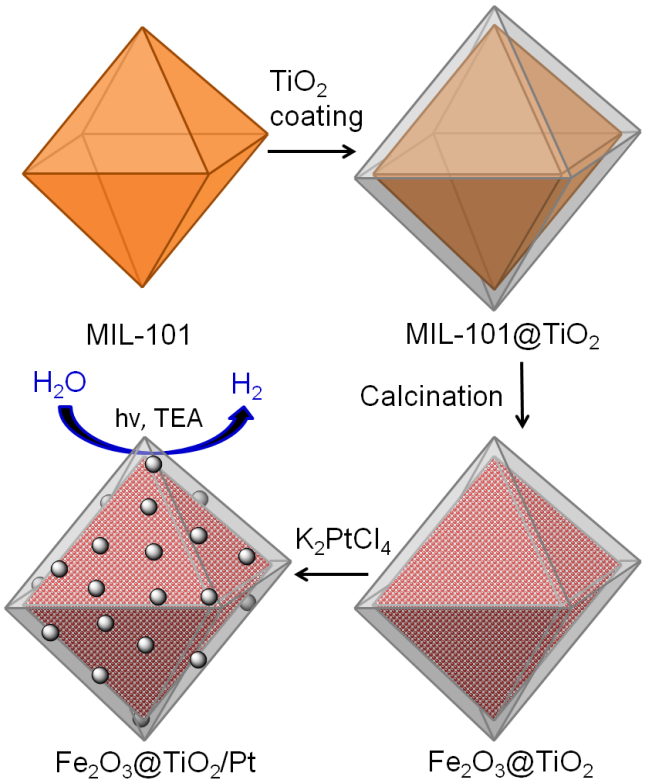

Figure 4.1. MOF-templated synthesis of Fe_2O_3@TiO_2 by coating MIL-101 with TiO_2 followed by calcination, and its use for photocatalytic hydrogen production after depositing Pt particles.

4.2. Results and Discussion

4.2.1. Synthesis and characterization of Fe_2O_3@TiO_2

Nanoscale MOFs with the MIL-101[32] structure and the formula $Fe_3OCl(H_2O)_2(BDC)_3$ (BDC = benzene dicarboxylate) were synthesized by microwaving a solution of benzene dicarboxylic acid (H_2BDC) and $FeCl_3 \cdot 6H_2O$ in N,N'-dimethylformamide (DMF) at 150 ºC.[33] The resulting octahedral nanoparticles had dimensions of 400-800 nm by transmission

electron microscopy (TEM) (Fig. 4.2a) and scanning electron microscopy (SEM) (Fig. 4.3a), and were confirmed to have the MIL-101 structure by powder X-ray diffraction (PXRD) (Fig. 4.4). MIL-101 materials are extremely porous and are composed of trivalent metal clusters linked together by BDC bridging ligands.

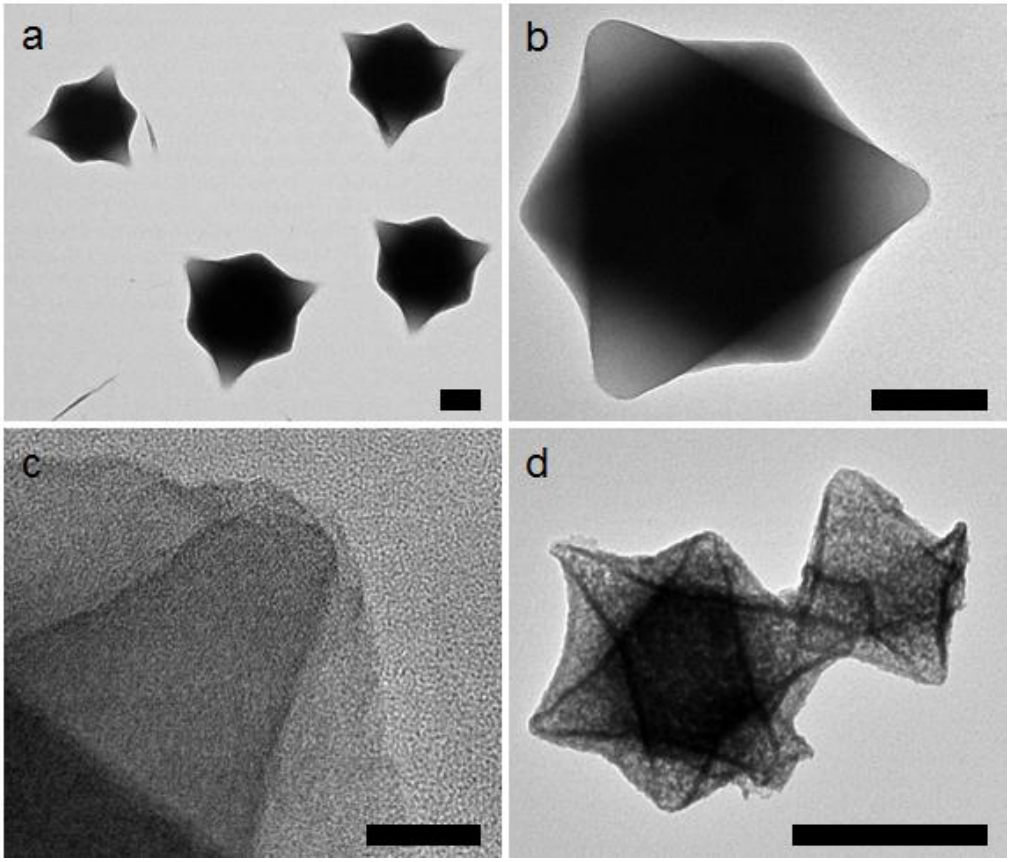

Figure 4.2. TEM images of (a) MIL-101, (b) MIL-101@TiO_2, (c) a tip of MIL-101@TiO_2, and (d) Fe_2O_3@TiO_2. The scale bars represent 200 nm for (a, b, and d), and 20 nm for (c).

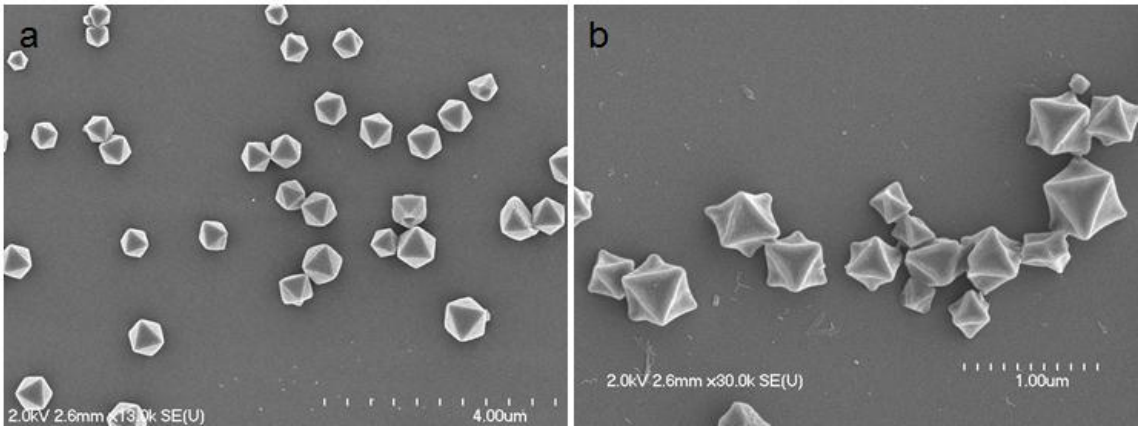

Figure 4.3. SEM images of (a) MIL-101 and (b) MIL-101@TiO_2.

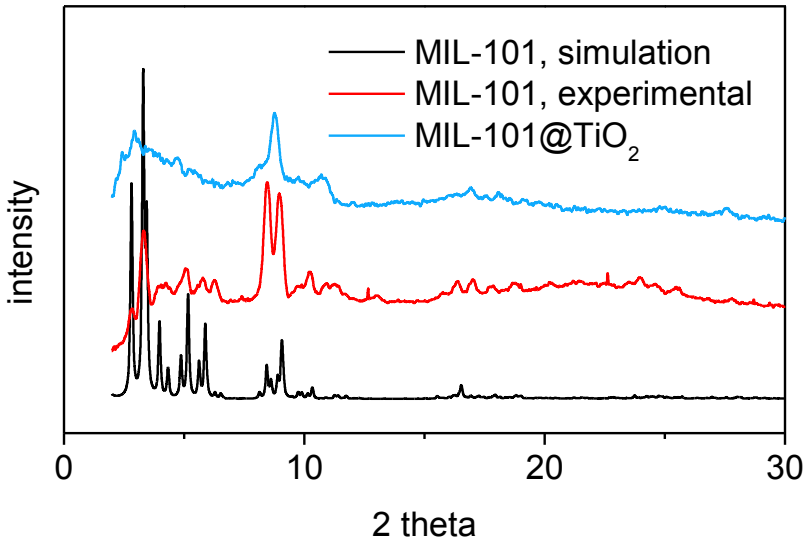

Figure 4.4. PXRD patterns of MIL-101 (simulated and experimental) and MIL-101@TiO_2.

The MIL-101 particles were coated with an amorphous shell of titania by acid-catalyzed hydrolysis and condensation of titanium(IV) bis(ammonium lactato)dihydroxide (TALH) in water.[34] The coated particles were isolated by centrifugation and washed several times with water and ethanol. The thickness of the TiO_2 coating could be controlled by adjusting the concentration of acid or the reaction time (Fig. 4.8). A typical sample used for photocatalysis was prepared by coating MIL-101 with titania for 2 h in 0.1 M HCl, resulting

in particles that appeared similar to the original MIL-101 particles by TEM (Fig. 4.2b-c), but contained Ti as shown by energy dispersive X-ray spectroscopy (EDS) (Fig. 4.5). Thermogravimetric analysis (TGA) showed 5.6% additional weight remaining at 600 ºC due to the titania coating (Fig. 4.6). Scanning TEM coupled with EDS (STEM-EDS) was used in an effort to measure the TiO_2 shell thickness (Fig. 4.7). While Fe and Ti are both detected across the whole measured area of the particle, individual areas where a particular element dominates could not be delineated, due to low spatial resolution. Inductively coupled plasma mass spectrometry (ICP-MS) was used to precisely determine the Fe and Ti content, after digesting the particles in concentrated H_2SO_4. The atomic ratio of Ti to Fe (0.25) was used to calculate the thickness of the TiO_2 layer, assuming an average MIL-101 edge length of 600 nm and densities of 0.62 and 3.89 g/cm^3 for MIL-101 and titania, respectively. The amorphous titania shell was estimated to be 1.2 nm thick, assuming it formed a contiguous shell on the MIL-101 particles. Although there is some loss of crystallinity indicated by PXRD, peaks from MIL-101 appear in the pattern for the coated particles, indicating that MIL-101 does not decompose under coating conditions (Fig. 4.4). There were no additional peaks appearing in the PXRD pattern for the core-shell particles, suggesting that the titania shell was amorphous.

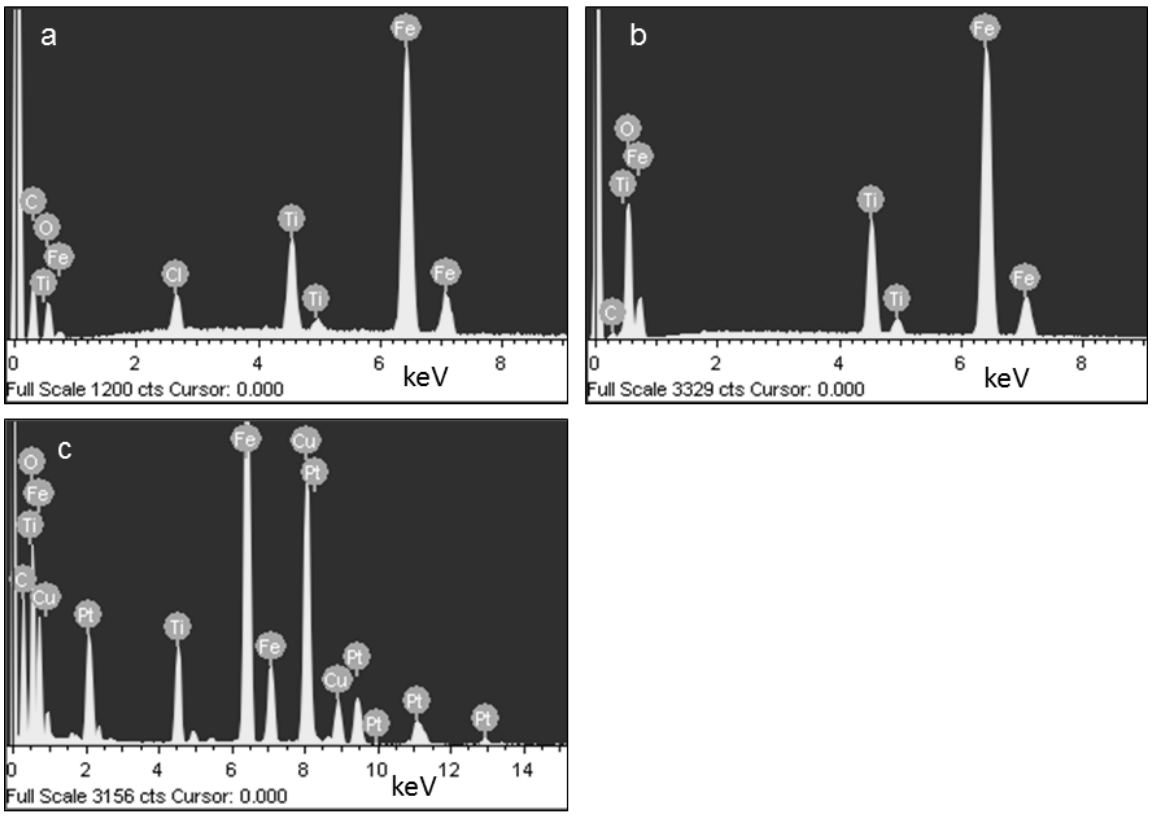

Figure 4.5. EDS spectra of (a) MIL-101@TiO_2, (b) Fe_2O_3@TiO_2, and (c) Fe_2O_3@TiO_2/Pt. The Cu in (c) comes from the Cu grid sample holder.

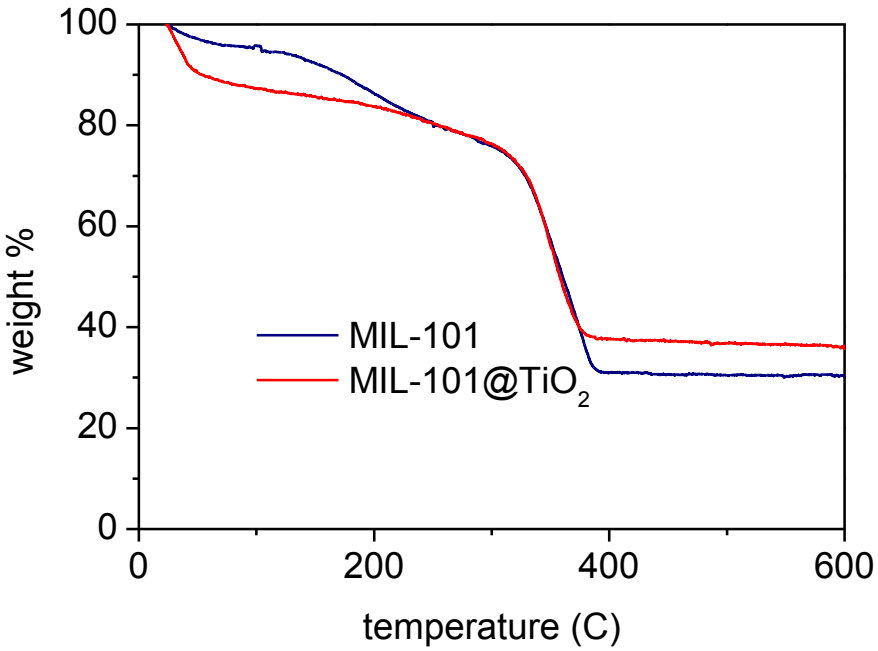

Figure 4.6. TGA of MIL-101 and MIL-101@TiO_2.

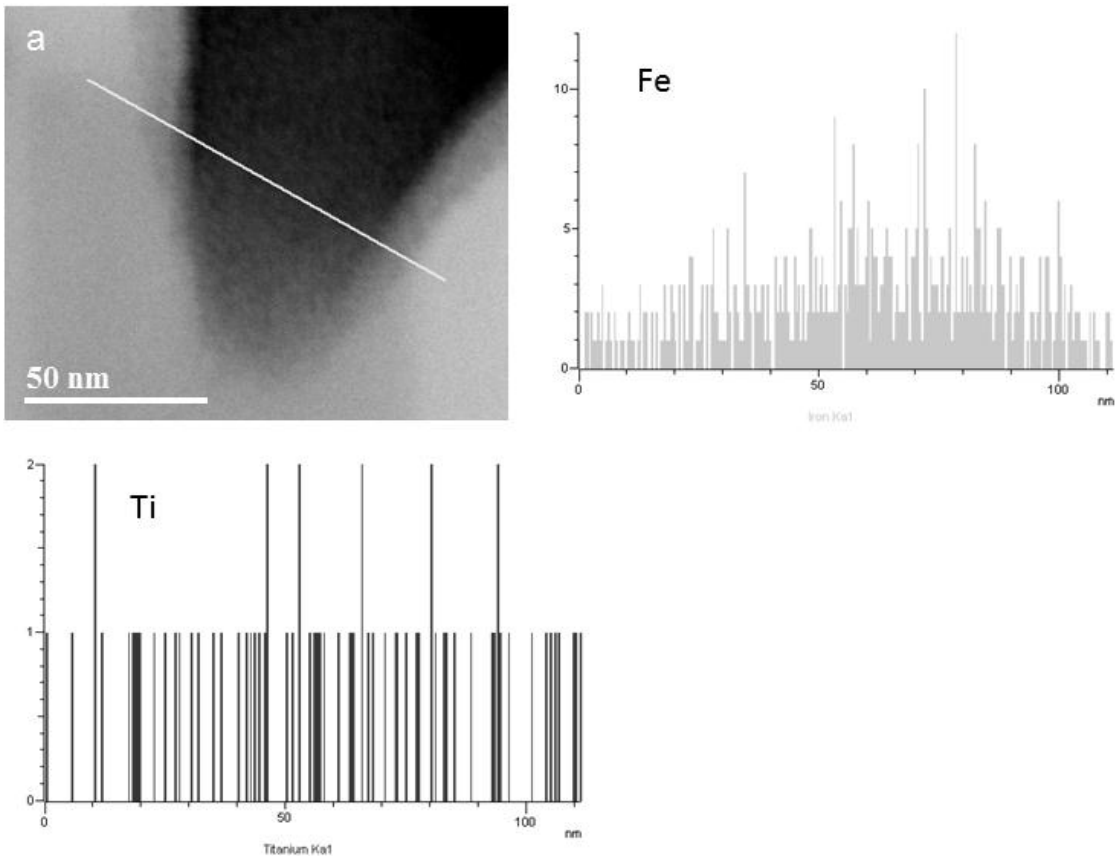

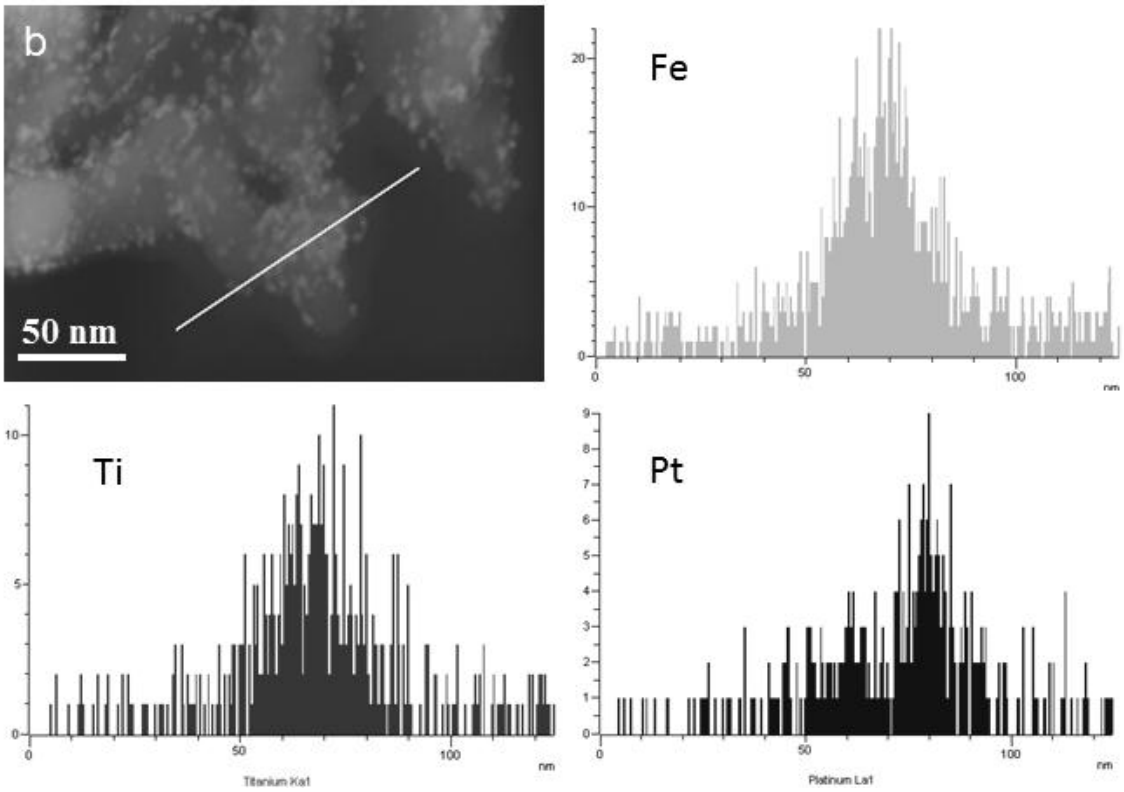

Figure 4.7. STEM-EDS line scans of (a) MIL-101@TiO_2 (a tip of an octahedral particle) and (b) Fe_2O_3@TiO_2/Pt.

The core-shell particles were calcined at 550 ºC in air for 16 h, resulting in a color change from orange to dark red, due to conversion of the MIL-101 core into iron oxide. The calcined particles, like the core-shell particles, are dispersible in water, indicating that the particles remain discrete and do not fuse together. PXRD showed that both the core and shell were crystallized by calcination and the PXRD peaks matched those of the anatase phase of TiO_2 and the hematite phase of Fe_2O_3 (α-Fe_2O_3) (Fig. 4.9). The amount of Fe and Ti, as determined by ICP-MS, corresponded to calcined particles containing 80 wt% Fe_2O_3 and 20 wt% TiO_2. TEM shows octahedral shells with no visibly distinct TiO_2 and Fe_2O_3 regions (Fig. 4.2d). Due to the very large pore volume of MIL-101 (2.0 cm^3/g), the non-porous Fe_2O_3 particles formed by calcination of this template occupy much less volume, resulting in a

hollow particle. When uncoated MIL-101 particles were calcined, the resulting Fe_2O_3 did not remain in an octahedral structure, but formed irregular particles of ~50 nm fused into clusters (Fig. 4.10). This further confirms the presence of a TiO_2 shell that acts as a support for Fe_2O_3 particles as they are formed from MIL-101 during calcination. High-resolution TEM (HRTEM) was used to observe the individual crystallites of each metal oxide in the composite material. HRTEM reveals that each octahedral shell is composed of roughly spherical individual crystalline domains, with dimensions around 10 nm, of both TiO_2 and Fe_2O_3, blended together (Fig. 4.11). The region shown in Fig. 4.11a is a tip of an octahedral particle shown in Fig. 4.2d at a much higher magnification. Lattice fringes are visible, and lattice d-spacings of both 0.354 and 0.251 nm were measured, corresponding to the {101} plane of anatase (d=0.352 nm) and the {110} plane of hematite (d=0.252 nm), respectively. Fig. 4.11b shows a crystallite of anatase, while Fig. 4.11c shows an area with several crystalline domains with identified regions of anatase and hematite in intimate contact. A nitrogen adsorption isotherm was acquired for Fe_2O_3@TiO_2 at 77 K, resulting in a BET surface area of 11.6 m^2/g (Fig. 4.12).

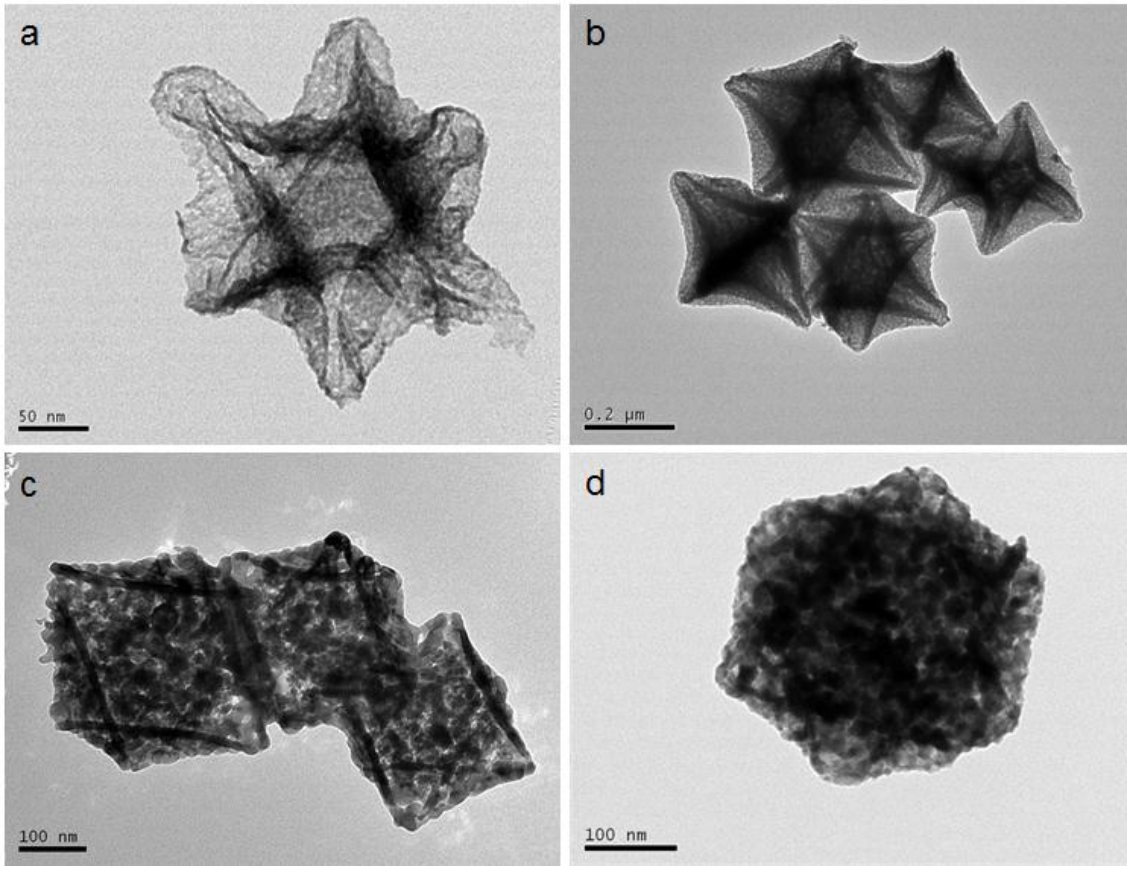

Figure 4.8. TEM images of Fe_2O_3@TiO_2 with varying shell thickness.

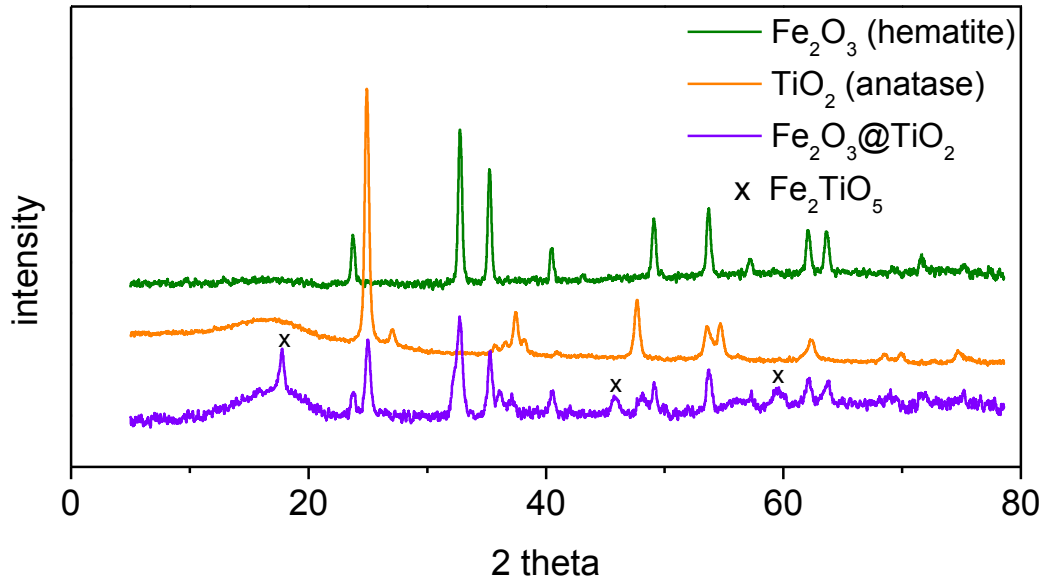

Figure 4.9. PXRD patterns for Fe_2O_3@TiO_2, hematite Fe_2O_3, and anatase TiO_2.

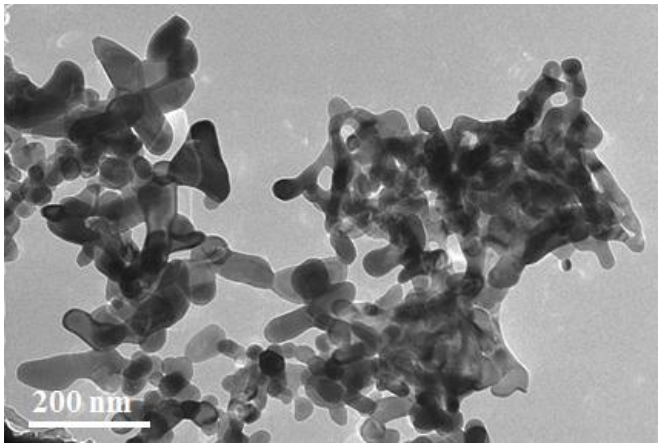

Figure 4.10. TEM image of Fe_2O_3 made by calcination of uncoated MIL-101.

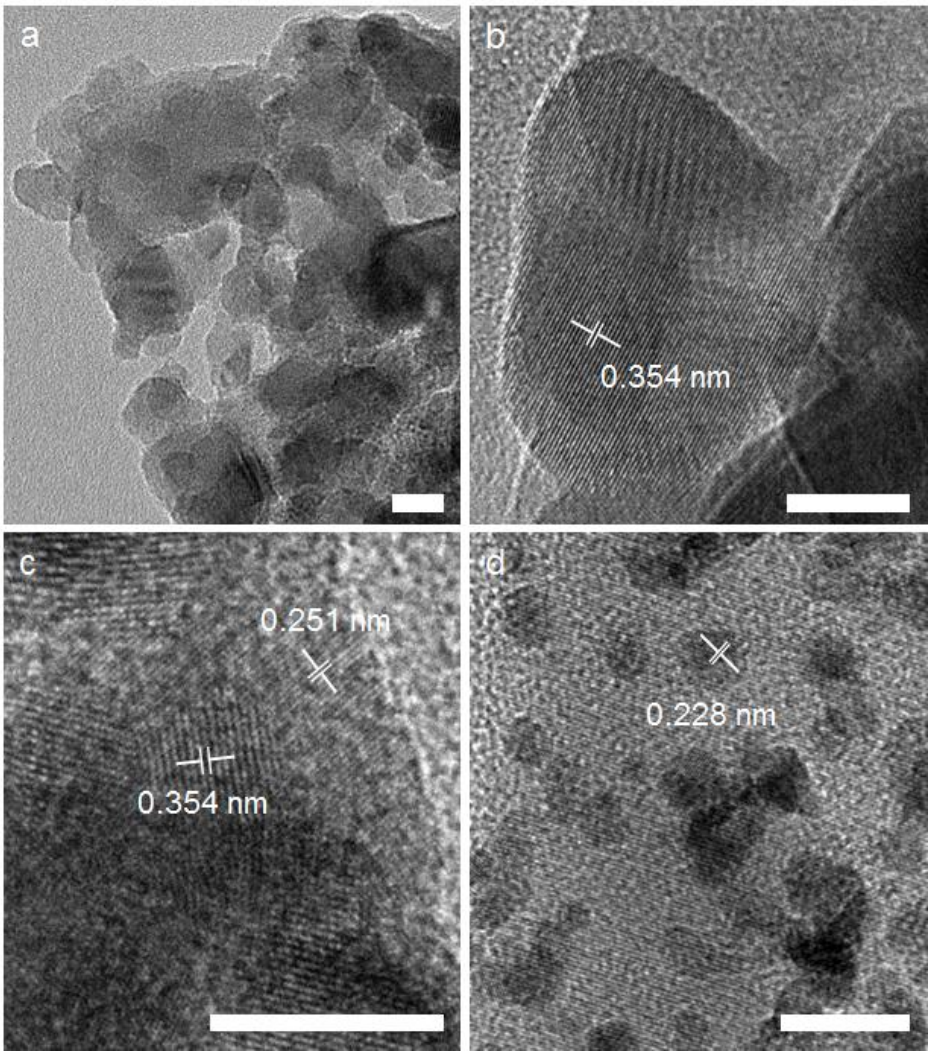

Figure 4.11. HRTEM images of Fe_2O_3@TiO_2, both as-synthesized (a-c) and after Pt particles have been deposited (d). Lattice fringes can be seen for Fe_2O_3, TiO_2, and Pt, and d-spacing measurements are shown in (b-d). The scale bars represent 10 nm.

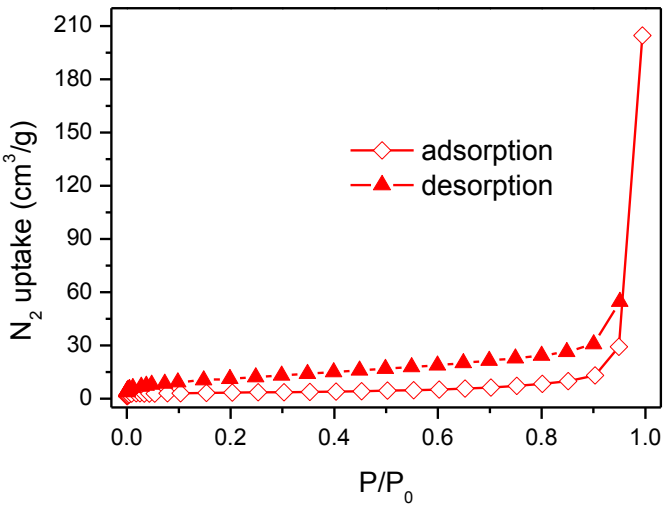

Figure 4.12. N_2 adsorption isotherm at 77 K for Fe_2O_3@TiO_2, giving a BET surface area of 11.6 m^2/g.

There are three peaks in the PXRD pattern of Fe_2O_3@TiO_2 (at 17.8°, 45.4°, and 59.1°) that do not match either anatase or hematite. These peaks are from the pseudobrookite mixed metal oxide phase (Fe_2TiO_5), which probably arises from the formation of an Fe-rich layer at the surface of TiO_2.[35] Fe_2TiO_5 shares the same pseudobrookite structure (and PXRD pattern) with $FeTi_2O_5$ and some phases of Ti_3O_5. These isostructural relationships can be represented by a line within an Fe_2O_3-Ti_2O_3-TiO_2 phase diagram, which presents a range of possible Ti oxides and Fe-Ti mixed oxide solid solutions (Fig. 4.13). The structure that pure Ti_3O_5 adopts at room temperature is quite different from pseudobrookite, but there is a phase transition to a slightly monoclinically deformed version of the orthorhombic pseudobrookite structure (anosovite) around 120 ºC.[36] This high-temperature structure is stabilized at room temperature by a small amount of Fe doping. While it seems possible that Fe-doped Ti_3O_5

could be formed during calcination, the black color characteristic of Ti_3O_5 was not observed experimentally. $FeTi_2O_5$ was also ruled out because it is not stable below 1135 ºC.[37]

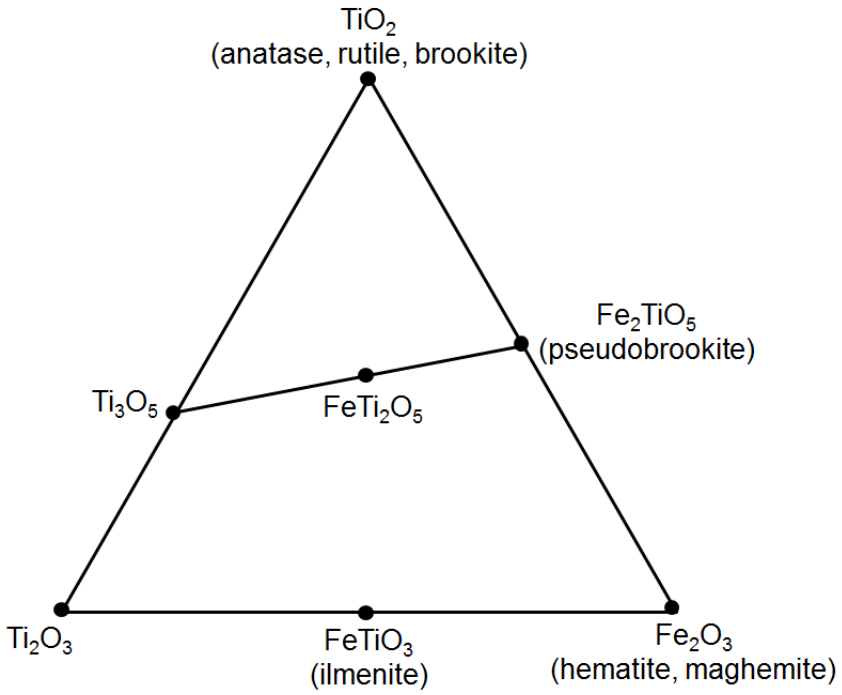

Figure 4.13. Fe_2O_3-Ti_2O_3-TiO_2 phase diagram.

4.2.2. Diffuse reflectance

Diffuse reflectance spectroscopy was used to measure the UV-vis absorbance of MIL-101, MIL-101@TiO_2, Fe_2O_3@TiO_2, a physical mixture of Fe_2O_3 and TiO_2, Fe_2O_3 (hematite) alone, and TiO_2 (anatase) alone (Fig. 4.14, 4.15). $BaSO_4$ was used as a blank, and absorbance was expressed by treating the reflectance data with the Kubelka-Munk function (f(R) = (1-R)^2/(2R), R = reflectance with the reflectance at 1000 nm set at 100%). The absorbance spectrum for MIL-101@TiO_2 showed a combination of the spectral features of MIL-101 and TiO_2 alone, with TiO_2 absorbing mainly UV light while MIL-101 absorption extends into the visible range. Commercially available 32 nm anatase nanoparticles showed an absorption

edge at 390 nm, corresponding to a band gap of 3.18 eV (3.2 eV typically reported). Hematite Fe_2O_3 nanoparticles were made by calcining uncoated MIL-101, and showed an absorption edge at 585 nm, corresponding to a band gap of 2.12 eV (2.1 eV typically reported). The physical mixture was prepared by combining Fe_2O_3 and TiO_2 together in the same ratio as found in the composite material, giving a spectrum with a combination of Fe_2O_3 and TiO_2 features. While the composite material also displays the absorption edges seen for both Fe_2O_3 and TiO_2 alone, it also shows increased absorption from 330-460 nm. This feature is not present in the physical mixture and indicates that some of the TiO_2 is doped with Fe.[38, 39] The band gap of Fe_2TiO_5 is 2.2 eV,[35] so any contribution at the onset of absorption from this phase would overlap with Fe_2O_3 absorption.

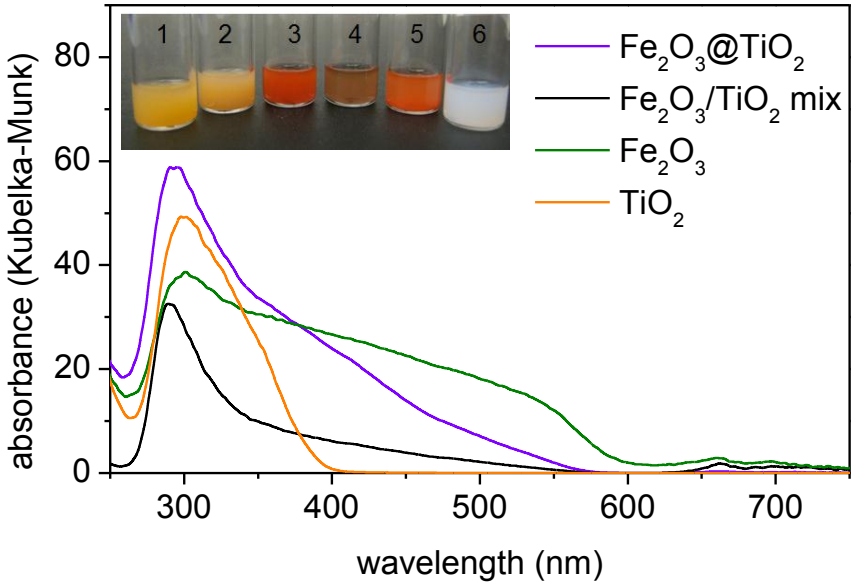

Figure 4.14. UV-vis diffuse reflectance spectra of Fe_2O_3@TiO_2, a physical mixture of Fe_2O_3 and TiO_2, Fe_2O_3 alone, and TiO_2 alone. The inset shows a photograph of dispersions of MIL-101 (1), MIL-101@TiO_2 (2), Fe_2O_3@TiO_2 (3), Fe_2O_3@TiO_2/Pt (4), Fe_2O_3 (5), and TiO_2 (6) in ethanol.

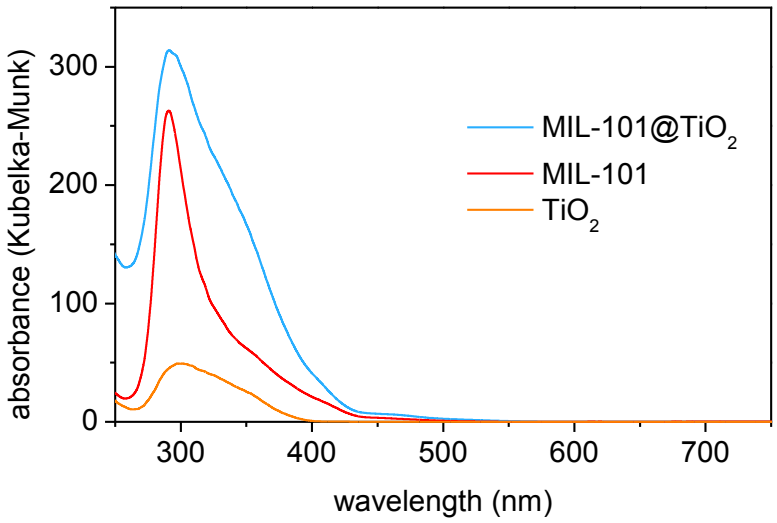

Figure 4.15. UV-vis diffuse reflectance spectra of MIL-101, MIL-101@TiO_2, and TiO_2.

4.2.3. Photocatalytic Hydrogen Production

No single material has been identified that is ideal for visible light-driven water splitting. The conduction band must be at higher energy (more negative reduction potential) than the H^+/H_2 couple (0 V vs NHE), and the valence band must be at lower energy (more positive reduction potential) than the H_2O/O_2 couple (1.23 V vs NHE), but the band gap must be less than 3 eV. TiO_2 has been widely studied as a photocatalyst, and has suitable band positions, but absorbs only UV light.[40] Fe_2O_3 absorbs visible light, but its conduction band is not at high enough energy to drive H_2 generation.[41] The photocatalytic activity of the Fe_2O_3@TiO_2 material in combination with K_2PtCl_4 was tested by measuring photoinduced hydrogen production from water, with triethylamine (TEA) as a sacrificial reducing agent. A Xe-lamp was used as a light source, with a cut-off filter to allow only light above a particular wavelength to pass through. A co-catalyst such as Pt or RuO_2 is typically needed to promote surface H_2 formation.[42] K_2PtCl_4 was reduced to form Pt nanoparticles during the reaction, causing a change in the color of the material from dark red to brown. The presence of Pt in

the material recovered after hydrogen production was confirmed by EDS and PXRD (Fig. 4.5, 4.16). The additional peaks in the PXRD pattern at 39.7º and 46.4º are from Pt. HRTEM images show 2-4 nm Pt particles dispersed throughout that material (Fig. 4.2d, 4.16) with a lattice d-spacing of 0.228 nm, close to the 0.226 nm d-spacing expected for the {111} plane of Pt. STEM-EDS was also performed on this material, but again, the spatial resolution was too low to precisely delineate the $Pt/TiO_2/Fe_2O_3$ boundaries. H_2 was measured in the headspace over photodriven reactions by gas chromatography (GC). GC was performed at various time points over 48 h during a reaction with 0.5 mg $Fe_2O_3@TiO_2$ in 20/1 v/v H_2O/TEA, driven by visible light with a 420 nm cut-off filter (Fig. 4.18a, 4.19). The amount of H_2 produced increases linearly during this entire time period, with a total of 30.0 μmol H_2 per mg of material produced after 48 h. $Fe_2O_3@TiO_2$ is a heterogeneous catalyst that can be recovered from a reaction mixture and reused with a fresh solution. The same material was used three times to test for recyclability; it was recovered from the previous run and dispersed in fresh solution for runs 2 and 3. The catalyst produced 0.8 μmol of H_2 after 3 h during the first use and showed no change in efficiency during the second or third use (Fig. 4.18b, 4.20). While TEM images of the recovered material show that many of the octahedral shells break apart (Fig. 4.17), PXRD shows that the material remains unchanged with the same crystalline phases (Fig. 4.16). An intact particle is shown in Fig. 4.17a, while broken pieces are shown in Fig. 4.17b-d. In the absence of TEA, there is very little (<0.1 μmol) H_2 detected, indicating that a sacrifical reducing agent is necessary to balance the reduction half-reaction of water splitting (Fig. 4.18c, 4.21).

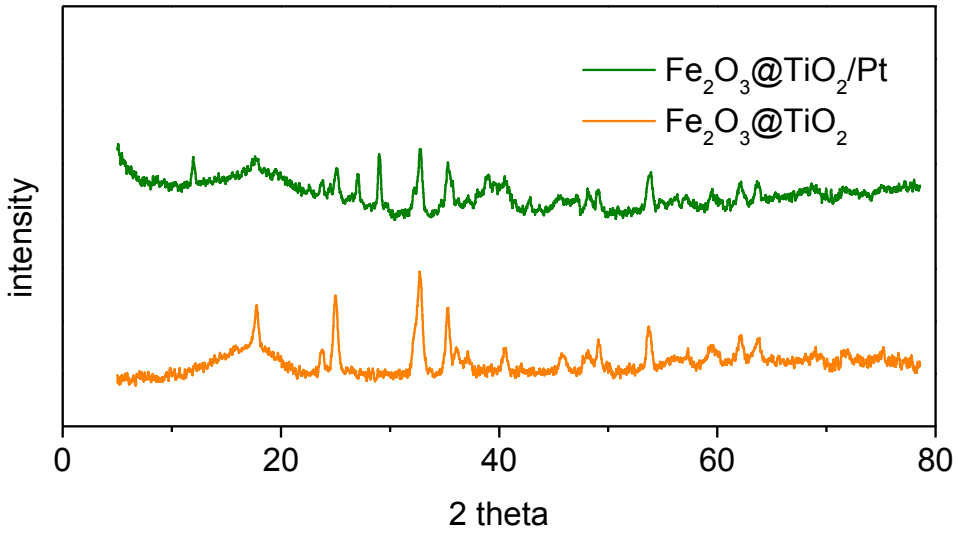

Figure 4.16. PXRD patterns of Fe_2O_3@TiO_2/Pt after catalysis, compared to Fe_2O_3@TiO_2 before catalysis.

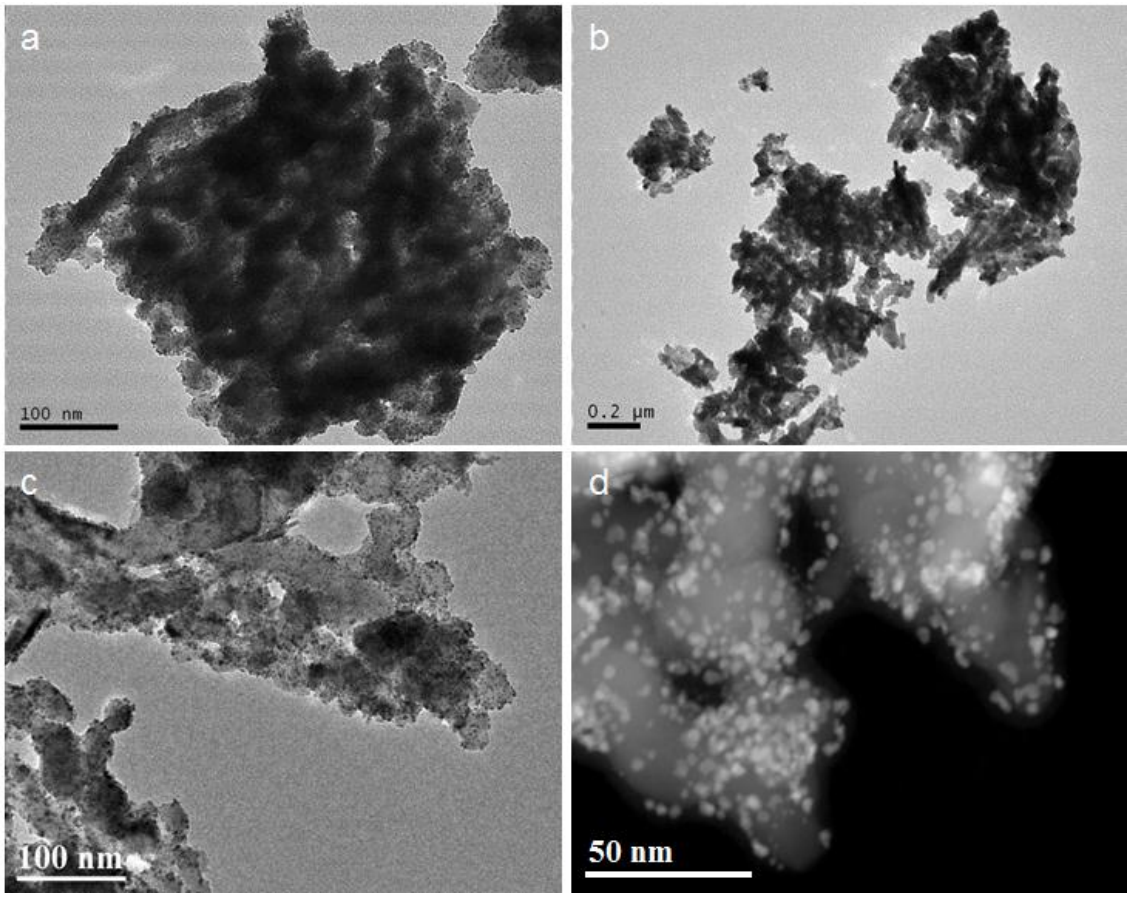

Figure 4.17. TEM images of Fe_2O_3@TiO_2/Pt recovered after catalysis. The Pt nanoparticles appear as dark spots in the bright field images (a-c), and as bright spots in the dark field image (d).

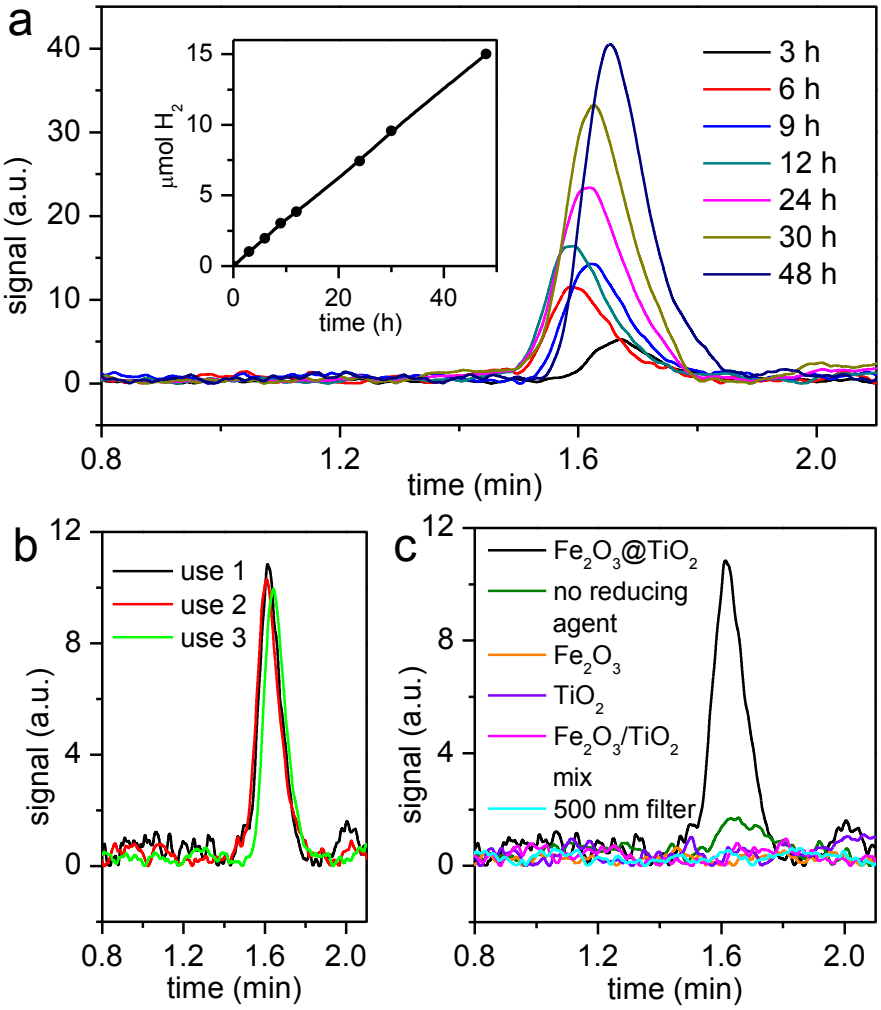

Figure 4.18. The H_2 peaks in GC traces of the headspace over photodriven reactions using 0.5 mg of catalyst. (a) H_2 produced by Fe_2O_3@TiO_2 in 20/1 v/v H_2O/TEA at various time points over 48 h, with a 420 nm filter. The inset shows the amount of H_2 produced over this time period. (b) Reuse experiments with the same catalyst in fresh solution for 3 h each time. (c) Control experiments over 3 h using no reducing agent, Fe_2O_3 alone, TiO_2 alone, a Fe_2O_3@ TiO_2 mixture, or a 500 nm filter.

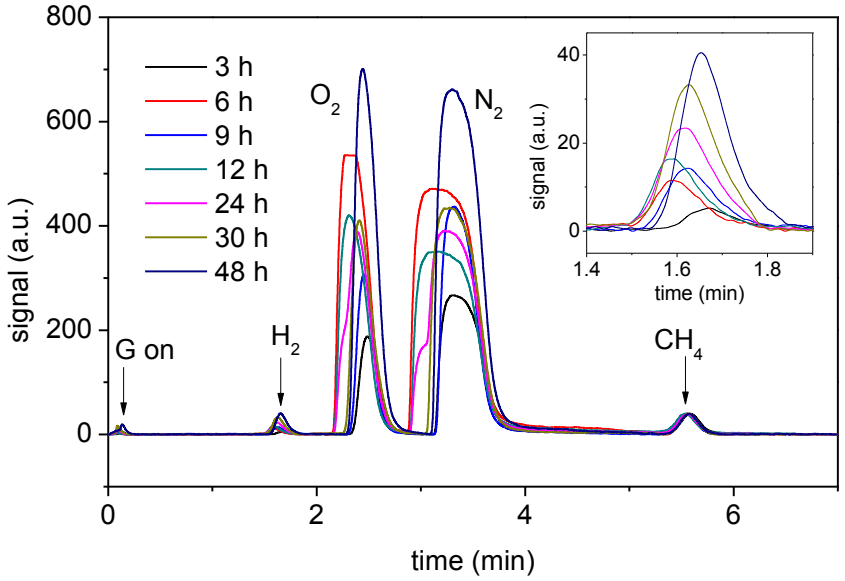

Figure 4.19. Full GC traces of the headspace over a photodriven reaction (420 nm cut off filter) with 0.5 mg Fe_2O_3@TiO_2 in 20/1 v/v H_2O/TEA at various time points over 48 h.

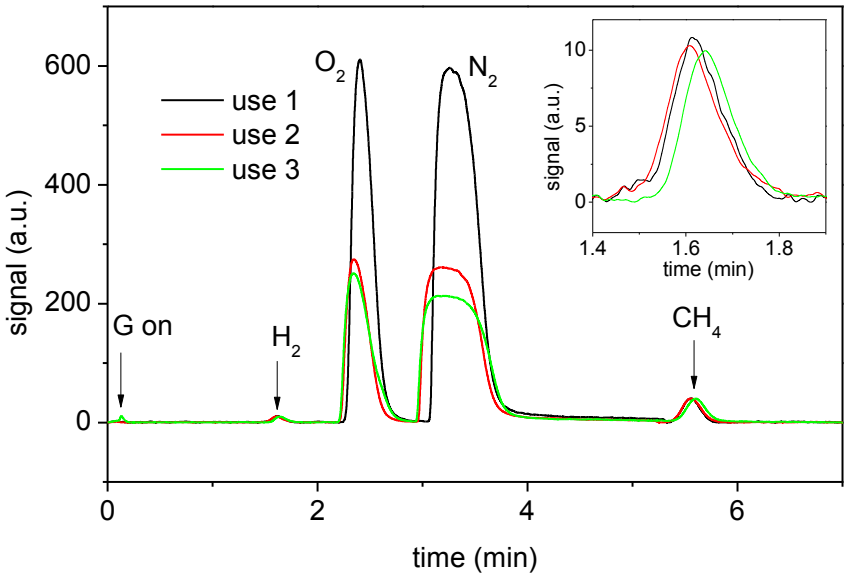

Figure 4.20. Full GC traces of the headspace over photodriven reactions (420 nm cut off filter) with 0.5 mg Fe_2O_3@TiO_2, used three times, in 20/1 v/v H_2O/TEA after 3 h.

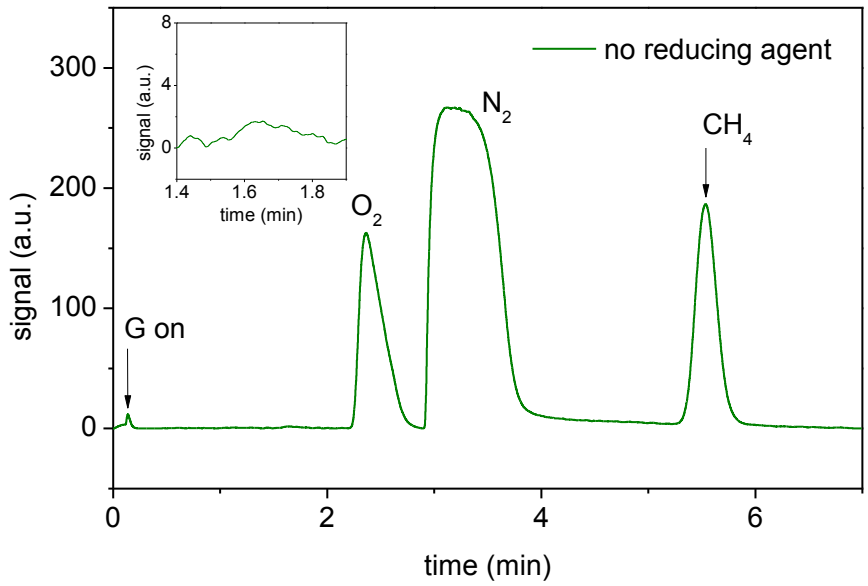

Figure 4.21. Full GC traces of the headspace over a photodriven reaction (420 nm cut off filter) with 0.5 mg Fe_2O_3@TiO_2 in H_2O, without any TEA, after 3 h.

No pure component in the material is able to generate H_2 using visible light. Fe_2O_3 or Fe_2TiO_5 alone can not catalyze H_2 production because their conduction bands are below the potential for proton reduction. TiO_2 alone can not catalyze H_2 production because it does not absorb visible light. Reactions were carried out using similar conditions, but with Fe_2O_3 alone and TiO_2 alone, to confirm that neither of these materials could catalyze the reaction. As expected, in both cases, no H_2 was detected in the headspace after 3 h (Fig. 4.18c, 4.22). A similar reaction was also carried out using a physical mixture of Fe_2O_3 and TiO_2. The conduction band of Fe_2O_3 is below that of TiO_2 and the valence band of Fe_2O_3 is above that of TiO_2. Therefore, electrons excited to the conduction band of Fe_2O_3 by visible light are not able to transfer to the TiO_2 conduction band and photogenerated holes are not able to transfer to the TiO_2 valence band. These energy differences prevent TiO_2 from producing H_2 using visible light energy harvested by Fe_2O_3, and no H_2 was detected using a physical mixture of the two.

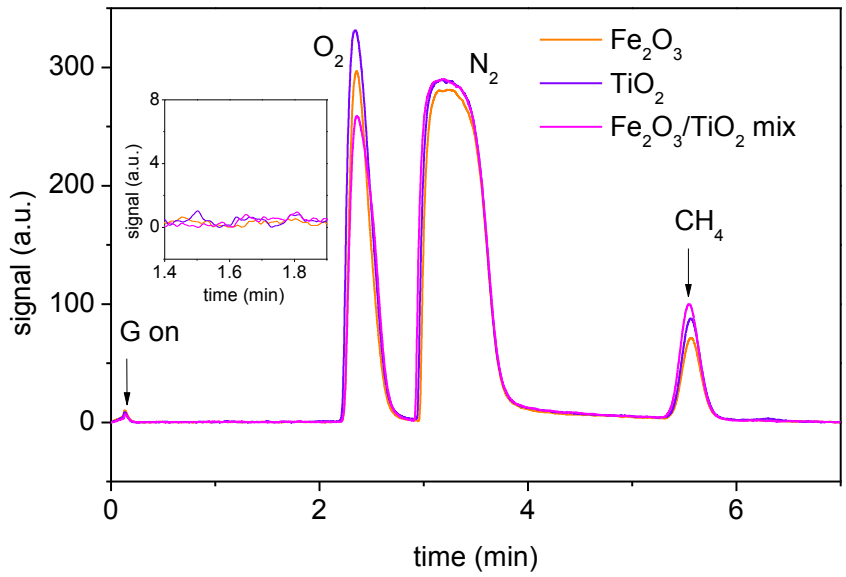

Figure 4.22. Full GC traces of the headspace over photodriven reactions (420 nm cut off filter) with 0.5 mg Fe_2O_3, TiO_2, or a Fe_2O_3/TiO_2 mixture in 20/1 v/v H_2O/TEA after 3 h.

A reaction was carried out with Fe_2O_3@TiO_2 using a 500 nm cut-off filter to determine if Fe-doped TiO_2 could be responsible for the photocatalytic activity. Fe-doping in TiO_2 raises the potential of the valence band, making the band gap of Fe-doped anatase between that of Fe_2O_3 and pure TiO_2.[39, 43, 44] This method of narrowing the band gap of TiO_2 by doping has been investigated extensively as a way of sensitizing TiO_2 to visible light.[35, 40, 45, 46] Light with wavelengths higher than 500 nm (and lower than 590 nm) is absorbed by Fe_2O_3, but may be too low in energy to be absorbed by Fe-doped TiO_2. For example, TiO_2 doped with 6.7 atomic % Fe (based on Ti) is reported to have a band gap of 2.7 eV,[43] which would correspond to absorbance of light with wavelength <460 nm. Using similar conditions as the reaction that produces H_2 from Fe_2O_3@TiO_2 with a 420 nm filter, no H_2 is detected with a 500 nm filter (Fig. 4.18c, 4.23), consistent with Fe-doped TiO_2 as the catalytic component of the composite material (Fig. 4.24). Apparently, during calcination, some Fe^{3+}

from MIL-101 is incorporated into TiO_2 as it crystallizes while some turns into Fe_2O_3. Both Fe_2TiO_5 and Ti-doped Fe_2O_3 were ruled out as potential photocatalytically active components because their conduction bands are below the potential for proton reduction, and their small bandgaps (2.2 and 2.1 eV, respectively) would allow light absorption when a 500 nm filter is used.[43]

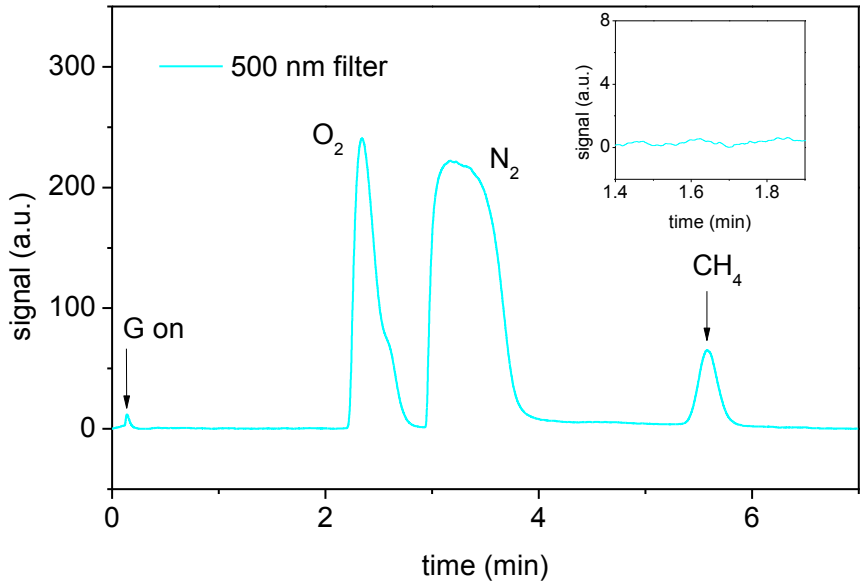

Figure 4.23. Full GC traces of the headspace over photodriven reactions (500 nm cut off filter) with 0.5 mg Fe_2O_3@TiO_2 in 20/1 v/v H_2O/TEA after 3 h.

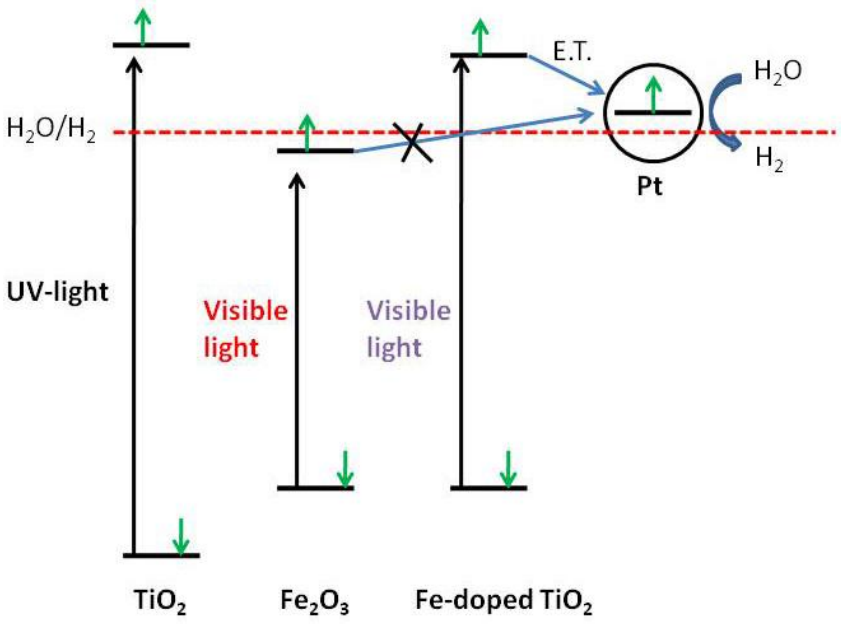

Figure 4.24. Band structure of TiO_2, Fe_2O_3, and Fe-doped TiO_2 showing how Fe-doped TiO_2 is able to catalyze H_2 production from H_2O with the aid of Pt.

4.3. Conclusion

We have developed a novel MOF-templated approach to synthesize a mixed metal oxide nanocomposite material by first creating core-shell particles, then calcining to decompose the core. This facile method produces crystalline octahedral nanoshells composed of hematite Fe_2O_3 nanoparticles embedded in anatase TiO_2 with some Fe doping. This material has interesting photophysical properties as it enables photocatalytic hydrogen production from water using visible light, while neither component alone is able to do so. The versatile MOF-templated nanocomposite synthesis procedure can be readily modified, by varying the type of MOF (both the metal ions and coordinating moieties) and the coating material, to prepare new nanocomposite materials with desirable synergistic properties.

4.4. Experimental Details

4.4.1 Materials and methods

All chemicals were purchased from Fisher Scientific or Sigma Aldrich, except TiO_2 which was purchased from Alfa Aesar, and used without further purification. Microwave reactions were carried out in a CEM MARS 5 microwave. Scanning electron microscopy (SEM) was obtained on a Hitachi 4700 Field Emission Scanning Electron Microscope. A Cressington 108Auto Sputter Coater equipped with a Au/Pd (80/20) target and MTM-10 thickness monitor was used to coat samples before SEM imaging. Energy dispersive X-ray spectroscopy (EDS) was used to determine elemental composition of the particles, using an Oxford 7200 IncaPentaFET-x3 Energy Dispersive X-ray Spectrometer. The EDS data was processed with the Inca Microanalysis Suite. Each EDS sample was prepared by placing a powder sample on carbon tape. Low-resolution transmission electron microscopy (TEM) was obtained on a JEOL 100CX-II Transmission Electron Microscope, and high-resolution TEM (HRTEM) and scanning TEM-EDS (STEM-EDS) was obtained on a JEOL 2010F-FasTEM. SEM micrographs were obtained on glass slides or carbon tape, and TEM micrographs were obtained on carbon-coated copper grids. Thermogravimetric analysis (TGA) was carried out on a Shimadzu TGA-50 equipped with a platinum pan, and samples were heated at a rate of 4°C/min under air. Powder x-ray diffraction (PXRD) data was gathered on a Bruker SMART APEX II diffractometer using Cu radiation, and powder patterns were analyzed with the APEX II package using the phase ID plugin. Diffuse reflectance UV-Vis spectra were obtained using a Shimadzu UV-3600 UV-VIS-NIR spectrophotometer. A $BaSO_4$ plate was used as a blank to establish a baseline, and samples were ground onto $BaSO_4$ plates to acquire diffuse reflectance spectra. A Varian 820-MS Inductively Coupled Plasma-Mass Spectrometer (ICP-MS) was used to measure Fe and Ti content. Nitrogen adsorption

experiments were performed with a Quantachrome Autosorb-1C. Amounts of H_2 generated in the photocatalysis experiments were determined by gas chromatography (GC) using an SRI 8610C Gas Chromatograph.

4.4.2. Synthesis of template and composite materials

Synthesis of MIL-101: BDC (1.532 g, 9.22 mmol) and $FeCl_3 \cdot 6H_2O$ (2.492 g, 9.22 mmol) were dissolved in 200 mL DMF. This solution was heated by microwave in sealed vessels at 400 W for 15 min at 150 ºC. The resulting particles were isolated by centrifugation at 11,000 rpm for 10 min, washed with ethanol and water several times by sonication followed by centrifugation, and then dispersed in water. Yield: 543.7 mg (94.7%).

Synthesis of MIL-101@TiO_2 and Fe_2O_3@TiO_2: MIL-101 (200 mg) was dispersed in 96.725 mL 0.1 M HCl and TALH (3.275 mL of 50 wt% solution in water, 2.00 g TALH) was added. The dispersion was stirred at room temperature for 2 h. The resulting coated particles were isolated by centrifugation as described above, and dried. Yield: 140.8 mg (70.4% based on MIL-101 used). Dried MIL-101@TiO_2 was calcined in a furnace at 550 ºC in air for 16 h.

4.4.3. Procedure for hydrogen production experiments

Samples for photoinduced hydrogen production were prepared in 8 mL septum-sealed glass vials. Typically, 0.5 mg of Fe_2O_3@TiO_2 (5.0 μmol Fe, 1.25 μmol Ti) was dispersed in 2 mL of H_2O with 0.1 mL of TEA, and K_2PtCl_4 (3.70 μmol) was added. The sample vials were capped and deoxygenated by bubbling nitrogen through them for 15 min. 50 μL of methane gas (1 atm, room temperature) was added to each vial as an internal standard. The vials were placed in front of a 450 W Xe-lamp with a 420 nm cut-off filter (unless otherwise noted) and were stirred magnetically. The hydrogen evolution reaction lasted for 3 hours

except for the time-dependent experiments. 0.5 mL of the gas in the headspace of the vial was analyzed by GC to determine the amount of hydrogen generated. A valve rotation (G on/off) technique was used in the GC analysis of multiple gases in the headspace. Column 1 was a 15 m Restek MXT-1 column, and column 2 was a 6‘ silica gel column. Helium carrier gas was used at 5 psi, and a helium ionization detector was used. In a typical run, the column temperature was kept at 40 ^{o}C for 4 min, raised to 80 ^{o}C over 2 min, kept at 80 ^{o}C for 1 min, then allowed to cool down. Under these operating conditions, the retention times were: 1.58-1.66 min for H_2, 2.29-2.44 min for O_2, 3.09-3.29 min for N_2, and 5.52-5.59 min for CH_4. The detected O_2 and N_2 in these experiments came from residual air in the GC injector.

4.5. References

(1) Hoffmann, M.R.; Martin, S.T.; Choi, W.; Bahnemann, D.W. *Chem. Rev.* **1995**, *95*, 69.

(2) Fox, M.A.; Dulay, M.T. *Chem. Rev.* **1993**, *93*, 341.

(3) Kay, A.; Cesar, I.; Grätzel, M. *J. Am. Chem. Soc.* **2006**, *128*, 15714.

(4) Cowan, A.J.; Barnett, C.J.; Pendlebury, S.R.; Barroso, M.; Sivula, K.; Grätzel, M.; Durrant, J.R.; Klug, D.R. *J. Am. Chem. Soc.* **2011**, *133*, 10134.

(5) Mills, A.; Davies, R.H.; Worsley, D. *Chem. Soc. Rev.* **1993**, 417.

(6) Youngblood, W. J.; Lee, S.-H.A.; Maeda, K.; Mallouck, T. E. *Acc. Chem. Res.* **2009**, *42*, 1966.

(7) Lewis, N.S. *Nature* **2001**, *414*, 589.

(8) Shangguan, W. *Sci. Technol. Adv. Mat.* **2007**, *8*, 76.

(9) Kuang, S.; Yang, L.; Luo, S.; Cai, Q. *Appl. Surf. Sci.* **2009**, *255*, 7385.

(10) Kida, T.; Guan, G.; Yoshida, A. *Chem. Phys. Lett.* **2003**, *371*, 563.

(11) Barroso, M.; Cowan, A.J.; Pendlebury, S.R.; Grätzel, M.; Klug, D.R.; Durrant, J.R. *J. Am. Chem. Soc.* **2011**, *133*, 14868.

(12) Srinivasan, S.S.; Wade, J.; Stefanakos, E.K. *J. Nanomater.* **2006**, 87326-1.

(13) Li, S.; Lin, Y.-H.; Zhang, B.-P.; Li, J.-F.; Nan, C.-W. *J. Appl. Phys.* **2009**, *105*, 054310-1.

(14) Luo, J.; Maggard, P.A. *Adv. Mater.* **2006**, *18*, 514.

(15) Evans, O.R.; Lin, W. *Acc. Chem. Res.* **2002**, *35*, 511.

(16) Wang, C.; Zhang, T.; Lin, W. *Chem. Rev.* **2012**, *112*, 1084.

(17) Rowsell, J.L.C.; Yaghi, O.M. *Angew. Chem. Int. Ed.* **2005**, *44*, 4670.

(18) Kensali, B.; Cui, Y.; Smith, M.R.; Bittner, E.W.; Bockrath, B.C.; Lin, W. *Angew. Chem. Int. Ed.* **2005**, *44*, 72.

(19) Dincă, M.; Long, J.R. *Angew. Chem. Int. Ed.* **2008**, *47*, 6766.

(20) Lin, W. *MRS Bull* **2007**, *32*, 544.

(21) Nickerl, G.; Henschel, A.; Grunker, R.; Gedrich, K.; Kaskel, S. *Chem. Ing. Tech.* **2011**, *83*, 90.

(22) Allendorf, M.D.; Bauer, C.A.; Bhakta, R.K.; Houk, R.J.T. *Chem. Soc. Rev.* **2009**, *38*, 1330.

(23) Allendorf, M.D.; Houk, R.J.T.; Andruszkiewicz, L.; Talin, A.A.; Pikarsky, J.; Choudhury, A.; Gall, K.A.; Hesketh, P.J. *J. Am. Chem. Soc.* **2008**, *130*, 14404.

(24) Chen, B.; Wang, L.; Xiao, Y.; Fronczek, F.R.; Xue, M.; Cui, Y.; Qian, G. *Angew. Chem. Int. Ed.* **2009**, *48*, 500.

(25) Xie, Z.; Ma, L.; deKrafft, K.E.; Jin, A.; Lin, W. *J. Am. Chem. Soc.* **2010**, *132*, 922.

(26) Rieter, W.J.; Pott, K.M.; Taylor, K.M.; Lin, W. *J. Am. Chem. Soc.* **2008**, *130*, 11584.

(27) Horcajada, P.; Chalati, T.; Serre, C.; Gillet, B.; Sebrie, C.; Baati, T.; Eubank, J.F.; Heurtaux, D.; Clayette, P.; Kreuz, C.; Chang, J.S.; Hwang, Y.K.; Marsaud, V.; Bories, P.N.; Cynober, L.; Gil, S.; Férey, G.; Couvreur, P.; Gref, R. *Nat. Mater.* **2010**, *9*, 172.

(28) Huxford, R.C.; Della Rocca, J.; Lin, W. *Curr. Opinion Chem. Biol.* **2010**, *14*, 262.

(29) Rieter, W.J.; Taylor, K.M.; Lin, W. *J. Am. Chem. Soc.* **2007**, *129*, 9852.

(30) Jiang, H.L.; Liu, B.; Lan, Y.Q.; Kuratani, K.; Akita, T.; Shioyama, H.; Zong, F.; Xu, Q. *J. Am. Chem. Soc.* **2011**, *133*, 11854.

(31) Schröder, F.; Esken, D.; Cokoja, M.; van den Berg, M.W.E.; Lebedev, O.I.; Van Tendeloo, G.; Walaszek, B.; Buntkowsky, G.; Limbach, H.-H.; Chaudret, B.; Fischer, R.A. *J. Am. Chem. Soc.* **2008**, *130*, 6119.

(32) Férey, G.; Mellot-Draznieks, C.; Serre, C.; Millange, F.; Dutour, J.; Surblé, S.; Margiolaki, I. *Science* **2005**, *309*, 2040.

(33) Taylor-Pashow, K.M.L.; Della Rocca, J.; Xie, Z.; Tran, S.; Lin, W. *J. Am. Chem. Soc.* **2009**, *131*, 14261.

(34) Lee, S.; Drwiega, J.; Wu, C.-Y.; Mazyck, D.; Sigmund, W.M. *Chem. Mater.* **2004**, *16*, 1160.

(35) Litter, M.I.; Navío, J.A. *J. Photoch. Photobio. A* **1996**, *98*, 171.

(36) Åsbrink, S.; Magnéli, A. *Acta Cryst.* **1959**, *12*, 575.

(37) Guo, W.Q.; Malus, S.; Ryan, D.H.; Altounian, Z. *J. Phys.: Condens. Matter* **1999**, *11*, 6337.

(38) Adán, C.; Carbajo, J.; Bahamonde, A.; Oller, I.; Malato, S.; Martínez-Arias, A. *Appl. Catal. B* **2011**, *108-109*, 168.

(39) Nagaveni, K.; Hegde, M.S.; Madras, G. *J. Phys. Chem. B* **2004**, *108*, 20204.

(40) Thompson, T.L.; Yates, Jr., J.T. *Chem. Rev.* **2006**, *106*, 4428.

(41) Sivula, K.; Le Formal, F.; Grätzel, M. *Chem. Sus. Chem* **2011**, *4*, 432.

(42) Ranjit, K.T.; Viswanathan, B. *J. Photoch. Photobio. A* **1997**, *108*, 79.

(43) Thimsen, E.; Biswas, S.; Lo, C.S.; Biswas, P. *J. Phys. Chem. C* **2009**, *113*, 2014.

(44) George, S.; Pokhrel, S.; Ji, Z.; Henderson, B.L.; Xia, T.; Li, L.; Zink, J.I.; Nel, A.E.; Mädler, L. *J. Am. Chem. Soc.* **2011**, *133*, 11270.

(45) Singh, D.; Singh, N.; Sharma, S.D.; Kant, C.; Sharma, C.P.; Pandey, R.R.; Saini, K.K. *J. Sol-Gel Sci. Technol.* **2011**, *58*, 269.

(46) Rane, K.S.; Mhalsiker, R.; Yin, S.; Sato, T.; Cho, K.; Dunbar, E.; Biswas, P. *J. Solid State Chem.* **2006**, *179*, 3033.

CHAPTER 5

Electrochemical Water Oxidation with Carbon-Grafted Molecular Complexes

(Portions of this chapter were adapted with permission from deKrafft, K.E.; Wang, C.; Xie, Z.; Su, X.; Hinds, B.J.; Lin, W. *ACS Appl. Mater. Interfaces* **2012**, *4*, 608.

5.1. Introduction

5.1.1. Water oxidation

Large-scale production of clean energy from renewable sources is needed to meet the growing global energy demand.[1] Among all the renewable energy sources, sunlight provides the most attractive long-term solution because of its vast abundance with an estimated solar radiation of 120,000 terawatts on the earth's surface. However, the diurnal and diffuse nature of local solar radiation makes it imperative to develop cost-effective storage of harvested solar energy. A potential solution is to store solar energy in reactive chemical bonds in the form of chemical fuels such as hydrogen or hydrocarbons.[2]

With the input of solar energy, hydrogen or hydrocarbons can be produced by water splitting or by CO_2 reduction with water, respectively. In both processes, catalytic water oxidation constitutes a key half reaction. The complex process of removing four electrons and four protons from two water molecules with concomitant formation of an O-O bond in this half reaction ($2H_2O \rightarrow O_2 + 4H^+ + 4e^-$) has made catalytic water oxidation a major challenge for several decades.[3-5] A large number of homogeneous water oxidation catalysts (WOCs) have been developed based on Ru complexes,[4, 6-8] Ir complexes,[9-11] Fe complexes,[12,

[13] and polyoxometalates.[14-16] Several heterogeneous WOCs such as cobalt oxide[17-19] and iridium oxide nanoparticles[20, 21] have been integrated into electrochemical or photoelectrochemical cells.[22-24] Ir complexes have also been doped into metal-organic frameworks to serve as heterogeneous WOCs.[25] All of these known WOCs, however, present many practical problems; molecular catalysts are prone to decomposition while inorganic catalysts lack tunability. The progress on water oxidation catalysis, in fact, significantly lags behind the development of catalysts for the proton reduction half reaction ($2H^+ + 2e^- \rightarrow H_2$) of water splitting.[22, 26-28]

The efficacy of a homogeneous WOC is typically evaluated by carrying out water oxidation with an external oxidant (such as Ce^{4+}, E°=1.72 V) under strongly acidic conditions (e.g., pH <1). Some of these oxidants possess excessive oxidation power compared to the thermodynamic potential of 1.17 V at pH 1 for water oxidation, and can lead to the decomposition of otherwise stable catalysts. In solution, it can be difficult to determine if the initial complex is responsible for all catalytic activity or if it is a precursor to other catalytic species formed *in situ*. Alternative strategies are needed to assess the WOC potential of molecular complexes, particularly those based on earth-abundant first-row transition metals which tend to be more susceptible to decomposition. To this end, molecular Ir and Ru complexes were grafted onto carbon electrodes via covalent attachment and evaluated for electrochemical water oxidation.

5.1.2. Catalysts on surfaces

Immobilization of molecular catalysts on electro-active surfaces is a key consideration in constructing solar water splitting devices. Placing the catalyst at an interface reduces the amount of catalyst needed and may enhance rates. Grafting WOCs onto

electrodes can also potentially stabilize active intermediates and limit the extent of oxidative degradation. When grafted, molecules are spatially separated and will not deactivate via intermolecular pathways. Several homogeneous and heterogeneous WOCs have been immobilized onto electrodes for electrochemical water oxidation, either by anchoring molecular WOCs to oxide electrodes through phosphonate groups[29] or by deposition of nanoparticle or polyoxometalate WOCs onto electrodes.[17, 30] We hypothesized that direct, covalent bonding of WOCs to the electrodes would allow enhanced catalytic rates and robust attachment, compared to existing immobilization strategies. Carbon electrodes are inexpensive and can be easily modified by chemical means.[31] Diazonium grafting is a well-established technique for covalent attachment of functional molecules to carbon electrodes.[32, 33] Diazonium salts with suitable substituent groups are typically employed and can be used for anchoring other molecules via standard amide or other coupling chemistry. A molecular proton reduction catalyst has been, for example, anchored to carbon electrodes by this two-step grafting method through the formation of amide linkages.[27] We attached molecular WOCs to carbon electrodes in a single step using diazonium-functionalized derivatives of Ir and Ru complexes; analogous complexes are known to be active for chemically-driven homogeneous water oxidation.[10]

This grafting strategy may allow for systematic evaluation of different molecular WOCs under tunable conditions that are more relevant to those found in a functional water splitting device, as opposed to evaluation in solution with a chemical oxidant with a fixed redox potential. The catalytic activities can be accurately determined as the amount of grafted catalyst can be quantified, even when redox peaks are not present, which is often the case. Grafting also allows the electrochemical response of WOCs to be studied without

complications encountered in solution electrochemistry related to WOC adsorption, film formation, or insolubility. The grafting strategy also allows the measurement of WOC activities at various pH values which is not possible for Ce^{4+} and other inorganic oxidant driven water oxidation reactions.

5.2. Results and Discussion

5.2.1. Molecular water oxidation catalysts

Five new WOCs with amine pendant groups were first synthesized. The Ir complexes [Cp*IrCl(4-NH_2-bpy)]Cl (Cp* = pentamethylcyclopentadienyl, bpy = 2,2′-bipyridine) (**A**) and [Cp*IrCl(5-NH_2-bpy)]Cl (**B**), a pair of isomers, were synthesized by allowing one half equivalent of $[IrCp^*Cl_2]_2$ to react with 4-NH_2-bpy or 5-NH_2-bpy. The complex [Cp*IrCl(*p*-NH_2-ppy)] (ppy=2-phenylpyridine) (**C**) was synthesized similarly, but with *p*-NH_2-ppy instead of bpy to result in a neutral complex. The Ru complexes [Ru(Mebimpy)(4-NH_2-bpy)OTf]OTf (Mebimpy = 2,6-bis(benzimidazol-2-yl)pyridine, OTf = triflate) (**D**) and [Ru(tpy)(4-NH_2-bpy)Cl]Cl (tpy = 2,6-bis(2-pyridyl)pyridine) (**E**) were synthesized by allowing one half equiv. of $[((Mebimpy)ClRu)_2Cl_2]$ or one equiv. of $Ru(tpy)Cl_3$, respectively, to react with 4-NH_2-bpy. These new complexes were characterized by nuclear magnetic resonance spectroscopy (NMR), mass spectrometry (MS), and cyclic voltammetry (CV). The structure of **E** was also established by single crystal X-ray diffraction. **A**-**E** all show catalytic currents by CV in aqueous solutions (pH=5), consistent with electrochemically-driven water oxidation (Fig. 5.1a-b). **A**-**C** were also shown to be active homogenous catalysts for water oxidation when driven chemically in aqueous solution (pH=1) with Ce^{4+} from cerium ammonium nitrate as the sacrificial oxidant (Fig. 5.2). Oxygen was detected in the headspace

over a 0.1 M HNO_3 solution (pH = 1) containing 50 mM CAN and 25 µM catalyst. If all of the Ce^{4+} were reduced, the maximum turnover number (TON) in each case would be 500. The harsh conditions cause instability of the catalysts, limiting the TON.

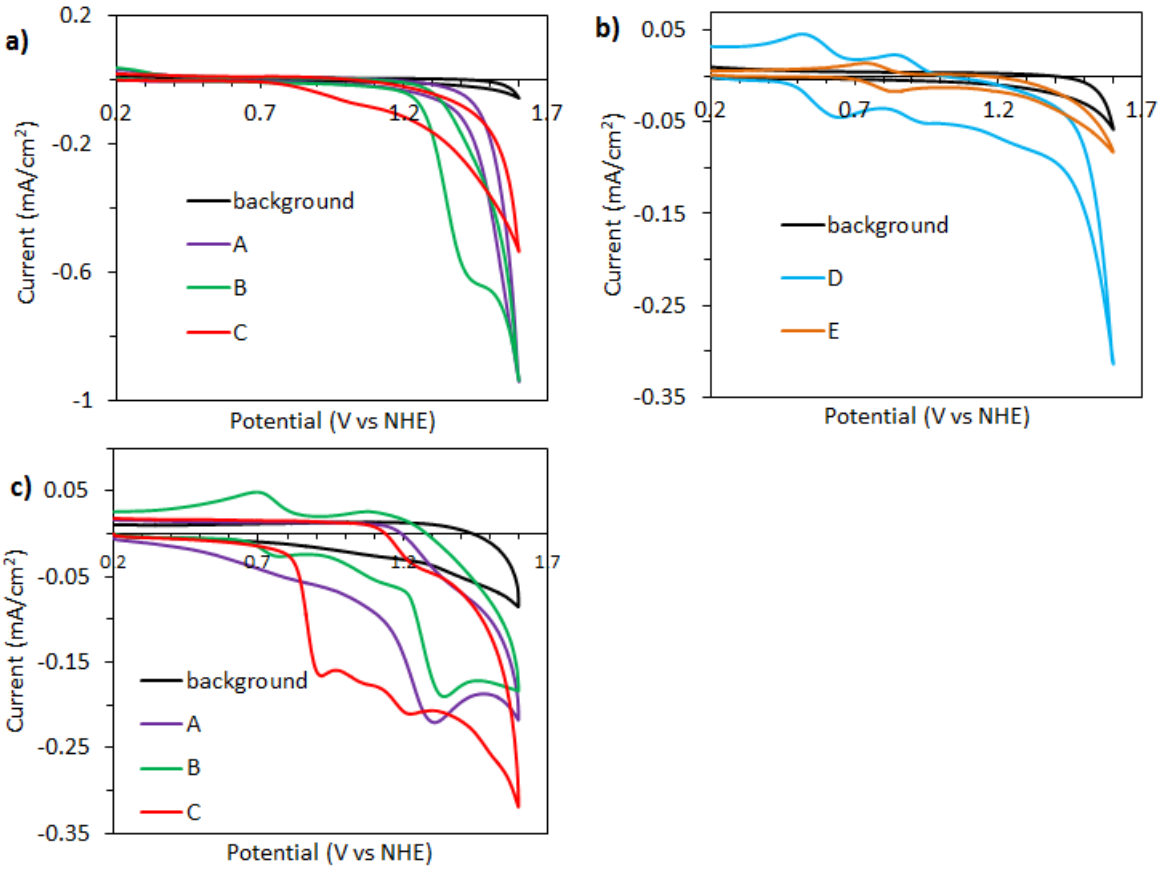

Figure 5.1. Solution CVs of **A**-**E** with a blank solution shown for comparison. (a) CVs of (a) 2 mM **A**, 2 mM **B**, and <1 mM **C** (only slightly soluble), and (b) 0.5 mM **D** and 1 mM **E** in acetate buffer at pH 5. (c) CVs of 0.66 mM **A**, 0.66 mM **B**, and 0.58 mM **C** in acetonitrile containing 0.1 M tetrabutylammonium hexafluorophosphate. All CVs were done using glassy carbon with a scan rate of 100 mV/s.

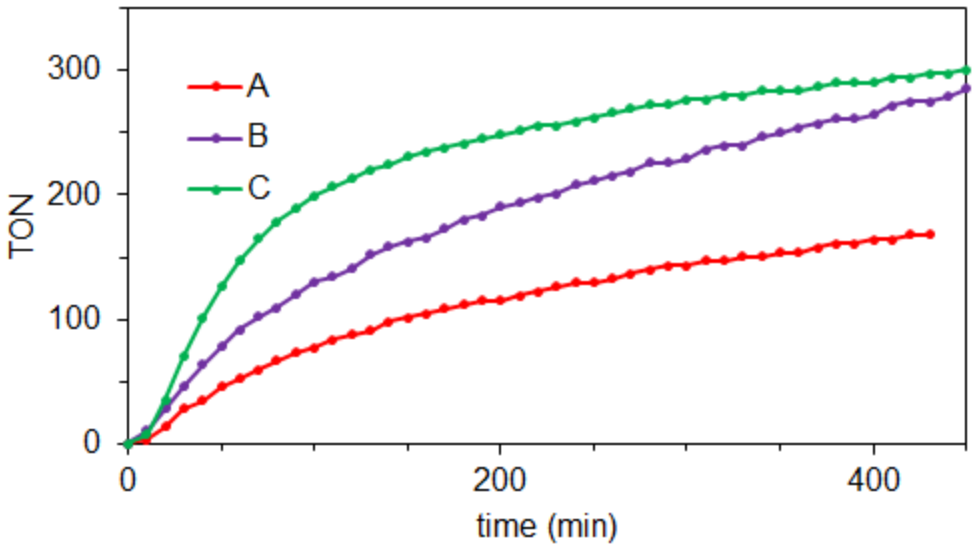

Figure 5.2. Homogeneous chemically-driven water oxidation with **A**-**C** using Ce^{4+} as an oxidant. TON is based on oxygen detected in the headspace over the reaction.

5.2.2. Catalysts grafted onto electrodes

Each of the complexes was grafted onto glassy carbon electrodes by a direct, diazonium grafting method to lead to samples **1**-**5** (Fig. 5.3). Prior to grafting, the electrode was polished and oxidized by applying a potential of 1.6 V vs the normal hydrogen electrode (NHE) for 2 min to obtain a reproducible background current, which is due to a combination of water oxidation and carbon oxidation.[34] The amino group of each complex was converted into a diazonium group *in situ* by addition of HCl and $NaNO_2$ to an aqueous solution of the complex, and $NaBF_4$ was added to stabilize the diazonium salt. The resulting solution was degassed and used for electroreduction of the diazonium salt by applying a potential of -0.4 V vs NHE for 4 min. Grafting was done on a 1.13 cm^2 area of the planar electrode. The grafted electrode was rinsed with water and methanol. Three samples were made identically for each catalyst in order to obtain averaged CV and catalyst loading data for determination of turnover frequencies (TOFs). The orientation of a complex relative to the surface is shown

for **1** in Fig. 5.3, which is modeled based on a published crystal structure for [Cp*IrCl(ppy)].[35]

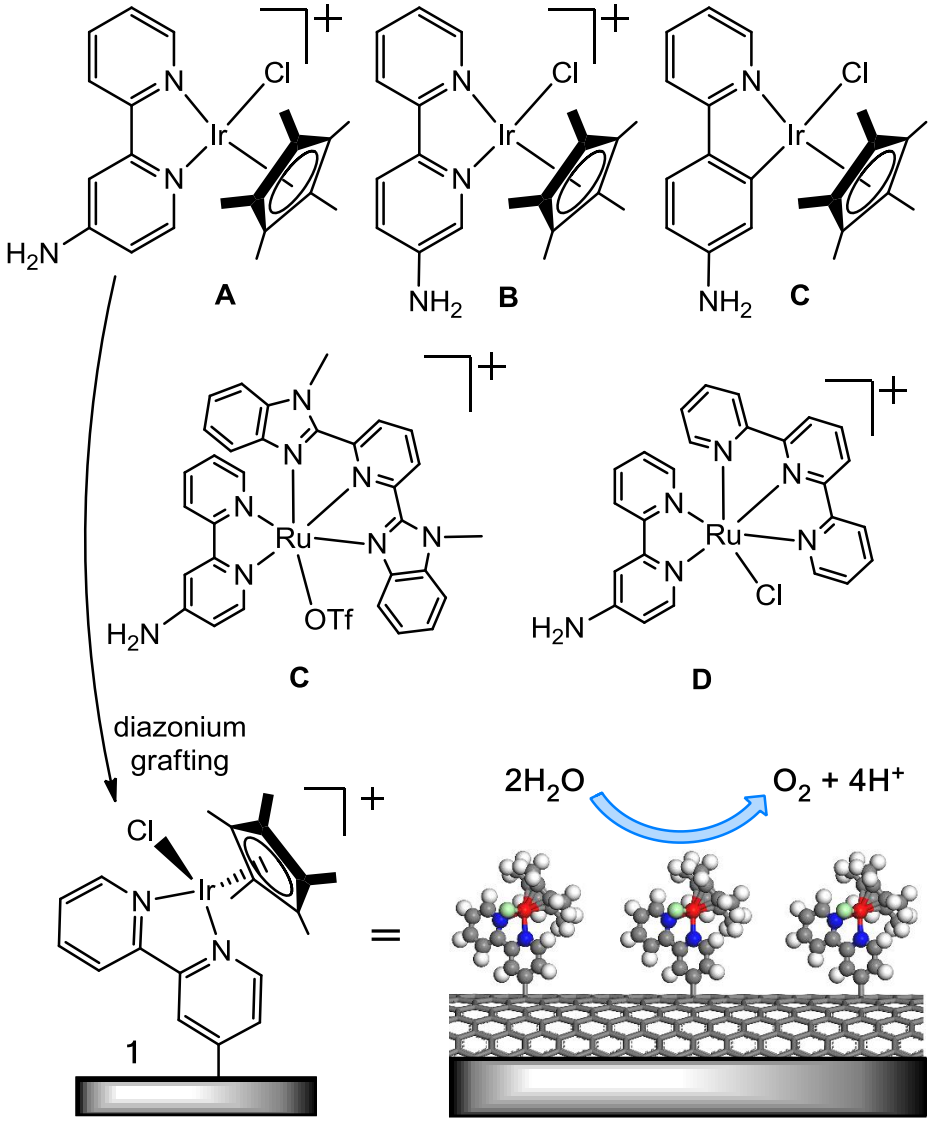

Figure 5.3. Molecular iridium WOCs have been covalently attached to carbon electrodes for efficient electrochemical water oxidation. Amino-functionalized derivatives (**A**-**E**) of WOCs were converted into diazonium salts, which were then grafted by electroreduction to result in functionalized glassy carbon electrodes **1**-**5,** respectively (only **1** is shown).

5.2.3. Cyclic voltammetry

We first examined the electrocatalytic water oxidation activity of **1**-**5** by CV. The CV scans were carried out in the 0.2 – 1.6 V range vs NHE with a scan rate of 100 mV/s in an acetic acid/sodium acetate buffer at pH 5. A platinum counter electrode and Ag/AgCl reference electrode were used for all electrochemical experiments. Catalytic currents from water oxidation at 1.6 V are 226±13, 16±5, 55±9, 50±7, and 48±21 μA/cm^2 over the background for **1**-**5** respectively (Fig. 5.4). Compounds **A**-**E** thus retain their electrocatalytic activity toward water oxidation after being grafted on carbon electrodes. The background current was determined to be 93±6 μA/cm^2 at 1.6 V using an electrode that underwent electroreduction with a blank solution that was otherwise identical to a catalyst solution, and was subtracted from the currents of samples **1**-**5**. The effects on current due to the electroreduction process and physisorbed catalysts have been eliminated by performing ten CV scans after grafting, so that the reported currents represent only catalytic current from grafted molecules.

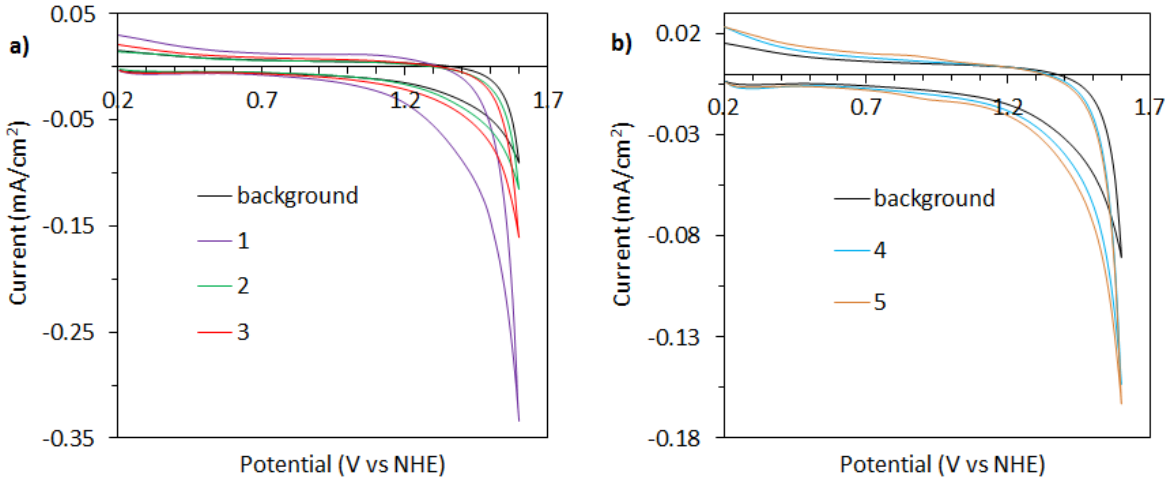

Figure 5.4. Stabilized CVs for (a) **1**-**3** and (b) **4**-**5**, compared to background, at 100 mV/s in acetate buffer (pH=5).

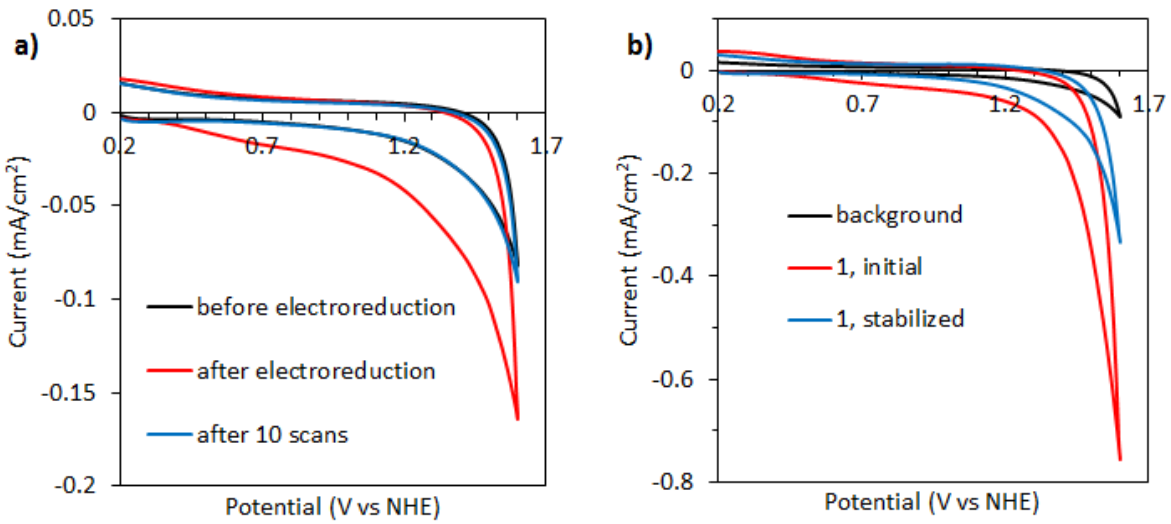

Figure 5.5. (a) CVs of a bare glassy carbon electrode at a scan rate of 100 mV/s in acetate buffer (pH=5). A scan was done before and after electroreduction using a blank solution identical to the catalyst solutions used to make **1-5** (but without any catalyst) then after 10 more scans. (b) CVs of **1** initially after grafting and after the CV response has stabilized, at a scan rate of 100 mV/s in acetate buffer (pH=5). A CV of a bare electrode is shown for comparison.

The Ir^{3+} and Ru^{2+} complexes must reach higher oxidation states before they are able to drive water oxidation. The only grafted electrode that shows any redox couple in water is **5**, with a small very broad pair of peaks with $E_{1/2}$ = 0.9 V (Fig. 5.6). This redox couple is shifted to higher potential compared to the corresponding peaks in the solution CV ($E_{1/2}$ = 0.79 V) under otherwise similar conditions. The redox peaks in buffer become much broader and less prominent when the complex is grafted. The inhibited response seen for this couple as well as the lack of peaks in **1-4** is likely due to the slow proton migration rate of proton coupled electron transfer steps.[36] The redox events that occur at the onset of water oxidation may also be obscured by the catalytic wave.[9] Redox peaks are also seen for **5** in acetonitrile ($E_{1/2}$ = 0.65 V), in which they are much more prominent and well-defined than they are in water. Fig. 5.7 shows CVs of **1** at different scan rates ranging from 20-400 mV, with the current (*I*) normalized by dividing by the square root of the scan rate. The normalized

catalytic current increases as scan rate decreases, indicating a catalytic process with a rate-limiting chemical step before quick electron transfer.[36, 37]

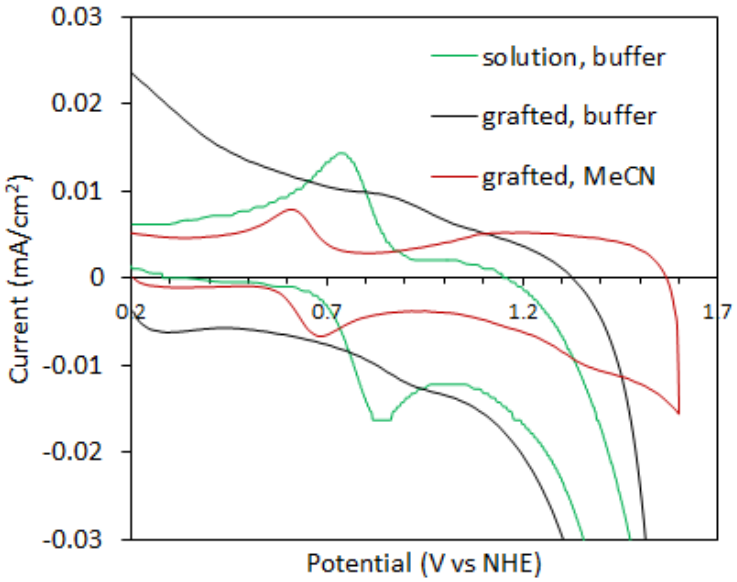

Figure 5.6. CVs of **E** in solution (1 mM) in acetate buffer (pH=5) and **5** in acetate buffer and acetonitrile containing 0.1 M tetrabutylammonium hexafluorophosphate. All CVs were done with a scan rate of 100 mV/s.

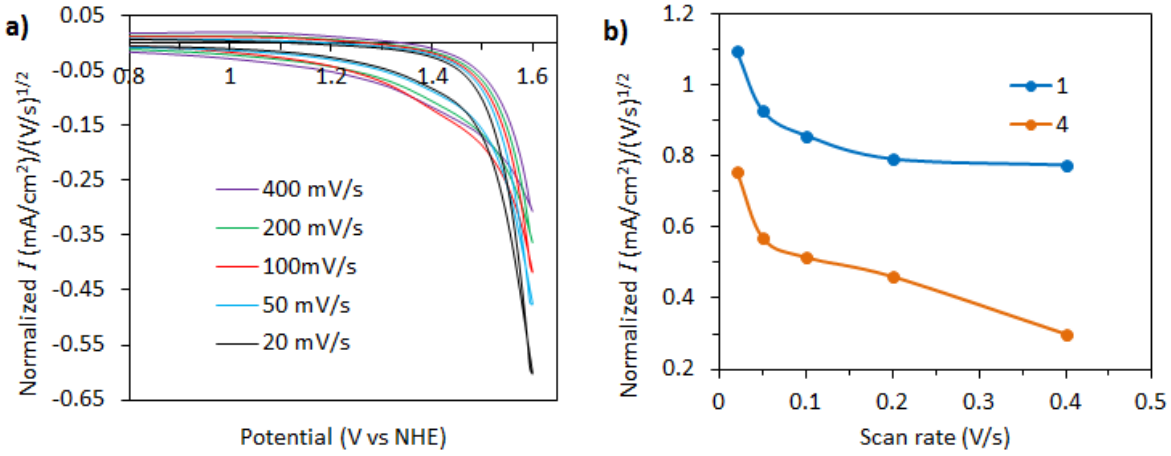

Figure 5.7. (a) Scan rate normalized CVs of **1** from 20-400 mV/s, with background subtracted. (b) The current at 1.6 V divided by the square root of the scan rate versus the scan rate for **1** and **4**.

5.2.4. Catalyst turnover frequency

Catalyst loadings in samples **1**-**5** were determined by inductively coupled plasma mass spectrometry (ICP-MS). The grafted complex was removed from the electrode using a piranha solution, and the amount of Ir or Ru was measured by ICP-MS. Catalyst loadings were quite different among **A**-**E**, with average loadings of 0.36, 0.091, 0.043, 0.039, and 0.071 nmol/cm^2, corresponding to surface coverages of **A**-**E** at 2.18, 0.55, 0.26, 0.23, and 0.43 molecules/nm^2 for **1**-**5**, respectively. The coverage on **1** is estimated to be about a monolayer. The loading efficiency may be related to the solubility of the complex in the solution used for grafting, as charged Ir complexes **A** and **B** were completely soluble while neutral Ir complex **C** was only slightly soluble and resulted in lower loading. The loading efficiency is also likely dependent on the reduction potential needed to initiate the grafting reaction in each case. The reduction potential at which grafting occurs is not clear due to the overwhelming background reduction current at 0.2 to -0.4 V (Fig. 5.8).

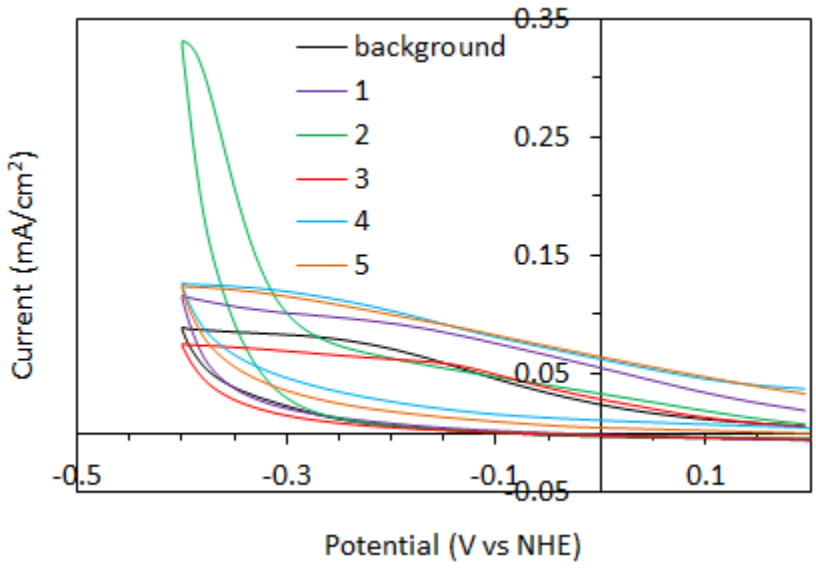

Figure 5.8. CVs of the catalyst solutions used for grafting to make **1**-**5**, from 0.2 to -0.4 V at 100 mV/s.

The TOF for each catalyst was calculated based on the current at 1.6 V and the catalyst loading as measured by ICP-MS. The TOF is the molecules of O_2 produced per molecule of catalyst per unit time, assuming 100% Faradaic efficiency (which is justified below). The ability to measure the amount of catalyst on the grafted electrodes provides an advantage over studying these WOCs electrochemically in solution. The solution CVs of the Ir complexes lack observable redox peaks (for reasons explained above), so TOFs cannot be calculated and compared amongst various catalysts. The potential of 1.6 V corresponds to an overpotential of 0.66 V, as the thermodynamic potential for water oxidation at pH 5 is 0.94 V vs NHE. The TOFs were 1.67±0.25, 0.59±0.34, 3.31±0.27, 3.33±0.38, and 1.78±0.76 s^{-1} for **1-5**, respectively. The Cp*Ir complex with the more electron-donating ppy ligand, **3**, is a more active WOC electrochemically than either of the Cp*Ir complexes with a bpy ligand, as is also observed in chemically-driven catalysis with Ce^{4+} as the sacrificial oxidant. It is apparent from the difference in TOF between **1** and **2** that the position of attachment on the pyridine ring affects the rate of water oxidation. Catalysis is significantly hindered when ppy is attached to the electrode at the 5 position, compared to the 4 position, presumably due to electronic effects or unfavorable interaction with the glassy carbon surface. Although unlikely, we cannot rule out the possibility that the carbon surface could mediate the catalytic reaction to cause different activity dependent on catalyst orientation. The overpotential used in Ce^{4+}-driven water oxidation is 0.55 V, since the thermodynamic potentials for Ce^{4+} reduction and H_2O oxidation at pH 1 are 1.72 and 1.17, respectively. The TOF for **A** in Ce^{4+} solution was only 0.0167 s^{-1} for the first hour, after which TOF decreased rapidly. At pH 5, a potential of 1.49 V would correspond to a 0.55 V overpotential, at which the TOF for **1** is

0.51 s^{-1}. This comparison demonstrates that faster catalytic rates can be achieved by evaluating molecular catalysts electrochemically rather than by using a chemical oxidant.

Table 5.1. Catalyst current, loading, and TOF[a]

Sample	Current[b] ($\mu A/cm^2$)	Loading (molecules/nm^2)	TOF (s^{-1})
1	226 ± 13	2.18 ± 0.44	1.67 ± 0.25
2	16 ± 5	0.55 ± 0.16	0.59 ± 0.34
3	55 ± 9	0.26 ± 0.03	3.31 ± 0.27
4	50 ± 7	0.23 ± 0.01	3.33 ± 0.38
5	48 ± 21	0.43 ± 0.14	1.78 ± 0.76

[a]Averaged over three replicates. Error is standard deviation. [b]At 1.6 V, with background subtracted.

5.2.5. Controlled potential electrolysis

We further examined the stability of the carbon-grafted WOCs during electrochemical water oxidation reactions. A stability test was carried out on **1** over three hours (Fig. 5.9a). Five functionalized electrodes were prepared identically, and controlled potential electrolysis was done at 1.6 V with three of them for 1, 2, or 3 hours. The remaining two electrodes did not undergo electrolysis; one was only rinsed, and the other underwent ten CV scans. The sample that was only rinsed contained 4.83 molecules/nm^2. Much of this was lost during the 10 CV scans that resulted in a stable response, to leave 1.97 molecules/nm^2. The catalyst lost during the scans was likely not covalently bound. Most of the remaining bound catalyst is then lost more slowly over three hours of electrolysis, leaving 0.10 molecules/nm^2. The loss of catalyst is likely due to loss of carbon from the surface of the electrode, rather than catalyst decomposition, as carbon is oxidized at the potential used.

It is not possible to determine TOF from the CV for catalyst remaining after electrolysis, because the background current increases a great deal during electrolysis. This increase is probably due to an increase in surface hydrophilicity and surface roughening, as observed by scanning electron microscopy (SEM), resulting in increased surface area (Fig. 5.9b-c). The electrode surface still appears smooth after 40 min, when most of the grafted catalyst remains on the electrode. The roughening of the surface becomes apparent after 10 days of electrolysis, when no catalyst remains on the surface. Carbon oxidation, and thereby loss of grafted catalyst, is a potential problem when using glassy carbon at the oxidative potentials needed to drive water oxidation. However, this problem could be overcome by using a carbon electrode with a stable surface. Recently, a Ru-bis(tpy) complex was tethered to a conductive diamond electrode, and very little loss in electrochemical activity was observed after one million CV scans to 1.5 V vs NHE.[38] The issue of catalyst loss due to carbon oxidation as seen in the present study could be alleviated with the use of a conductive diamond electrode.

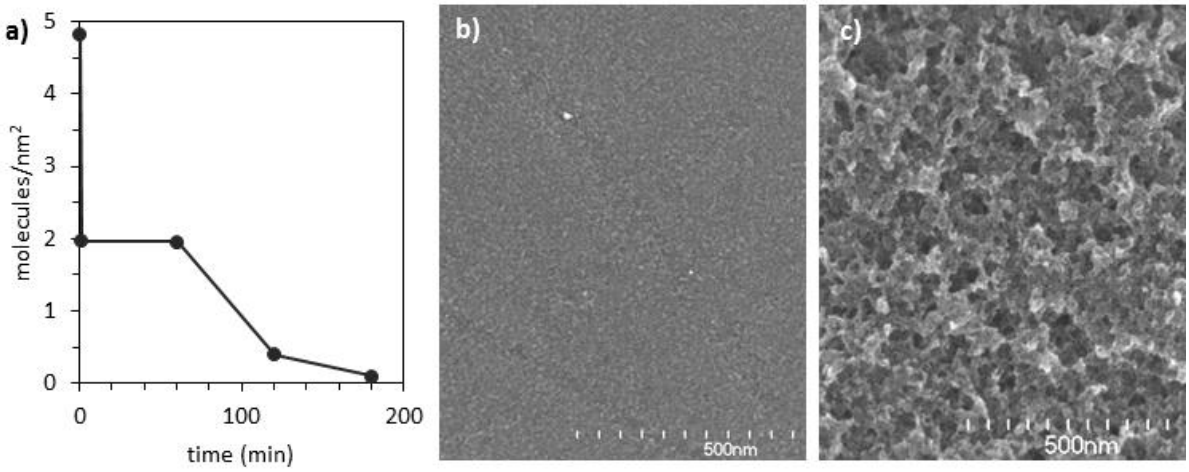

Figure 5.9. (a) Catalyst loading for **1** during controlled potential electrolysis in acetate buffer (pH=5) at 1.6 V. SEM images of glassy carbon electrode **1** after (b) 40 min of electrolysis and after (c) 10 days of electrolysis.

The current from **1** during one hour of electrolysis can be compared to the current from a bare electrode to determine sustained TOF during electrolysis as well as TON after one hour (Fig. 5.10a). This type of measurement is problematic with molecular WOCs in solution due to the deposition of films on the electrode that contain electroactive species different from the catalysts in the bulk solutions.[39] After subtracting the background, the current at 1 h is 14.2 $\mu A/cm^2$, resulting in a TOF of 0.113 s^{-1}. The total charge passed by the catalyst in 1 h corresponds to 238 nmol of O_2 and a TON of 644 in 1 h. TON could be limited by oxygen bubble formation on the electrode, which is observed during electrolysis. Bubbles would prevent diffusion of water to the surface-bound WOCs. Even considering this, the TON for **1** is much higher than the TON of ~150 obtained before the same catalyst is nearly deactivated after 7.5 hours of Ce^{4+}-driven water oxidation. This comparison suggests that the surface grafting strategy might have significantly stabilized the WOC, presumably by shutting down the intermolecular decomposition pathways. The possibility of catalyzed oxidation of the carbon electrode by the Ir and Ru complexes was a concern; however, the background current increases nearly the same amount during an hour of electrolysis with both **1** and a blank electrode (Fig. 5.10c). If the complex were catalyzing carbon oxidation, a greater increase in background current would be expected for the grafted electrode. A rapid loss of the complex from the electrode would also be observed, as it is anchored by C-C bonds, but there is very little loss of catalyst during the first hour of electrolysis. The loss of the molecular WOCs from the carbon electrode due to carbon oxidation makes it difficult to determine TOF or TON beyond 1 h. Electrolysis was also done on **4** for 1 h (Fig. 5.10b) in order to compare the catalytic activity to that achieved by attaching a phosphonate derivative

of **D** to an electrode surfaces as reported by Meyer et al.[29] The phosphonate derivative produced a sustained current of 14.8 μA/cm^2 at a loading of 0.72 molecules/nm^2 when electrolysis was performed at 1.85 V, giving a TOF of 0.36 s^{-1}. In comparison, the amount of catalyst remaining on **4** after 1 h was 0.13 molecules/nm^2, with a current of 8.8 μA/cm^2 (background subtracted) at 1 h, resulting in a TOF of 1.0 s^{-1}.

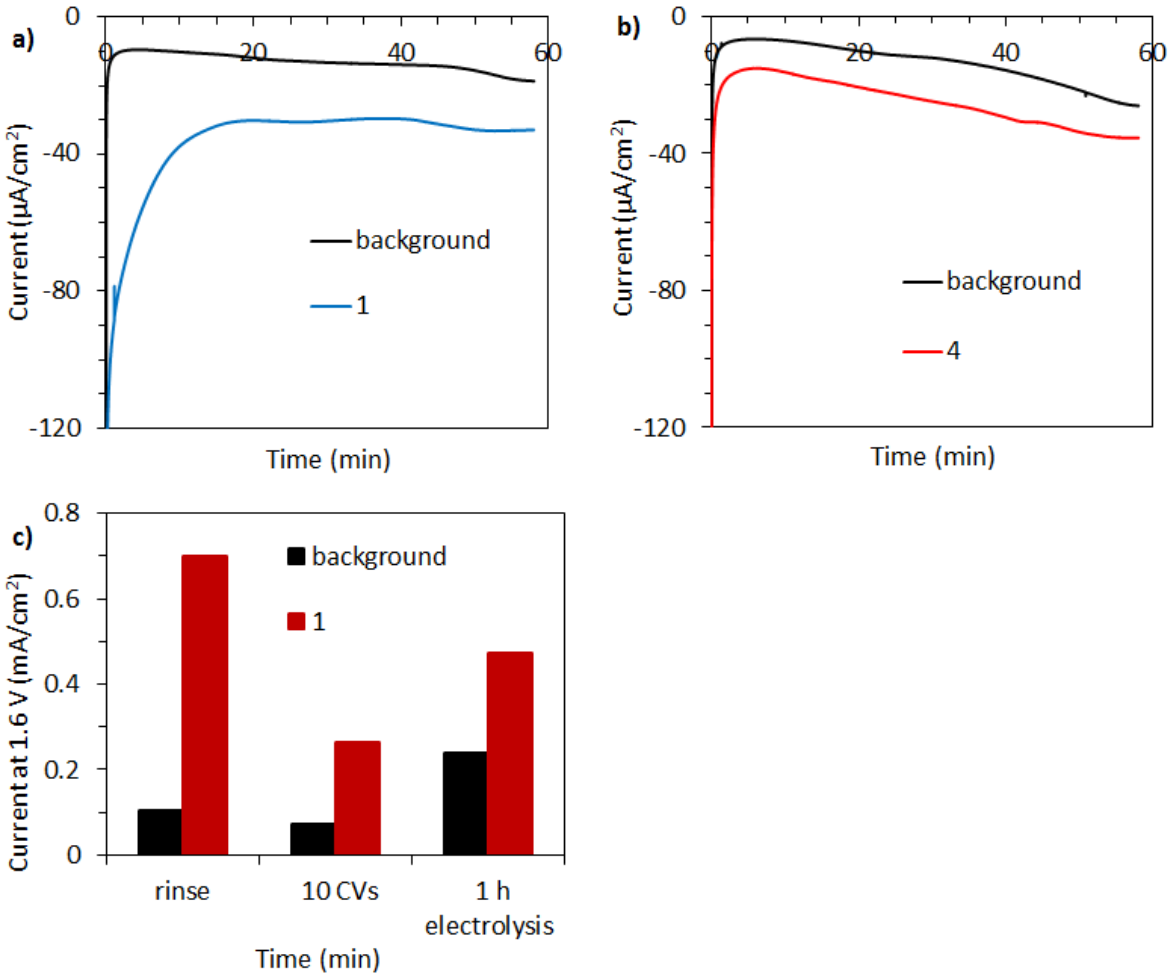

Figure 5.10. Current during 1 h of electrolysis in acetate buffer (pH=5) at 1.6 V for (a) **1** and (b) **4**, and a bare electrode. (c) The CV current at 1.6 V for both a blank electrode and **1** at three different stages: after only rinsing the grafted electrode, after 10 CVs have been run to stabilize the current, and after 1 h of electrolysis has been performed at 1.6 V.

5.2.6. Oxygen detection

Oxygen was detected in solution during 1 h of electrolysis with **1** at 1.6 V using a luminescence-based sensor (Fig. 5.11). Since the amount of oxygen generated is quite small, the distribution of oxygen in the bubbles on the electrode surface, in the solution, and in the headspace makes it difficult to directly quantify the oxygen generation Faradaic efficiency. We resorted to an indirect determination by comparison with electrochemical water oxidation with IrO_2 nanoparticles, which are known to produce O_2 from H_2O with 100% Faradaic efficiency.[21] A similar amount of O_2 is detected in the headspace when a similar amount of charge is passed by IrO_2 nanoparticles over the same period of time. The Faradaic efficiency for **1** can be considered close to 100% by comparison with the oxygen detected during water oxidation with IrO_2 nanoparticles. The background current has been subtracted when considering the amount of charge contributing to oxygen production. While there is a significant amount of charge passed while performing electrolysis with a bare electrode, there is virtually no O_2 detected. Most of this background current is likely due to oxidation of the carbon electrode, but the amounts of generated gases are too small to be detected by common methods like gas chromatography. The O_2 generation results confirm that the enhancement in current is not due to Ir-complex-catalyzed carbon oxidation. If much of the current from the grafted catalysts were coming from CO_2 generation, the amount of O_2 detected would be significantly lower than that detected during water oxidation with IrO_2. The same is true for CO_2 generation from oxidation of the organic ligands of the complexes. In any case, only a small fraction of the current could be attributed to ligand oxidation due to the very small amount of catalyst used (0.41 nmol). Oxidation of the acetate buffer is not a contributing factor under the conditions used, as CV scans on blank and grafted electrodes performed in 0.1 M KNO_3 (at pH 5) are similar to those performed in acetate buffer.

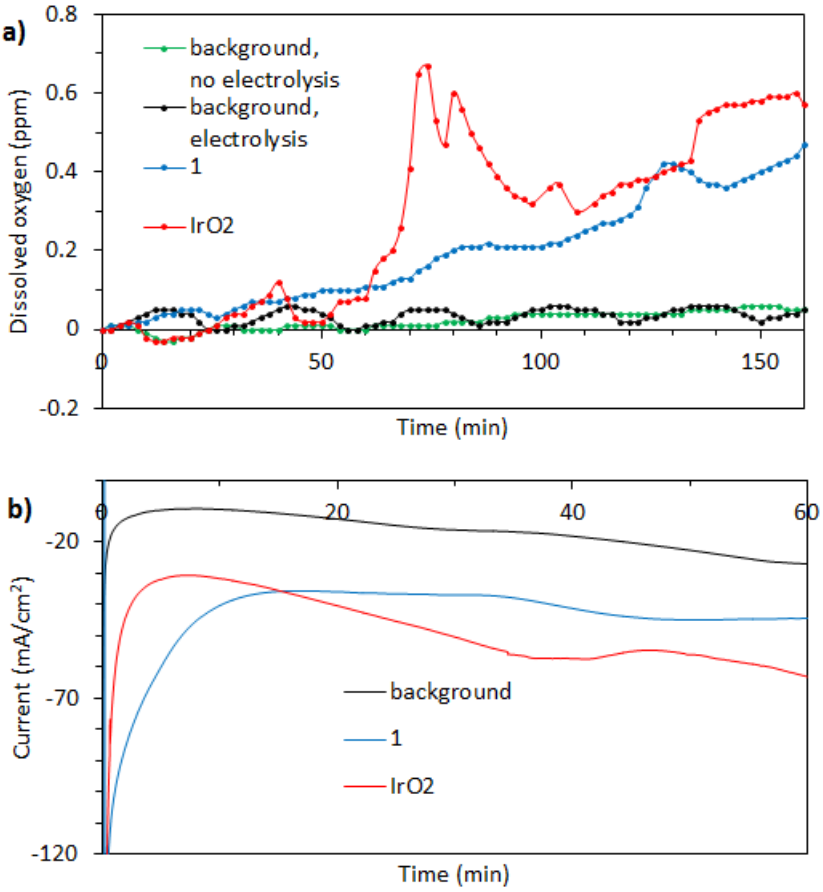

Figure 5.11. (a) Oxygen was detected in solution during 60 min of controlled potential electrolysis at 1.6 V, and for 100 min afterward, with a bare glassy carbon electrode, **1**, and 0.1 mM IrO_2 solution. All experiments were done in buffer at pH 5. (b) The current during electrolysis.

5.2.7. Active catalytic species

Grafting of molecular WOCs also allows for the identification of active catalytic species by surface spectroscopic measurements and other studies, which will help understanding of the electrochemical water oxidation reactions. For example, there is some concern that the formation of a metal oxide under the conditions used for water oxidation could be responsible for the catalytic activity of some molecular WOCs.[40, 41] X-ray photoelectron spectroscopy (XPS) was carried out on **1** to rule out the formation of IrO_2 (Fig.

5.12a). The Ir $4f_{7/2}$ peak was located at 62.9 eV for the Ir^{3+} complex on **1** after grafting, before any water oxidation was performed. The peak stays at the same binding energy after 40 min and even after 900 min of controlled potential electrolysis at 1.6 V. The Ir $4f_{7/2}$ peak for IrO_2 occurs at 61.6±0.5 eV,[42] therefore, the XPS data indicates that the Ir complex does not turn into IrO_2 under the conditions used for water oxidation. The intensity of the Ir signal decreases over time due to loss of the complex from the surface, as discussed previously. Anchoring of the molecular WOCs also allows the water oxidation to be carried out at different pHs, providing further evidence against IrO_2 formation. IrO_2 is not stable at pH 1 and becomes inactive after ~30 min, as demonstrated by performing water oxidation with Ce^{4+} at pH 1 (Fig. 5.13). Oxygen was detected in the gas phase over a 0.1 M HNO_3 solution (pH=1) containing 101 mM cerium ammonium nitrate and 24 μM IrO_2. If all of the Ce^{4+} were reduced, the maximum TON would be 1050. Most catalytic activity is lost after about 30 min, before all of the Ce^{4+} has been reduced. A sample of **1** was prepared and soaked in 0.1 M HNO_3 for 1 h, then 10 CVs were run from 0.2-1.8 V to stabilize the current (Fig. 5.12b). The electrode was then soaked in 0.1 M HNO_3 for 1 more hour and 10 more scan cycles were performed before acquiring a second CV. Bare glassy carbon was treated in a similar manner as **1** for background comparison. A strong water oxidation wave is present for **1** and remains even after soaking at pH 1 for another hour. The retention of catalytic activity at pH 1 argues against the formation of IrO_2 as the active catalyst. Our results are in excellent agreement with a recent study by Crabtree, Brudvig, and co-workers using piezoelectric gravimetry to distinguish between homogeneous and heterogeneous catalytic water oxidation using molecular Ir complexes.[39]

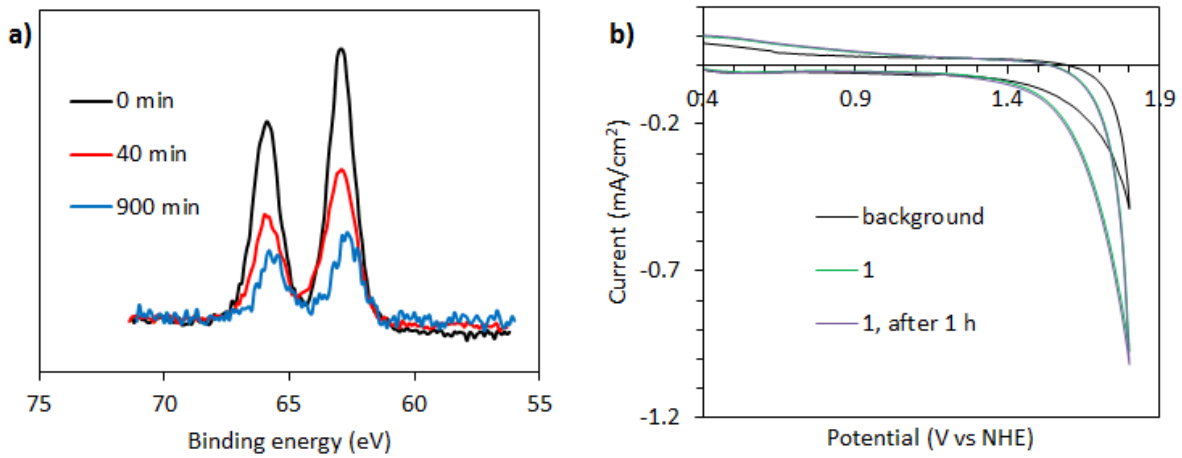

Figure 5.12. (a) XPS Ir 4f peaks from **1** after 0, 40, and 900 min of electrolysis at 1.6 V. (b) CVs of **1** done in 0.1 M HNO_3 (pH=1) from 0.4-1.8 V with a scan rate of 100 mV/s.

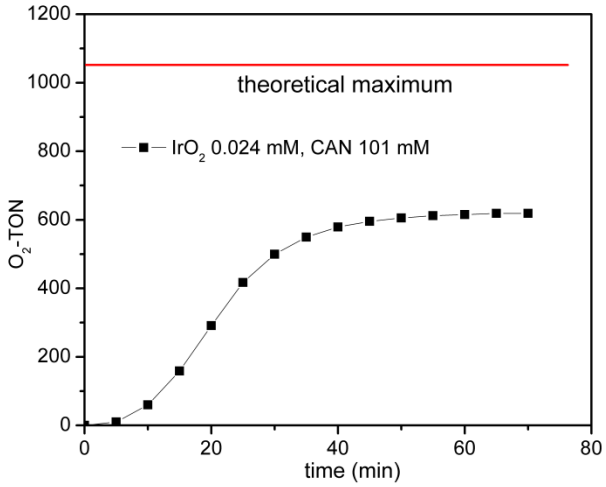

Figure 5.13. Homogeneous chemically-driven water oxidation with IrO_2 nanoparticles using Ce^{4+} as an oxidant. TON was based on oxygen detected in the gas phase over the reaction.

5.3. Conclusion

Grafting molecular Ir and Ru complexes directly and covalently to carbon electrodes demonstrates a new way to study molecular WOCs. As opposed to Ce^{4+}-driven water oxidation, electrochemical water oxidation using grafted WOCs can be carried out under tunable conditions, which is more relevant to identifying typically less stable molecular

WOCs based on first-row transition metals. This method provides a more accurate way of assessing the true activity of a WOC without decomposition due to unnecessarily harsh conditions. Combining this new surface attachment strategy with newly developed molecular WOCs that are active and earth-abundant can lead to a potentially practical solution for storing solar energy in chemical fuels.

5.4. Experimental Details

5.4.1 Materials and methods

All starting materials were purchased from Aldrich and Fisher, unless otherwise noted, and used without further purification. ^{1}H NMR, ^{1}H-^{1}H COSY NMR and ^{1}H-^{1}H NOESY NMR spectra were recorded on Bruker NMR 400 NB and 400 DRX Spectrometers at 400 MHz and referenced to the proton resonance resulting from incomplete deuteration of deuterated chloroform ($CDCl_3$, δ 7.26), deuterated dimethyl sulfoxide (DMSO-d_6, δ 2.50), deuterated methanol (MeOD, 3.34 δ). Mass spectrometric (MS) analyses were conducted using positive-ion electrospray ionization on a Bruker BioTOF Mass Spectrometer. A Varian 820-MS Inductively Coupled Plasma-Mass Spectrometer (ICP-MS) was used to determine Ir and Ru complex loading on electrodes. The complexes were removed from the electrode by soaking the electrode in a 3:1 v/v solution of concentrated H_2SO_4 and 30% H_2O_2 (piranha solution). After soaking for two hours, the piranha solution was diluted with H_2O to prepare the samples for ICP-MS. X-ray photoelectron spectroscopy (XPS) was also used to characterize the grafted electrodes. A Kratos Axis Ultra DLD X-ray Photoelectron Spectrometer was used with a monochromatic Al X-ray source at 150 W. The pass energy used was 80 eV for the entire spectral region from 0-1200 eV, and 20 eV for the individual

element spectra. Scanning electron microscopy (SEM) was used to image the electrodes, using a Hitachi 4700 field emission scanning electron microscope. Cyclic voltammograms (CVs) and controlled potential electrolysis were done using a PAR Model 263A potentiostat. Most electrochemical data for the grafted electrodes was obtained in a CH_3CO_2H/CH_3CO_2Na buffer solution at pH 5 and 0.1 M ionic strength. Some experiments were done at lower pH in 0.1 M HNO_3 (pH=1). A Pt wire counter electrode and a Ag/AgCl reference electrode were used for all experiments, and iR compensation was used for all CVs. Oxygen was detected with a luminescence-based YSI Professional Optical Dissolved Oxygen (ProODO) sensor. All oxygen detection experiments were performed in airtight vessels that had been purged with Ar or N_2 until the oxygen reading on the sensor was very close to zero. For oxygen detection in the gas phase, only the headspace was purged. For oxygen detection in solution, both the solution and headspace were purged.

Calculations: The catalyst loading on the electrodes was determined by ICP-MS detection of Ir and Ru. The number of Ir or Ru sites was then used to calculate turnover frequency (TOF) based on the number of O_2 molecules generated per catalyst molecule. The CV peak current at 1.6 V taken at 100 mV/s was used to determine the number of electrons transferred per unit time. Background current from a bare glassy carbon electrode was subtracted. This was converted to the amount of O_2 being generated, based on 100% current efficiency and 4 electrons being produced for every O_2 molecule. TOF was also calculated from stabilized current during electrolysis, reflecting sustained water oxidation rate. TON was determined for a time period of 1 h based on the total charge passed after background subtraction.

5.4.2. Synthesis and characterization of complexes

Synthesis of 4-amino-2,2'-bipyridine (4-NH_2-bpy) and 5-amino-2,2'-bipyridine (5-NH_2-bpy). Both NH_2-bpy ligands were synthesized by following a published procedure.[43]

Synthesis of 2-(*p*-aminophenyl)pyridine (*p*-NH_2-ppy). *p*-NH_2-ppy was synthesized by following a published procedure.[44]

Synthesis of 2,6-bis(1-methylbenzimidazol-2-yl)pyridine (Mebimpy). 2,6-bis(benzimidazol-2-yl)pyridine (bimpy) was synthesized by following a published procedure.[45] Bimpy was used to synthesize Mebimpy by following a published procedure.[46]

Synthesis of dichloropentamethylcyclopentadienyl iridium dimer. $[Cp^*IrCl_2]_2$ was synthesized by following a published procedure.[47]

Synthesis of trichloro(2,6-bis(1-methylbenzimidazol-2-yl)pyridyl)ruthenium(III). [Ru(Mebimpy)Cl_3] was synthesized by following a published procedure.[48]

Synthesis of [(Ru(Mebimpy)Cl)$_2$$Cl_2$]. [Ru(Mebimpy)$Cl_3$] was prepared first, then used to synthesize [((Mebimpy)ClRu)$_2$$Cl_2$], both by following a published procedure.[48]

Synthesis of Ru(tpy)Cl_3. Ru(tpy)Cl_3 was synthesized by following a published procedure.[49]

Synthesis of chloro(η^5-pentamethylcyclopentadienyl)(4-amino-2,2'-bipyridine-N,N')iridium(III) chloride ([Cp*IrCl(4-NH_2-bpy)]Cl , A). A mixture of $[Cp^*IrCl_2]_2$ (60 mg, 0.075 mmol) and 4-amino-2,2'-bipyridine (26 mg, 0.15 mmol) in 5 mL of dimethylformamide (DMF) was stirred at room temperature under argon for 15 h. Half of the solvent was then removed by distillation under vacuum. Addition of diethyl ether (20 mL) resulted in the precipitation of the complex as the chloride salt. The solid was washed with diethyl ether and hexane to give the product. Yield: 50 mg (64 %). ^{1}H NMR ($CDCl_3$):

8.92 (d, 1H), 8.32 (d, 1H), 8.25 (d, 1H), 8.17 (t, 1H), 7.75 (m, 1H), 7.51 (s, 1H), 6.86 (m, 1H), 1.68 (s, 15H). MS (ESI): 534.09 m/Z, expected 534.13 m/Z for $[M]^+$.

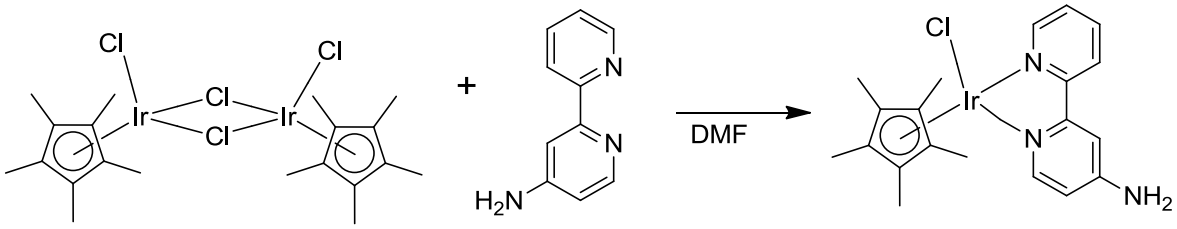

Figure 5.14. Synthesis of **A**.

Synthesis of chloro(η^5-pentamethylcyclopentadienyl)(5-amino-2,2'-bipyridine-N,N')iridium(III) chloride ([Cp*IrCl(5-NH$_2$-bpy)]Cl , B). A mixture of $[Cp^*IrCl_2]_2$ (30 mg, 0.038 mmol) and 4-amino-2,2'-bipyridine (13 mg, 0.075 mmol) in 2.5 mL of dimethylformamide (DMF) was stirred at room temperature under argon for 15 h. Half of the solvent was then removed by distillation under vacuum. Addition of diethyl ether (10 mL) resulted in the precipitation of the complex as the chloride salt. The solid was washed with diethyl ether and hexane to give the product. Yield: 30 mg (71 %). ^{1}H NMR (DMSO-d_6): 8.83 (d, 1H), 8.38 (d, 1H), 8.35 (d, 1H), 8.29 (d, 1H), 8.18 (t, 1H), 7.64 (t, 1H), 7.34 (dd, 1H), 1.67 (s, 15H). MS (ESI): 534.14 m/Z, expected 534.13 m/Z for $[M]^+$.

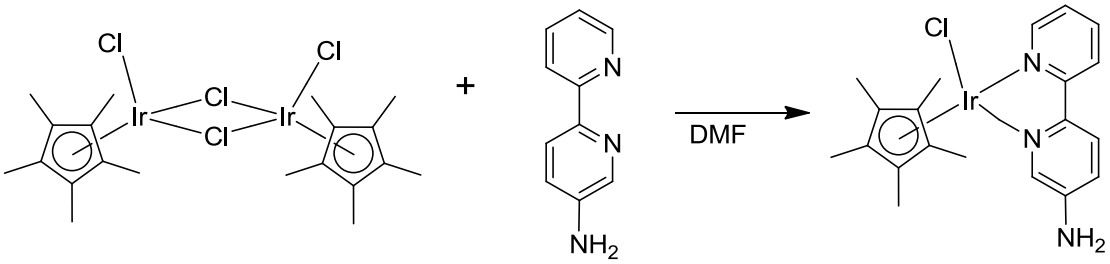

Figure 5.15. Synthesis of **B**.

Synthesis of chloro(η^5-pentamethylcyclopentadienyl)(2-(*p*-aminophenyl)pyridine-C^2,N')iridium(III) ([Cp*IrCl(*p*-NH_2-ppy)], C). A mixture of $[Cp^*IrCl_2]_2$ (100 mg, 0.13 mmol), NaOAc (21 mg, 0.26 mmol), and 2-(*p*-aminophenyl)pyridine (44 mg, 0.26 mmol) in 5 mL of DMF was stirred at room temperature under argon overnight. Half of the solvent was then removed by distillation under vacuum. Addition of diethyl ether (20 mL) resulted in the precipitation of the complex. The solid was washed with diethyl ether and hexane to give the product. Yield: 80 mg (62 %). ^{1}H NMR ($CDCl_3$): 8.55 (d, 1H), 7.57 (d, 1H), 7.50 (t, 1H), 7.45 (d, 1H), 7.08 (s, 1H), 6.87 (t, 1H), 6.35 (d, 1H), 1.65 (s, 15H). MS (ESI): 497.15 m/Z, expected 497.16 m/Z for $[M\text{-}Cl]^+$.

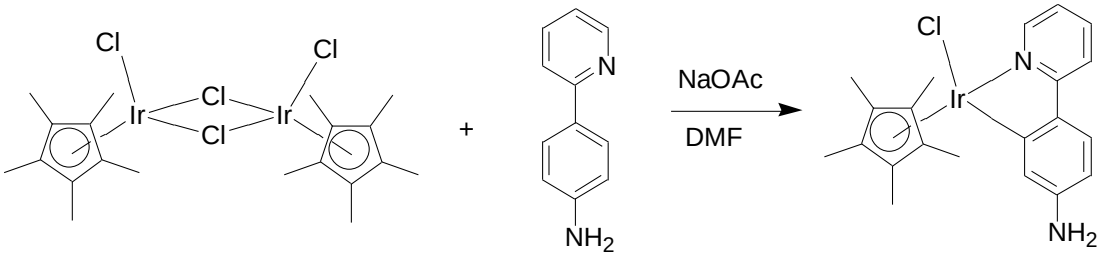

Figure 5.16. Synthesis of **C**.

Synthesis of triflato(2,6-bis(1-methylbenzimidazol-2-yl)pyridyl)(4-amino-2,2'-bipyridine-N,N')ruthenium(II) triflate ([Ru(Mebimpy)(4-NH_2-bpy)OTf]OTf, D). [Ru(Mebimpy)(4-NH_2-bpy)Cl]Cl was synthesized first, then converted into **D**. $[((Mebimpy)ClRu)_2Cl_2]$ (100mg, 0.098 mmol) and 4-amino-2,2'-bipyridine (34 mg, 0.196 mmol) were suspended in 15 mL 2:1 EtOH:H_2O, and the mixture was degassed by nitrogen bubbling. The suspension was heated at reflux for 4 h, and 5 mL 20% aqueous LiCl solution was added. The solution was allowed to cool overnight. The brown microcrystalline solid formed was then isolated by filtration and washed with water and ether. Yield: 80 mg (60%). The resultant [Ru(Mebimpy)(4-NH_2-bpy)Cl]Cl complexes were a pair of stereo-isomers (**D'**-

1:**D'-2** = 4:5). See the ^{1}H NMR and ^{1}H-^{1}H COSY NMR (MeOD) spectra below. MS (ESI): 647.05 m/Z, expected 647.11 m/Z for $[M]^{+}$.

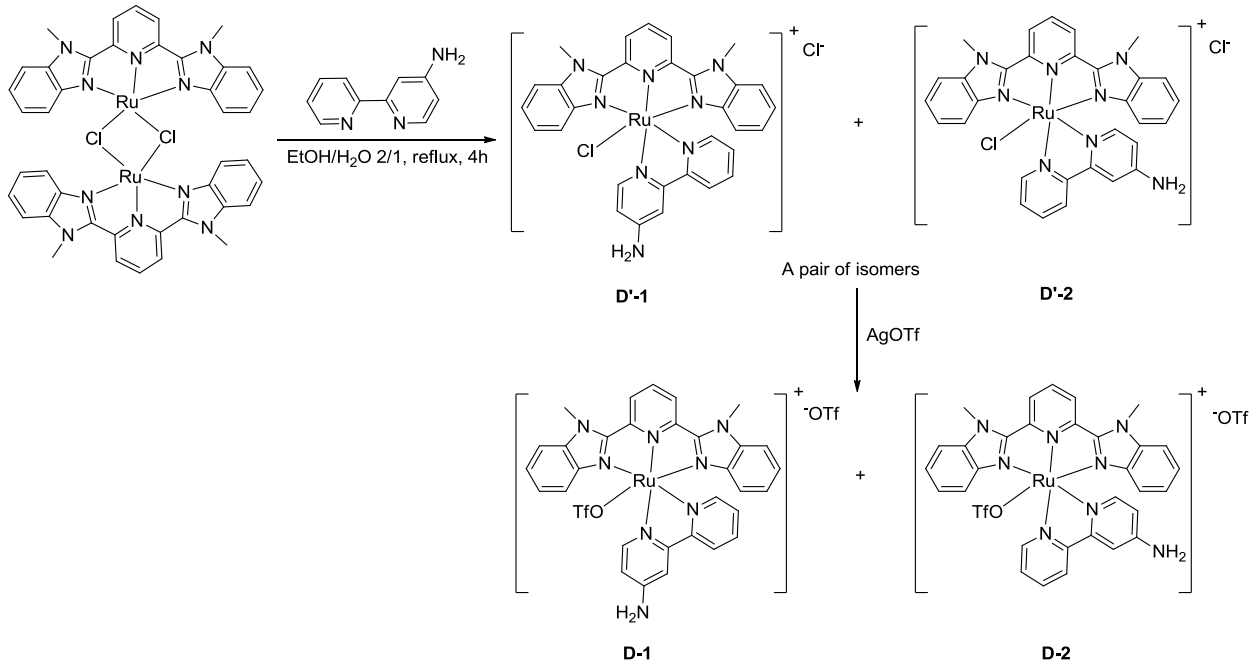

Figure 5.17. Synthesis of **D'**.

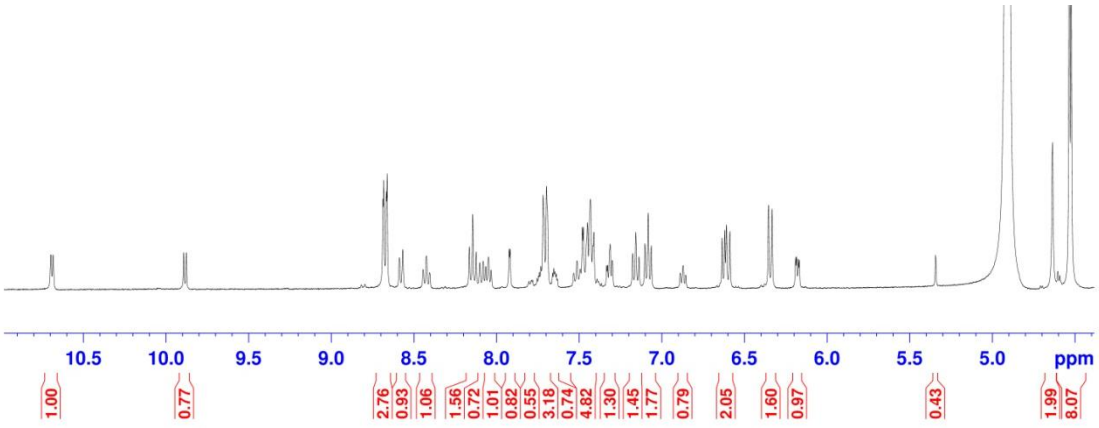

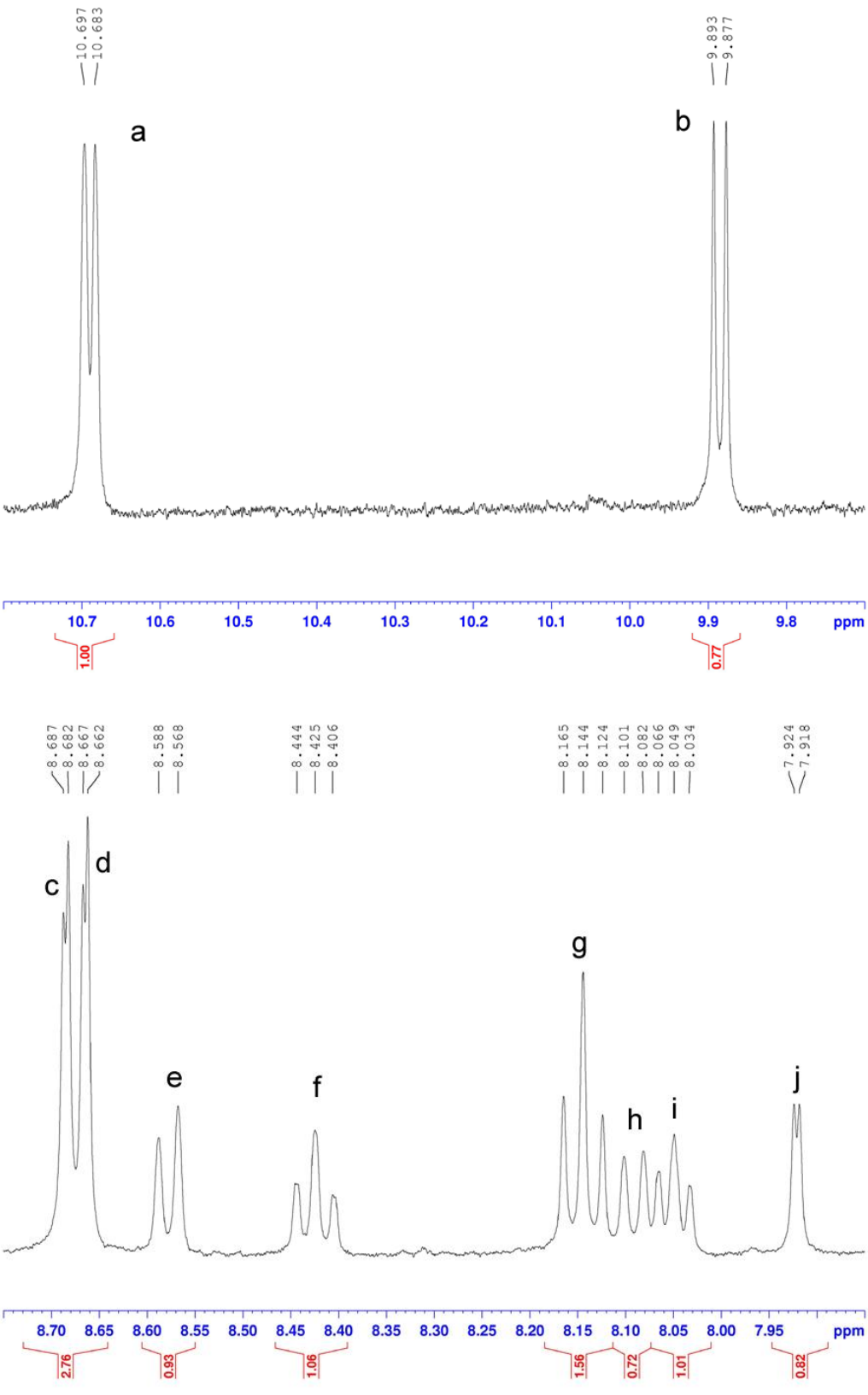
10.697
10.683
9.893
9.877
a
b
10.7
10.6
10.5
10.4
10.3
10.2
10.1
10.0
9.9
9.8
ppm
1.00
0.77
8.687
8.682
8.667
8.662
8.588
8.568
8.444
8.425
8.406
8.165
8.144
8.124
8.101
8.082
8.066
8.049
8.034
7.924
7.918
c
d
e
f
g
h
i
j
8.70
8.65
8.60
8.55
8.50
8.45
8.40
8.35
8.30
8.25
8.20
8.15
8.10
8.05
8.00
7.95
ppm
2.76
0.93
1.06
1.56
0.72
1.01
0.82

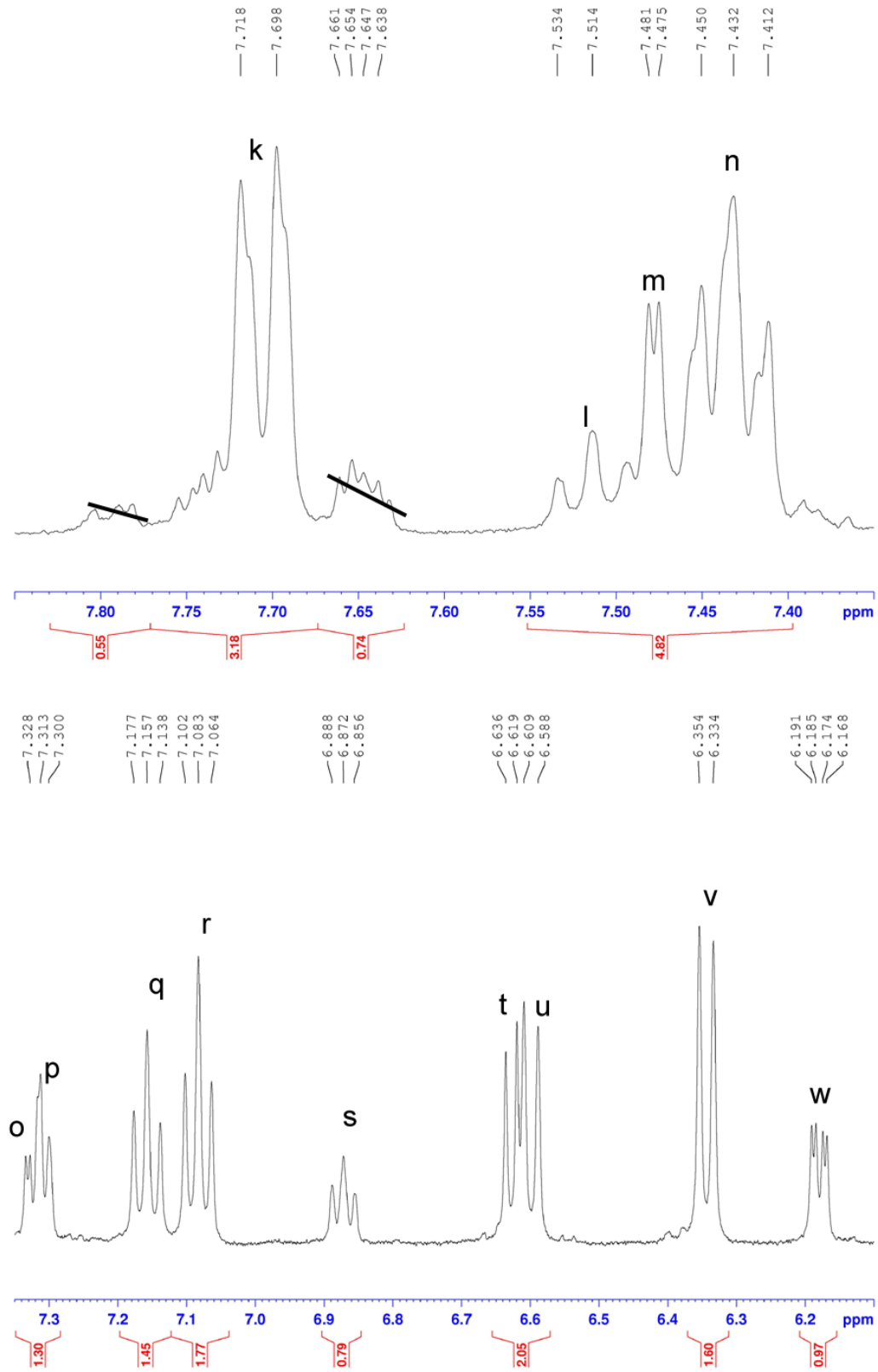
7.718
7.698
7.661
7.654
7.647
7.638
7.534
7.514
7.481
7.475
7.450
7.432
7.412
k
l
m
n
7.80
7.75
7.70
7.65
7.60
7.55
7.50
7.45
7.40
ppm
0.55
3.18
0.74
4.82
7.328
7.313
7.300
7.177
7.157
7.138
7.102
7.083
7.064
6.888
6.872
6.856
6.636
6.619
6.609
6.588
6.354
6.334
6.191
6.185
6.174
6.168
o
p
q
r
s
t
u
v
w
7.3
7.2
7.1
7.0
6.9
6.8
6.7
6.6
6.5
6.4
6.3
6.2
ppm
1.30
1.45
1.77
0.79
2.05
1.60
0.97

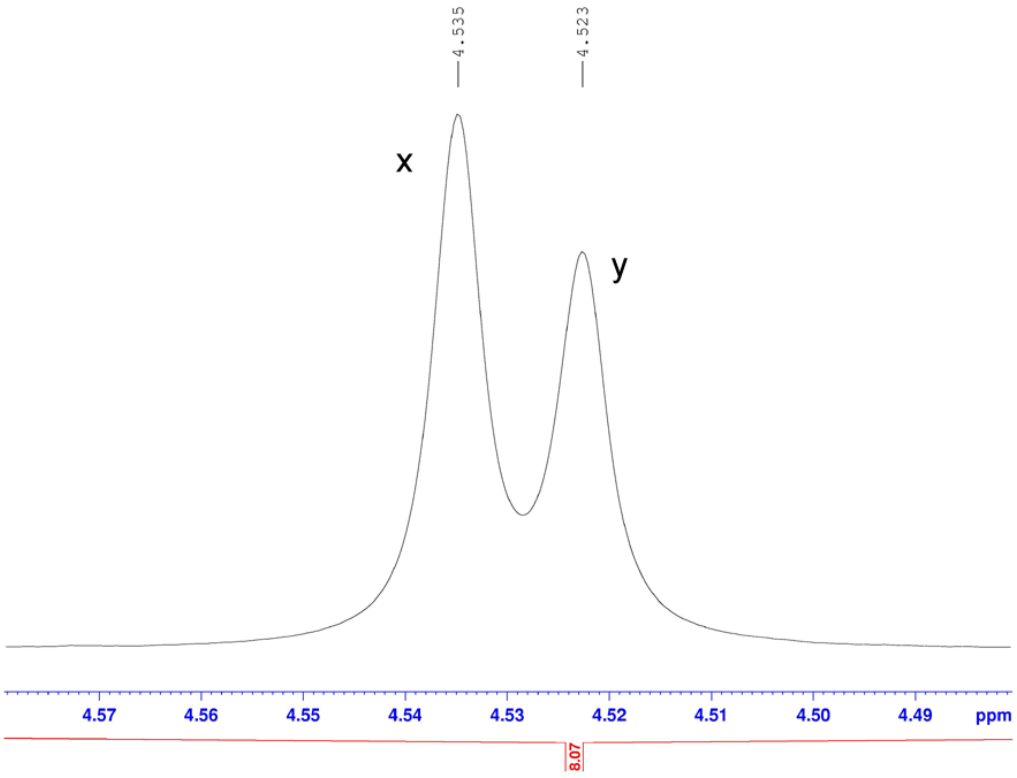

Figure 5.18. ^{1}H-NMR spectrum of **D'**.

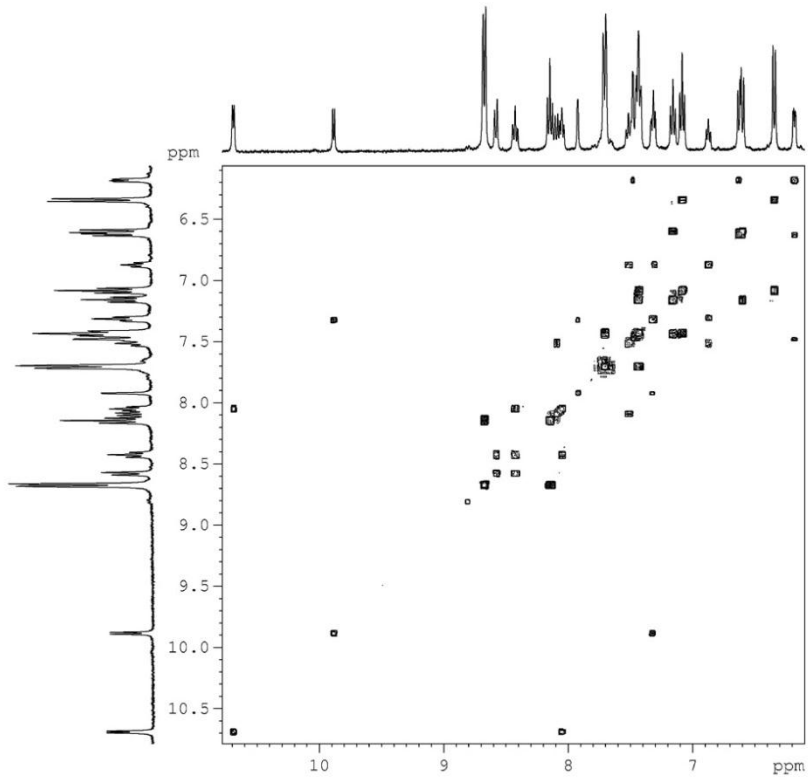

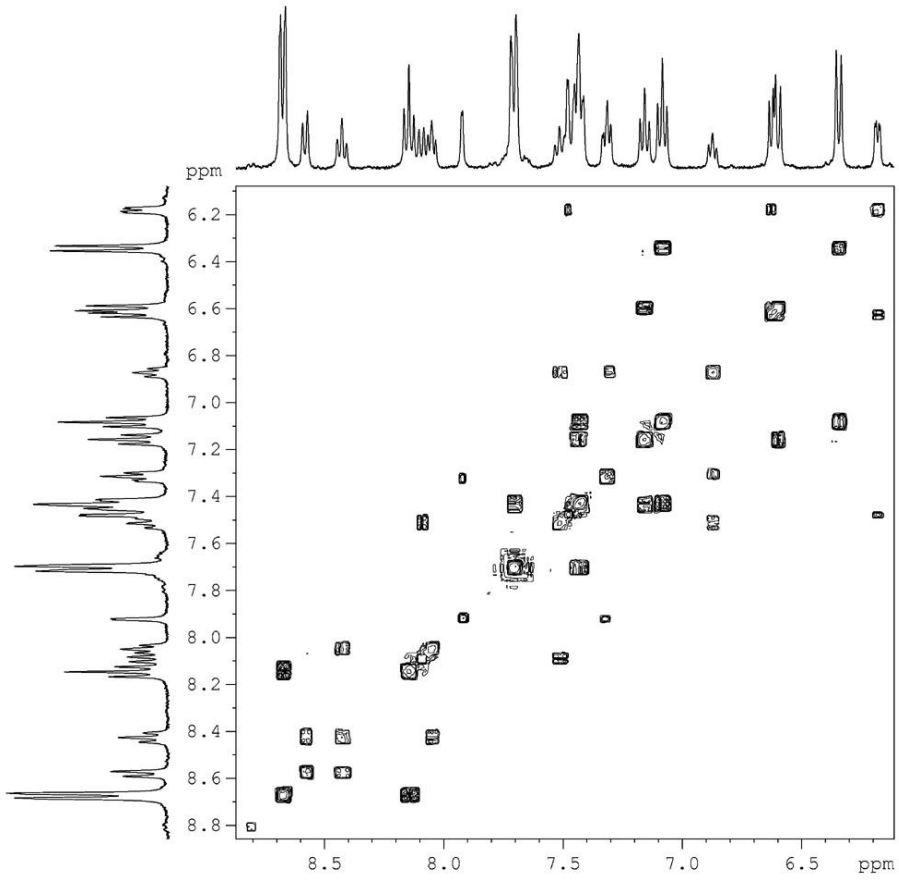

Figure 5.19. ^{1}H-^{1}H COSY NMR spectrum of **D'**.

Summary of COSY NMR correlations (cross peaks): a–i , b–o , c/d–g , e–f , f–i , h–l , j–o , k–n , l–s , m–w , n–q , n–r , p–s , q–u , r–v , t–w

These correlations give seven separate sets of coupled protons (all aromatic): a-i-f-e, w-t-m, b-o-j, h-l-s-p, k-n-q-u, k-n-r-v, c/d-g

By combining the information of coupled protons with the chemical shifts of these protons, as well as the peak integration, all of the peaks were assigned.

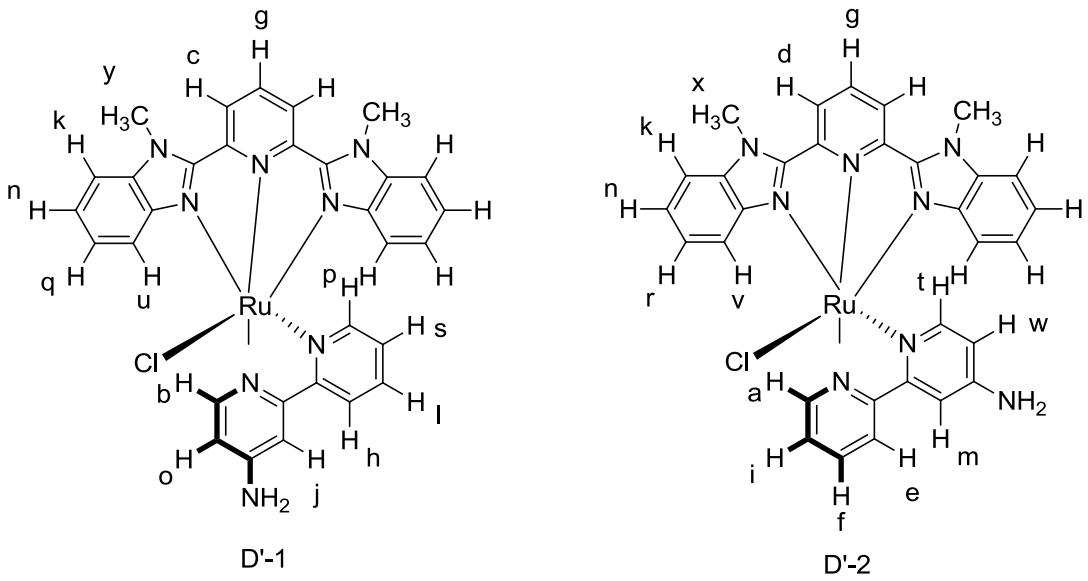

Figure 5.20. Assignment of peaks in the ^{1}H NMR spectrum for **D'**.

D was prepared from **D'** by a procedure published for [Ru(Mebimpy)(bpy)OTf]OTf.[48] [Ru(Mebimpy)(4-NH_2-bpy)Cl]Cl (1 eq.) and AgOTf (2.1 eq; OTf = triflate anion) were dissolved in methanol and stirred under nitrogen at room temperature overnight. The silver chloride was then removed by filtration. Two drops of triethylamine was added to the filtrate and the solution was slightly heated to precipitate the excess Ag^{+}. The cloudy solution was filtered through Celite and taken to dryness by rotary evaporation. Diethyl ether was added and the solid was filtered, washed with ether, and air-dried. The resultant complexes were also a pair of isomers (**D-1**:**D-2** = 4:5). See the ^{1}H NMR spectrum (MeOD) of the mixture below. MS (ESI): 761.0 m/Z, expected 760.08 m/Z for $[M]^{+}$.

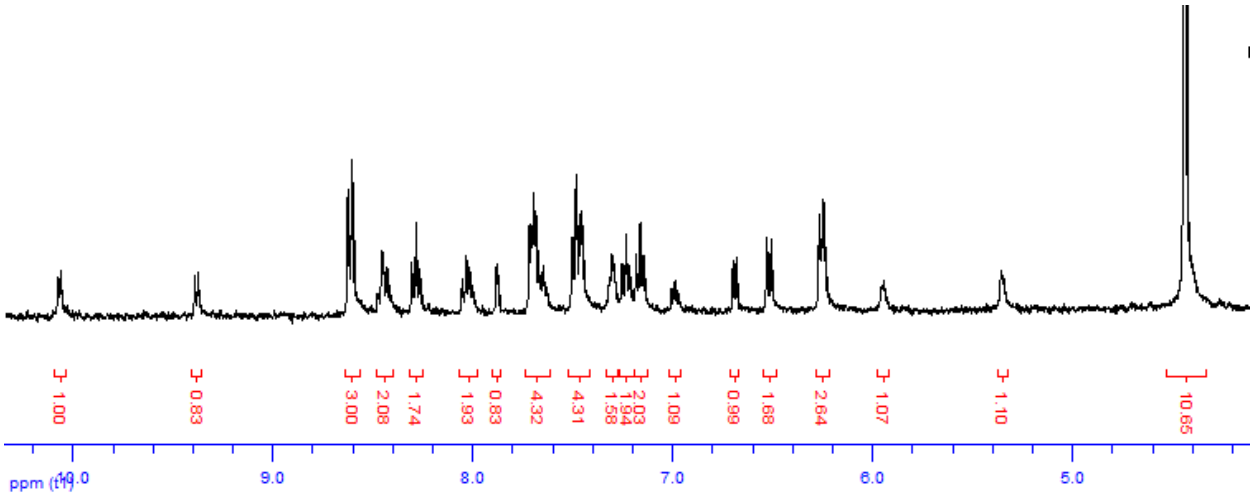

Figure 5.21. ^{1}H-NMR spectrum of **D**.

Synthesis of chloro(2,6-bis(2-pyridyl)pyridine)(4-amino-2,2'-bipyridine-N,N')ruthenium(II) chloride ([Ru(tpy)(4-NH$_2$-bpy)Cl]Cl, E). **E** was synthesized by a modification of a procedure published for [Ru(tpy)(bpy)Cl]Cl.[49] A 1.00 g quantity of Ru(tpy)Cl$_3$ (2.27 mmol) and 0.39 g (2.27 mmol) of 4-amino-2,2'-bipyridine were heated at reflux for 4 h in 400 mL of 75% EtOH/25% H_2O containing 0.2g (~25 mmol) of LiCl and 1 mL of triethylamine as a reductant. After hot filtration, the solution volume was reduced to ~100 mL under rotary evaporation. The pot contents were then chilled in a refrigerator for 24 h. The solid was collected by filtration and was washed with 30 mL of acetone and 200 mL of anhydrous ether, then air-dried. The resultant compounds are a pair of stereo-isomers. The solids have been recrystallized in hexane/chloroform several times in an effort to enrich one of the isomers. The final product contains the isomers in a 2:1 ratio of **E-1** and **E-2**, based on integration of ^{1}H NMR (MeOD) peaks (see below). ^{1}H-^{1}H COSY NMR and ^{1}H-^{1}H NOESY NMR spectra are also shown below. MS (ESI): 541.1 m/Z, expected 541.05 m/Z for $[M]^{+}$. The structure of the complex was further confirmed by single crystal X-ray diffraction on one of the stereo-isomers (**E-2**).

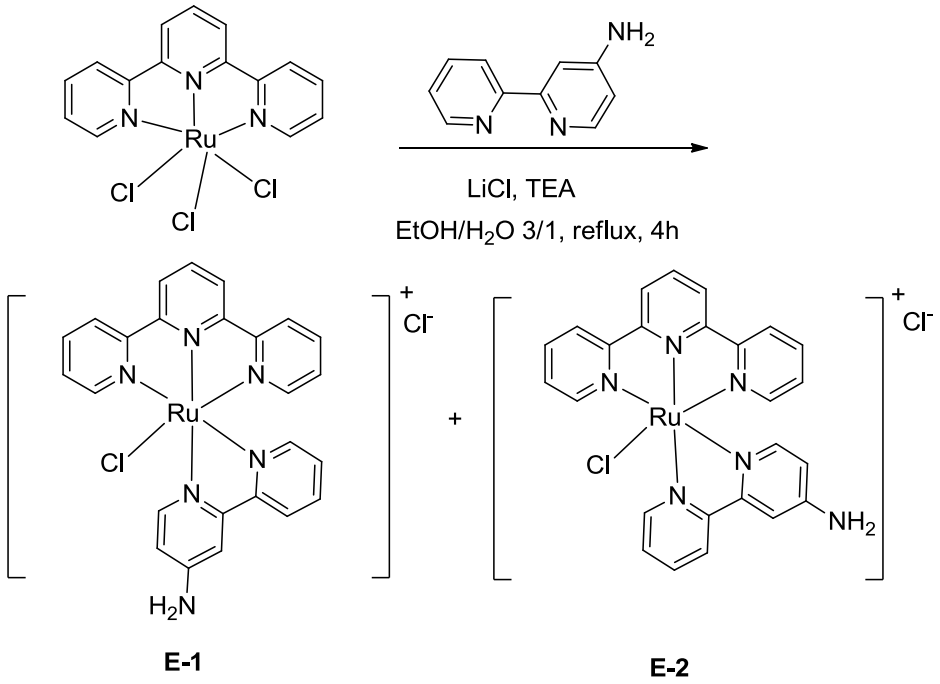

Figure 5.22. Synthesis of **E**.

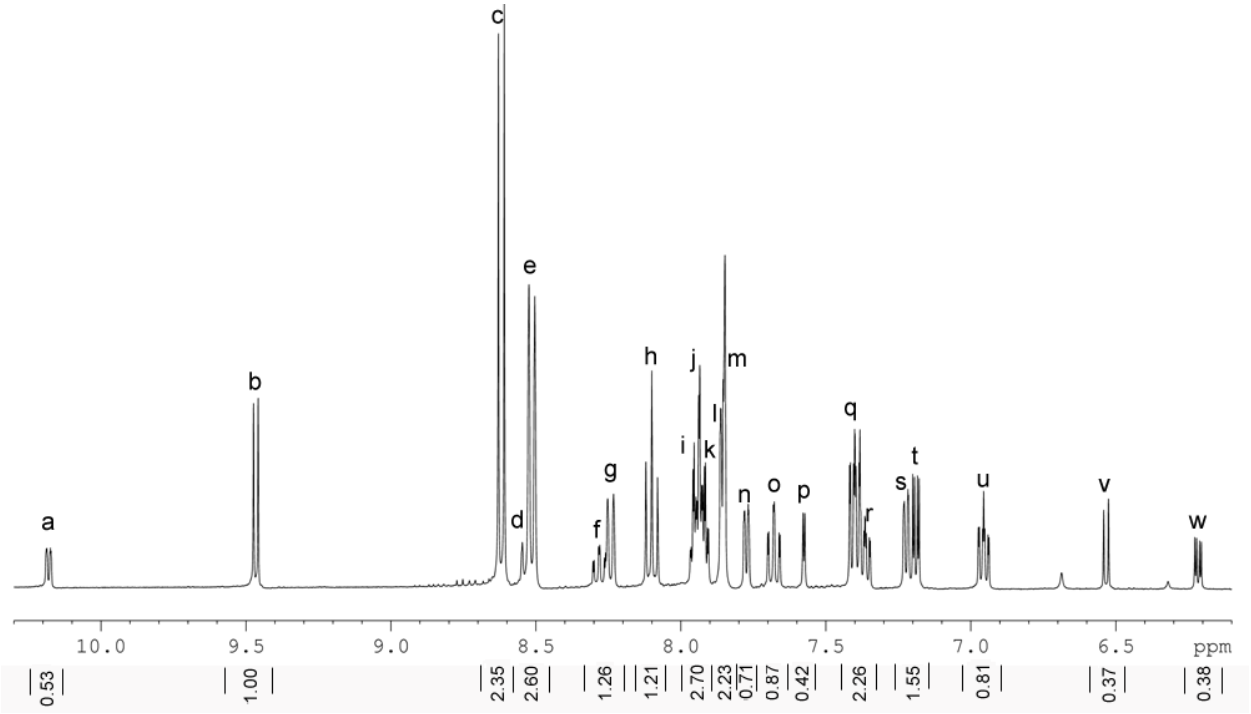

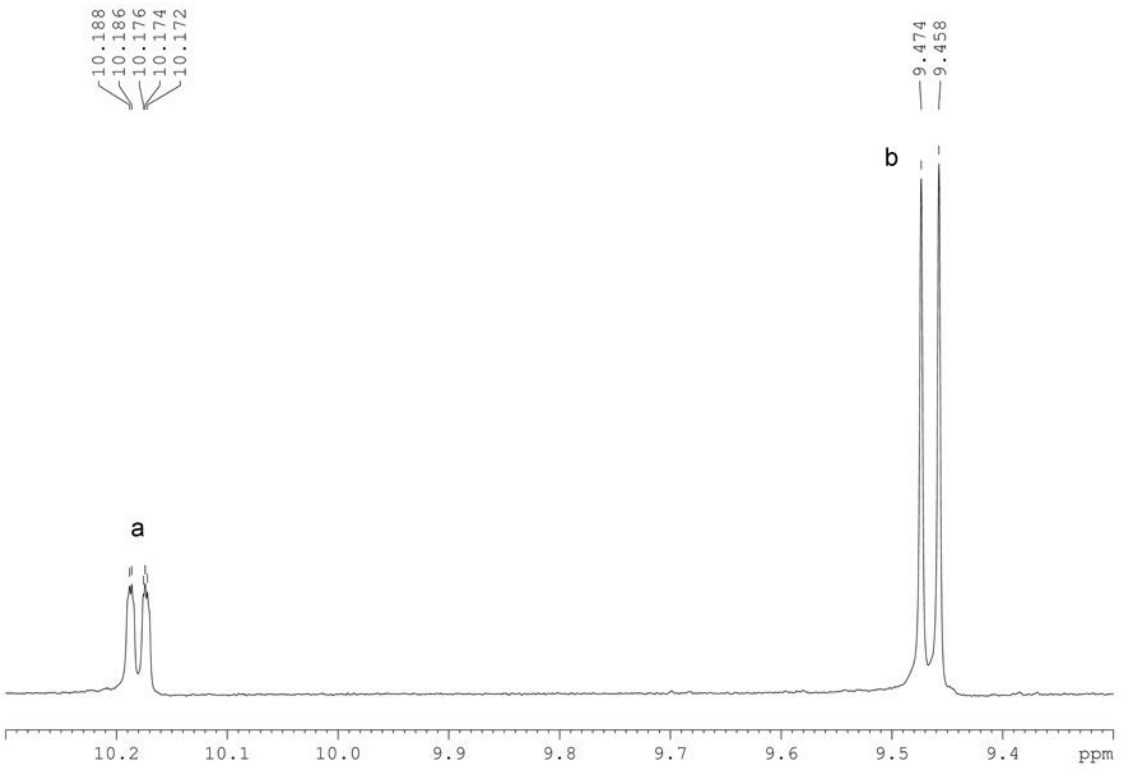
10.188
10.186
10.176
10.174
10.172
9.474
9.458
a
b
10.2
10.1
10.0
9.9
9.8
9.7
9.6
9.5
9.4
ppm

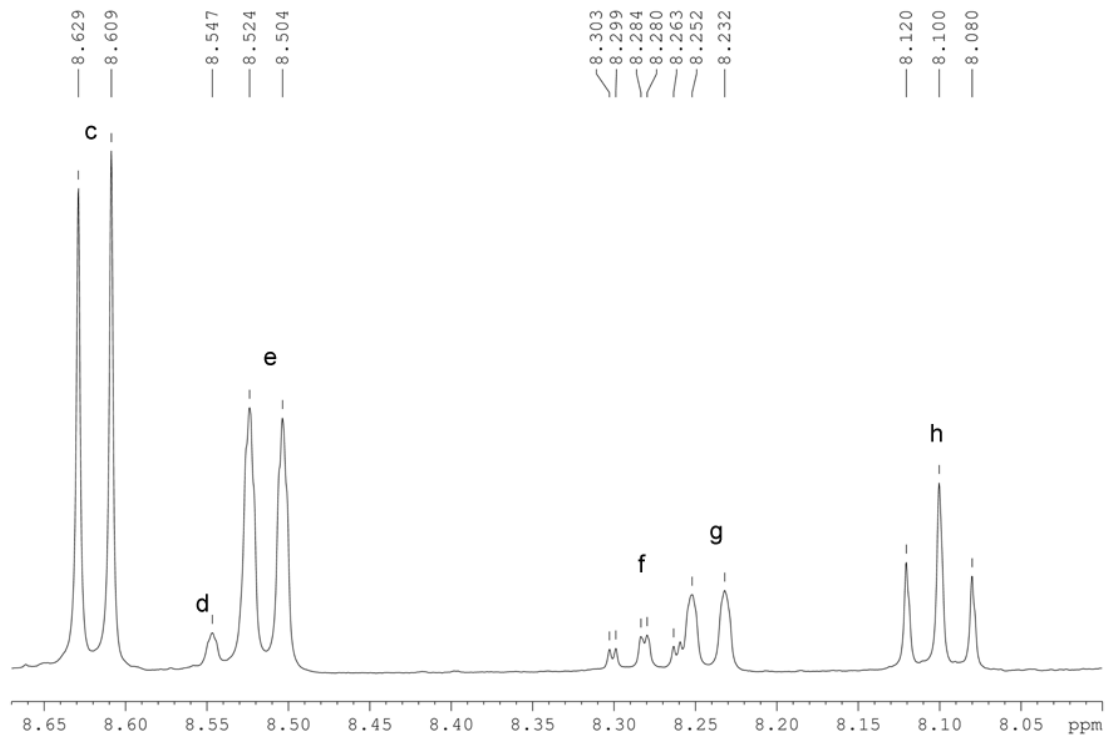
8.629
8.609
8.547
8.524
8.504
8.303
8.299
8.284
8.280
8.263
8.252
8.232
8.120
8.100
8.080
c
d
e
f
g
h
8.65
8.60
8.55
8.50
8.45
8.40
8.35
8.30
8.25
8.20
8.15
8.10
8.05
ppm

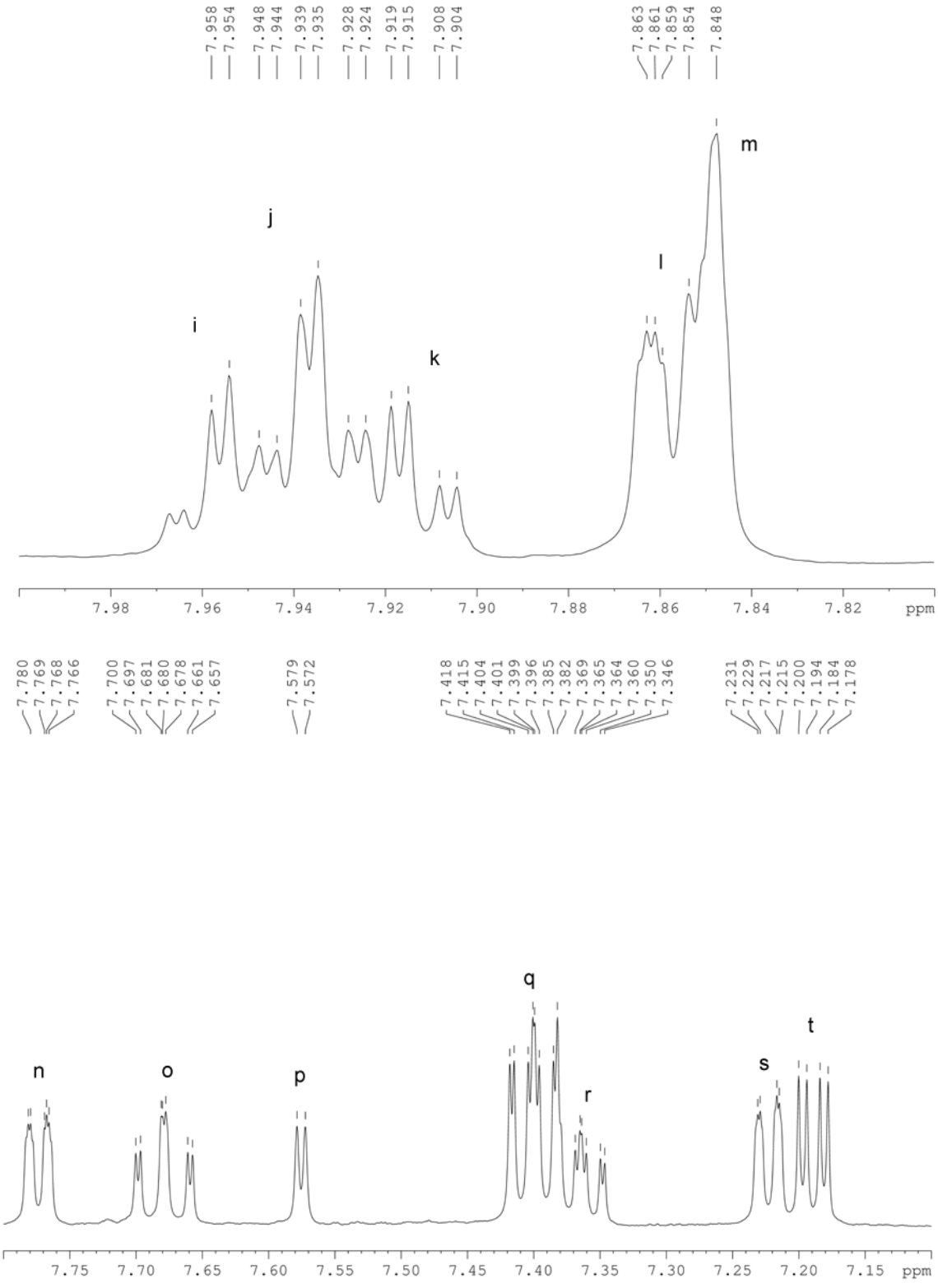
7.958
7.954
7.948
7.944
7.939
7.935
7.928
7.924
7.919
7.915
7.908
7.904
7.863
7.861
7.859
7.854
7.848
i
j
k
l
m
7.98
7.96
7.94
7.92
7.90
7.88
7.86
7.84
7.82
ppm
7.780
7.769
7.768
7.766
7.700
7.697
7.681
7.680
7.678
7.661
7.657
7.579
7.572
7.418
7.415
7.404
7.401
7.399
7.396
7.385
7.382
7.369
7.365
7.364
7.360
7.350
7.346
7.231
7.229
7.217
7.215
7.200
7.194
7.184
7.178
n
o
p
q
r
s
t
7.75
7.70
7.65
7.60
7.55
7.50
7.45
7.40
7.35
7.30
7.25
7.20
7.15
ppm

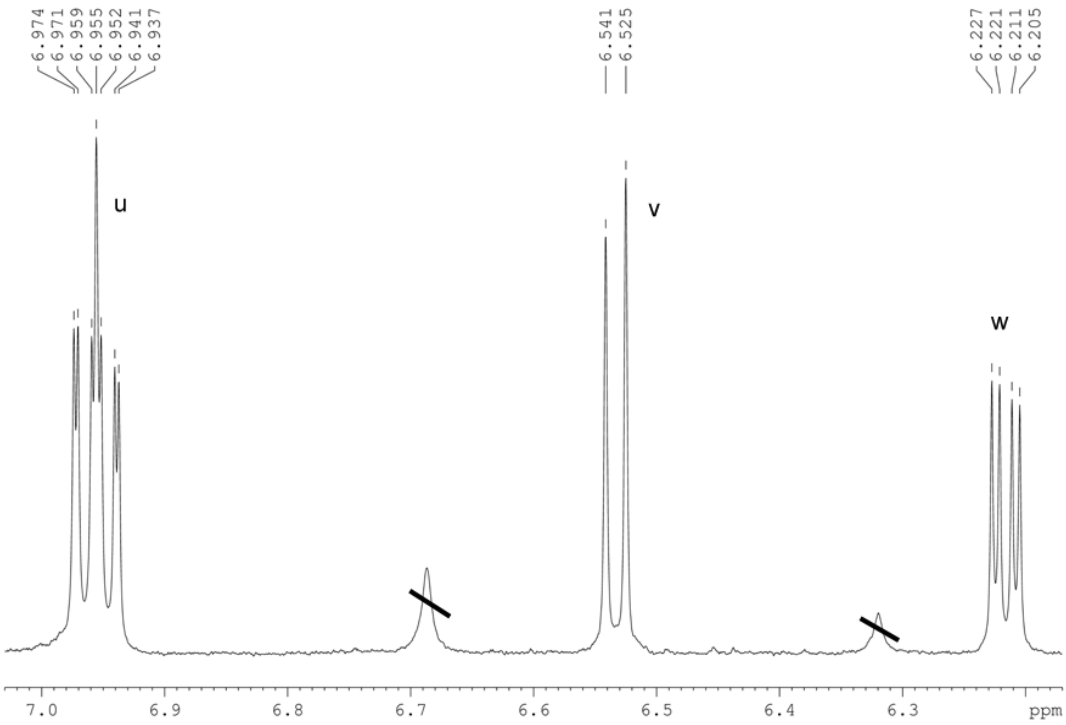

Figure 5.23. ^{1}H-NMR spectrum of **E**.

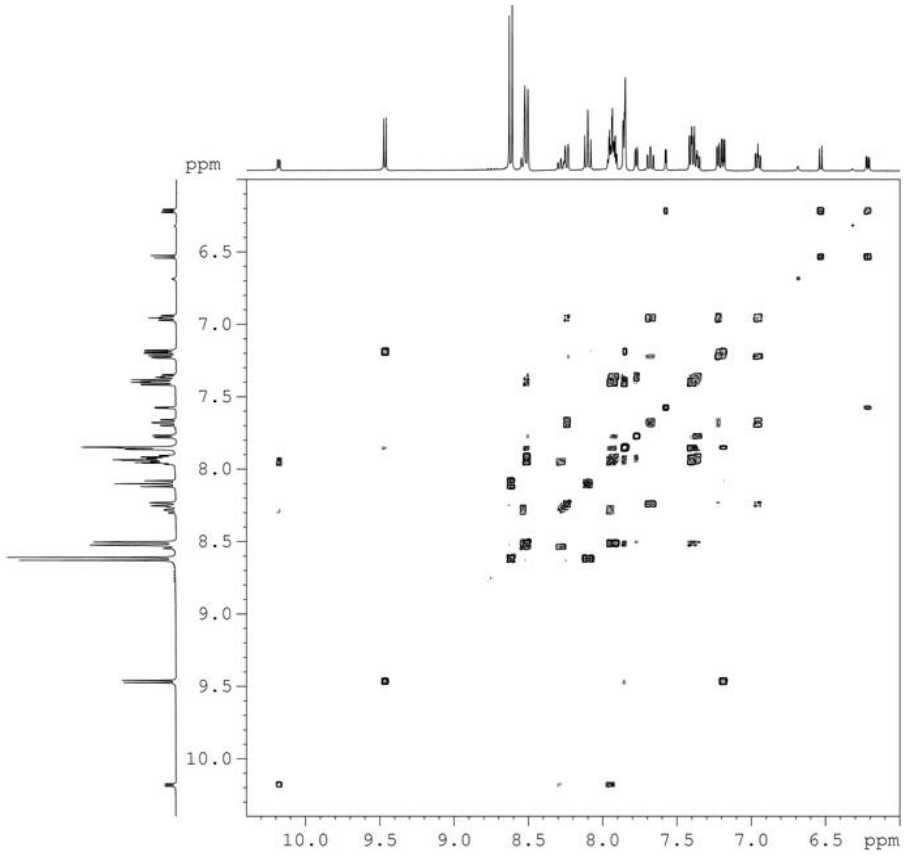

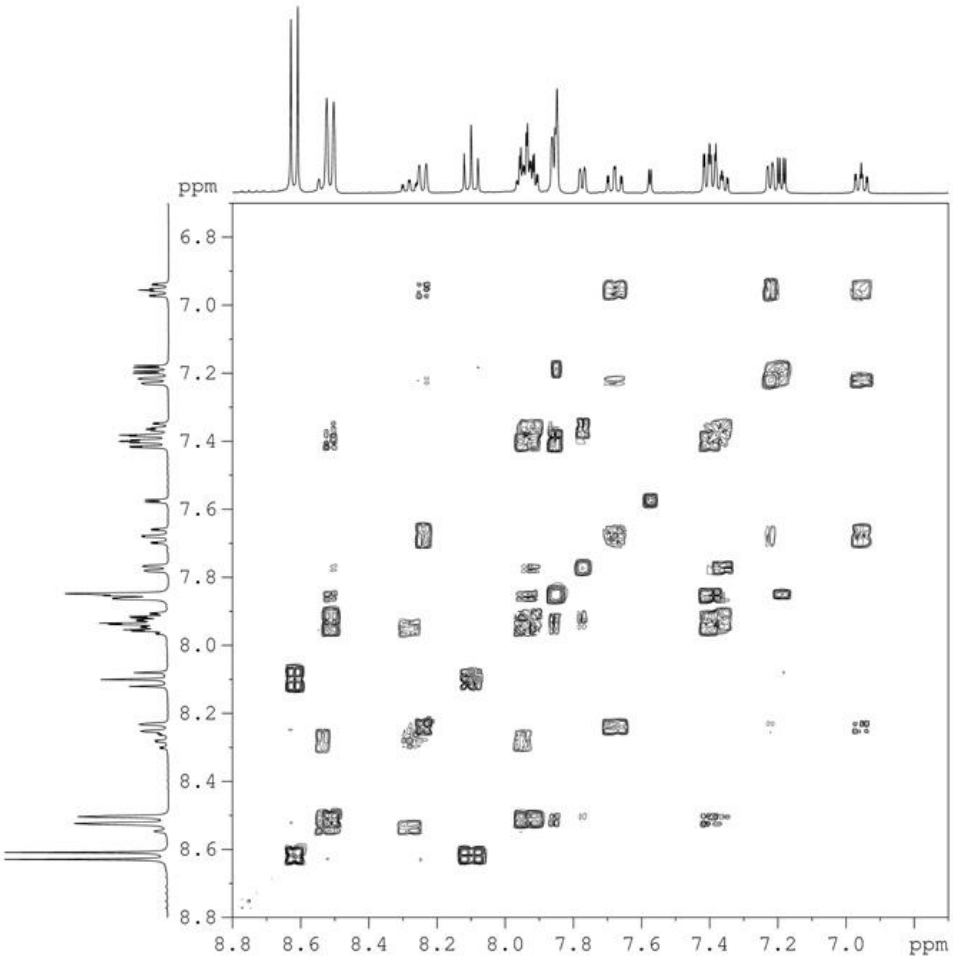

Figure 5.24. ^{1}H-^{1}H COSY NMR spectrum of **E**.

Summary of COSY NMR correlations (cross peaks): a–i (strong), a–f (weak), b–t (strong), b–m (weak), c–h (strong), d–f (strong), e–k (strong), e–r (weak), f–i (strong), g–o (strong), j–q (strong), j–l (weak), k–r (strong), l–q (strong), m–t (strong), n–r (strong), o–u (strong), p–w (weak), s–u (strong), v–w (strong)

These correlations give seven separate sets of coupled protons (all aromatic): a-i-f-d, v-w-p, b-t-m, s-u-o-g, e-j-q-l, e-k-r-n, h-c

By combining the information of coupled protons with the chemical shifts of these protons, as well as the peak integration, all peaks were assigned. One feature of the complex structure

is that the s and v protons are inside the shielding region of the aromatic ring current of the tpy ligand. As a result, the ^{1}H-NMR chemical shifts of these protons are in the high field region.

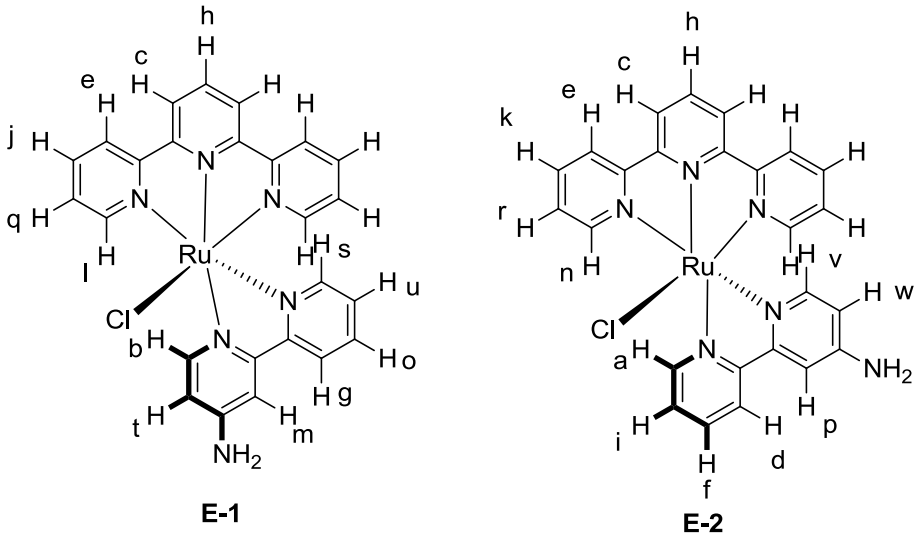

Figure 5.25. Assignment of peaks in the 1H-NMR spectrum of **E**.

The peak assignment was further confirmed by the ^{1}H-^{1}H NOESY NMR spectrum. The additional cross peaks between protons s and l, s and q, and u and q result from through-space interactions between these protons in close proximity.

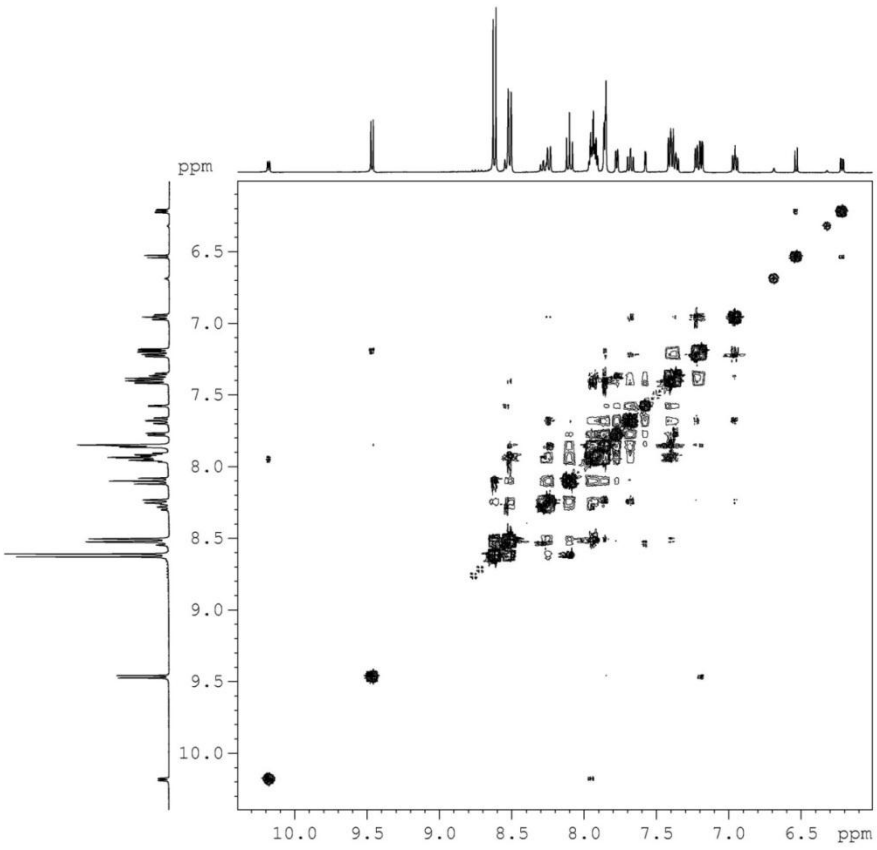
ppm
6.5
7.0
7.5
8.0
8.5
9.0
9.5
10.0
10.0 9.5 9.0 8.5 8.0 7.5 7.0 6.5 ppm

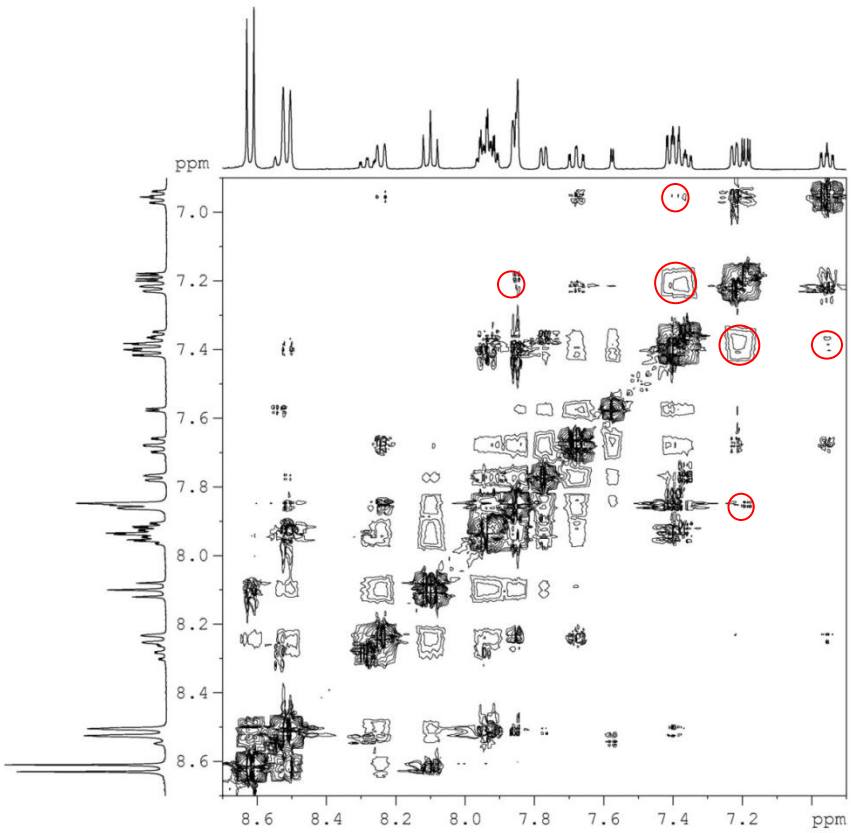
ppm
7.0
7.2
7.4
7.6
7.8
8.0
8.2
8.4
8.6
8.6 8.4 8.2 8.0 7.8 7.6 7.4 7.2 ppm

Figure 5.26. ^{1}H-^{1}H NOESY NMR spectrum of **E**.

Table 5.2. Crystal data and structure refinements for **E-2**.

Empirical formula	$C_{27}H_{20}Cl_7N_7O_3Ru$
Formula weight	839.72
Temperature (K)	100
Wavelength (Å)	1.54178
Crystal system	Monoclinic
Space group	$P2_1/c$
Unit cell dimensions	a = 8.4872(2)
	b = 20.0430(6)
	c = 19.7656(5)
	α = 90
	β = 97.157(2)
	γ = 90
Volume ($Å^3$)	3336.11(15)
Z	4
Density (calcd. g/cm^3)	1.672
Absorption coeff. (mm^{-1})	9.321
F(000)	1672
Crystal size (mm)	0.81×0.06×0.06
Crystal color & shape	Purple, block
θ range data collection	3.15 – 56.47
Limiting indices	$-8 < h < 7$
	$-19 < k < 21$
	$-21 < l < 18$
Reflections collected	8706
Independent reflections	4196
R(int)	0.0491
Data/restraints/parameters	4196/1/381

Goodness-of-fit on F^2	1.127
Final R indices [I>2σ(I)]	R1 = 0.1099
	wR2 = 0.2660
R indices (all data)	R1 = 0.1258
	wR2 = 0.2760

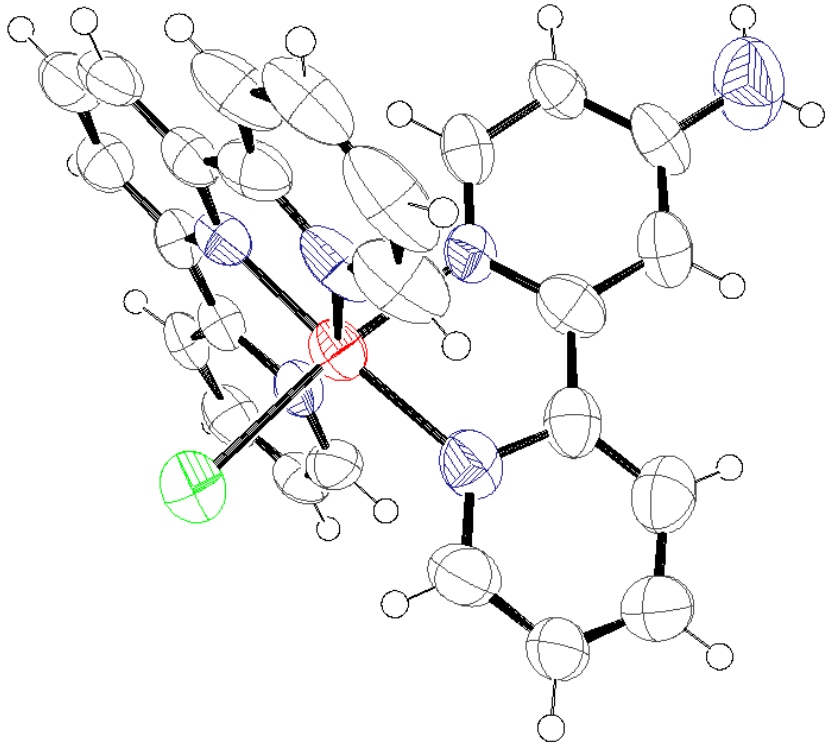

Figure 5.27. Structure of **E-2** as determined by single-crystal X-ray diffraction.

5.4.3. Functionalization of electrodes

This procedure is a modification of a published procedure.[50] Planar glassy carbon electrodes were grafted with complexes **A**-**E** to produce functionalized electrodes **1**-**5**, respectively. A solution of the complex was prepared by dissolving 1.35 mg of **A**, 1.35 mg of **B**, 1.26 mg of **C**, 2.16 mg of **D**, or 1.40 mg of **E** (2.38 µmol) in 1.46 mL of H_2O. Then 15.5 µL (188 µmol) of concentrated HCl was added to the solution. After cooling to 0 °C, a

solution of 0.328 mg (4.75 μmol) $NaNO_2$ in 164 μL cold water was added dropwise to the solution containing the complex. The solution was kept at 0 °C with stirring for 1 h to allow for a complete reaction, as indicated by a color change. A solution of 0.522 mg (4.75 μmol) $NaBF_4$ in 261 μL cold water was added to the solution to stabilize the diazonium salt. This final solution was purged with Ar and used to perform diazonium grafting of the complex onto glassy carbon by applying a potential of -0.4 V vs NHE for 4 min. The functionalized area of the glassy carbon was circular with a diameter of 12 mm. The electrode was rinsed thoroughly with methanol and water before using.

5.4.4. Elimination of background

For **1**-**5**, the first scan right after grafting shows a large increase in peak current compared to the background scan taken before grafting. The peak current decreases during several subsequent scans, eventually stabilizing at a current significantly higher than the background. Some of the current from the first few scans can be attributed to changes to the electrode during the electroreduction process. Control experiments were carried out by performing electroreduction with a blank solution that was otherwise identical to a catalyst solution, and then performing CV on the electrode. The first scan done after the electroreduction process had significantly higher current than the scan taken before electroreduction. After about five scans, the current stabilizes at a level only slightly elevated (<10%) over the background scan obtained before electroreduction. The average peak current (at 1.6 V) obtained by this method over three runs was 93±6 $\mu A/cm^2$. This background current has been subtracted from the catalytic currents for **1**-**5** for calculations of catalytic activities. Some of the initial current enhancement after grafting is likely attributable to catalyst that is physisorbed to the electrode. ICP-MS reveals a large drop in catalyst loading

between a grafted electrode that has only been rinsed and one that has undergone several scans to remove physisorbed catalyst. CV currents were stabilized by performing ten CV scans after grafting.

5.4.5. Oxygen detection

Oxygen was detected in solution during 60 min of controlled potential electrolysis at 1.6 V, and for 100 min afterward, with a bare glassy carbon electrode, **1**, and 0.1 mM IrO_2 solution. Oxygen was also measured over the same period without electrolysis to demonstrate that the oxygen detected is due to catalytic activity, not a leak. All experiments were done in buffer at pH 5. The current during electrolysis, corresponding to total charges passed of 67.8 mC for the blank electrode, 182 mC for **1**, and 204 mC for IrO_2. Both of the blanks (with and without) electrolysis showed a small increase of 0.05 ppm in dissolved oxygen over 160 min. For the blank without electrolysis, the increase could either be due to a small leak of air into the system or instrument fluctuation. Since the blank with electrolysis shows the same increase, it appears that bare glassy carbon does not produce any O_2. After subtracting background, if 100% of the charge passed during electrolysis went toward O_2 formation, the dissolved oxygen concentrations would be 1.57 ppm for **1** and 1.88 ppm for IrO_2. The actual oxygen concentrations at the final data points are 0.42 ppm for **1** and 0.52 ppm for IrO_2, after subtracting background. This results in 27% Faradaic efficiency in both cases. Since IrO_2 is known to produce O_2 from H_2O with 100% efficiency, the grafted catalyst in **1** must also be operating at close to 100% efficiency. Several experimental difficulties result in the observed efficiency being much lower than 100%. Bubble formation on the working electrode is observed during electrolysis, which is likely responsible for the delayed response in detecting oxygen. The dissolution of bubbles into solution appears to

account for the quick increases in oxygen concentration, while the decreases can be attributed to diffusion of O_2 into the headspace of the reaction vessel, where the concentration is too low to be detected. The equilibrium between oxygen in the bubbles, solution, and headspace complicates the detection of oxygen in solution. However, the oxygen that is detected for **1** can be considered to correspond to 100% Faradaic efficiency by comparison with the oxygen detected during water oxidation with IrO_2.

5.5. References

(1) Lewis, N. S.; Nocera, D. G. *P. Natl. Acad. Sci. USA* **2006**, *103*, 15729.

(2) Turner, J. A. *Science* **2004**, *305*, 972.

(3) Eisenberg, R.; Gray, H. B. *Inorg. Chem.* **2008**, *47*, 1697.

(4) Concepcion, J. J.; Jurss, J. W.; Brennaman, M. K.; Hoertz, P. G.; Patrocinio, A. D. T.; Iha, N. Y. M.; Templeton, J. L.; Meyer, T. J. *Acc. Chem. Res.* **2009**, *42*, 1954.

(5) Gust, D.; Moore, T. A.; Moore, A. L. *Acc. Chem. Res.* **2009**, *42*, 1890.

(6) Gersten, S. W.; Samuels, G. J.; Meyer, T. J. *J. Am. Chem. Soc.* **1982**, *104*, 4029.

(7) Duan, L.; Fischer, A.; Xu, Y.; Sun, L. *J. Am. Chem. Soc.* **2009**, *131*, 10397.

(8) Gong, K.; Du, F.; Xia, Z.; Durstock, M.; Dai, L. *Science* **2009**, *323*, 760.

(9) McDaniel, N. D.; Coughlin, F. J.; Tinker, L. L.; Bernhard, S. *J. Am. Chem. Soc.* **2008**, *130*, 210.

(10) Hull, J. F.; Balcells, D.; Blakemore, J. D.; Incarvito, C. D.; Eisenstein, O.; Brudvig, G. W.; Crabtree, R. H. *J. Am. Chem. Soc.* **2009**, *131*, 8730.

(11) Blakemore, J. D.; Schley, N. D.; Balcells, D.; Hull, J. F.; Olack, G. W.; Incarvito, C. D.; Eisenstein, O.; Brudvig, G. W.; Crabtree, R. H. *J. Am. Chem. Soc.* **2010**, *132*, 16017.

(12) Ellis, W. C.; McDaniel, N. D.; Bernhard, S.; Collins, T. J. *J. Am. Chem. Soc.* **2010**, *132*, 10990.

(13) Fillol, J. L.; Codolá, Z.; Garcia-Bosch, I.; Gómez, L.; Pla, J. J.; Costas, M. *Nat. Chem.* **2011**, *3*, 807.

(14) Geletii, Y. V.; Huang, Z.; Hou, Y.; Musaev, D. G.; Lian, T.; Hill, C. L. *J. Am. Chem. Soc.* **2009**, *131*, 7522.

(15) Yin, Q.; Tan, J. M.; Besson, C.; Geletii, Y. V.; Musaev, D. G.; Kuznetsov, A. E.; Luo, Z.; Hardcastle, K. I.; Hill, C. L. *Science* **2010**, *328*, 342.

(16) Murakami, M.; Hong, D.; Suenobu, T.; Yamaguchi, S.; Ogura, T.; Fukuzumi, S. *J. Am. Chem. Soc.* **2011**, *133*, 11605.

(17) Kanan, M. W.; Nocera, D. G. *Science* **2008**, *321*, 1072.

(18) Kanan, M. W.; Surendranath, Y.; Nocera, D. G. *Chem. Soc. Rev.* **2009**, *38*, 109.

(19) Jiao, F.; Frei, H. *Angew. Chem. Int. Ed.* **2009**, *48*, 1841.

(20) Yagi, M.; Tomita, E.; Sakita, S.; Kuwabara, T.; Nagai, K. *J. Phys. Chem. B* **2005**, *109*, 21489.

(21) Nakagawa, T.; Bjorge, N. S.; Murray, R. W. *J. Am. Chem. Soc.* **2009**, *131*, 15578.

(22) Youngblood, W. J.; Lee, S.-H. A.; Kobayashi, Y.; Hernandez-Pagan, E. A.; Hoertz, P. G.; Moore, T. A.; Moore, A. L.; Gust, D.; Mallouk, T. E. *J. Am. Chem. Soc.* **2009**, *131*, 926.

(23) Youngblood, W. J.; Lee, S -H. A.; Maeda, K.; Mallouk, T. E. *Acc. Chem. Res.* **2009**, *42*, 1966.

(24) Zong, R.; Thummel, R. P. *J. Am. Chem. Soc.* **2005**, *127*, 12802.

(25) Wang, C.; Xie, Z.; deKrafft, K. E.; Lin, W. *J. Am. Chem. Soc.* **2011**, *133*, 13445.

(26) Fukuzumi, S.; Yamada, Y.; Suenobu, T.; Ohkubo, K.; Kotani, H. *Energy Environ. Sci.* **2011**, *4*, 2754.

(27) Le Goff, A.; Artero, V.; Jousselme, B.; Tran, P. D.; Guillet, N.; Métayé, R.; Fihri, A.; Palacin, S.; Fontecave, M. *Science* **2009**, *326*, 1384.

(28) Helm, M. L.; Stewart, M. P.; Bullock, R. M.; DuBois, M. R.; DuBois, D. L. *Science* **2011**, *333*, 863.

(29) Chen, Z.; Concepcion, J. J.; Jurss, J. W.; Meyer, T. J. *J. Am. Chem. Soc.* **2009**, *131*, 15580.

(30) Toma, F. M.; Sartorel, A.; Iurlo, M.; Carraro, M.; Parisse, P.; Maccato, C.; Rapino, S.; Gonzalez, B.R.; Amenitsch, H.; Da Ros, T.; Casalis, L.; Goldoni, A.; Marcaccio, M.; Scorrano, G.; Scoles, G.; Paolucci, F.; Prato, M.; Bonchio, M. *Nat. Chem.* **2010**, *2*, 826.

(31) Hou, Y.; Cheng, Y.; Hobson, T.; Liu, J. *Nano Lett.* **2010**, *10*, 2727.

(32) Allongue, P.; Delamar, M.; Desbat, B.; Fagebaume, O.; Hitmi, R.; Pinson, J.; Savéant, J. M. *J. Am. Chem. Soc.* **1997**, *119*, 201.

(33) Pinson, J.; Podvorica, F. *Chem. Soc. Rev.* **2005**, *34*, 429.

(34) Engstrom, R. C.; Strasser, V. A. *Anal. Chem.* **1984**, *56*, 136.

(35) Boutadla, Y.; Al-Duaij, O.; Davies, D. L.; Griffith, G. A.; Singh, K. *Organometallics* **2009**, *28*, 433.

(36) Chen, Z.; Concepcion, J. J.; Hu, X.; Yang, W.; Hoertz, P. G.; Meyer, T. J. *P. Natl. Acad. Sci. USA* **2010**, *107*, 7225.

(37) Zanello, *Inorganic Electrochemistry: Theory, Practice, and Application;* The Royal Society of Chemistry: Cambridge, 2003.

(38) Ruther, R. E.; Rigsby, M. L.; Gerken, J. B.; Hogendoorn, S. R.; Landis, E. C.; Stahl, S. S.; Hamers, R. J. *J. Am. Chem. Soc.* **2011**, *133*, 5692.

(39) Schley, N. D.; Blakemore, J. D.; Subbaiyan, N. K.; Incarvito, C. D.; D'Souza, F.; Crabtree, R. H.; Brudvig, G. W. *J. Am. Chem. Soc.* **2011**, *133*, 10473.

(40) Grotjahn, D. B.; Brown, D. B.; Martin, J. K.; Marelius, D. C.; Abadjian, M.-C.; Tran, H. N.; Kalyuzhny, G.; Vecchio, K. S.; Specht, Z. G.; Cortes-Llamas, S. A.; Miranda-Soto, V.; van Niekerk, C.; Moore, C. E.; Rheingold, A. L. *J. Am. Chem. Soc.* **2011**, *133*, 19024.

(41) Hong, D.; Murakami, M.; Yamada, Y.; Fukuzumi, S. *Energy Environ. Sci.* **2012**, *5*, 5708.

(42) Wagner, C. D.; Naumkin, A. V.; Kraut-Vass, A.; Allison, J. W.; Powell, C. J.; Rumble, J. R. NIST X-ray Photoelectron Spectroscopy Database. http://srdata.nist.gov/xps/ (accessed June 27, 2011).

(43) Zhou, Z.; Sarova, G. H.; Zhang, S.; Ou, Z.; Tat, F. T.; Kadish, K. M.; Echegoyen, L.; Guldi, D. M.; Schuster, D. I.; Wilson, S. R. *Chem. Eur. J.* **2006**, *12*, 4241.

(44) Kim, S.-H.; Rieke, R. D. *Tetrahedron Lett.* **2009**, *50*, 6985.

(45) Xu, X.; Xi, Z.; Chen, W.; Wang, D. J. *Coord. Chem.* **2007**, *60*, 2297.

(46) Zhang, W.; Sun, W.-H.; Zhang, S.; Hou, J.; Wedeking, K.; Schultz, S.; Fröhlich, R.; Song, H. *Organometallics* **2006**, *25*, 1968.

(47) Ball, R. G.; Graham, W. A. G.; Heinekey, D. M.; Hoyano, J. K.; McMaster, A. D.; Mattson, B. M.; Michel, S. T. *Inorg. Chem.* **1990**, *29*, 2023.

(48) Concepcion, J. J.; Tasi, M.-K.; Muckerman, J. M.; Meyer, T. J. *J. Am. Chem. Soc* **2010**, *132*, 1545.

(49) Takeuchi, K. J.; Thompson, M. S.; Pipes, D. W.; Meyer, T. J. *Inorg. Chem.* **1984**, *23*, 1845.

(50) D'Amours, M.; Bélanger, D. *J. Phys. Chem. B* **2003**, *107*, 4811.